Delft University of Technology

Spatio-Temporal Environment Monitoring Leveraging Sparsity

Roy, Venkat

DOI
10.4233/uuid:f6e26091-5885-4949-b1b0-a388e1bff3d3

Publication date
2018

Document Version
Final published version

Citation (APA)
Roy, V. (2018). *Spatio-Temporal Environment Monitoring Leveraging Sparsity*. [Dissertation (TU Delft), Delft University of Technology]. https://doi.org/10.4233/uuid:f6e26091-5885-4949-b1b0-a388e1bff3d3

Important note
To cite this publication, please use the final published version (if applicable).
Please check the document version above.

Copyright
Other than for strictly personal use, it is not permitted to download, forward or distribute the text or part of it, without the consent of the author(s) and/or copyright holder(s), unless the work is under an open content license such as Creative Commons.

Takedown policy
Please contact us and provide details if you believe this document breaches copyrights.
We will remove access to the work immediately and investigate your claim.

This work is downloaded from Delft University of Technology.
For technical reasons the number of authors shown on this cover page is limited to a maximum of 10.

Spatio-Temporal Environment Monitoring Leveraging Sparsity

Ph.D. Thesis

Venkat Roy

Spatio-Temporal Environment Monitoring Leveraging Sparsity

Proefschrift

ter verkrijging van de graad van doctor
aan de Technische Universiteit Delft,
op gezag van de Rector Magnificus Prof. dr. ir. T.H.J.J. van der Hagen,
voorzitter van het College van Promoties,
in het openbaar te verdedigen op maandag 15 oktober 2018 om 12:30 uur

door

Venkat ROY
Master of Technology, University of Calcutta, India

geboren te Pondicherry, India.

Dit proefschrift is goedgekeurd door de promotoren.

Samenstelling promotiecommissie bestaat uit:

Rector magnificus	voorzitter
Prof. dr. ir. G.J.T. Leus	Technische Universiteit Delft, promotor
Prof. dr. A. Yarovoy	Technische Universiteit Delft, promotor

Onafhankelijke leden:

Prof. dr. ir. H.W.J. Russchenberg	Technische Universiteit Delft
Prof. H. Messer	Tel Aviv University, Israel
Prof. dr. ir. R. Uijlenhoet	Wageningen University and Research
Dr. A. Simonetto	IBM Research, Ireland
Prof. dr. ir. M.C. Veraar	Technische Universiteit Delft (reserve lid)

ISBN # 978-94-6380-073-0

All rights reserved. No part of the material protected by this copyright notice may be reproduced or utilized in any form or by any means, electronic or mechanical, including photocopying, recording or by any information storage and retrieval system, without prior written permission of the author.

Copyright ©2018 by Venkat Roy

Cover design: Linda van Zijp // StudioLIN.

Printed by: proefschriftmaken (www.proefschriftmaken.nl)

To the wonderful world of science and technology...

"....The woods are lovely, dark and deep,
But I have promises to keep,
And miles to go before I sleep,
And miles to go before I sleep."

-Robert Frost, "*Stopping by Woods on a Snowy Evening*".

Summary

Reliable prediction and monitoring of dynamically changing environments are essential for a safer and healthier society. Sensor networks play a significant role in fulfilling this task. The two fundamental aspects of environmental sensor networks (ESNs) include the need for accuracy as well as low-complexity and energy-efficient sensing modalities. One of the wonted challenges of ESNs is high resolution environment monitoring in the presence of sensing overheads (such as number of sensors, battery life, maintenance). Limiting the number of sensing resources yet still guarantee a desired resolution of the unknown environmental field necessitates resource-efficient sensing framework. On the other hand, the physical behavior of many environmental fields can be predicted using statistical models. Cognizance of the physical properties of environmental fields motivates opportunistic sensor placement to dynamically monitor the environment. In this thesis, we present signal processing methods for resource-efficient environment monitoring exploiting the physical properties of environmental fields. We mainly focus on a general class of environmental fields that obey standard physical properties (such as diffusion, advection) responsible for the spatio-temporal evolution of the field.

We first discuss different mathematical representations to link the sensor measurements with the unknown field intensities. Statistical characterizations of different physical properties of environmental fields such as space-time correlation and the dynamics of field propagation are also discussed. A comprehensive environment monitoring framework is presented that encompasses sensor management, measurement accumulation, and field estimation.

We propose a spatio-temporal sensor management method which can be applied for stationary as well as non-stationary environmental fields. We formulate a unified optimization framework that provides the number and the most informa-

tive sensing locations to deploy sensors guaranteeing a desired estimation accuracy in terms of the mean square error (MSE). The main objective is to implement "sparse-sensing" in an environment monitoring perspective while also achieving a prescribed accuracy. We also propose different strategies to solve the proposed optimization problem for both online and offline applications.

We present a practical example of environment monitoring, i.e., dynamic rainfall monitoring using rain-induced attenuation measurements from commercial microwave links. We describe different methods to incorporate some physical properties of rainfall (such as the physics behind the rainfall propagation, spatial effects such as sparsity, correlation etc.) in the dynamic monitoring setup. We also compare the estimation performance of the developed technique with standard estimators such as an extended Kalman filter (EKF).

We extend the proposed sparsity-enforcing spatio-temporal sensor management method for a broader class of environmental fields consisting of a combination of both stationary and non-stationary components. We develop an algorithm for sensor placement followed by field estimation using a kriged Kalman filter (KKF), which is used for the estimation of the aforementioned type of field.

We also consider the scenario, where the prior physical knowledge regarding the environmental field is either unavailable or inaccurate. In these circumstances, we discuss some methods to estimate the underlying dynamics of the field, i.e., the state/process model using the observed measurements. While estimating the process model, we consider both the scenario, where the true value/ground truth of the field is known as well as the scenario where it is unknown.

Contents

Summary **iii**

1 Introduction **1**

1.1 Motivation 1

1.2 Signal processing and environment-monitoring: a brief survey . . 3

1.3 Outline of the thesis 5

1.4 Related contributions 9

2 Environmental Field Estimation: The Signal Processing Perspective **11**

2.1 Measurement models 12

2.1.1 Linear measurement model 12

2.1.2 Non-linear measurement model 13

2.1.3 Measurement noise 13

2.2 Prior information regarding environmental fields 14

2.2.1 Spatial and temporal variability 14

2.2.2 Dynamic models 16

2.2.3 Other prior information 20

2.3 Hierarchical modelling 21

2.4 Sensor management and environment monitoring 21

2.4.1 Description of the proposed environment monitoring framework 21

2.4.2 Mapping of the developed framework to the chapters of the thesis 23

3 Spatio-Temporal Sensor Management for Environmental Field Estimation 25
3.1 Prior art and contributions 26
3.2 Measurement model and problem statement 28
3.2.1 Measurement model 28
3.2.2 Problem statement 30
3.3 Statistical characterization of the field 30
3.4 Estimation performance metric 35
3.4.1 Effect of spatio-temporal correlation 37
3.4.2 Highly correlated fields 37
3.4.3 Uncorrelated fields 38
3.5 Generalized sensor placement problem 39
3.6 Iterative saddle point method for sensor placement 40
3.6.1 Primal-dual iterations 41
3.7 Iterative reweighted ℓ_1-norm minimization algorithm to improve sparsity 42
3.7.1 Primal-dual iterations with the iterative reweighted ℓ_1-norm minimization 43
3.8 Simulation result 44
3.8.1 Sensor placement for stationary field estimation 44
3.8.2 Sensor placement for non-stationary field estimation . . . 45
3.8.3 Analysis of the performance metric 51
3.9 Conclusion 53
3.10 Appendix 55

4 Spatio-Temporal Environmental Field Estimation Exploiting Prior Information 57
4.1 Prior art and contributions 58
4.2 Measurement model 62
4.3 Spatio-temporal variability of rainfall 64
4.3.1 Spatial variability of $\mathbf{u}_t$ 64
4.3.2 State model 65
4.4 Dynamic rainfall mapping 67
4.4.1 Limitations of standard EKF 68
4.4.2 Available prior knowledge regarding rainfall field 69
4.4.3 Estimation of $\mathbf{u}_t$ 70
4.4.4 Constrained MAP estimator for $\mathbf{u}_t$ 71

4.5 Selection of the representation basis 71
4.6 Selection of the tuning parameter 73
4.7 Simulation results 74
4.7.1 Ground truth with known dynamics 75
4.7.2 Ground truth with unknown dynamics 76
4.7.3 Measurements 78
4.7.4 Dynamic rainfall monitoring 78
4.7.5 Performance metrics 85
4.7.6 Spatial rainfall mapping (no dynamics) 88
4.8 Conclusion 88

5 Spatio-Temporal Sensor Placement for Kriged Kalman Filter (KKF) 91
5.1 Prior art and contributions 92
5.2 Measurement model and problem statement 94
5.2.1 Measurement model 94
5.2.2 Main problem statement 95
5.3 Modelling of the spatio-temporal variability 96
5.3.1 Spatial variability 96
5.3.2 State model 97
5.4 Simple KKF estimator and estimation error covariance 97
5.5 Performance metrics as a function of $\mathbf{w}_t$ 100
5.6 KKF with Sensor Placement 103
5.6.1 Sensor placement problem as an SDP 103
5.6.2 Spatial sensor placement for stationary field estimation . . 107
5.6.3 Sparsity-enhancing iterative design 108
5.6.4 KKF algorithm with sensor placement 109
5.7 Simulation results 109
5.7.1 Sensor placement followed by field estimation using KKF 111
5.7.2 Performance analysis 113
5.7.3 Spatial sensor placement for stationary field estimation . . 116
5.8 Conclusion and Future work 117

6 Dynamic Model Estimation Followed by Field Estimation 121
6.1 Prior art and contributions 122
6.2 Measurement model and problem statement 123
6.2.1 Measurement model 123
6.2.2 State model 123

6.2.3 Problem statement 124
6.3 Estimation of $\mathbf{H}_t$ using the known true value 125
6.3.1 Simulation results 126
6.4 Estimation of $\mathbf{H}_t$ using prior information 126
6.4.1 Modelling assumption of $\mathbf{H}_t$ 128
6.4.2 Estimation of $\mathbf{H}_t$ 130
6.4.3 Dynamics estimation followed by state estimation 131
6.4.4 Simulation results 132
6.5 Conclusion 135

7 Conclusion and Future Research Directions 137
7.1 Conclusions 137
7.2 Future research directions 138

Bibliography 141

Samenvatting 152

Propositions 155

Acknowledgments 157

Curriculum Vitae 161

List of Publications 163

Glossary 165

List of Figures

1.1 Diverse environmental fields and heterogeneous sensing modalities (image courtesy: Google images). 4

2.1 Spherical semivariogram and the covariance function ($N_0 = 0$, $S_0 = 5.3328$ (for rainfall field the unit is mm^2), $d = 17$ km. . . . 16

2.2 Proposed framework for dynamic environment monitoring 22

3.1 Plot of the space-time variation of the covariance function ($s_h = 5;\ s_\tau = 5,\ \sigma_u^2 = 1$). 31

3.2 Spatio-temporal evolution of the field in 10×10 square km area; Spatial resolution: 1×1 square km; $\mathbf{D}_t = \mathbf{I}_2$; $\nu = 0.4$; $\mathbf{q}_t \sim \mathcal{N}(\mathbf{0}_{100}, 10^{-3}\mathbf{I}_{100})$; Displacement due to advection, i.e., $\mathbf{a}_t$ on every snapshot is given by $[0.5, 0.5]^T,\ [1.5, 1.5]^T,\ [0, 2]^T,\ [0, 2]^T,\ [1.5, -1.5]^T,\ [0.5, -1.5]^T,\ [1.5, -1.5]^T$ where $t = 1, \ldots, 7$ min. 34

3.3 MSE variation with s_h and s_τ; ($N = 25,\ N_\mathrm{s} = 4,\ \sigma_u^2 = 1,\ \sigma_e^2 = 0.1$). . 36

3.4 Service area with the candidate sensing locations. 46

3.5 Sensor placement pattern ($s_h = 5;\ s_\tau = 2$) (before randomization). . . 46

3.6 Sensor placement pattern ($s_h = 5;\ s_\tau = 2$) (after randomization). . . . 47

3.7 Sensor placement pattern ($s_h = 7;\ s_\tau = 3$) (before randomization). . . 47

3.8 Sensor placement pattern ($s_h = 7;\ s_\tau = 3$) (after randomization). . . . 48

3.9 Multiple snapshots ahead sensor placement pattern for non-stationary field (before randomization). 48

3.10 Multiple snapshots ahead sensor placement pattern for non-stationary field (after randomization). 49

3.11 Sensor deployment pattern for $\mathbf{H}_t = \mathbf{H}$. 51

3.12 Sensor deployment pattern for a time-varying advection parameter $\mathbf{a}_t$. . 52
3.13 MSE comparison with random sensor placement (stationary field; $N = 100$, $N_\mathrm{s} = 1$). 53
3.14 MSE comparison with random sensor placement (non-stationary field; $N = 25$, $N_\mathrm{s} = 3$). 54
3.15 MSE comparison with random sensor placement (non-stationary field; $N = 100$, $\sigma_e^2 = 1$). 54

4.1 Rainfall intensity (mm/hr) measured by microwave links, rain gauges, and radar, in two places in Israel: (A) Tel-Aviv and (B) Haifa : source of figure *Messer et al.* 2006 [1]. 59
4.2 Proposed dynamic rainfall monitoring framework. 59
4.3 Spatio-temporal evolution of the rainfall (mm) (known dynamics); The matrices $\mathbf{H}_t = \mathbf{H}$ for $t = 2, \ldots, 8$ are known and given in Section 4.7.1. The states are generated using the state model. 77
4.4 Spatio-temporal evolution of the rainfall (mm) (unknown dynamics). The states are generated using the ground truth. 77
4.5 Locations of the M microwave links from where the measurements are collected (area: Amsterdam, The Netherlands). 79
4.6 Estimate of the spatial rainfall (mm) map ($\hat{\mathbf{u}}_2$) with perfectly known dynamics (Figure 4.3); (Algorithm 2). 80
4.7 Estimate of the spatial rainfall (mm) map ($\hat{\mathbf{u}}_8$) with perfectly known dynamics (Figure 4.3); Algorithm 2. 80
4.8 Estimate of the spatial rainfall (mm) map ($\hat{\mathbf{u}}_2$) with perfectly known dynamics (Figure 4.3); Algorithm 3. 81
4.9 Estimate of the spatial rainfall (mm) map ($\hat{\mathbf{u}}_8$) with perfectly known dynamics (Figure 4.3); (Algorithm 3). 81
4.10 Pixel-wise comparison of the estimates [Algorithm 2 (known dynamics)]. 82
4.11 Pixel-wise comparison of the estimates [Algorithm 3 (known dynamics)]. 82
4.12 Estimate of the spatial rainfall (mm) map ($\hat{\mathbf{u}}_1$) with unknown dynamics (Figure 4.4). 83
4.13 Estimate of the spatial rainfall (mm) map ($\hat{\mathbf{u}}_8$) with unknown dynamics (Figure 4.4). 84
4.14 Pixel-wise comparison of the estimates [Algorithm 3, (Gaussian random walk)]; Performance comparison on real data. 84

4.15 Estimate of the spatial rainfall (mm) map ($\hat{\mathbf{u}}_1$) with unknown dynamics (Figure 4.4) (exploiting only sparsity and non-negativity). . 89
4.16 Estimate of the spatial rainfall (mm) map ($\hat{\mathbf{u}}_8$) with unknown dynamics (Figure 4.4) (exploiting only sparsity and non-negativity). . 89
4.17 Pixel-wise comparison of the estimates (exploiting only sparsity and non-negativity (no dynamics, linear model, performance comparison on real data)). 90

5.1 Squared exponential covariance function for different values of θ (variance $\sigma_{\mathrm{s}}^2 = 1$). 98
5.2 Service area with $N = 36$ candidate sensing locations. 98
5.3 Spatial covariance matrix. 99
5.4 Plot of the condition number of $\mathbf{\Sigma}_{\mathrm{s}}$ vs. θ with different number of candidate sensing locations (N). 100
5.5 MSE of the estimate of $\mathbf{s}_t$ vs. θ for different numbers of candidate sensing locations (N); $M_t = N$; $\sigma_{\mathrm{e}}^2 = 1$; The spatial resolution is increased by representing one pixel of Fig. 5.2 by 4 pixels. 101
5.6 Field distribution at $t = 0$ with a single source: $K = 1$, $\boldsymbol{\rho}_1 = [1.5, 1.5]^T$, $s_1 = 2$, $d_1 = 1$. 110
5.7 Spatio-temporal evolution of $\mathbf{u}_t$ in a 6×6 square km area; Spatial resolution: 1×1 square km; Time varying $\mathbf{H}_t$ for $t = 1, \ldots, 8$; strength of spatial correlation: $\theta = 1$. 112
5.8 Spatio-temporal evolution of $\mathbf{u}_t$ in a 6×6 square km area; Spatial resolution: 1×1 square km; Time varying $\mathbf{H}_t$ for $t = 1, \ldots, 8$; strength of spatial correlation: $\theta = 4$. 112
5.9 Selected sensing locations to estimate the field with the first scenario of the true value. 114
5.10 Selected sensing locations to estimate the field with the second scenario of the true value. 114
5.11 Comparison of the KKF estimate with the true value (Fig. 5.7) with the measurements from the selected locations shown in Fig. 5.9. . 115
5.12 Comparison of the KKF estimate with the true value (Fig. 5.8) with the measurements from the selected locations shown in Fig. 5.10. . 115
5.13 Comparison of the performance metric for the random placement, proposed method, and the best case. 116
5.14 Spatial covariance matrix generated by the squared exponential function ($\sigma_{\mathrm{s}}^2 = 0.01, \theta = 2$) 117

5.15 Randomly generated spatial covariance matrix 118
5.16 Sensor placement pattern for the $\mathbf{\Sigma}_{\mathrm{s}}$ as shown in Fig. 5.14. 118
5.17 Sensor placement pattern for the $\mathbf{\Sigma}_{\mathrm{s}}$ as shown in Fig. 5.15. 119

6.1 Discretized service area with $N = 64$ pixels. 124
6.2 Overall system model with inputs and outputs. 125
6.3 Field distribution at $t = 0$. 127
6.4 Spatio-temporal evolution of $\mathbf{u}_t$ in a 6×6 square km area; Spatial resolution: 1×1 square km. 127
6.5 Estimation comparsion for $N = 36$ pixels for $T = 8$ snapshots. . . 128
6.6 Initial state $\mathbf{u}_0$ at $t = 0$, which is used to initialize Algorithm 4, i.e., $\hat{\mathbf{u}}_{0|0} = \mathbf{u}_0$. 133
6.7 True spatio-temporal evolution of the rainfall field (mm). 133
6.8 Locations of the M microwave links from where the measurements are collected. 134
6.9 Estimated spatio-temporal evolution of the rainfall field (mm). 134
6.10 Estimation comparsion for $N = 625$ pixels for $T = 8$ snapshots. . 135

List of Tables

4.1 Performance comparison with EKF (with thresholding); Perfectly known dynamics ($\sigma_s^2 = 10^{-4},\ \sigma_e^2 = 10^{-3}$). 87
4.2 Performance comparison with EKF (with thresholding); Dynamics is assumed to be a Gaussian random walk ($\sigma_s^2 = 10^{-4},\ \sigma_e^2 = 10^{-3}$). 87

Chapter 1

Introduction

Human interests to know more about the spatial and temporal diversity of environmental fields motivate the development of sophisticated environment monitoring systems. In this era of drastic change of earth environment and expeditious urbanization, advanced environment monitoring is of paramount interest. The fundamental necessities of such a monitoring system mainly include correct prediction of environmental conditions and disaster management, which satisfy both economical and societal needs. In this thesis work, we use statistical signal processing tools to develop opportunistic environment monitoring methods which efficiently utilize the available sensing resources as well as maintain a specified monitoring accuracy. To accomplish the aforementioned task we exploit several physical properties of the environmental fields.

In this chapter, we first elaborate the motivation of the research. Then we present a brief literature survey of the application of signal processing methods in the state-of-the-art environment monitoring techniques. We finally illustrate an outline of the thesis work highlighting the major contributions.

1.1 Motivation

Sensor networks are omnipresent in our everyday life. They are useful both in the form of wired or wireless and micro or macro sensor networks [2], [3]. Specifically, wireless sensor networks (WSNs) are popular because of their flexibility in terms of their deployment and use [2]. Environment monitoring is an important application of wireless sensor networks. Environment monitoring can be performed

by two types of sensor networks. Firstly, a homogeneous sensor network, i.e., a network of dedicated sensors to monitor any specific type of environmental field such as a temperature monitoring network, which only consists of thermal sensors. Secondly, a heterogeneous sensor network [4], which consists of different types of fixed/mobile sensors to monitor a single type or multiple types of environmental fields. An example of a heterogeneous sensor network could be a precipitation monitoring network, where the precipitation is measured using the data collected from rain gauges, radar measurements, microwave link (used for cellular communication) attenuations [5] and reactions of general people in social media (social sensing).

- *Design challenges:* Sensor networks, homogeneous as well as heterogeneous, confront some traditional challenges in terms of their design and implementation. The usual problems include constraints related to the sensing resources (cost, power, life-time of sensor nodes), bandwidth requirements (to communicate between the sensor nodes and the data fusion center/processing unit and/or inter-sensor communication), memory requirements (for high resolution field estimation applications), and maintenance of dedicated sensors (in case of remote deployment).

- *Cognizance of physical properties and smart placement:* One plausible solution of all the aforementioned problems could be minimization of the total number of sensors by optimizing their locations. This can be achieved by a smart sensor placement methodology that maintains the monitoring accuracy and also saves sensing resources.

  For environmental field estimation, the aforementioned cost-effective sensor deployment method can be improved by the proper knowledge of some physical properties of the field. These properties could be related to the spatio-temporal variability of the field. Based on these properties, the prior knowledge can be modelled statistically. When the prior knowledge is already available through a statistical model then the sensor deployment method can be viewed as a *model-driven* approach. When the statistical characteristics of the field are estimated from the available data/measurements then the sensor deployment method can be termed as a *data-driven* approach. The available/estimated statistical properties of the field can also be utilized in the estimation of the field from the measurements collected from the deployed sensors in the selected locations.

Design of a "*resource-efficient environmental sensor network*" is the main motivation of this thesis work. The major research questions addressed in this thesis are mentioned below.

- **How to design a parsimonious (sparse over space and time in terms of sensing resources) environmental sensor network that offers a desired monitoring accuracy?**
- **How to estimate an environmental field with a pre-specified spatio-temporal resolution, using a limited number of sensing resources exploiting the physical properties of the field?**
- **How to efficiently exploit the prior information regarding the environmental field for sensor placement as well as estimation, in both the *model-driven* and the *data-driven* approach?**

We mainly exploit tools from statistical signal processing and linear algebra to solve the opportunistic sensor placement and environmental field estimation problems.

The types of environmental fields can be diverse such as precipitation fields (rain, snow), air pollution, concentration of some specific gas/aerosol in the atmosphere, chemical vapor from volcanic eruption, surface temperature and water vapor concentration, ground layer ozone. The types of heterogeneous sensing equipments can be static sensors like weather radar, rain gauges, microwave links, dedicated fixed sensors for air quality measurement and mobile sensors like robotic sensors, sensors mounted on bikes, smart phone sensors, reaction of people in social media (facebook, twitter etc.). A pictorial representation of the diverse environmental fields and some heterogeneous sensing equipments are shown in Figure 1.1.

The research work performed in this thesis work is partly sponsored by the TU Delft project "Sensing Heterogeneous Information Network Environment (SHINE)" [6]. The main objective of this project was the self-organization of the heterogeneous sensing resources for environment monitoring.

1.2 Signal processing and environment-monitoring: a brief survey

The task of monitoring the spatio-temporal evolution of an environmental field using the measurements from homogeneous/heterogeneous sensors involves many

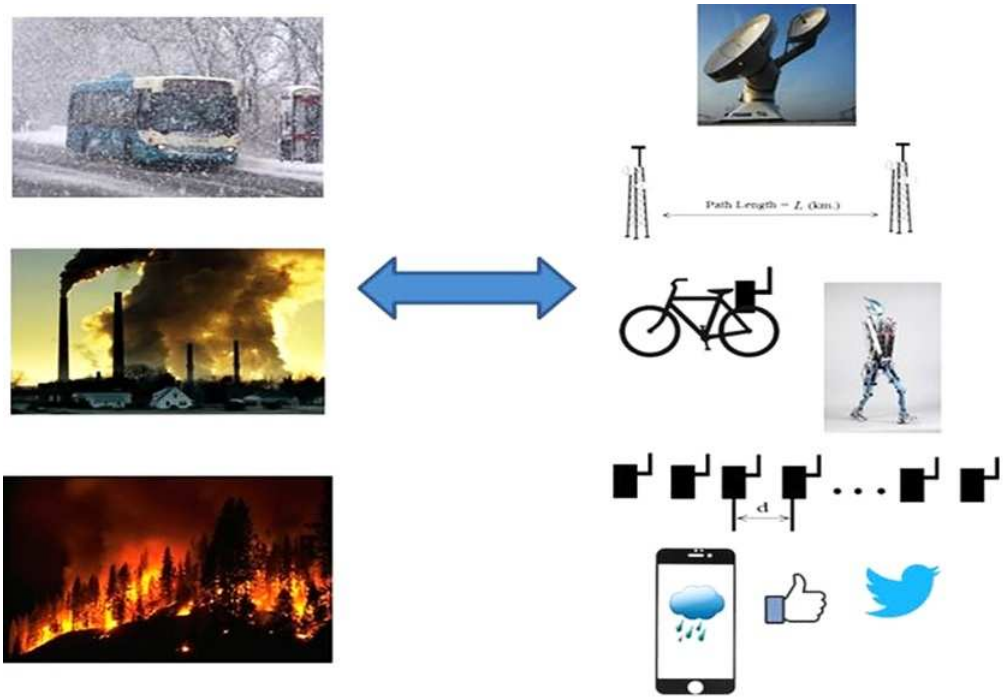

Figure 1.1: Diverse environmental fields and heterogeneous sensing modalities (image courtesy: Google images).

branches of electrical and computer engineering. Statistical signal processing is one of the important tools which can be very useful for modelling, prediction, estimation, noise reduction and outlier rejection for environmental signals. There is a huge plethora of research work available regarding the statistical analysis of environmental data [7]. Here, we mention a few contributions related to the application of signal processing in environment monitoring. However, the detailed literature reviews based on the specific problem statements are presented in every chapter.

The infrastructure and importance of homogeneous as well as heterogeneous environmental sensor networks are presented in [4]. Challenges of practical environment monitoring methods are mentioned in [8] in the context of the "SensorScope" project [9]. Practical problems related to the environment such as estimating the spatio-temporal concentration of radioactive substances in the atmosphere due to nuclear experiments can be modelled as a regularized inverse problem [10]. Signal processing tools can be exploited for outlier rejection in non-Gaussian noise scenarios in inverse problems related to the atmosphere [11]. Tradi-

tional signal processing tools like weighted least squares (WLS) and the extended Kalman filter (EKF) can be used for spatio-temporal rainfall monitoring, where the data are collected from the rain-induced attenuation measurements of the microwave links used for wireless communication [12], [13]. Environment monitoring can be viewed as a field estimation problem, where the detection of the field-generating source (if unknown) and the estimation of the spatio-temporal distribution of the field are equally important. In many cases, the source generates a diffusive field (such as some gas vapor, pollutants, hazardous chemicals). The mathematical analysis of the detection and estimation of the location of these types of sources is presented in [14]. In [15], the source estimation as well as diffusive field reconstruction methods are presented. In [16] a data assimilation algorithm for advection models for cloud motion analysis are developed.

The exploitation of prior statistical knowledge, resulting in Bayesian methods, is also highly cultivated for environment monitoring [17]. Statistical knowledge regarding the spatial variability of the environmental field can be exploited in the interpolation of the field magnitude at the unobserved locations [18]. Prior information regarding the dynamics of the field can be combined with the spatial variability in order to monitor the field dynamically [19], [20]. Statistical knowledge regarding the space-time variability can also be exploited in the design of network protocols for a WSN [21].

In [22], it is shown that in some circumstances the mathematical tool of compressive sensing (CS) [23] can be applied for environment monitoring. The prior knowledge regarding the sparse behavior of the source can be exploited in diffusive field estimation problems [24].

1.3 Outline of the thesis

Chapter 2:

In this chapter, we first discuss the mathematical representation of the models by which the data/measurements and the environmental field to be measured are related. We also present an overview of the different statistical modelling approaches of some physical properties of the environmental fields, which can be used as prior information. As the physical properties of a general class of environmental fields, we include correlation over space and time, dynamics of the field and some spatial properties. Finally, we present a generalized environment monitoring framework that encompasses all the objectives of this thesis. Also, the connections between

the objectives of the chapters and the presented environment monitoring framework are discussed in this chapter.

Chapter 3:

In this chapter, we present opportunistic sensor placement methods over space and time for environmental field estimation. We develop a unified framework to manage the sensing resources when the environmental field is spatio-temporally stationary as well as non-stationary.

The main contributions of this chapter are given below.

- We first present a general time-varying linear measurement model that incorporates the spatio-temporal selection of the locations to deploy the sensors. We discuss how to select at any time the most informative set of sensors such that some predefined estimation accuracy is achieved.
- We present the statistical characterization of a general class of environmental fields for both stationary and non-stationary types. Resorting to the Bayesian philosophy, we develop a generalized performance metric (in terms of mean square error (MSE)) that can be used for sensor placement, when the field is stationary as well as non-stationary.
- We discuss a mathematical framework to efficiently exploit the spatio-temporal correlation information of the environmental field in order to optimize the number of sensing locations.
- We propose a first-order iterative saddle-point method that enforces sparsity in the selection of the informative sensing locations over space and time. We study the spatio-temporal constellation of the selected sensing locations with different statistical characterizations of the field such as a high/low correlation and a time-varying/time-invariant dynamic model.

The contributions of this chapter are published as

- V. Roy and G. Leus, “Correlation-aware sparsity-enforcing sensor placement for spatio-temporal field estimation,” in *Proc. IEEE International Conference on Acoustics, Speech and Signal Processing (ICASSP)*, Brisbane, Australia, April 2015, pp. 340-343.
- V. Roy, A. Simonetto, and G. Leus, “Spatio-temporal sensor management for environmental field estimation,” *Elsevier Signal Processing*, vol. 128, November 2016, pp. 369-381.

Chapter 4:

In this chapter, we present a practical example of environmental field estimation. We consider the application of spatio-temporal rainfall monitoring. Standard precipitation monitoring techniques are generally rain gauges or weather radar. Here, we focus on a recently developed method for rainfall monitoring which is based on the attenuation measurements from microwave links used for wireless communication.

The contributions of this chapter are presented below.

- We first describe the measurement model that represents the mapping between the attenuation measurements and the spatial rainfall distribution (with a predefined resolution) in an area. Because of the measurement type, the model is non-linear, underdetermined and time-varying.

- To estimate the rainfall field from the aforementioned measurement setup we develop a framework that exploits some physical properties of the field such as spatial sparsity (in a suitable representation basis) and non-negativity.

- We develop a sparsity regularized and non-negativity constrained sequential estimator for dynamic rainfall monitoring. The representation basis for the sparsity and the tuning parameter that regulates the amount of sparsity are dynamically tuned for every snapshot.

- Finally, we evaluate the performance of the developed algorithm and also compare it with an ordinary EKF. By several simulation studies, we show that the proposed method outperforms an ordinary EKF, when the rainfall dynamics are not perfectly known.

The contributions of this chapter are published as

- V. Roy, S. Gishkori, and G. Leus, "Spatial rainfall mapping from path- averaged rainfall measurements exploiting sparsity," in *Proc. IEEE Global Conference on Signal and Information Processing (GlobalSIP),*, Atlanta, USA, December 2014, pp. 321-325.

- V. Roy, S. Gishkori, and G. Leus, "Dynamic rainfall monitoring using microwave links," *EURASIP Journal on Advances in Signal Processing*, vol. 2016, no. 1, December 2016, pp. 1-17.

Chapter 5:

In this chapter, we propose a spatio-temporal sensor placement followed by an estimation method for a general class of environmental fields which is the combination of a non-stationary and a stationary component. A typical approach to dynamically monitor these types of fields is the kriged Kalman filter (KKF), which is a combination of kriging (for the estimation of the stationary component) and a Kalman filter (for the estimation of the non-stationary component).

The contributions of this chapter are discussed below.

- We address the fact that when the environmental field has both a stationary and non-stationary component, the stationary component acts as a spatially correlated noise term while estimating the non-stationary component. We also consider the situation, where the spatial covariance matrix of the stationary component can be highly ill-conditioned.
- We present an analytical formalism to develop a combined performance metric for the estimation of the stationary as well as the non-stationary component of the field. We use this metric for sparsity-enforcing sensor placement using a KKF. The proposed methodology tackles the aforementioned situations of correlated noise and an ill-conditioned spatial covariance matrix.
- Finally, we present a semidefinite programming (SDP) approach for sparsity-enhancing sensor placement that incorporates a flexible resource constraint. The selected sensing locations over time are used for field estimation using a simple KKF.

The contributions of this chapter are submitted as

- This chapter is submitted as: V. Roy, A. Simonetto, and G. Leus, "Spatio-temporal field estimation using kriged Kalman filter (KKF) with sparsity-enforcing sensor placement, submitted to *Sensors*, April, 2018.

Chapter 6:

In the aforementioned chapters, we mainly discuss sensor placement and field estimation methods assuming that the prior statistical information regarding the field is perfectly known. But in many practical scenarios this is not the case. In this chapter, we discuss some methods by which we can estimate the prior knowledge regarding the field using the measurements.

The contribution of this chapter are given below.

- We consider the dynamics/process model of the field as prior information, which we need to estimate from the available measurements. We consider both the scenarios, where the true value/ground truth of the field is perfectly known and unknown.
- We consider the measurement model to be linear and develop a sparsity-leveraging method for the estimation of the process model. The estimated process model is then used for prediction in the sequential estimation of the field using a Kalman filter.

Chapter 7:

We review the key contributions of the thesis and present the conclusions in this chapter. Finally, the future research directions are highlighted.

1.4 Related contributions

In this thesis, we have mainly considered the application of environmental field estimation. But the developed framework of sensor management can be equivalently applied for localizing a target. We have used a similar framework as described in Chapter 3 for sensor selection for direction of arrival (DOA) estimation. One example application of this technique is the off-line selection of antennas, while planning stations for radio astronomy in which resources like the number of antennas, available aperture etc. are already known, and are generally limited.

The aforementioned work is briefly described below.

- We propose a method for array design for a linear array with fixed aperture and inter-element spacing.
- We formulate the array design as a sensor selection problem, where the array element selection is performed such that it achieves a desired Cramér-Rao bound (CRB) for estimating the DOA of a single source.
- The sidelobes generated due to the nonuniformity of the sensor selection are suppressed in a specified angular sector via sensor selection.
- We cast the aforementioned problems as a combined semidefinite programming (SDP) problem.

The work is published as

- V. Roy, S. P. Chepuri, and G. Leus, “Sparsity-enforcing sensor selection for DOA estimation,” in *Proc. IEEE Computational Advances in Multi-Sensor Adaptive Processing (CAMSAP)*, Saint Martin, December 2013, pp. 340-343.

Chapter 2

Environmental Field Estimation: The Signal Processing Perspective

One of the principle objectives of any environmental sensor network (ESN) [4], [9] is to extract meaningful information from the observed data. The observations or measurements are generally collected over space and time by homogeneous and/or heterogeneous sensing equipments. Spatio-temporal measurements collected either in a centralized or distributed manner are corrupted by different kinds of noises incurred in the measurement process. Statistical signal processing tools can be leveraged to model the sensor measurements, to estimate the field from these measurements, and also to model the prior knowledge about the physical properties of the field to be estimated. Further, the modelled prior knowledge along with the collected measurements can be exploited to dynamically monitor the field in an efficient manner.

In this chapter, we describe the mathematical representations of the different types of measurement models used in this thesis work. We also present a brief review of the existing modelling approaches of the spatio-temporal variability and dynamic models for a general class of environmental fields. Finally, we discuss a generalized spatio-temporal field monitoring framework, which can be viewed as a backbone of all the spatial/temporal/spatio-temporal field estimation setups used in the rest of the chapters of this thesis.

The outline of the chapter is as follows. In Section 2.1, we discuss different types of measurement models. The different statistical modelling approaches for the prior information regarding the environmental field are presented in Section

2.2. The concept of hierarchical modelling of the data and the prior information is presented in Section 2.3. In Section 2.4, we present the architecture of a generalized dynamic environment monitoring framework.

2.1 Measurement models

We denote the unknown physical field as $u_t(\mathbf{x})$, which is a continuous function of the location index $\mathbf{x} \in \mathbb{R}^2$ and $t \in \mathbb{R}$ is a time index. We consider a uniform spatial discretization of the entire service area of interest into a set of N spatial points given by $\{\mathbf{x}_1, \ldots, \mathbf{x}_N\}$. These points are considered as the points of interest (POI), where we would like to estimate the field. The overall unknown field vector at time t is denoted by $\mathbf{u}_t = [u_t(\mathbf{x}_1), \ldots, u_t(\mathbf{x}_N)]^T$. The aforementioned representation can be used to represent a uniform tessellation of the entire service area, where the set of N points given by $\{\mathbf{x}_1, \ldots, \mathbf{x}_N\}$ defines N pixels of the same area. The area of a pixel is decided by the required spatial resolution. We also make an assumption that the magnitude of the field is the same everywhere within a pixel.

The measurements/observations collected by the sensors can be related to the physical field vector by a measurement/data/observation model. Mathematically, a generalized measurement model can be represented by

$$y_{i,t} = \phi_{i,t}(u_{j,t}) + e_{i,t},\ i = 1, \ldots, M,\ j = 1, \ldots, N, \tag{2.1}$$

where $y_{i,t}$ is the i-th spatial measurement and $u_{j,t} = u_t(\mathbf{x}_j) = [\mathbf{u}_t]_j$ is the magnitude of the field at location $\mathbf{x}_j$ at time t. The function $\phi_{i,t}(\cdot)$ describes the mapping between the true value of the field and the i-th measurement at time t. The parameter $e_{i,t}$ is the noise incurred in the measurement process, which is assumed to be additive in nature.

2.1.1 Linear measurement model

A simplification of the generalized measurement model of (2.1) is a linear measurement model. Considering all the M measurements at time t as mentioned in (2.1), a linear measurement model can be represented in matrix vector form as

$$\mathbf{y}_t = \mathbf{\Phi}_t \mathbf{u}_t + \mathbf{e}_t, \tag{2.2}$$

where $\mathbf{y}_t \in \mathbb{R}^M$ represents the M measurements at time t. The $M \times N$ matrix $\mathbf{\Phi}_t$ is generally termed as the measurement/observation/sensing matrix. The noise components associated with the M measurements are given by $\mathbf{e}_t \in \mathbb{R}^M$. Based

on the number of available measurements (M) and the dimension of the unknown field vector (N), a linear measurement model can be underdetermined, i.e, $M < N$ or overdetermined, i.e, $M > N$. Depending upon the application, the elements of the measurement matrix could be real or complex.

One simple example of a linear measurement model is $\mathbf{\Phi}_t \in \{0, 1\}^{M \times N}$. In this case, if $[\mathbf{\Phi}_t]_{ij} = 1$ for some j and $[\mathbf{\Phi}_t]_{ij} = 0$ for the other j's, where $j = 1, \ldots, N$, then it can be considered that the i-th measurement is a noisy version of the field value at the j-the pixel. A more general representation of the measurement matrix assumes that $\mathbf{\Phi}_t \in \mathbb{R}^{M \times N}$. In this case, the rows of $\mathbf{\Phi}_t$ are modelled as real regression vectors to represent the i-th measurement as a weighted linear combination of the elements of $\mathbf{u}_t$.

2.1.2 Non-linear measurement model

The non-linear version of the generalized measurement model of (2.1) can be represented as

$$\mathbf{y}_t = \mathbf{\Phi}_t(\mathbf{u}_t) + \mathbf{e}_t, \tag{2.3}$$

where $\mathbf{\Phi}_t(\cdot) : \mathbb{R}^N \rightarrow \mathbb{R}^M$ is a non-linear mapping between the true field values and the measurements. In the context of environment monitoring applications, a practical example of a non-linear measurement model is measuring the rainfall depth in a given area, where the measurements are computed using the rain-induced attenuations of the microwave links present in that area [12] [25]. A detailed description of the aforementioned measurement model is presented in Chapter 4.

2.1.3 Measurement noise

The collected observations from different sensing equipments over space and time are corrupted by errors. These errors in the measurement process are generally modelled as measurement noise. The measurement noise can originate from electronic noise, calibration errors of the data collecting devices, weather related impairments (for outdoor monitoring networks), maintenance related issues, human related errors, etc. Due to the lack of knowledge regarding the true magnitude and uncertain behavior of these noise components, they are generally modelled as stochastic processes [7].

It is generally assumed that the measurement noise is independent of the true field to be estimated. But the noise components can be correlated over space or time [26] or spatio-temporally uncorrelated. In this thesis, we have considered both

of the aforementioned types of measurement noises. The probability distribution function (pdf) of the measurement noise can vary with the type of the measurement procedure.

2.2 Prior information regarding environmental fields

The knowledge regarding the physical properties of the environmental fields can be statistically modelled as prior information. This prior information can be exploited for the field estimation as well as for placing the sensors in the informative locations. Generally, the field is modelled as a random process and categorized as a spatio-temporally stationary or non-stationary process. However, physical information can also be exploited, when it is assumed that the field is deterministic.

2.2.1 Spatial and temporal variability

Let us consider that the field at time t is represented by an N dimensional discrete random process $\mathbf{u}_t = [u_t(\mathbf{x}_1), \ldots, u_t(\mathbf{x}_N)]^T$. In order to interpolate the field at all the N POIs over time, information regarding the space-time variability of the field can be exploited along with the measurements. The spatio-temporal nature of the field in a specified geographic area can be characterized by the trend and the space-time interaction of the field between different regions of the given area. These can be modelled as the first and the second order statistics of the field. The mean and the covariance of the field can be represented as,

$$\mathbb{E}[u_t(\mathbf{x}_j)] = \mu_t(\mathbf{x}_j), \tag{2.4}$$

$$\begin{aligned} \mathrm{cov}[u_{t_1}(\mathbf{x}_i), u_{t_2}(\mathbf{x}_j)] &= \mathbb{E}[(u_{t_1}(\mathbf{x}_i) - \mu_{t_1}(\mathbf{x}_i))(u_{t_2}(\mathbf{x}_j) - \mu_{t_2}(\mathbf{x}_j)] \\ &= f(\mathbf{x}_i, \mathbf{x}_j; t_1, t_2), \end{aligned} \tag{2.5}$$

where $i, j = 1, \ldots, N$. The function $f(\mathbf{x}_i, \mathbf{x}_j; t_1, t_2)$ is defined as a covariance function which can be modelled as a parameterized function. It should be noted that the parameters of $f(\mathbf{x}_i, \mathbf{x}_j; t_1, t_2)$ or the value of $\mathrm{cov}[u_{t_1}(\mathbf{x}_i), u_{t_2}(\mathbf{x}_j)]$ can be empirically estimated from the available data. The covariance function can be separable as well as non-separable in space and time dimensions [27]. A valid covariance function $f(\mathbf{x}_i, \mathbf{x}_j; t_1, t_2)$ needs to satisfy some mathematical conditions [27], [7].

Spatio-temporal stationarity

A field is considered to be spatio-temporally *second order stationary / weakly stationary / wide sense stationary (WSS)* and *isotropic* if the following conditions are satisfied [28], [7]:

$$\mathbb{E}[u_t(\mathbf{x}_j)] = \mu,\ \forall t,\ j = 1, \ldots, N \tag{2.6}$$

$$\mathrm{cov}[u_{t_1}(\mathbf{x}_i), u_{t_2}(\mathbf{x}_j)] = f(\|\mathbf{x}_i - \mathbf{x}_j\|_2; t_1 - t_2). \tag{2.7}$$

The notion of stationarity can also be defined individually for space or time [7].

Variogram and covariance

In spatial statistics, one important measure of spatial variability for a WSS discrete spatial random process $u_t(\mathbf{x}_i)$ can be expressed by the variogram $2\gamma(\mathbf{x}_i, \mathbf{x}_j)$, or semi-variogram $\gamma(\mathbf{x}_i, \mathbf{x}_j)$, for all $i, j = 1, \ldots, N$. This metric is widely used in spatial prediction or kriging [29]. Mathematically, the variogram can be defined as

$$2\gamma(\mathbf{x}_i, \mathbf{x}_j) = \mathrm{var}[u_t(\mathbf{x}_i) - u_t(\mathbf{x}_j)] = \mathbb{E}[(u_t(\mathbf{x}_i) - u_t(\mathbf{x}_j))^2]. \tag{2.8}$$

The semivariogram can also be related to the spatial covariance between the locations $\mathbf{x}_i$ and $\mathbf{x}_j$ as

$$\begin{aligned}\gamma(\mathbf{x}_i, \mathbf{x}_j) &= \frac{1}{2}\mathrm{var}[u_t(\mathbf{x}_i) - u_t(\mathbf{x}_j)] \\ &= \frac{1}{2}\mathbb{E}[(u_t(\mathbf{x}_i) - \mu)^2] + \frac{1}{2}\mathbb{E}[(u_t(\mathbf{x}_j) - \mu)^2] - \mathbb{E}[(u_t(\mathbf{x}_i) - \mu)(u_t(\mathbf{x}_j) - \mu)] \\ &= \sigma_u^2 - \mathrm{cov}(u_t(\mathbf{x}_i), u_t(\mathbf{x}_j)). \end{aligned} \tag{2.9}$$

Here, we consider that the variance of the stationary field is given by $\sigma_u^2 = \mathbb{E}[(u_t(\mathbf{x}_i) - \mu)^2] = \mathbb{E}[(u_t(\mathbf{x}_j) - \mu)^2]$.

One common example of a semivariogram is a spherical semivariogram function used for modelling precipitation [30] [31]. Considering spatial stationarity and isotropy, the spherical semivariogram model can be expressed as

$$\gamma(h) = \begin{cases} N_0 + S_0 \left[\frac{3h}{2d} - \frac{h^3}{2d^3}\right] & \text{if } 0 < h \leq d, \\ N_0 + S_0 & \text{if } h > d, \end{cases} \tag{2.10}$$

where $h \triangleq \|\mathbf{x}_i - \mathbf{x}_j\|_2$ is the distance between two locations. The parameters that characterize a variogram model are the sill $N_0 + S_0$ of the variogram ($\gamma(h)$

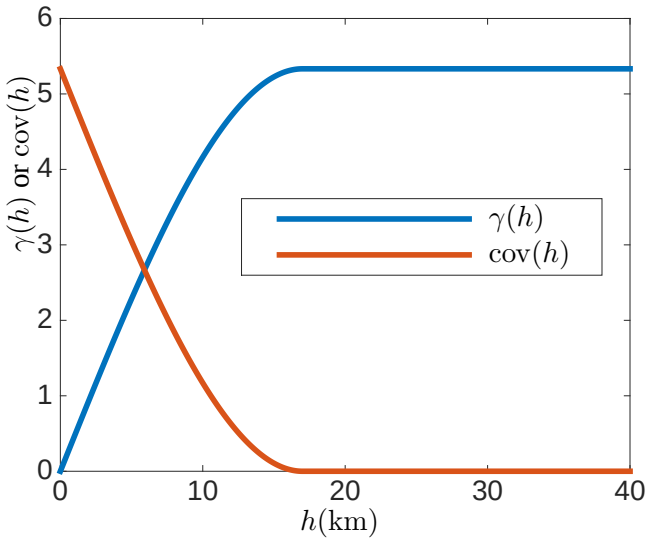

Figure 2.1: Spherical semivariogram and the covariance function ($N_0 = 0$, $S_0 = 5.3328$ (for rainfall field the unit is mm^2), $d = 17$ km.

for $h \to \infty$) with S_0 as the partial sill, the nugget N_0 (non-zero value of $\gamma(h)$ for $h \to 0$), and the range d (value of h for which the variogram reaches the sill). Assuming second-order stationarity, as discussed before, the covariance function can be expressed as a function of h by $\mathrm{cov}(h) = (N_0 + S_0) - \gamma(h)$ [28]. An example of a spherical variogram and the corresponding covariance function is plotted in Fig. 2.2.1.

2.2.2 Dynamic models

The spatio-temporal evolution of the environmental processes can be described by different dynamic models. There are both deterministic as well as stochastic approaches to model the dynamics of the environmental fields.

Partial differential equation (PDE) based modelling

Different physical phenomena responsible for the spatio-temporal evolution of environmental fields can be mathematically expressed by PDEs. Some examples of these phenomena are diffusion, advection, convection and their combined effects.

As before, let us consider that $u_t(\mathbf{x})$ represents a spatio-temporally continuous and deterministic envtironmental field. The diffusion phenomenon can then be

expressed as

$$\frac{\partial u_t(\mathbf{x})}{\partial t} = \nabla \cdot [\mathbf{D}\nabla u(\mathbf{x}, t)], \tag{2.11}$$

where $\nabla = [\frac{\partial}{\partial \mathbf{x}}, \frac{\partial}{\partial \mathbf{y}}]$ is the gradient operator, $\mathbf{D} \in \mathbb{S}^2_{++}$ is the diffusion coefficient/diffusivity, and $\cdot$ is the vector dot product or inner product. Similarly, the advection phenomenon, i.e, the transition of some field (e.g. some particle, pollutant, some specific gas, water vapour) due to the influence of some velocity vector field [7] (e.g., wind) can be represented by

$$\frac{\partial u(\mathbf{x}, t)}{\partial t} + \mathbf{a} \cdot \nabla u(\mathbf{x}, t) = 0, \tag{2.12}$$

where $\mathbf{a}$ is the velocity vector field, which is considered to be solenoidal, i.e, $\nabla.\mathbf{a} = 0$. The combined effect of both diffusion and advection phenomena can be observed in many environmental fields (e.g., movement of pollutants, rainfall [32]).

The aforementioned modelling of the dynamics can also be represented in a stochastic framework, where the field can be modelled as a stochastic variable and a random noise term (also known as a stochastic forcing term) is added to the PDEs (2.11), (2.12) [32]. In such scenarios, the dynamic model is a stochastic partial differential equation (SPDE) [33], [32].

Integro-difference equation (IDE) based modelling

When the field dynamics are modelled using a PDE as mentioned in the previous section, it is generally considered that the field is spatio-temporally continuous. Another modelling approach, where it is considered that the field is spatially continuous but temporally discrete is the integro-difference equation (IDE) based dynamical model [34] [35]. A discrete time IDE with a stochastic process noise term can be represented by

$$u_t(\mathbf{x}) = \int_{\mathcal{A}} h(\mathbf{x}, \mathbf{x}'; \boldsymbol{\theta}) u_{t-1}(\mathbf{x}') d\mathbf{x}' + q_t(\mathbf{x}), \quad \mathbf{x}' \in \mathcal{A} \subset \mathbb{R}^2, \tag{2.13}$$

where $q_t(\mathbf{x})$ is generally modelled as a spatially coloured yet temporally white process noise term. The function $h(\mathbf{x}, \mathbf{x}'; \boldsymbol{\theta})$ models the spatio-temporal interaction of the field which is parameterized by a set of time-varying or time-invariant deterministic or random parameters $\boldsymbol{\theta}$. The parameters of the interaction function can also depend on the temporal sampling interval.

Spatio-temporally discrete process model

Let us consider that the field is spatially discrete over N pixels as well as temporally discrete. At time t, the spatial field distribution is represented by the N dimensional field vector $\mathbf{u}_t$. In this case, a generalized discrete-time process model can be written as

$$\mathbf{u}_t = \mathbf{H}_t(\mathbf{u}_{t-1}) + \mathbf{q}_t, \tag{2.14}$$

where $\mathbf{H}_t(\cdot) : \mathbb{R}^N \to \mathbb{R}^N$ is a non-linear mapping representing the spatio-temporal interaction of the field. A simplified version of (2.14) is a linear state model given by $\mathbf{u}_t = \mathbf{H}_t\mathbf{u}_{t-1} + \mathbf{q}_t$, where $\mathbf{H}_t \in \mathbb{R}^{N\times N}$ is also known as a propagator matrix/state transition matrix and $\mathbf{q}_t \in \mathbb{R}^N$ is the process noise vector. The elements of the state transition matrix can be perfectly known a priori or estimated from the data or modelled by some parametric function (e.g., Gaussian dispersal kernel [35]) whose parameters can be either deterministic or random. Possibly, the simplest example of a linear process model can be a scaled Gaussian random walk model, where $\mathbf{H}_t = \alpha\mathbf{I}_N$ with $\alpha < 1$ a scaling parameter. It should be mentioned here that the maximum eigenvalue of $\mathbf{H}_t$ should be less than 1 to avoid an explosive growth of the process [7].

Markov property

While modelling the spatio-temporal evolution of a stochastic process, a common assumption is the Markov assumption. Let us consider that the joint pdf of the spatio-temporally discrete stochastic process $\mathbf{u}_t$, for $t = 0, \ldots, T$ snapshots is given by $p(\mathbf{u}_0, \ldots, \mathbf{u}_T)$. The joint pdf can be expressed in terms of the conditional dependencies of the states at different times by the following chain rule of probabilities, which can be derived from Bayes' theorem. This is given as

$$p(\mathbf{u}_0, \ldots, \mathbf{u}_T) = p(\mathbf{u}_T|\mathbf{u}_{T-1}, \ldots, \mathbf{u}_0)p(\mathbf{u}_{T-1}|\mathbf{u}_{T-2}, \ldots, \mathbf{u}_0) \ldots p(\mathbf{u}_1|\mathbf{u}_0)p(\mathbf{u}_0). \tag{2.15}$$

The first-order Markov property simplifies the above joint pdf by assuming that the state at time t is solely conditioned by the state at time $t-1$ [7] as was also assumed in (2.14). This gives $p(\mathbf{u}_T|\mathbf{u}_{T-1}, \ldots, \mathbf{u}_0) = p(\mathbf{u}_T|\mathbf{u}_{T-1})$. Based on this assumption, the chain rule in (2.15) can be simplified as

$$\begin{aligned} p(\mathbf{u}_0, \ldots, \mathbf{u}_T) &= p(\mathbf{u}_T|\mathbf{u}_{T-1})p(\mathbf{u}_{T-1}|\mathbf{u}_{T-2}) \ldots p(\mathbf{u}_1|\mathbf{u}_0)p(\mathbf{u}_0) \\ &= p(\mathbf{u}_0)\prod_{t=1}^{T} p(\mathbf{u}_t|\mathbf{u}_{t-1}). \end{aligned} \tag{2.16}$$

The Markov assumption is a common assumption to stochastically model the dynamics of a complex environmental process where the joint pdf is computationally intractable.

Characterization of the process noise

The process noise is generally considered to be a zero mean spatially colored yet temporally white component and indepedendent of the field. However, depending on the field it can also be non-zero mean. In that case, if the mean is known then it can be subtracted from $\mathbf{u}_t$. If the spatial covariance matrix of $\mathbf{q}_t$ is given by $\mathbf{Q}$ then assuming spatial isotropy and stationarity of the random process $\mathbf{q}_t$, the elements of $\mathbf{Q}$ can be represented by the Matèrn covariance function as,

$$[\mathbf{Q}]_{ij} = \sigma_s^2 \frac{2^{1-p}}{\Gamma(p)} \left[\frac{\sqrt{2p}\|\mathbf{x}_i - \mathbf{x}_j\|_2}{\gamma} \right]^p K_p \left(\frac{\sqrt{2p}\|\mathbf{x}_i - \mathbf{x}_j\|_2}{\gamma} \right), \tag{2.17}$$

where $\Gamma(\cdot)$ is the Gamma function, $K_p(\cdot)$ is the modified Bessel function of the second kind, and γ is a positive shaping parameter [7]. With $p \to \infty$ and $p = 1/2$, (2.17) becomes the squared exponential and exponential covariance function, respectively i.e., $[\mathbf{Q}]_{ij} = \sigma_s^2 \exp\left(-\frac{\|\mathbf{x}_i - \mathbf{x}_j\|_2^2}{2\gamma^2}\right)$, and $[\mathbf{Q}]_{ij} = \sigma_s^2 \exp\left(-\frac{\|\mathbf{x}_i - \mathbf{x}_j\|_2}{\gamma}\right)$. The process noise covariance matrix can also be time-varying.

Estimating the dynamic model

In many real circumstances, the underlying dynamics of the process are either unknown or guided by the combination of many complicated physical processes. In these cases, the dynamic model can be estimated using the available measurements. Mathematical tools from the field of *system identification* [36] can be used to compute the process model using the measurements. The process of modelling the dynamics can be broadly classified into two types which are *gray box* and *black box* approaches. In gray box modelling, some physical knowledge regarding the evolution of the process is known but in black box modelling it is assumed that no prior knowledge about the dynamics is available [36]. In a Bayesian setup, for a parameterized state model, if the prior pdf of the parameters are already available, then the posterior pdf can be computed and a Markov chain Monte Carlo (MCMC) method can be used to calculate the model parameters [7], [32] (used for modelling the dynamics of rainfall).

2.2.3 Other prior information

In the previous sections, we discussed the statistical modelling of the correlations over space and time as well as some dynamic models for a general class of environmental fields. Beyond these information, there are many other physical properties of the environmental fields which can be exploited as prior information in the estimation procedure. In this section, we mention two properties of the environmental signals which are extensively used in this thesis.

Sparsity

At any time, the environmental field can be assumed to be a sparsely distributed environmental field over the entire service area. Otherwise, spatial sparsity can also be introduced by representing $\mathbf{u}_t$ in a sparsity-promoting complete or overcomplete dictionary $\mathbf{\Psi}$ [37]. Some examples of complete orthonormal dictionaries include a wavelet, discrete cosine transform (DCT), and Fourier basis. Denoting $\mathbf{u}_t = \mathbf{\Psi}\mathbf{z}_t$, (i.e., $\mathbf{z}_t = \mathbf{\Psi}^{-1}\mathbf{u}_t$ in case of a complete dictionary) sparsity is measured by the number of non-zero entries in $\mathbf{z}_t$, i.e., $\|\mathbf{z}_t\|_0$. Sparsity can also be exploited over time as well, where the field has zero or very low intensity over multiple snapshots.

The aformentioned prior information can be exploited after a convex relaxation, i.e., $\|\mathbf{z}_t\|_1$, as a sparsity-promoting prior in the field reconstruction problem for a underdetermined measurement setup [23], [38]. It has already been proved that an ℓ_1 regularized reconstruction method is very helpful, when the number of measurements is much smaller than the dimension of the unknown sparse signal. This has been successfully implemented in many fields such as image processing, seismology, localization and tracking, radar applications [23]. The use of an ℓ_1 prior can also be viewed in a Bayesian perspective, where the prior pdf on the signal is assumed to be a Laplace distribution [38].

Non-negativity

In many environmental applications, the unknown field to be estimated can be assumed to be non-negative (such as a rainfall field). In this case, the prior information $\mathbf{u}_t \geq \mathbf{0}_N$ (element-wise inequality) can be used as a constraint to restrict the solution to remain in the non-negative orthant. This helps to avoid the generation of an unrealistic estimate and helps maintaining the accuracy of a sequential estimator, where the estimate of the current snapshot is predicted by the past estimate

and corrected by the measurement.

2.3 Hierarchical modelling

In the aforementioned sections, we have briefly illustrated different methods of data collection, i.e., measurement models. We have also discussed different modelling approaches of the prior information regarding the environmental fields. All of these can be represented in a hierarchical fashion, where at any time instance t, the available measurements are given by $\mathbf{y}_t$, the unknown stochastic field vector is given by $\mathbf{u}_t$, and the prior information regarding the field is characterized by a stochastic or deterministic parameter vector $\boldsymbol{\theta}_t$. For example, the process model in (2.13) is parameterized by the set of parameters θ. It should be noted that the measurements are conditioned on the unknown field and the field is conditioned on the parameters governing the field, i.e, $\boldsymbol{\theta}_t$. Depending on the statistical nature of the parameters $\boldsymbol{\theta}_t$, i.e, stochastic or deterministic, there are two types of hierarchical modelling approaches which are Bayesian hierarchical modelling (BHM) and empirical hierarchical modelling (EHM), respectively [7] [39] .

2.4 Sensor management and environment monitoring

As discussed in Chapter 1, one of the most wonted problems of dynamic environmental monitoring using an ESN is the handling of the resource related constraints. These include the sensing hardware cost, memory requirements, life-time related issues, bandwidth etc. Under these circumstances, efficient utilization of the sensing resources is desirable in order to perform the monitoring task with a desired accuracy using a limited number of resources. We propose a centralized multi-step approach for dynamic environment monitoring with opportunistic sensor placement.

2.4.1 Description of the proposed environment monitoring framework

The overall block diagram of the proposed environment monitoring framework is presented in Fig. 2.2.

Inputs:

The inputs to the proposed monitoring framework are

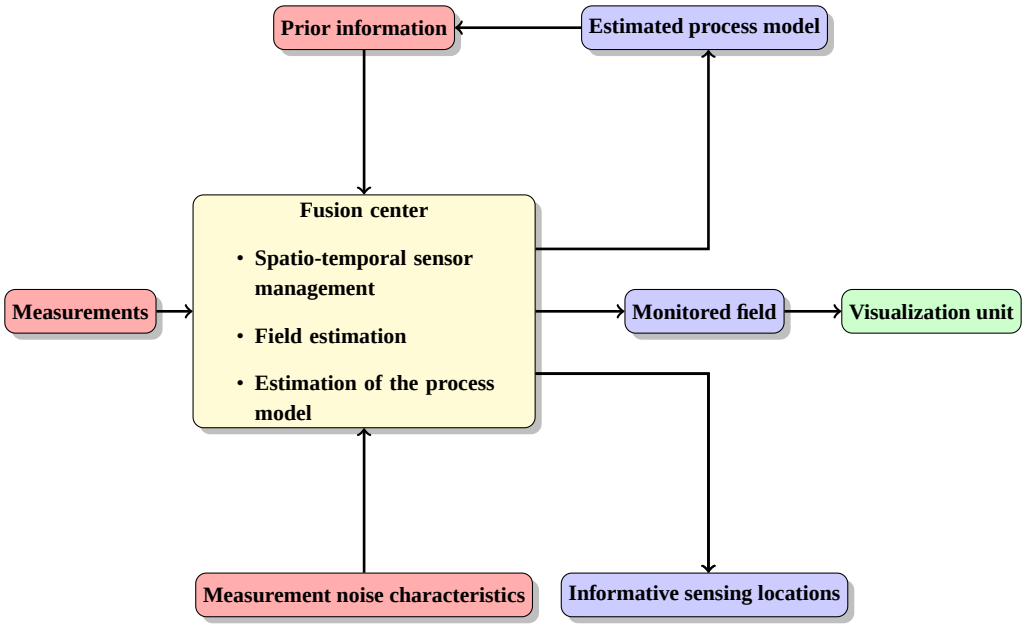

Figure 2.2: Proposed framework for dynamic environment monitoring

- measured spatio-temporal data,
- measurement noise statistics, and
- available prior information regarding the field.

Outputs:

The outputs of the proposed monitoring framework are

- estimated field with a desired resolution,
- informative sensing locations, and
- physical properties of the field
  (if the measurements are used to estimate the process model).

It should be noted that the two principle objectives of the presented model are *spatio-temporal sensor placement* and *field estimation*. These two aforementioned tasks can be performed either on a *single snapshot* basis or on a *multiple snapshot* basis depending upon the availability of the data and the computational resources.

2.4.2 Mapping of the developed framework to the chapters of the thesis

The blockdiagram shown in Fig. 2.2 encompasses the objectives of the different chapters of the thesis. The links between the chapters and the different functions of the models are presented as follows.

- Spatio-temporal sensor management ⇒ Chapter 3.
- Dynamic field (rainfall field) estimation exploiting prior information ⇒ Chapter 4.
- Dynamic field estimation using only the measurements from the selected sensing locations ⇒ Chapter 5.
- Estimation of the process model followed by field estimation ⇒ Chapter 6.

Chapter 3

Spatio-Temporal Sensor Management for Environmental Field Estimation

Monitoring an environmental field, e.g., humidity, precipitation, surface temperature, pollution concentration is generally performed by a network of dedicated sensors deployed in an intelligent constellation. The sensitivity of the estimation performance depends strongly on the sensor deployment (static) or movement (dynamic) strategies. In a centralized framework, due to the resource-related constraints of the sensors (e.g., life-time and bandwidth), it is always desirable to use a limited number of sensors to perform the sensing task with a predefined accuracy.

In this chapter, we develop spatio-temporal sensor management methods enforcing sparsity over space as well as time in terms of sensing resources. Leveraging the space-time stationarity, an environmental field can be estimated with a desired spatio-temporal resolution based on recorded measurements. If the field is non-stationary, it can be monitored dynamically based on the collected measurements and predictions can be made through a state model, if known a priori. We develop algorithms to implement sparse sensing, i.e., sensing only the most informative locations in space and time for both spatio-temporally stationary and non-

This chapter is published as: V. Roy, A. Simonetto, and G. Leus, "Spatio-temporal sensor management for environmental field estimation," *Elsevier Signal Processing*, vol. 128, November 2016, pp. 369-381.

stationary field monitoring applications. The selected sensing locations form an underdetermined measurement model which can be used to estimate the field exploiting the prior knowledge regarding the space-time variability of the field. The task of locating the most informative sensing locations can be performed for both multiple snapshots and a single snapshot based on the availability of prior knowledge (space-time correlation and dynamics) regarding the field, available computing power and the application. We formulate the centralized sensor placement problems for the estimation of both stationary and non-stationary fields as relaxed convex optimization problems, constrained by static or dynamic performance criteria.

The outline of the chapter is as follows. In Section 3.1, we present a brief survey of related works and the main contributions of this chapter. The measurement model and the main problem statement are presented in Section 3.2. In Section 3.3, the statistical characterizations of the environmental field are described. The generalized mean square error (MSE) matrix of a linear minimum mean square error (LMMSE) estimator is derived in Section 3.4 for both stationary and non-stationary field estimation problems. In Section 3.5, we formally address the sensor placement problems for both stationary and non-stationary field estimation applications. An iterative saddle point method is formulated in Section 3.6 to solve the proposed sensor placement problems. To enhance the spatio-temporal sparsity in sensor placement, we combine the aforementioned saddle point method with an iterative reweighted ℓ_1-norm minimization algorithm. The iterative sparsity-enhancing saddle point method is presented in Section 3.7. Simulation studies are presented in Section 3.8. The final conclusions are presented in Section 3.9.

3.1 Prior art and contributions

Sensor selection promoting sparsity both for linear as well as non-linear measurement models is extensively studied for field estimation [40], localization [41], and tracking [42] problems. Specifically for spatial field estimation, sparsity-aware kriging [43] and correlation-aware sensor placement [44] promoting sparsity are also proposed. The problem of performance-aware sensor selection constrained by the number of resources has been well-formulated as a convex problem in [45], for statistical A, D, and E optimality criteria [46]. Also a distributed implementation of the sparsity inducing sensor selection problem is presented in [47]. The problem of sensor placement for field estimation has also been solved using tools from network and information theory. In [48], information theoretic approaches are adopted for placing sensors to estimate Gaussian processes, where the submodularity of the

mutual information between the sensor locations is exploited. To monitor a dynamic process, periodic sensor activation and deactivation is optimal for an infinite time horizon [49], and it is shown to be approximately optimal for a finite time window [50]. In [51], a sparsity-enforcing sensor scheduling method is presented and applied to monitor a dynamic field.

Computational complexity is an issue for realistic sensor placement problems, where the service area is quite large. As mentioned earlier, the accuracy-constrained sensor selection problem can be formulated as a convex problem and solved using off the shelf solvers like CVX [52] and SeDuMi [53]. But to select sensing locations over a large service area and/or multiple time snapshots these solvers can be computationally inefficient. In [40] and [51], alternating direction method of multipliers (ADMM) and accelerated proximal gradient method (APGM) algorithms are used to improve the speed of the sensor selection process.

In this work, we select the most informative sensing locations for the estimation of a general class of environmental fields. The main difference of this work with the standard sensor selection literature (like [41], [45], [47], [54]) is the primary measurement model, which we consider to be underdetermined. Resorting to the Bayesian philosophy, we exploit the available prior statistical knowledge regarding the unknown field. In the first case, we model the field as a *spatio-temporally stationary* stochastic process. The spatio-temporal covariance structure is considered to be known as prior information. In the second case, the field is considered to be *non-stationary*, where the prior knowledge comes from the known dynamics. For a non-stationary field, we specifically model the spatio-temporal evolution using a state model incorporating some common physical phenomena present in many environmental processes like diffusion and advection [7].

The estimation of the field intensities with a prescribed resolution can be performed offline based on recorded measurements at different locations over multiple snapshots if the field is spatio-temporally stationary. If the field is non-stationary, then first and second order statistics can be computed multiple snapshots ahead based on the available prior statistics and the dynamics of the field. This allows for dynamic estimation of the non-stationary field multiple snapshots ahead.

In both of these scenarios, it is always useful to know the best time/place to deploy the sensors in order to reduce the number of sensors to economize the overall processing time and power. The importance of sensor placement for stationary and non-stationary environmental field estimation applications is briefly elucidated in the next paragraph.

One plausible application of sensor placement for stationary field estimation

could be the deployment of rain gauges in an area for long term precipitation monitoring, where stationarity is a valid assumption [55]. A dynamic deployment of sensors is needed for spatio-temporal field tracking applications like robotic sensor networks, social sensing, and mobile sensor networks (sensors deployed on vehicles, bikes) for environment monitoring as well as disaster management. For many such applications, it is essential to know the locations where to deploy/move the sensors in the next snapshots. For the aforementioned applications, a single snapshot or multiple snapshots ahead sensor placement method can be applied for the sensor deployment over upcoming snapshots, if the dynamics for the future snapshots are known a priori.

The main contributions of this chapter are summarized below.

- Sensor placement problems for both spatio-temporally stationary and non-stationary environmental field estimation are formulated as convex optimization problems with similar structures but with different Bayesian performance metrics.

- A mathematical framework to efficiently utilize the spatial/temporal correlation information of the environmental field is developed to optimize the required number of sensing locations.

- A first-order iterative sparsity-enhancing saddle-point method is developed to solve the sensor placement problems.

To enforce sparsity in selecting the optimal sensing locations and time instances, we follow the iterative reweighted $\ell_1$minimization technique [56]. Numerical experiments are carried out to select the optimal sensing locations for different stationary and non-stationary environmental field models.

3.2 Measurement model and problem statement

3.2.1 Measurement model

We assume a finite uniform pixelation of the entire service area of interest into N pixels, where we would like to estimate the field intensities. The field intensity at N pixels at time index $t = 1, 2, \ldots$ can be represented by $\mathbf{u}_t \in \mathbb{R}^N$. It is assumed that the field intensities are the same everywhere within a pixel. The elements of $\mathbf{u}_t$ are given by $[\mathbf{u}_t]_j = u_t(\mathbf{x}_j)$, for $j = 1, \ldots, N$, where $u_t(\mathbf{x})$ is the continuous function

representing the field at time t at any arbitrary position $\mathbf{x} \in \mathbb{R}^2$ and $\mathbf{x}_j \in \mathbb{R}^2$ is the centroid of the j-th pixel.

The measurements are given by $\mathbf{y}_t \in \mathbb{R}^{M_t}$, collected from M_t sensing locations (pixels) of the aforementioned service area. Only a single dimension of $\mathbf{u}_t$ is measured by a sensor deployed at any of the N pixels. The measurement model is underdetermined as $M_t < N$. The *linear time-varying underdetermined* measurement model can be constructed as

$$\mathbf{y}_t = \mathbf{C}_t \mathbf{u}_t + \mathbf{e}_t, \tag{3.1}$$

where the measurement matrix $\mathbf{C}_t \in \{0,1\}^{M_t \times N}$ maps M_t measurements from N pixels in $\mathbf{y}_t$. The measurement matrix can be constructed by $\mathbf{C}_t = \mathrm{diag}_X(\mathbf{w}_t)$, where $\mathbf{w}_t = [w_{t1}, \ldots, w_{tN}]^T \in \{0,1\}^N$ is the *sensor location selection vector* for time t, and $\mathrm{diag}_X(\mathbf{w}_t)$ removes the all zero rows from $\mathrm{diag}(\mathbf{w}_t)$. It signifies that if we have $[\mathbf{w}_t]_j = 1(0)$, then the j-the field location is selected (not selected) for sensor deployment at time t. The measurement matrix $\mathbf{C}_t$ is related to the sensor location selection vector $\mathbf{w}_t$ by the relations

$$\mathbf{C}_t^T \mathbf{C}_t = \mathrm{diag}(\mathbf{w}_t); \qquad \mathbf{C}_t \mathbf{C}_t^T = \mathbf{I}_{M_t}. \tag{3.2}$$

The M_t measurements are corrupted by additive spatio-temporally white Gaussian noise $\mathbf{e}_t \sim \mathcal{N}(\mathbf{0}, \sigma_e^2 \mathbf{I}_{M_t})$, where σ_e^2 is the noise variance. Further, we also assume that $\mathbf{e}_t$ is uncorrelated with $\mathbf{u}_t$.

Any spatio-temporal distribution of the field, i.e., the field intensities at the N pixels for any observation window of N_s snapshots, can be represented by the vector $\tilde{\mathbf{u}}_t = [\mathbf{u}_t^T, \ldots, \mathbf{u}_{t+N_\mathrm{s}-1}^T]^T \in \mathbb{R}^{NN_\mathrm{s}}$. In this case, the overall measurement model to estimate the field at N locations over any N_s snapshots can be expressed as

$$\tilde{\mathbf{y}}_t = \tilde{\mathbf{C}}_t \tilde{\mathbf{u}}_t + \tilde{\mathbf{e}}_t, \tag{3.3}$$

where $\tilde{\mathbf{C}}_t = \mathrm{blkdiag}(\mathbf{C}_t, \ldots, \mathbf{C}_{t+N_\mathrm{s}-1}) \in \{0,1\}^{\tilde{M}_t \times NN_\mathrm{s}}$, with $\tilde{M}_t = \sum_{\tau=0}^{N_\mathrm{s}-1} M_{t+\tau}$ and $\mathrm{blkdiag}(\cdot)$ denoting a block diagonal matrix. The measurements are given as $\tilde{\mathbf{y}}_t = [\mathbf{y}_t^T, \ldots, \mathbf{y}_{t+N_\mathrm{s}-1}^T]^T$ of length $\tilde{M}_t$ and the noise components at all snapshots are represented by the vector $\tilde{\mathbf{e}}_t = [\mathbf{e}_t^T, \ldots, \mathbf{e}_{t+N_\mathrm{s}-1}^T]^T$ of the same length as $\tilde{\mathbf{y}}_t$. The noise vector $\tilde{\mathbf{e}}_t$ is spatio-temporally white and characterized by $\tilde{\mathbf{e}}_t \sim \mathcal{N}(\mathbf{0}_{\tilde{M}_t},\ \sigma_e^2 \mathbf{I}_{\tilde{M}_t})$. By using the relation (3.2), we obtain

$$\tilde{\mathbf{C}}_t^T \tilde{\mathbf{C}}_t = \mathrm{blkdiag}(\mathrm{diag}(\mathbf{w}_t), \ldots, \mathrm{diag}(\mathbf{w}_{t+N_\mathrm{s}-1})) \tag{3.4}$$

$$= \mathrm{diag}(\tilde{\mathbf{w}}_t), \tag{3.5}$$

where $\tilde{\mathbf{w}}_t = [\mathbf{w}_t^T, \ldots, \mathbf{w}_{t+N_\mathrm{s}-1}^T]^T$ is the sensor location selection vector for the N locations in all the N_s snapshots.

3.2.2 Problem statement

The optimal placement of the sensors at the informative locations can be formulated as a *sensor location selection* problem, i.e., the design of a selection vector $\tilde{\mathbf{w}}_t \in \{0,1\}^{NN_\mathrm{s}}$. However, generally choosing the best subset of sensing locations achieving some desired estimation performance is a combinatorially complex problem. A standard approach to tackle this problem is to relax it into a convex problem, which can be efficiently solved in polynomial time [45], [47], [41]. In this case, a sparsity-enforcing, performance-constrained design of $\tilde{\mathbf{w}}_t$ can be obtained by solving

$$\hat{\tilde{\mathbf{w}}}_t = \underset{\tilde{\mathbf{w}}_t \in [0,1]^{NN_\mathrm{s}}}{\arg\min} \{\|\tilde{\mathbf{w}}_t\|_1, \ \text{s.t. } g(\tilde{\mathbf{w}}_t) \leq \gamma\}, \tag{3.6}$$

where $g(\tilde{\mathbf{w}}_t)$ is a performance metric expressed as a function of the selection vector, and γ is the desired threshold on the performance. After solving (3.6), we obtain $\tilde{\mathbf{w}}_t \in [0,1]^{NN_\mathrm{s}}$. To generate a Boolean selection vector $\tilde{\mathbf{w}}_t \in \{0,1\}^{NN_\mathrm{s}}$ from $\tilde{\mathbf{w}}_t \in [0,1]^{NN_\mathrm{s}}$, we can adopt the randomized rounding technique of [41] or a simple thresholding. The randomization is done by simply generating random realizations of $\tilde{\mathbf{w}}_t$ with the probability that $[\tilde{\mathbf{w}}_t]_k = 1$ specified by $[\hat{\tilde{\mathbf{w}}}_t]_k$, where $k = 1, \ldots, NN_\mathrm{s}$. The realizations satisfying $g(\tilde{\mathbf{w}}_t) \leq \gamma$ are selected and the minimum ℓ_0 norm realization is picked up, whose support denotes the sparsest optimal sensor placement scheme.

3.3 Statistical characterization of the field

In this work, two statistical characterizations of the field vector $\mathbf{u}_t$ are considered.

Stationary field

In the first case, we consider the elements of $\mathbf{u}_t$, i.e., $[\mathbf{u}_t]_j = u_t(\mathbf{x}_j)$ for $j = 1, \ldots, N$, to be Gaussian random variables. We further assume they are realizations of a spatio-temporally (second-order) stationary isotropic process [7] with mean $\mathbb{E}[u_t(\mathbf{x}_j)] = \mu_\mathrm{s}$ for all t and $j = 1, \ldots, N$. The spatio-temporal covariance matrix is derived from a space-time separable exponential covariance function. For any temporal lag τ, i.e., the time difference between the snapshots $\mathbf{u}_t$ and $\mathbf{u}_{t-\tau}$, and

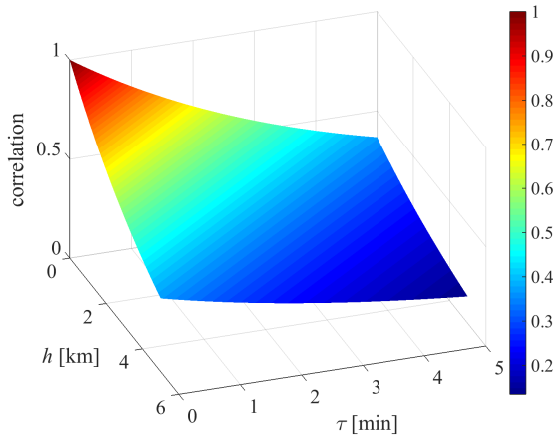

Figure 3.1: Plot of the space-time variation of the covariance function ($s_h = 5;\ s_\tau = 5,\ \sigma_u^2 = 1$).

any two spatial locations $\mathbf{x}_i, \mathbf{x}_j$, with $d_{ij} \triangleq \|\mathbf{x}_i - \mathbf{x}_j\|_2$, the elements of the spatial covariance matrix for lag τ, which is denoted as $\mathbf{\Gamma}_\tau$, are modelled as

$$\begin{aligned}[\mathbf{\Gamma}_\tau]_{ij} &= [\mathbb{E}[(\mathbf{u}_t - \mu_\mathrm{s}\mathbf{1}_N)(\mathbf{u}_{t-\tau} - \mu_\mathrm{s}\mathbf{1}_N)^T]]_{ij} \\ &= \sigma_u^2 \exp[-\frac{1}{s_h} d_{ij} - \frac{1}{s_\tau}|\tau|]. \end{aligned} \tag{3.7}$$

Here, $\mathbb{E}[(u_t(\mathbf{x}_j) - \mu_\mathrm{s})^2] = \sigma_u^2$ and s_h, s_τ are the positive correlation parameters representing the strengths of the spatial and the temporal correlations, respectively. Increasing (or decreasing) s_h and s_τ, we model higher (or lower) spatial and temporal correlations, respectively. We assume that the parameters σ_u^2, s_h and s_τ are all known a priori. The nature of the covariance function of (3.7) with different lags over space and time is shown in Fig. 3.1. The overall spatio-temporal covariance matrix can be expressed as $\tilde{\mathbf{\Gamma}}_t = \mathbb{E}[(\tilde{\mathbf{u}}_t - \tilde{\boldsymbol{\mu}}_t)(\tilde{\mathbf{u}}_t - \tilde{\boldsymbol{\mu}}_t)^T] \in \mathbb{S}_{++}^{NN_\mathrm{s}}$, where $\tilde{\boldsymbol{\mu}}_t = \mathbb{E}[\tilde{\mathbf{u}}_t] = \mu_s \mathbf{1}_{NN_\mathrm{s}}$. The diagonal and off-diagonal blocks of $\tilde{\mathbf{\Gamma}}_t$ are given by

$$\tilde{\mathbf{\Gamma}}_t = \begin{bmatrix} \mathbf{\Gamma}_0 & \dots & \mathbf{\Gamma}_{-N_\mathrm{s}+1} \\ \vdots & \ddots & \vdots \\ \mathbf{\Gamma}_{N_\mathrm{s}-1} & \dots & \mathbf{\Gamma}_0 \end{bmatrix}. \tag{3.8}$$

It should be noted that, if the field is spatio-temporally uncorrelated then the spatio-temporal covariance matrix is simply given as $\tilde{\mathbf{\Gamma}}_t = \sigma_u^2 \mathbf{I}_{NN_\mathrm{s}}$.

Non-stationary field

In the second case, we consider $\mathbf{u}_t$ to be a non-stationary environmental field. The spatio-temporal evolution of the environmental field can be described by an integro-difference equation (IDE) [7]. For a specific sampling interval T_s (i.e., the time duration between two consecutive time indices) the discrete time IDE can be represented as,

$$u_t(\mathbf{x}) = \int_{\mathcal{R}_\mathrm{s}} f(\mathbf{x}, \mathbf{x}') u_{t-1}(\mathbf{x}') d\mathbf{x}' + q_t(\mathbf{x}), \tag{3.9}$$

where $\mathcal{R}_\mathrm{s} \subset \mathbb{R}^2$ is the service area of interest. The spatio-temporal evolution of $u_t(\mathbf{x})$ is modelled by the function $f(\mathbf{x}, \mathbf{x}')$. Here, $q_t(\mathbf{x})$ is the Gaussian process noise which can be spatially coloured but is temporally white. The space-time interaction function $f(\mathbf{x}, \mathbf{x}')$ can be modeled as a time-varying parameterized kernel function $f(\mathbf{x}, \mathbf{x}') = \nu h_t(\mathbf{x}, \mathbf{x}', \boldsymbol{\theta}_t)$, where the parameters of the function, i.e., $\boldsymbol{\theta}_t$, can be deterministic or random. The parameter ν is a positive scaling parameter to ensure the stability of the process [35]. In this case, the IDE is given as

$$u_t(\mathbf{x}) = \nu \int_{\mathcal{R}_s} h_t(\mathbf{x}, \mathbf{x}'; \boldsymbol{\theta}_t) u_{t-1}(\mathbf{x}') d\mathbf{x}' + q_t(\mathbf{x}). \tag{3.10}$$

It should be noted that, the state models in (3.9) and (3.10) are infinite dimensional. One way to approximate these to finite dimensional models is by using a spectral representation of $f(\cdot)$ or $h_t(\cdot)$, and $u_t(\cdot)$ using a known orthonormal basis and selecting only the K dominant coefficients [19].

However, here we have considered a finite uniform spatial discretization of the field into N pixels. A spatio-temporally discrete process model can be represented as

$$u_t(\mathbf{x}_i) = \nu \sum_{j=1}^{N} h_t(\mathbf{x}_i, \mathbf{x}_j; \boldsymbol{\theta}_t) u_{t-1}(\mathbf{x}_j) + q_t(\mathbf{x}_i), \tag{3.11}$$

where $i = 1, \ldots, N$. Here, we assume that the parameters of the kernel function, i.e., $\boldsymbol{\theta}_t$, are perfectly known and deterministic. It should be noted that the parameters of the kernel function can depend upon the temporal sampling interval T_s.

Spatial phenomena like advection and diffusion can be modelled by changing the translation and dilation parameters of a Gaussian kernel [32], [35]. More specifically, we consider a time-varying 2D Gaussian kernel

$$h_t(\mathbf{x}_i, \mathbf{x}_j) = \exp[-(\mathbf{x}_i - \mathbf{x}_j - \mathbf{a}_t)^T \mathbf{D}_t^{-1} (\mathbf{x}_i - \mathbf{x}_j - \mathbf{a}_t)], \tag{3.12}$$

where the translation parameter $\mathbf{a}_t \in \mathbb{R}^2$ and the dilation parameter $\mathbf{D}_t \in \mathbb{S}^2_{++}$ model the advection and the isotropic/anisotropic diffusion, respectively. In this

case, the parameter vector of the kernel function, i.e, $\boldsymbol{\theta}_t$ in (3.11), contains the elements of $\mathbf{a}_t$ and $\mathbf{D}_t$. Here, we model $\mathbf{a}_t$ as the time-varying displacement and $\mathbf{D}_t$ as the time-varying diffusion in every T_s seconds. Note that, $\mathbf{a}_t$ and $\mathbf{D}_t$ can also be varied over space in order to model more complicated dynamics of the field [35]. The directions of anisotropy of diffusion can be incorporated through $\mathbf{D}_t$. Otherwise, isotropic diffusion can be modelled as $\mathbf{D}_t = \kappa_t \mathbf{I}_2$, with $\kappa_t > 0$. For example, like (3.12), modelling the function $h_t(\cdot)$ as a *Gaussian dispersal kernel* can be used for short term rainfall prediction [32]. The above approach can be generalized to describe the dynamics of many environmental phenomena such as the distribution of pollutants, movement of aerosols, vapour concentrations, etc. that possess properties like advection, diffusion, etc.

Let us now assume a state transition/propagator matrix $\mathbf{H}_t \in \mathbb{R}^{N\times N}$ which is modelled using a simple 2D Gaussian kernel whose elements are given by $[\mathbf{H}_t]_{ij} = \nu h_t(\mathbf{x}_i, \mathbf{x}_j)$. After proper vectorization of the field intensities and the process noise for the N pixels, the overall state model can be represented as

$$\mathbf{u}_t = \mathbf{H}_t \mathbf{u}_{t-1} + \mathbf{q}_t. \tag{3.13}$$

Here, $\mathbf{q}_t \sim \mathcal{N}(\mathbf{0}, \mathbf{Q}_t)$ is the spatially colored yet temporally white Gaussian process noise. In Fig. 3.2, an example of the spatio-temporal evolution of the field is shown with a time-invariant isotropic diffusion and a time-varying advection. The initial state of $\mathbf{u}_t$, i.e., the state at $t = 0$ is generated by a simple Gaussian function. In Fig. 3.2, it is seen that the field is isotropically diffused as well as shifted in different directions given by the advection vector $\mathbf{a}_t$ changing with time t.

In this case, the field is statistically characterized by the dynamics as

$$p(\mathbf{u}_t|\mathbf{u}_{t-1}) \sim \mathcal{N}(\mathbf{H}_t\mathbf{u}_{t-1}, \mathbf{Q}_t). \tag{3.14}$$

The N_s snapshots ahead first and second order statistics of the field can be derived using the state model. In this case, the N_s snapshots ahead mean and covariance matrix, i.e., $\tilde{\boldsymbol{\mu}}_t = \mathbb{E}[\tilde{\mathbf{u}}_t]$ and $\tilde{\boldsymbol{\Gamma}}_t = \mathbb{E}[(\tilde{\mathbf{u}}_t - \tilde{\boldsymbol{\mu}}_t)(\tilde{\mathbf{u}}_t - \tilde{\boldsymbol{\mu}}_t)^T]$ can be computed in the following way. Using (3.13), the mean can be computed as

$$\tilde{\boldsymbol{\mu}}_t = \begin{bmatrix} \mathbf{H}_t\mathbb{E}[\mathbf{u}_{t-1}] \\ \mathbf{H}_{t+1}\mathbf{H}_t\mathbb{E}[\mathbf{u}_{t-1}] \\ \vdots \\ \mathbf{H}_{t+N_\mathrm{s}-1}\mathbf{H}_{t+N_\mathrm{s}-2}\ldots\mathbf{H}_t\mathbb{E}[\mathbf{u}_{t-1}] \end{bmatrix} = \begin{bmatrix} \boldsymbol{\mu}_t \\ \boldsymbol{\mu}_{t+1} \\ \vdots \\ \boldsymbol{\mu}_{t+N_\mathrm{s}-1} \end{bmatrix}. \tag{3.15}$$

The time-dependent covariance matrix for any N_s snapshots, i.e., $\tilde{\boldsymbol{\Gamma}}_t$ is given by

$$\tilde{\boldsymbol{\Gamma}}_t = \tilde{\mathbf{R}}_t - \tilde{\boldsymbol{\mu}}_t\tilde{\boldsymbol{\mu}}_t^T, \tag{3.16}$$

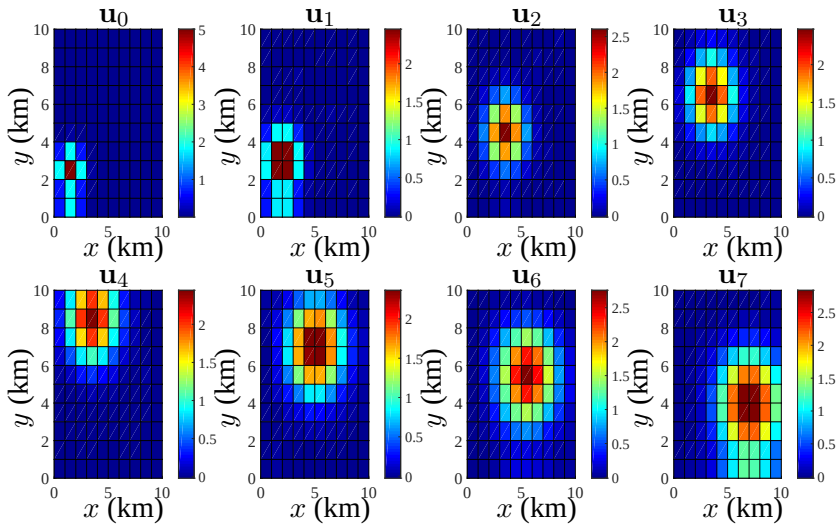

Figure 3.2: Spatio-temporal evolution of the field in 10×10 square km area; Spatial resolution: 1×1 square km; $\mathbf{D}_t = \mathbf{I}_2$; $\nu = 0.4$; $\mathbf{q}_t \sim \mathcal{N}(\mathbf{0}_{100}, 10^{-3}\mathbf{I}_{100})$; Displacement due to advection, i.e., $\mathbf{a}_t$ on every snapshot is given by $[0.5, 0.5]^T$, $[1.5, 1.5]^T$, $[0, 2]^T$, $[0, 2]^T$, $[1.5, -1.5]^T$, $[0.5, -1.5]^T$, $[1.5, -1.5]^T$ where $t = 1, \ldots, 7$ min.

where the correlation matrix $\tilde{\mathbf{R}}_t = \mathbb{E}[\tilde{\mathbf{u}}_t \tilde{\mathbf{u}}_t^T]$ is given by

$$\tilde{\mathbf{R}}_t = \begin{bmatrix} \mathbb{E}[\mathbf{u}_t \mathbf{u}_t^T] & \ldots & \mathbb{E}[\mathbf{u}_t \mathbf{u}_{t+N_\mathrm{s}-1}^T] \\ \vdots & \ddots & \vdots \\ \mathbb{E}[\mathbf{u}_{t+N_\mathrm{s}-1} \mathbf{u}_t^T] & \ldots & \mathbb{E}[\mathbf{u}_{t+N_\mathrm{s}-1} \mathbf{u}_{t+N_\mathrm{s}-1}^T] \end{bmatrix}. \tag{3.17}$$

The diagonal blocks of $\tilde{\mathbf{R}}_t$ are given as

$$\mathbf{R}_{t+\tau} = \mathbb{E}[\mathbf{u}_{t+\tau} \mathbf{u}_{t+\tau}^T] = \mathbf{H}_{t+\tau} \mathbf{R}_{t+\tau-1} \mathbf{H}_{t+\tau}^T + \mathbf{Q}_{t+\tau}, \tag{3.18}$$

where $\tau = 0, \ldots, N_\mathrm{s} - 1$. The general form of the right and left off-diagonal blocks of $\tilde{\mathbf{R}}_t$ can be given for any two temporal lags τ_m and τ_n, where $\tau_m = 0, \ldots, N_\mathrm{s} - 1$, $\tau_n = 0, \ldots, N_\mathrm{s} - 1$ and $\tau_m \neq \tau_n$. The right off-diagonal blocks $(\tau_m < \tau_n)$ are given as

$$\mathbb{E}[\mathbf{u}_{t+\tau_m} \mathbf{u}_{t+\tau_n}^T] = \mathbf{R}_{t+\tau_m} \mathbf{H}_{t+\tau_m+1}^T \ldots \mathbf{H}_{t+\tau_n-1}^T \mathbf{H}_{t+\tau_n}^T, \tag{3.19}$$

and the left off-diagonal blocks $(\tau_m > \tau_n)$ are given as

$$\mathbb{E}[\mathbf{u}_{t+\tau_m} \mathbf{u}_{t+\tau_n}^T] = \mathbf{H}_{t+\tau_m} \mathbf{H}_{t+\tau_m-1} \ldots \mathbf{H}_{t+\tau_n+1} \mathbf{R}_{t+\tau_n}, \tag{3.20}$$

where $\mathbf{R}_{t+\tau_m}$ and $\mathbf{R}_{t+\tau_n}$ can be computed by the recursive relationships of (3.18). Substituting (3.17) into (3.16) and using the expression of (3.15) only the diagonal blocks of $\tilde{\mathbf{\Gamma}}_t$ can be recursively represented as

$$\mathbf{\Gamma}_{t+\tau} = \mathbb{E}[(\mathbf{u}_{t+\tau} - \boldsymbol{\mu}_{t+\tau})(\mathbf{u}_{t+\tau} - \boldsymbol{\mu}_{t+\tau})^T] \tag{3.21}$$

$$= \mathbf{H}_{t+\tau}(\mathbf{R}_{t+\tau-1} - \boldsymbol{\mu}_{t+\tau-1}\boldsymbol{\mu}_{t+\tau-1}^T)\mathbf{H}_{t+\tau}^T + \mathbf{Q}_{t+\tau} \tag{3.22}$$

$$= \mathbf{H}_{t+\tau}\mathbf{\Gamma}_{t+\tau-1}\mathbf{H}_{t+\tau}^T + \mathbf{Q}_{t+\tau}, \tag{3.23}$$

where $\tau = 0, \ldots, N_\mathrm{s} - 1$.

Note that, at any time t, the N_s *snapshots ahead* first and second order statistics of the field can be precomputed if $\mathbb{E}[\mathbf{u}_{t-1}]$, $\mathbf{\Gamma}_{t-1}$, $\mathbf{H}_{t+\tau}$, and $\mathbf{Q}_{t+\tau}$ for $\tau = 0, \ldots, N_s - 1$ are all known a priori. One way to estimate the first and second order statistics of $\mathbf{u}_{t-1}$ is to use a "sequential minimum mean square error (MMSE) estimator", i.e., a standard Kalman filter [57] that uses the previous measurements up to time $t-1$. Let us assume that this estimate is given by $\hat{\mathbf{u}}_{t-1}$, with an estimation error covariance matrix $\mathbf{\Sigma}_{t-1}$, i.e., $\mathbf{\Sigma}_{t-1} = \mathbb{E}[(\mathbf{u}_{t-1} - \hat{\mathbf{u}}_{t-1})(\mathbf{u}_{t-1} - \hat{\mathbf{u}}_{t-1})^T]$. We use these as the first and second order statistics of the state $\mathbf{u}_{t-1}$, i.e., $\mathbf{u}_{t-1} \sim \mathcal{N}(\hat{\mathbf{u}}_{t-1}, \mathbf{\Sigma}_{t-1})$.

3.4 Estimation performance metric

In this section, the performance metric, i.e., $g(\tilde{\mathbf{w}}_t)$ as mentioned in (3.6) is derived for both stationary and non-stationary field estimation problems. In the measurement model of (3.3), the unknown parameter $\tilde{\mathbf{u}}_t$ is statistically characterized by $\tilde{\mathbf{u}}_t \sim \mathcal{N}(\tilde{\boldsymbol{\mu}}_t, \tilde{\mathbf{\Gamma}}_t)$. The mean and the covariance matrix can be computed for both the stationary and the non-stationary fields as mentioned in the previous section.

The unknown parameter $\tilde{\mathbf{u}}_t$ can be estimated using an LMMSE estimator [57], i.e., $\hat{\tilde{\mathbf{u}}}_t = \tilde{\boldsymbol{\mu}}_t + \sigma_e^{-2}(\tilde{\mathbf{\Gamma}}_t^{-1} + \sigma_e^{-2}\tilde{\mathbf{C}}_t^T\tilde{\mathbf{C}}_t)\tilde{\mathbf{C}}_t^T(\tilde{\mathbf{y}}_t - \tilde{\mathbf{C}}_t\tilde{\boldsymbol{\mu}}_t)$. The MSE matrix, i.e., $\mathbb{E}[(\tilde{\mathbf{u}}_t - \hat{\tilde{\mathbf{u}}}_t)(\tilde{\mathbf{u}}_t - \hat{\tilde{\mathbf{u}}}_t)^T]$ is then given by

$$\mathbf{\Sigma}_t(\mathbf{w}_t, \ldots, \mathbf{w}_{t+N_\mathrm{s}-1}) = (\tilde{\mathbf{\Gamma}}_t^{-1} + \sigma_e^{-2}\tilde{\mathbf{C}}_t^T\tilde{\mathbf{C}}_t)^{-1}. \tag{3.24}$$

We mention that (3.24) is considered as the generalized expression (for both stationary and non-stationary field estimation) of the MSE matrix in this work. The performance metric to estimate the field at N locations over N_s snapshots is quantified as $\mathrm{tr}[\mathbf{\Sigma}_t(\mathbf{w}_t, \ldots, \mathbf{w}_{t+N_\mathrm{s}-1})]$ or $\mathrm{tr}[\mathbf{\Sigma}_t(\tilde{\mathbf{w}}_t)]$. By using the relation of (3.5), the performance metric in (3.24) can be written as

$$\mathbf{\Sigma}_t(\mathbf{w}_t, \ldots, \mathbf{w}_{t+N_\mathrm{s}-1}) = (\tilde{\mathbf{\Gamma}}_t^{-1} + \sigma_e^{-2}\mathrm{diag}(\tilde{\mathbf{w}}_t))^{-1}. \tag{3.25}$$

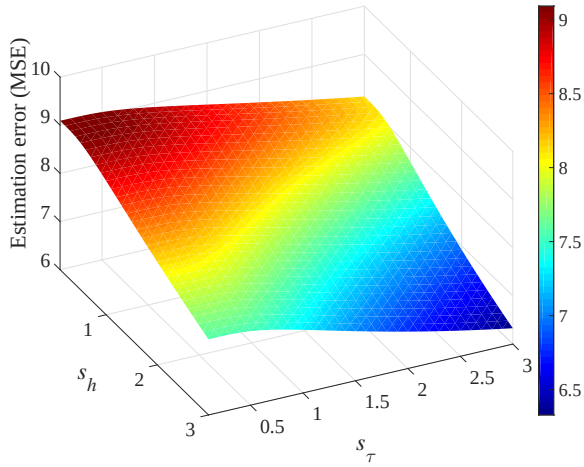

Figure 3.3: MSE variation with s_h and s_τ; ($N = 25,\ N_\mathrm{s} = 4,\ \sigma_u^2 = 1,\ \sigma_e^2 = 0.1$).

Here, we assume that $\tilde{\mathbf{\Gamma}}_t$ is well-conditioned and accurately invertible. We will come back to this issue later on in this section.

Remark (Recursive performance metric) : When the field is non-stationary as mentioned in the previous section, we can use $\mathbf{u}_{t-1} \sim \mathcal{N}(\hat{\mathbf{u}}_{t-1}, \mathbf{\Sigma}_{t-1})$ to compute the N_s snapshots ahead first and second order statistics, i.e, $\tilde{\boldsymbol{\mu}}_t$ and $\tilde{\mathbf{\Gamma}}_t$. The expression of the MSE matrix of (3.25) can be evaluated by substituting $\mathbf{u}_{t-1} \sim \mathcal{N}(\hat{\mathbf{u}}_{t-1}, \mathbf{\Sigma}_{t-1})$ in the recursive relationship of (3.23). After the aforementioned substitutions, for $N_\mathrm{s} = 1$, the performance metric of (3.25), i.e., $\mathbf{\Sigma}_t(\tilde{\mathbf{w}}_t)$, becomes $\mathbf{\Sigma}_t(\mathbf{w}_t)$. This is given as

$$\begin{aligned}\mathbf{\Sigma}_t(\mathbf{w}_t) &= [(\mathbf{H}_t\mathbf{\Sigma}_{t-1}(\mathbf{w}_{t-1})\mathbf{H}_t^T + \mathbf{Q}_t)^{-1} + \sigma_e^{-2}\mathbf{C}_t^T\mathbf{C}_t]^{-1} \\ &= [(\mathbf{H}_t\mathbf{\Sigma}_{t-1}(\mathbf{w}_{t-1})\mathbf{H}_t^T + \mathbf{Q}_t)^{-1} + \sigma_e^{-2}\mathrm{diag}(\mathbf{w}_t)]^{-1}. \qquad (3.26)\end{aligned}$$

This expression is the same as the single snapshot ahead update of the state error covariance matrix of a simple Kalman filter and is an explicit function of the selection vectors at time index t and $t-1$.

We can see that, for a large service area (large N) and/or high N_s, the computations of $\tilde{\boldsymbol{\mu}}_t$ and $\tilde{\mathbf{\Gamma}}_t$ as derived in (3.15) and (3.16), respectively, can be cumbersome from the *real time monitoring* perspective. However, in the simulation section we solve both the single snapshot and the multiple snapshots ahead sensor placement problems.

3.4.1 Effect of spatio-temporal correlation

The parameters s_h and s_τ control the strength of the spatial and temporal correlations, respectively. Increasing these values, the field becomes more correlated over space and time. Also for a fixed noise power, the MSE with all the candidate locations equipped with sensors, i.e., $\mathrm{tr}[\mathbf{\Sigma}_t(\mathbf{1}_N, \ldots, \mathbf{1}_N)]$, reduces as s_h and s_τ jointly increase as shown in Fig. 3.3. From the aforementioned analysis, it can be said that to achieve a desired estimation performance, less sensors are required to estimate a highly space-time correlated field than to estimate a lightly correlated field.

3.4.2 Highly correlated fields

For highly space-time correlated fields the spatio-temporal covariance matrix can be ill-conditioned [58], meaning that $\tilde{\mathbf{\Gamma}}_t$ in (3.25) is close to singular. In that case, the MSE matrix $\mathbf{\Sigma}_t$ can be computed using the alternate expression of (3.25) given by $\mathbf{\Sigma}_t(\mathbf{w}_t, \ldots, \mathbf{w}_{t+N_\mathrm{s}-1}) = \tilde{\mathbf{\Gamma}}_t - \tilde{\mathbf{\Gamma}}_t\tilde{\mathbf{C}}_t^T(\tilde{\mathbf{C}}_t\tilde{\mathbf{\Gamma}}_t\tilde{\mathbf{C}}_t^T + \sigma_e^2\mathbf{I}_{\tilde{M}_t})^{-1}\tilde{\mathbf{C}}_t\tilde{\mathbf{\Gamma}}_t$ which is obtained by applying the matrix inversion lemma (MIL) on (3.25). It should be noted that the alternate expression of the MSE can be used to compute the MSE without inverting ($\tilde{\mathbf{\Gamma}}_t$), but it is difficult to express it as an explicit function of $\mathbf{w}_t$.

We leverage the matrix inversion lemma (MIL) and a special regularization parameter to remove the ill-conditioning, as follows. Assuming a nonzero scalar constant $\beta \in \mathbb{R}$, the ill-conditioned matrix $\tilde{\mathbf{\Gamma}}_t$ can be regularized to a well-conditioned matrix $\mathbf{S}$ as

$$\mathbf{S} = \tilde{\mathbf{\Gamma}}_t + \beta\mathbf{I}_{NN_\mathrm{s}}. \tag{3.27}$$

We now substitute $\tilde{\mathbf{\Gamma}}_t = \mathbf{S} - \beta\mathbf{I}_{NN_\mathrm{s}}$ in the middle inverse of the right-most term of the aforementioned alternate expression of $\mathbf{\Sigma}_t(\mathbf{w}_t, \ldots, \mathbf{w}_{t+N_\mathrm{s}-1})$ and using the fact that $\tilde{\mathbf{C}}_t\tilde{\mathbf{C}}_t^T = \mathbf{I}_{\tilde{M}_t}$, we obtain

$$\begin{aligned}&\mathbf{\Sigma}_t(\mathbf{w}_t, \ldots, \mathbf{w}_{t+N_\mathrm{s}-1})\\ &\quad= \tilde{\mathbf{\Gamma}}_t - \tilde{\mathbf{\Gamma}}_t\tilde{\mathbf{C}}_t^T(\tilde{\mathbf{C}}_t\mathbf{S}\tilde{\mathbf{C}}_t^T + (\sigma_e^2 - \beta)\mathbf{I}_{\tilde{M}_t})^{-1}\tilde{\mathbf{C}}_t\tilde{\mathbf{\Gamma}}_t.\end{aligned} \tag{3.28}$$

Using the MIL we can write

$$\begin{aligned}&(\mathbf{S}^{-1} + (\sigma_e^2 - \beta)^{-1}\tilde{\mathbf{C}}_t^T\tilde{\mathbf{C}}_t)^{-1}\\ &\qquad= \mathbf{S} - \mathbf{S}\tilde{\mathbf{C}}_t^T(\tilde{\mathbf{C}}_t\mathbf{S}\tilde{\mathbf{C}}_t^T + (\sigma_e^2 - \beta)\mathbf{I}_{\tilde{M}_t})^{-1}\tilde{\mathbf{C}}_t\mathbf{S}.\end{aligned} \tag{3.29}$$

Using (3.29), we have the following matrix identity

$$\begin{aligned}&\tilde{\mathbf{C}}_t^T(\tilde{\mathbf{C}}_t\mathbf{S}\tilde{\mathbf{C}}_t^T + (\sigma_e^2 - \beta)\mathbf{I}_{\tilde{M}_t})^{-1}\tilde{\mathbf{C}}_t\\ &\qquad= \mathbf{S}^{-1}[\mathbf{S} - (\mathbf{S}^{-1} + (\sigma_e^2 - \beta)^{-1}\tilde{\mathbf{C}}_t^T\tilde{\mathbf{C}}_t)^{-1}]\mathbf{S}^{-1}.\end{aligned} \tag{3.30}$$

Substituting (3.30) into (3.28), the error expression of $\mathbf{\Sigma}_t(\mathbf{w}_t, \ldots, \mathbf{w}_{t+N_\mathrm{s}-1})$ can be viewed as a function of the space-time sensor location selection vectors given by

$$\begin{aligned}\mathbf{\Sigma}_t(\mathbf{w}_t, \ldots, \mathbf{w}_{t+N_\mathrm{s}-1}) &= \tilde{\mathbf{\Gamma}}_t - \tilde{\mathbf{\Gamma}}_t \mathbf{S}^{-1}[\mathbf{S} - (\mathbf{S}^{-1} + (\sigma_e^2 - \beta)^{-1}\tilde{\mathbf{C}}_t^T \tilde{\mathbf{C}}_t)^{-1}]\mathbf{S}^{-1}\tilde{\mathbf{\Gamma}}_t \\ &= \mathbf{A} + \mathbf{B}^T[\mathbf{S}^{-1} + (\sigma_e^2 - \beta)^{-1}\mathrm{diag}(\tilde{\mathbf{w}}_t)]^{-1}\mathbf{B}, \qquad (3.31)\end{aligned}$$

where the matrices $\mathbf{A} = \tilde{\mathbf{\Gamma}}_t - \tilde{\mathbf{\Gamma}}_t \mathbf{S}^{-1}\tilde{\mathbf{\Gamma}}_t$ and $\mathbf{B} = \mathbf{S}^{-1}\tilde{\mathbf{\Gamma}}_t$ are independent of the selection vectors, and therefore known a priori.

We notice that the MSE matrix $\mathbf{\Sigma}_t(\mathbf{w}_t, \ldots, \mathbf{w}_{t+N_\mathrm{s}-1})$ computed as in (3.31) does not involve any inversion of the possible ill-conditioned $\tilde{\mathbf{\Gamma}}_t$. The only inversions are of the regularized, and thus well-conditioned matrix $\mathbf{S}$.

Here we comment that, the regularization in (3.27) is valid for any nonzero $\beta \in \mathbb{R}$ if $\mathbf{S}$ is only desired to be invertible. However, to maintain the positive definiteness of $\mathbf{S}$ as well as $[\mathbf{S}^{-1} + (\sigma_e^2 - \beta)^{-1}\mathrm{diag}(\tilde{\mathbf{w}}_t)]$, we specifically choose $0 < \beta < \sigma_e^2$. The aforementioned restriction in the selection of β also helps to formulate the general sensor placement problem as a convex optimization problem which is detailed in the Section 3.5.

3.4.3 Uncorrelated fields

We mainly target the application of spatio-temporal monitoring of environmental fields like pollutant concentrations in the atmosphere, concentrations of some hazardous gas, rainfall, ground layer ozone, humidity, etc. Generally, these fields are spatio-temporally correlated. But in some scenarios the spatial/temporal correlation may be very small. In these cases, the off-diagonal elements of $\tilde{\mathbf{\Gamma}}_t$ are close to 0. For a spatio-temporally uncorrelated field, $\tilde{\mathbf{\Gamma}}_t$ can be modeled as $\tilde{\mathbf{\Gamma}}_t = \sigma_u^2 \mathbf{I}_{NN_\mathrm{s}}$. Then the MSE matrix is given by

$$\begin{aligned}\mathbf{\Sigma}_t(\mathbf{w}_t, \ldots, \mathbf{w}_{t+N_\mathrm{s}-1}) &= (\sigma_u^{-2}\mathbf{I}_{NN_\mathrm{s}} + \sigma_e^{-2}\tilde{\mathbf{C}}_t^T \tilde{\mathbf{C}}_t)^{-1} \\ &= (\sigma_u^{-2}\mathbf{I}_{NN_\mathrm{s}} + \sigma_e^{-2}\mathrm{diag}(\tilde{\mathbf{w}}_t))^{-1}. \qquad (3.32)\end{aligned}$$

Note that, if the field is uncorrelated the estimation error is mainly characterized by the signal to noise ratio (SNR) of the system, i.e., σ_u^2/σ_e^2. In this case, the term $\sigma_u^{-2}\mathbf{I}_{NN_\mathrm{s}}$ acts both as a regularization term ensuring the computability of (3.32) and as a scaling term for the MSE. For the current measurement model of (3.3), to estimate an uncorrelated field (with the same σ_u^2 over space and time) the number of sensors is more relevant for the estimation performance than their constellation as long as the MSE is considered to be the performance criterion.

3.5 Generalized sensor placement problem

A generalized performance metric to estimate both stationary and non-stationary fields can be formulated as $\mathrm{tr}[\mathbf{\Sigma}_t(\tilde{\mathbf{w}}_t)]$, where $\mathbf{\Sigma}_t(\tilde{\mathbf{w}}_t)$ is the generalized MSE matrix (3.24). Following the main optimization problem of (3.6), an offline selection of sensing locations from N locations over N_s snapshots can be performed by solving the following optimization problem

$$\hat{\tilde{\mathbf{w}}}_t = \underset{\tilde{\mathbf{w}}_t \in [0,1]^{NN_\mathrm{s}}}{\arg\min} \{\|\tilde{\mathbf{w}}_t\|_1, \ \text{ s.t. } \mathrm{tr}[\mathbf{\Sigma}_t(\tilde{\mathbf{w}}_t)] \leq \gamma'\}, \tag{3.33}$$

where γ' is a threshold on the estimation performance. An extra set of affine constraints can be added to the problem of (3.33), to restrict the minimum number of sensing locations to be selected at every time index t. This is given as

$$\|\mathbf{w}_{t+\tau}\|_1 \geq p, \quad \tau = 0, \ldots, N_\mathrm{s} - 1. \tag{3.34}$$

This constraint enforces at least p sensors to be selected at every snapshot. This is an optional design constraint to efficiently utilize the available sensors in every snapshot. Spatial selection of sensing locations can be performed in a more efficient manner by employing a structural constraint on $\mathbf{w}_{t+\tau}$ like group sparsity. The evolution of $\mathbf{w}_t$ can also be controlled by using a smoothing penalty in the cost function of (3.33), where the sensing locations are selected on a single snapshot basis [59].

Considering the general form of the performance metric, i.e., (3.31), the optimization problem of (3.33) can be formulated as a semidefinite program (SDP). For the N candidate sensing locations, the performance constraint can be expressed as N linear matrix inequalities (LMIs) [46], [45]. If the column vectors of the matrix $\mathbf{B}$ are given by $\mathbf{b}_j$, where $j = 1, \ldots, N$, then the SDP is given by

$$\hat{\tilde{\mathbf{w}}}_t = \underset{\tilde{\mathbf{w}}_t \in [0,1]^N, \mathbf{v} \in \mathbb{R}^N}{\arg\min} \|\tilde{\mathbf{w}}_t\|_1,$$

$$\text{s.t.} \quad \begin{bmatrix} v_j & \mathbf{b}_j^T \\ \mathbf{b}_j & \mathbf{S}^{-1} + (\sigma_e^2 - \beta)^{-1}\mathrm{diag}(\tilde{\mathbf{w}}_t) \end{bmatrix} \succeq 0, \quad j = 1, \ldots, N \tag{3.35}$$

$$\mathbf{1}^T\mathbf{v} \leq \gamma' - \mathrm{tr}(\mathbf{A}), \tag{3.36}$$

where we use the auxiliary variable $\mathbf{v} = [v_1, \ldots, v_N]^T$. The set of N LMIs in (3.35) signify the fact that $v_j \geq \mathbf{b}_j^T[\mathbf{S}^{-1} + (\sigma_e^2 - \beta)^{-1}\mathrm{diag}(\mathbf{w}_t)]^{-1}\mathbf{b}_j$, where $j = 1, \ldots, N$ (using the Schur complement of the block $\mathbf{S}^{-1} + (\sigma_e^2 - \beta)^{-1}\mathrm{diag}(\mathbf{w}_t)$).

The solution of the aforementioned optimization problem gives the sensor placement patterns achieving the desired estimation performance γ'. It is clear that lowering γ', i.e., putting a tighter threshold on the performance, more sensing locations need to be selected.

In practical scenarios, the performance threshold can generally be derived from the application, i.e., the nature of the field to be estimated, required resolution, etc. In the present work, we calculate the thresholds by scaling the best case, i.e., sensors are deployed in all N candidate locations. In other words, we consider $\gamma' = \zeta \mathrm{tr}[\mathbf{\Sigma}_t(\mathbf{1}_{NN_\mathrm{s}})]$, where $\zeta > 1$ is a positive scaling parameter.

3.6 Iterative saddle point method for sensor placement

From the above discussions, the structure of the general optimization problem, i.e., (3.33) with the performance metric (3.31), can be formulated as,

$$\hat{\mathbf{w}} = \underset{\mathbf{w}\in[0,1]^L}{\arg\min} \{\|\mathbf{w}\|_1 \ \text{ s.t. } \mathrm{tr}[\mathbf{B}^T(\mathbf{S}^{-1} + (\sigma_e^2 - \beta)^{-1}\mathrm{diag}(\mathbf{w}))^{-1}\mathbf{B}] - \gamma'' \leq 0\} \tag{3.37}$$

where $\gamma'' = \gamma - \mathrm{tr}(\mathbf{A})$, and the matrices $\mathbf{A}$ and $\mathbf{B}$ are independent of $\mathbf{w}$. In this section, we use $\mathbf{w}$ instead of $\tilde{\mathbf{w}}_t$ for the sake of notational simplicity. For the generalized sensor placement problem (i.e., stationary/non-stationary), the length of the selection vector is given as $L = NN_\mathrm{s}$. In this work, we consider the fact that the spatio-temporal covariance matrix is accurately invertible, i.e, we take $\beta = 0$, $\mathbf{B} = \mathbf{I}_L$, and $\mathbf{A} = \mathbf{0}_{L\times L}$. Using these the optimization problem of (3.37) can be given as

$$\hat{\mathbf{w}} = \underset{\mathbf{w}\in[0,1]^L}{\arg\min} \{\|\mathbf{w}\|_1 \ \text{ s.t. } \mathrm{tr}[\mathbf{Z}^{-1} + \sigma_e^{-2}\mathrm{diag}(\mathbf{w})]^{-1} - \gamma \leq 0\}, \tag{3.38}$$

where the matrix $\mathbf{Z}$ is the spatio-temporal covariance matrix. We define a function $h(\mathbf{w})$ as

$$h(\mathbf{w}) = \mathrm{tr}[\mathbf{Z}^{-1} + \sigma_e^{-2}\mathrm{diag}(\mathbf{w})]^{-1} - \gamma. \tag{3.39}$$

However, as mentioned earlier, the convex problem (3.38) can be easily formulated as an SDP and solved for $\mathbf{w}$ using off-the-shelf solvers like CVX [52] and SeDuMi [53]. The complexity of standard SDP problems are discussed in [60]. But for a large service area and/or many snapshots the number of unknowns (L), i.e., the number of LMIs becomes increasingly high. In this case, SDP based approaches using standard solvers can be time consuming. In this section, we propose an alternative approach to solve the optimization problem (3.38) directly.

3.6.1 Primal-dual iterations

We use an iterative saddle-point method [61], to solve the optimization problem (3.38). We adopt first-order methods rather than Newton's method because Newton's method requires the expression of the Hessian and also its inverse, which increases the computational complexity and leads to storage issues. First of all, we define the dual variable associated with the inequality constraint (3.38) as λ. Under convexity and Slater's condition (which holds for (3.38), given the choice of γ), we can prove that the dual variable λ lives in a bounded compact set $[0, \lambda_{\max}]$ [61, Lemma 3]. The value of $\lambda_{\max} > 0$ is easily computable a priori, given any Slater's vector. Let us now define the compact constraint sets, $\mathbb{X} \in [0,1]^L$ and $\mathbb{D} \in [0, \lambda_{\max}]$ for the primal and the dual variables $\mathbf{w} \in \mathbb{X}$, and $\lambda \in \mathbb{D}$, respectively. The Lagrangian function $\mathcal{L}(\mathbf{w}, \lambda) : \mathbb{X} \times \mathbb{D} \to \mathbb{R}$, for the optimization problem (3.37) is given by,

$$\mathcal{L}(\mathbf{w}, \lambda) = \mathbf{1}^T \mathbf{w} + \lambda\, h(\mathbf{w}). \tag{3.40}$$

The primal-dual iterations for $i \geq 0$ can be given as,

$$\hat{\mathbf{w}}^{i+1} = \mathcal{P}_{\mathbb{X}}[\hat{\mathbf{w}}^i - \alpha \nabla_{\mathbf{w}} \mathcal{L}(\hat{\mathbf{w}}^i, \hat{\lambda}^i)], \tag{3.41}$$

$$\hat{\lambda}^{i+1} = \mathcal{P}_{\mathbb{D}}[\lambda^i + \alpha \nabla_{\lambda} \mathcal{L}(\mathbf{w}^i, \lambda^i)], \tag{3.42}$$

where $\mathcal{P}_{\mathbb{X}}$ and $\mathcal{P}_{\mathbb{D}}$ are the projection operators onto the sets $\mathbb{X}$ and $\mathbb{D}$, respectively. The scalar $\alpha > 0$ is the step size. We define $\nabla_{\mathbf{w}}(\cdot)$ and $\nabla_{\lambda}(\cdot)$ as the gradients w.r.t. $\mathbf{w}$ and λ, respectively. Note that, the primal-dual iterations actually minimize $\mathcal{L}(\mathbf{w}, \lambda)$ w.r.t. $\mathbf{w}$ and maximize it w.r.t λ in order to achieve the saddle point $(\hat{\mathbf{w}}, \hat{\lambda})$ [61], which satisfies

$$\mathcal{L}(\hat{\mathbf{w}}, \lambda) \leq \mathcal{L}(\hat{\mathbf{w}}, \hat{\lambda}) \leq \mathcal{L}(\mathbf{w}, \hat{\lambda}), \quad \forall \mathbf{w} \in \mathbb{X}, \lambda \in \mathbb{D}. \tag{3.43}$$

The expressions of the gradients $\nabla_{\mathbf{w}}(\cdot)$ and $\nabla_{\lambda}(\cdot)$ are computed in the Appendix. They are given as

$$\nabla_{\mathbf{w}} \mathcal{L}(\hat{\mathbf{w}}^i, \hat{\lambda}^i) = \mathbf{1}_L + \hat{\lambda}^i \sigma_e^{-2} \mathrm{diag}(-[\mathbf{Z}^{-1} + \sigma_e^{-2} \mathrm{diag}(\hat{\mathbf{w}}^i)]^{-2}) \tag{3.44}$$

$$\nabla_{\lambda} \mathcal{L}(\hat{\mathbf{w}}^i, \hat{\lambda}^i) = \mathrm{tr}[\mathbf{Z}^{-1} + \sigma_e^{-2} \mathrm{diag}(\hat{\mathbf{w}}^i)]^{-1} - \gamma. \tag{3.45}$$

Due to compactness of the sets $\mathbb{X}$ and $\mathbb{D}$ and the invertibility of $\mathbf{Z}$, it can be proven that the gradients are bounded. And, in particular, we can write

$$\max\{\|\nabla_{\mathbf{w}} \mathcal{L}(\mathbf{w}, \lambda)\|, \|\nabla_{\lambda} \mathcal{L}(\mathbf{w}, \lambda)\|\} \leq C, \quad \forall \mathbf{w} \in \mathbb{X}, \lambda \in \mathbb{D}, \tag{3.46}$$

where $C > 0$ is a constant. With this in place, due to Propositions 1 and 2 of [61], the iterates $\{\hat{\mathbf{w}}^i, \hat{\lambda}^i\}$ converge weakly (in the ergodic mean sense) to a neighborhood of the saddle point of the Lagrangian (3.40). The size of the neighborhood (i.e., the asymptotical error bound) is proportional to αC^2. In addition, convergence goes as $O(1/i\alpha)$, i being the iteration counter. A similar result is also valid for the amount of constraint violation. In practice, in the simulation results, we will select the step size α to trade-off convergence speed and asymptotical error. The stopping criteria will be based either on a maximum number of iterations, or on a required tolerance on the value of $|h(\hat{\mathbf{w}}^i)|$.

3.7 Iterative reweighted ℓ_1-norm minimization algorithm to improve sparsity

The well-known convex approximation of the non-convex ℓ_0-norm is the sought-after ℓ_1-norm. However, there are better functions to model a sparsity-promoting cost like a sum of logarithms or a sum of inverse squared exponentials. Unfortunately both of these functions are non-convex.

For example, in the optimization problem of (3.6), the objective function can be replaced by a sparsity-promoting non-convex cost, i.e., $\sum_{l=1}^{L} \ln(\epsilon + [\mathbf{w}]_l)$. Here, $\epsilon > 0$ is used to maintain the stability of the sum of the logarithm cost. As mentioned in [56], such a log-concave function can be well approximated by its first order linear approximation. This means that minimizing $\sum_{l=1}^{L} \ln(\epsilon + [\mathbf{w}]_l)$ can be approximated by iteratively minimizing its linear approximation, i.e.,

$$\arg\min_{\mathbf{w}} \sum_{l=1}^{L} \frac{[\mathbf{w}]_l}{\epsilon + [\hat{\mathbf{w}}^j]_l}, \tag{3.47}$$

where $\hat{\mathbf{w}}^j$ is the estimate of $\mathbf{w}$ in the j-th iteration [56]. Following the derivation of [56], the optimization problem (3.6), can be formulated as the iterative reweighted ℓ_1-norm minimization given by

- **Initialize** $j = 0$, weight vector $\mathbf{z}^0 = \mathbf{1}_L$, ϵ, and maximum number of iterations J.
- **for** $j = 0, \ldots, J$

$$\hat{\mathbf{w}}^j = \arg\min_{\mathbf{w} \in [0,1]^L} \{(\mathbf{z}^j)^T \mathbf{w}, \quad \text{s.t.} \quad g(\mathbf{w}) \leq \gamma\}$$

- $[\mathbf{z}^{j+1}]_l = \frac{1}{\epsilon + [\hat{\mathbf{w}}^j]_l}$, for $l = 1, \ldots, L$
- **end**
- **set** $\hat{\mathbf{w}} = \hat{\mathbf{w}}^J$.

The aforementioned algorithm is envisaged to avoid the dependence of $\hat{\mathbf{w}}$ on the magnitude of its elements. Using this iterative approach, a higher weight is put on the smaller elements of $\mathbf{w}$ to push them towards 0, enhancing the sparsity in $\mathbf{w}$. On the other hand, it maintains the magnitude of the larger elements by putting a smaller weight. However, after this "sparsity-enhancing" iterative algorithm we still have $\hat{\mathbf{w}} \in [0, 1]^L$. After the computation of $\hat{\mathbf{w}}$ from the above iterative algorithm we compute $\mathbf{w} \in \{0, 1\}^L$ using simple thresholding and randomized rounding.

3.7.1 Primal-dual iterations with the iterative reweighted ℓ_1-norm minimization

The sparsity-enhancing iterative algorithm mentioned in the previous section can be implemented in combination with the saddle-point method. In this case, the Lagrangian can be formulated as

$$\mathcal{L}(\hat{\mathbf{w}}^j, \lambda) = (\mathbf{z}^j)^T \hat{\mathbf{w}}^j + \lambda \, h(\hat{\mathbf{w}}^j), \tag{3.48}$$

where $\mathbf{z}^j$ is the weighting vector of the j-th iteration of the iterative algorithm. As before, we can compute the saddle-point iterates with this new Lagrangian, which (for the same reasons as mentioned in Section 3.6.1) will converge weakly to a saddle point up to a bounded error.

In Algorithm 3, the saddle-point iterations for the reweighted ℓ_1 minimization are presented. The overall algorithm is implemented using two nested loops, where the inner loop (indexed by i) is used for the primal-dual iterations and the outer loop (indexed by j) is used for the iterative reweighted ℓ_1 algorithm.

To place the sensors dynamically every snapshot, the same Algorithm 3 is implemented for $t = 1, \ldots, T$ snapshots with $N_\mathrm{s} = 1$, i.e., $L = N$. The estimation error is initialized as $\mathbf{\Sigma}_0$ at $t = 0$. After estimating $\mathbf{w}_t$ at any t, the estimation error, i.e., $\mathbf{\Sigma}_t(\mathbf{w}_t)$ is updated based on the recursive relation of (3.26). We refer to this algorithm as Dynamic Iterative Sparsity-Enhancing Sensor Placement (DISESP).

Algorithm 1 Saddle point iterations enhancing sparsity

Initialize: $j = 0$, weight vector $\mathbf{z}^0 = \mathbf{1}_L$, α, I, J, tol, and ϵ.
for $j = 0, \ldots, J$
  solve the saddle point iterations
    while $i < I$ or $|h(\mathbf{w})| \geq \text{tol}$

$$\begin{aligned}\hat{\mathbf{w}}^{i+1,j} &= \mathcal{P}_{\mathbb{X}}[\hat{\mathbf{w}}^{i,j} - \alpha\nabla_{\mathbf{w}}[(\mathbf{z}^j)^T\hat{\mathbf{w}}^{i,j} + \hat{\lambda}^{i,j}\ h(\hat{\mathbf{w}}^{i,j})]],\\ \hat{\lambda}^{i+1,j} &= \mathcal{P}_{\mathbb{D}}[\hat{\lambda}^{i,j} + \alpha\nabla_{\lambda}[(\mathbf{z}^j)^T\hat{\mathbf{w}}^{i,j} + \hat{\lambda}^{i,j}\ h(\hat{\mathbf{w}}^{i,j})]]\end{aligned}$$

    end while
  update the weight vector by $[\mathbf{z}^{j+1}]_l = \frac{1}{\epsilon + [\hat{\mathbf{w}}^j]_l}$, where $l = 1, \ldots, L$.
end for
$\hat{\mathbf{w}} = \hat{\mathbf{w}}^J$.

3.8 Simulation result

In this section, we perform some numerical experiments for both stationary and non-stationary field estimation applications using the developed sensor placement method. Let us assume a service area of 10×10 square km which is discretized into $N = 100$ pixels of size 1 square km. The service area and the centroids of the pixels are shown in Fig. 3.4. We assume that all of these centroids are candidate sensing locations. They are row-wise indexed from top to bottom as shown in Fig. 3.4.

3.8.1 Sensor placement for stationary field estimation

Firstly, we assume that the environmental field is spatio-temporally stationary.

We consider to have $N_\text{s} = 3$ snapshots. In this case, the size of the spatio-temporal covariance matrix ($\tilde{\mathbf{\Gamma}}_t$) is 300×300. The temporal lags are $\tau = 0, 1, 2$ as $N_\text{s} = 3$. The diagonal and off-diagonal blocks of $\tilde{\mathbf{\Gamma}}_t$ are given by $\mathbf{\Gamma}_0 \in \mathbb{S}_{++}^{100}$ and $\mathbf{\Gamma}_2, \mathbf{\Gamma}_1,\ \mathbf{\Gamma}_{-1}, \mathbf{\Gamma}_{-2} \in \mathbb{S}_{++}^{100}$, respectively. The elements of these matrices are generated by the exponential covariance function mentioned in (3.7) (Section 3.3) with parameters $\sigma_u^2 = 1, s_h = 5, s_\tau = 2$. The d_{ij} parameters are computed from the distance matrix (matrix of all possible pair-wise Euclidean distances) of the pixel centroids as shown in Fig. 3.4. Based on these, $\tilde{\mathbf{\Gamma}}_t$ is a symmetric, positive-definite and block-toeplitz matrix.

The measurement noise variance is assumed to be $\sigma_e^2 = 1$. The performance threshold γ' is computed by scaling the best case MSE (i.e. $\text{tr}[\mathbf{\Sigma}_t(\mathbf{1}_{300})]$) by $\zeta = 2$.

The parameters of the sparsity-enforcing iterative algorithm are $\epsilon = 10^{-8}$ and $J = 5$. A constant step-size of $\alpha = 0.1/(NN_{\mathrm{s}})$ is used in the saddle point algorithm and the algorithm is iterated until a desired tolerance level (tol) or the maximum number of iterations (I) is achieved. Here, we take $\mathrm{tol} = 10^{-4}$ and $I = 300NN_s$.

The estimated sensor location selection vectors for $N_{\mathrm{s}} = 3$ snapshots, i.e., $\hat{\mathbf{w}}_1,\ \hat{\mathbf{w}}_2,\ \hat{\mathbf{w}}_3$ before and after the randomized rounding are shown in Fig. 3.5 and Fig. 3.6, respectively. In the next case, we keep the same γ' but assume that the field is spatio-temporally more correlated than the last time. In this case, we use $s_h = 7$ and $s_\tau = 3$. The resulting selected sensing locations, i.e., $\hat{\mathbf{w}}_1,\ \hat{\mathbf{w}}_2,\ \hat{\mathbf{w}}_3$ before and after the randomized rounding are shown in Fig. 3.7 and Fig. 3.8, respectively.

It is observed that less sensors are needed to achieve a desired estimation performance, when the field is highly correlated over space and/or time. We see that in Fig. 3.8 less sensing locations are selected than in Fig. 3.6. This observation is consistent with the fact that the Bayesian MSE is reduced as the correlation over space/time is increased, as shown in Fig. 3.3.

We study space-time sensor placement patterns for a simple exponential covariance function (uniformly decaying with increasing spatial/temporal lags). It can be conjectured that for such a covariance function the optimal sensor placement is more or less uniform over space and time. However, different sensor placement patterns can be observed for different spatio-temporal covariance matrices, i.e., $\tilde{\mathbf{\Gamma}}_t$.

3.8.2 Sensor placement for non-stationary field estimation

In this section, we consider that the environmental field is non-stationary. We consider that the dynamics, i.e, $\mathbf{H}_t$ for $t = 1, \ldots, 7$ snapshots (minutes) are assumed to be known a priori. We present two scenarios. First, we solve the multiple snapshots ahead sensor placement problem. We solve this only once without any updating although this could be considered as well. In the next case, we solve the single snapshot ahead sensor placement problem, where the performance metric is updated every snapshot. We consider the same service area as shown in Fig. 3.4.

Multiple snapshots ahead sensor placement

We consider $N_{\mathrm{s}} = 3$ snapshots. The parameters of the state transition matrix are given by $\nu = 0.4$, $\mathbf{D}_t = \mathbf{D} = \mathbf{I}_2$, which is an isotropic diffusion, and $\mathbf{a}_t = \mathbf{a} = [0.5, 0.5]^T$ for $\mathbf{H}_1,\ \mathbf{H}_2,\ \mathbf{H}_3$. We assume that the initial distribution of the field is given as $\mathbf{u}_0 \sim \mathcal{N}(\boldsymbol{\mu}_0, \mathbf{\Gamma}_0)$, where we take $\boldsymbol{\mu}_0 = \mathbf{1}_{100}$ and the elements of $\mathbf{\Gamma}_0 \in \mathbb{S}^{100}_{++}$ are given by (3.7) with parameters $\sigma_u^2 = 1,\ s_h = 1,\ s_\tau = 0,$

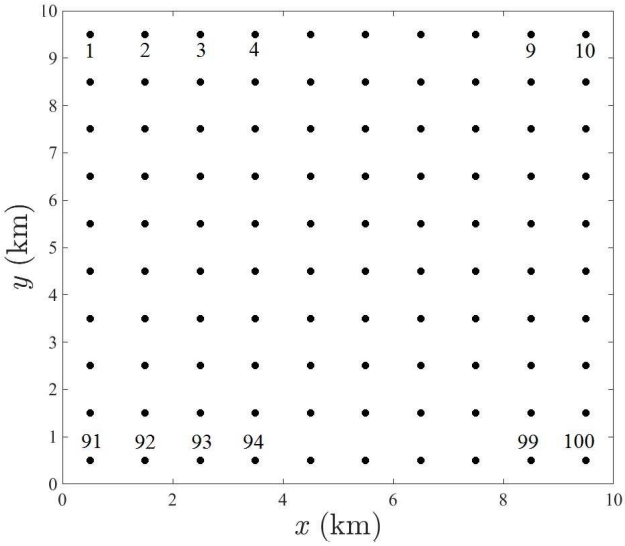

Figure 3.4: Service area with the candidate sensing locations.

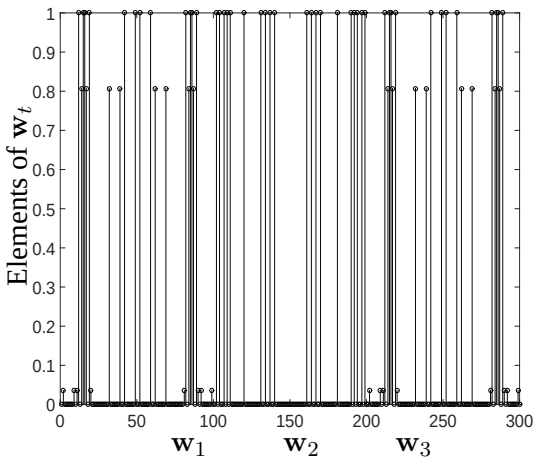

Figure 3.5: Sensor placement pattern ($s_h = 5;\ s_\tau = 2$) (before randomization).

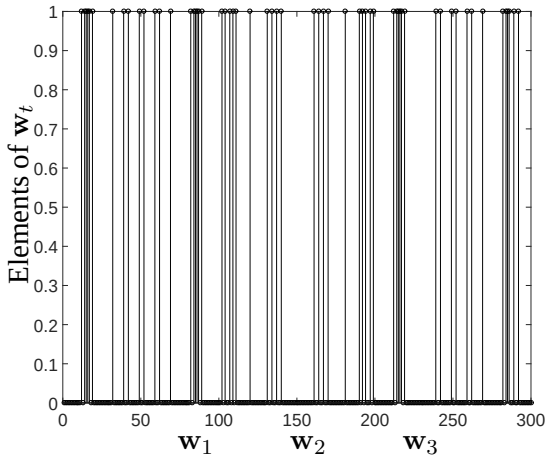

Figure 3.6: Sensor placement pattern ($s_h = 5;\ s_\tau = 2$) (after randomization).

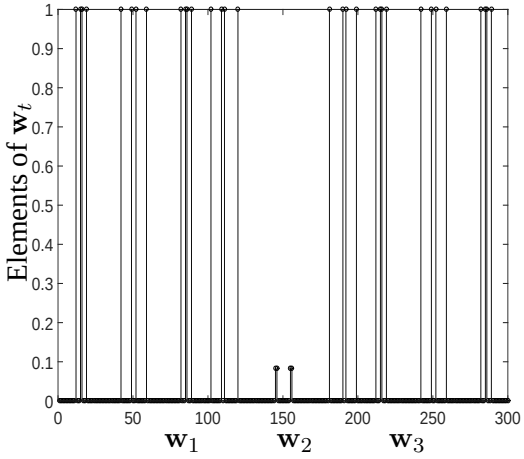

Figure 3.7: Sensor placement pattern ($s_h = 7;\ s_\tau = 3$) (before randomization).

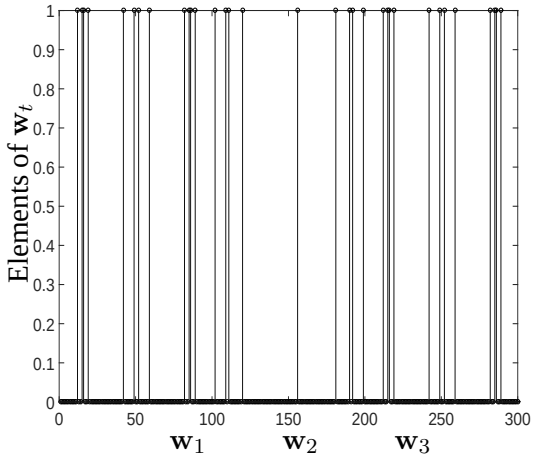

Figure 3.8: Sensor placement pattern ($s_h = 7;\ s_\tau = 3$) (after randomization).

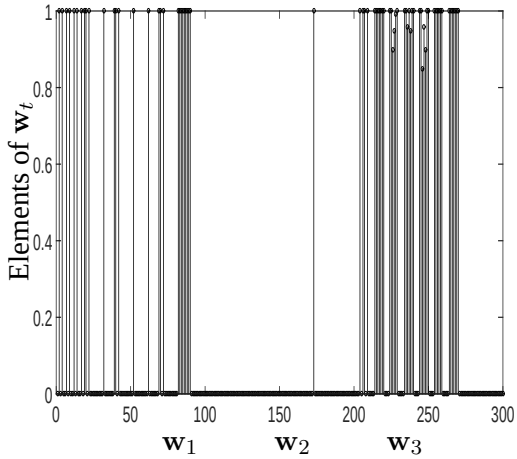

Figure 3.9: Multiple snapshots ahead sensor placement pattern for non-stationary field (before randomization).

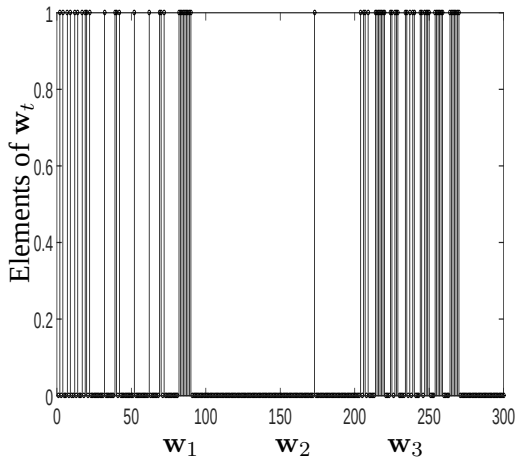

Figure 3.10: Multiple snapshots ahead sensor placement pattern for non-stationary field (after randomization).

i.e, $[\mathbf{\Gamma}_0]_{ij} = \exp[-d_{ij}]$ for $i, j = 1, \ldots, 100$. The process noise is characterized by $\mathbf{q}_t \sim \mathcal{N}(\mathbf{0}_{100}, 0.001\mathbf{I}_{100})$ for all t. The diagonal, right and left off-diagonal blocks of $\tilde{\mathbf{R}}_t$ are computed using (3.18), (3.19), and (3.20), respectively. Finally, the overall space-time covariance matrix is computed by $\tilde{\mathbf{\Gamma}}_t = \tilde{\mathbf{R}}_t - \tilde{\boldsymbol{\mu}}_t \tilde{\boldsymbol{\mu}}_t^T$, where $\tilde{\boldsymbol{\mu}}_t$ and $\tilde{\mathbf{R}}_t$ are computed using the expressions of (3.15) and (3.17), respectively. The measurement noise variance is assumed to be same as before, i.e., $\sigma_e^2 = 1$. The parameters of the iterative saddle point algorithm are also maintained to be the same as before. In this case, we again adopt the performance threshold γ' by scaling the best MSE by $\zeta = 2$. The sensor location selection vectors, i.e., $\hat{\mathbf{w}}_1,\ \hat{\mathbf{w}}_2,\ \hat{\mathbf{w}}_3$ (before and after randomization) are shown in Fig. 3.9 and Fig. 3.10, respectively.

It is seen that when the field is non-stationary, the selected sensing locations are less uniformly distributed than for the stationary field case. It is also seen that when a non-stationary field is to be estimated jointly using the measurements from multiple snapshots then measurements from alternate snapshots are more informative than measurements from consecutive snapshots. This makes sense as sensors in alternate snapshots are less correlated and the values for the middle snapshot can be easily predicted. The dependence on the dynamics is even more clearly observed in the next case, where we update the performance metric every snapshot.

Single snapshot ahead sensor placement

In this case, we select the sensing location for every snapshot, i.e., we consider $N_{\mathrm{s}} = 1$. To avoid the computation of $\tilde{\mathbf{\Gamma}}_t$ we update the performance metric every snapshot based on (3.26), i.e., we use the developed DISESP approach mentioned in Section 3.7.1.

Considering the same service area shown in Fig. 3.4, we would like to choose the sensing locations every snapshot dynamically. Note that, for every t we compute $\mathbf{w}_t$ (with the prior knowledge of $\mathbf{H}_t$, $\mathbf{Q}_t$, and the estimation error covariance of the previous snapshot, i.e., $\mathbf{\Sigma}_{t-1}$) whose support gives the locations where to move/place the sensors to estimate the field for the current snapshot. The scaling and diffusion parameters of the state transition matrix are given by $\nu = 0.4$ and $\mathbf{D}_t = \mathbf{D} = \mathbf{I}_2$, which are the same as before. For the advection, we consider two scenarios. In the first case, we assume that $\mathbf{a}_t$ is fixed for all t, i.e., we have $\mathbf{H}_t = \mathbf{H}$. In the next case, we change $\mathbf{a}_t$ every minute. In that case, the values of $\mathbf{a}_t$ for $t = 1, \ldots, 7$ are given as $[0.5, 0.5]^T$, $[1.5, 1.5]^T$, $[0, 2]^T$, $[0, 2]^T$, $[1.5, -1.5]^T$, $[0.5, -1.5]^T$, $[1.5, -1.5]^T$. Here, we mention that the parameters of the matrix $\mathbf{H}_t$ are chosen in such a way that the maximum eigenvalue of $\mathbf{H}_t$ is always less than 1, in order to assure the stability of the model. The measurement noise variance is assumed to be $\sigma_e^2 = 1$, for all t. The process noise is chosen to be the same as before. i.e., $\mathbf{q}_t \sim \mathcal{N}(\mathbf{0}_{100}, 0.001\mathbf{I}_{100})$ for all t. We assume that at time $t = 0$ the estimation error covariance is $\mathbf{\Sigma}_0 = \mathbf{I}_{100}$. The performance threshold γ' is dynamically computed by scaling the best case MSE, i.e., $\mathrm{tr}[\mathbf{\Sigma}_t(\mathbf{1}_{100})]$, by $\zeta = 1.3$ on every t. We perform $J = 3$ iterations of the iterative algorithm at every snapshot t. In order to improve the speed, the selected sensing locations are computed by thresholding w.r.t. 0 (i.e., setting the non-zero elements to 1) rather than performing randomization on every snapshot.

The resulting sensor placement patterns for the fixed and time-varying $\mathbf{H}_t$ are shown in Fig. 3.11 and Fig. 3.12, respectively. The y-axis represents the indices of the selected sensing locations indexed as shown in Fig. 3.4. The x-axis represents the time in minutes. In Fig. 3.11, it is seen that more or less the same subset of sensing locations are selected with increasing time as the state error covariance converges to the steady state. The number of required sensing locations for individual snapshots is also decreasing with time due to the reduction of the state error.

On the contrary, in Fig. 3.12 different sensing locations are selected with time due to the time-varying state transition matrix $\mathbf{H}_t$. It is seen that the number and position of the optimal sensing locations, achieving a prescribed estimation perfor-

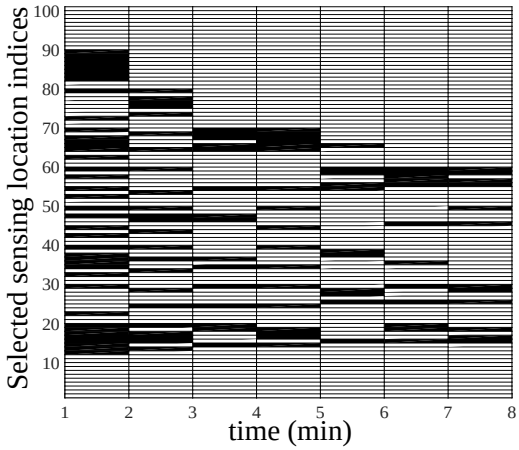

Figure 3.11: Sensor deployment pattern for $\mathbf{H}_t = \mathbf{H}$.

mance are guided by the dynamics of the field, as well as the required performance (which is also dependent on the noise level) of the system.

3.8.3 Analysis of the performance metric

In this section, we compare the performance of the developed sensor placement algorithm with random sensor placement in terms of their respective mean square errors for different measurement noise variances (σ_e^2). For every noise variance, 100 random realizations of the selection vector $\tilde{\mathbf{w}}_t \in \{0,1\}^{NN_\mathrm{s}}$ are generated with the same number of 1s generated by the proposed approach. The average MSE of all these realizations are compared with the achieved MSE using the proposed algorithm.

We consider two scenarios. In the first case, we consider the spatial sensor placement problem, i.e, $N_\mathrm{s} = 1$, to estimate a stationary field in the service area shown in Fig. 3.4, i.e., $N = 100$. The elements of the spatial covariance matrix $\tilde{\mathbf{\Gamma}}_t$ are generated using the exponential covariance function mentioned in (3.7) with $s_h = 5$. The comparison of the MSE for the proposed approach and the average MSE of random sensor placement for different noise variances is shown in Fig. 3.13. The standard deviation of the MSEs for different realizations of the random placement are also shown for every σ_e^2. In the second case, we consider the field to be non-stationary with the same $\mathbf{H}_t = \mathbf{H}$ as mentioned in Section 3.8.2. In this case, we consider $N = 25$ (5×5 square km service area with 25 pixels),

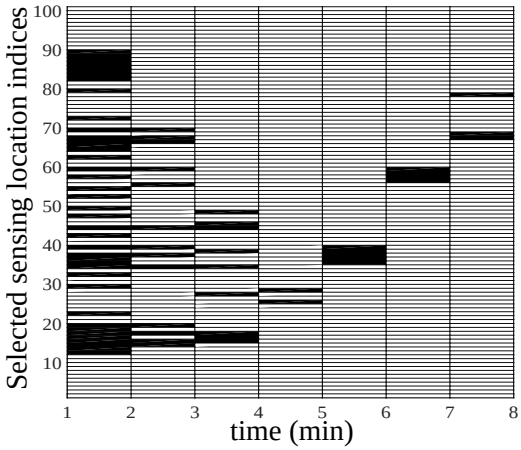

Figure 3.12: Sensor deployment pattern for a time-varying advection parameter $\mathbf{a}_t$.

$N_{\mathrm{s}} = 3$ and solve for $\tilde{\mathbf{w}}_t \in \{0,1\}^{75}$, i.e, in a multiple snapshots ahead fashion. The comparison of the MSE with random placement is shown in Fig. 3.14. In the last two cases, we consider $\zeta = 2$ and $\zeta = 1.5$, respectively.

In the third case, we consider the single snapshot ahead sensor placement problem, i.e., the performance metric is updated every iteration. We fix $\sigma_e^2 = 1$ and $\zeta = 2$. Every t, the MSE of the proposed approach and the average MSE for 100 different realizations of $\mathbf{w}_t \in \{0,1\}^N$ (with the same number of 1s generated by the proposed approach) are compared. We consider the same setup as mentioned in Section 3.8.2. The performance comparison is shown in Fig. 3.15.

First of all, it is observed that the achieved MSE using the proposed approach is lower than randomly placing the sensors for a given number of available sensing locations. It is also seen that when the field is stationary with a smoothly varying spatial covariance function, on average random placement performs well. The reason behind this is that a uniform placement is close to optimal in order to estimate a stationary field as observed in Fig. 3.6 and Fig. 3.8. So, the performance gap is not significant in this case, as long as the average MSE of the uniformly at random realizations is concerned. But there could be some realizations producing a high MSE, as seen by the standard deviation plot.

But when the field is non-stationary, the optimal sensor placement patterns are non-uniform over space and time as shown in Figures 3.10, 3.11, and 3.12 for multiple snapshots and single snapshot ahead sensor placements, respectively. They are mainly guided by the dynamics of the field. In this case, the performance gap

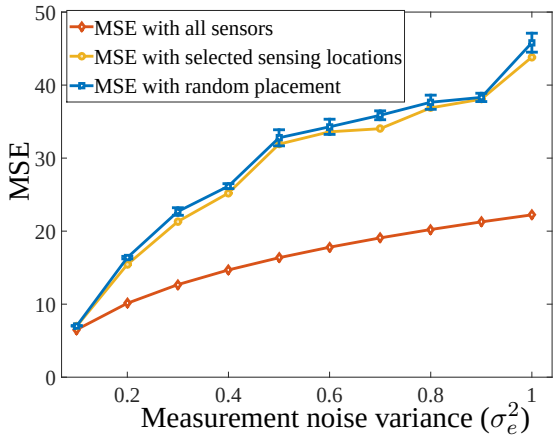

Figure 3.13: MSE comparison with random sensor placement (stationary field; $N = 100$, $N_s = 1$).

between the proposed approach and a random placement is significant.

3.9 Conclusion

We have presented sparsity-enforcing sensor placement methods for the estimation of both stationary and non-stationary spatio-temporal environmental fields. The developed methodologies can be used for both offline and online field estimation applications. They exploit the space-time correlation information as well as the dynamics of the field to deploy sensors at the most informative locations over space and time. We have also developed a sparsity-enforcing iterative first order approach to select the sensing locations that achieve a prescribed estimation accuracy in terms of the MSE. We further compared the performance of the developed sensor placement approach with random sensor placement.

It is observed that for an exponentially decaying stationary covariance function, the higher the spatio-temporal correlation the less sensing locations are needed. For a non-stationary field, the number and the position of the selected sensing locations are controlled by the dynamics of the field, the required estimation accuracy, and the noise level. If the dynamics are not changing with time then the same set of sensors are selected with time once the posterior error covariance reaches a steady state.

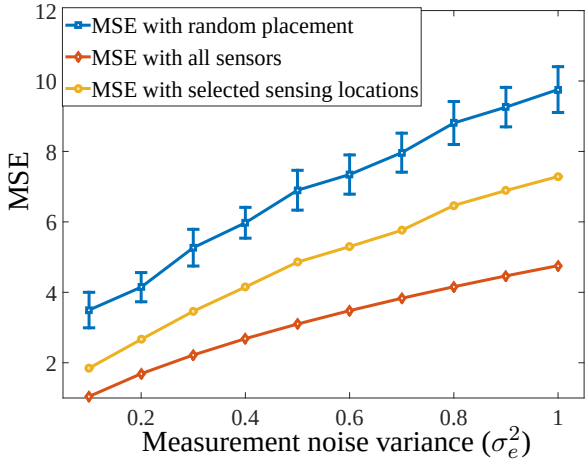

Figure 3.14: MSE comparison with random sensor placement (non-stationary field; $N = 25$, $N_\mathrm{s} = 3$).

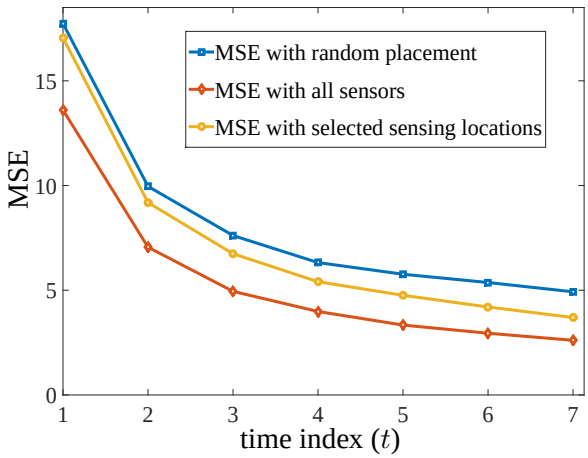

Figure 3.15: MSE comparison with random sensor placement (non-stationary field; $N = 100$, $\sigma_e^2 = 1$).

3.10 Appendix

In this section, we compute the derivatives of the Lagrangian which are used in (3.41) and (3.42). The derivatives w.r.t $\mathbf{w}$ and λ are given as

$$\nabla_{\mathbf{w}}\mathcal{L}(\mathbf{w},\lambda) = \mathbf{1}_L + \lambda\nabla_{\mathbf{w}}h(\mathbf{w}), \text{ and} \tag{3.49}$$

$$\nabla_{\lambda}\mathcal{L}(\mathbf{w},\lambda) = h(\mathbf{w}), \tag{3.50}$$

respectively. To compute $\nabla_{\mathbf{w}}h(\mathbf{w})$ we use the following identities for the differentiation of a scalar function of matrix and vector variables [62]. They are

$$\begin{aligned}\frac{\partial f(\mathbf{X}(\mathbf{w}))}{\partial[\mathbf{w}]_l} &= \text{tr}\left[\left(\frac{\partial f(\mathbf{X}(\mathbf{w}))}{\partial\mathbf{X}(\mathbf{w})}\right)^T\frac{\partial\mathbf{X}(\mathbf{w})}{\partial[\mathbf{w}]_l}\right], \text{ and}\\ \frac{\partial\text{tr}[\mathbf{X}^{-1}]}{\partial\mathbf{X}} &= -(\mathbf{X}^{-2})^T,\end{aligned}$$

where $l = 1,\ldots,L$. Now using the above identities we can compute,

$$\begin{aligned}\nabla_{\mathbf{w}}h(\mathbf{w}) &= \nabla_{\mathbf{w}}[\text{tr}[\mathbf{Z}^{-1} + \sigma_e^{-2}\text{diag}(\mathbf{w})]^{-1}]\\ &= \sigma_e^{-2}\text{diag}(-[\mathbf{Z}^{-1} + \sigma_e^{-2}\text{diag}(\mathbf{w})]^{-2}).\end{aligned} \tag{3.51}$$

Extended derivation: We consider $f(\mathbf{X}(\mathbf{w})) = h(\mathbf{w})$, where $\mathbf{X}(\mathbf{w}) = [\mathbf{Z}^{-1} + \sigma_e^{-2}\text{diag}(\mathbf{w})]$. Now, we compute the elements of the vector $\frac{\partial f(\mathbf{X}(\mathbf{w}))}{\partial\mathbf{w}} = \frac{\partial h(\mathbf{w})}{\partial\mathbf{w}} = \nabla_{\mathbf{w}}h(\mathbf{w})$ by,

$$\begin{aligned}\frac{\partial f(\mathbf{X}(\mathbf{w}))}{\partial[\mathbf{w}]_1} &= \text{tr}\left[\left(\frac{\partial f(\mathbf{X}(\mathbf{w}))}{\partial\mathbf{X}(\mathbf{w})}\right)^T\frac{\partial\mathbf{X}(\mathbf{w})}{\partial[\mathbf{w}]_1}\right]\\ &= \text{tr}[-[\mathbf{Z}^{-1} + \sigma_e^{-2}\text{diag}(\mathbf{w})]^{-2}\sigma_e^{-2}\mathbf{A}_1],\end{aligned}$$

where $\mathbf{A}_1$ is an $L \times L$ matrix with only one non-zero element at $(1,1)$ given as $[\mathbf{A}_1]_{11} = 1$. Similarly,

$$\frac{\partial f(\mathbf{X}(\mathbf{w}))}{\partial[\mathbf{w}]_L} = \text{tr}\left[\left(\frac{\partial f(\mathbf{X}(\mathbf{w}))}{\partial\mathbf{X}(\mathbf{w})}\right)^T\frac{\partial\mathbf{X}(\mathbf{w})}{\partial[\mathbf{w}]_L}\right] \tag{3.52}$$

$$= \text{tr}[-[\mathbf{Z}^{-1} + \sigma_e^{-2}\text{diag}(\mathbf{w})]^{-2}\sigma_e^{-2}\mathbf{A}_L], \tag{3.53}$$

where $\mathbf{A}_L$ is an $L \times L$ matrix with only one non-zero element at (L,L) given as $[\mathbf{A}_L]_{LL} = 1$. So, the overall gradient is computed as

$$\nabla_{\mathbf{w}}h(\mathbf{w}) = \left[\frac{\partial f(\mathbf{X}(\mathbf{w}))}{\partial[\mathbf{w}]_1},\ldots,\frac{\partial f(\mathbf{X}(\mathbf{w}))}{\partial[\mathbf{w}]_L}\right]^T. \tag{3.54}$$

Substituting the elements we have $\nabla_{\mathbf{w}}h(\mathbf{w}) = \sigma_e^{-2}\text{diag}(-[\mathbf{Z}^{-1}+\sigma_e^{-2}\text{diag}(\mathbf{w})]^{-2})$.

Chapter 4

Spatio-Temporal Environmental Field Estimation Exploiting Prior Information

Dynamic estimation of the spatio-temporal evolution of an environmental field using limited number of sensing resources is a challenging task. As discussed in Chapter 2, depending upon the sensing modality and the required resolution of the estimate, the observations can be modelled as linear/non-linear underdetermined/overdetermined measurement models. In these circumstances, prior information regarding the field can be exploited in order to estimate the field accurately. In this chapter, we focus on a practical example of environmental field monitoring, i.e., spatio-temporal rainfall monitoring. We describe a dynamic rainfall monitoring methodology using rain-induced attenuation measurements from microwave links exploiting some physical properties of rainfall.

Spatial rainfall mapping from the measurements of rain-induced attenuations collected from microwave links (used by cellular telecommunication networks) is an emerging technology which can serve as an alternative to traditional approaches like rain gauges and weather radar [5]. The motivation behind this methodology is to utilize existing systems such as cellular networks to improve the quality of

Part of this chapter is published as: V. Roy, S. Gishkori, and G. Leus, "Dynamic rainfall monitoring using microwave links," *EURASIP Journal on Advances in Signal processing*, vol. 2016, no. 1, pp. 1-17, December 2016

rainfall estimates using rain gauges and radar, as well as to use it as an independent rainfall measuring unit in areas, where traditional measuring modalities are scarce. To estimate the rainfall intensity dynamically from a limited number of non-linear measurements, we exploit the physical properties of rainfall such as spatial sparsity and non-negativity along with the dynamics of the rainfall intensity. We develop a dynamic state estimation algorithm, where the aforementioned spatial properties are utilized as prior information. The developed methodology is applied to dynamically monitor the rainfall field intensity in an area with a specified spatial resolution. The proposed methodology can be generalized for any dynamic field reconstruction, where the limited number of non-linear measurements are field intensities integrated over a linear path.

The outline of the chapter is as follows. In Section 4.1, the previous works in this field along with the main contributions of this chapter are presented. The measurement model for the dynamic rainfall mapping from microwave link attenuation measurements is presented in 4.2. In Section 4.3, spatial and temporal variability of the rainfall field are presented. The dynamic rainfall monitoring algorithm exploiting the physical information regarding the rainfall field is described in Section 4.4. In Sections 4.5 and 4.6, the methods for dynamic selection of the "sparsifying" basis and the selection of the tuning parameter regulating the sparsity are described. The simulation results for different scenarios (e.g., known or unknown spatio-temporal prior information) are presented in Section 4.7. Finally, the concluding remarks along with the challenges are presented in Section 4.8.

4.1 Prior art and contributions

One of the main motivations behind "rainfall monitoring using microwave link attenuation" is to utilize existing systems such as microwave links in the cellular networks to improve the quality of rainfall estimates using rain gauges and radar. It can also be used as an independent rainfall measuring unit. These can be applied mainly in the areas, where traditional measuring modalities are scarce. The attenuation measurements from microwave links can also be used for monitoring snowfall, fog and humidity [63]. However, practicability of spatio-temporal rainfall monitoring is exhibited in [1] by comparing its performance with rain gauges and radar. In Fig. 4.1, the comparison of the estimates of rainfall intensity (mm/hr) of rain-gauge, radar, and microwave link based estimates are presented [1]. Seminal works in this domain include tomographic rainfall mapping [64], and a stochastic implementation of the microwave tomographic inversion technique (MTIT) [65].

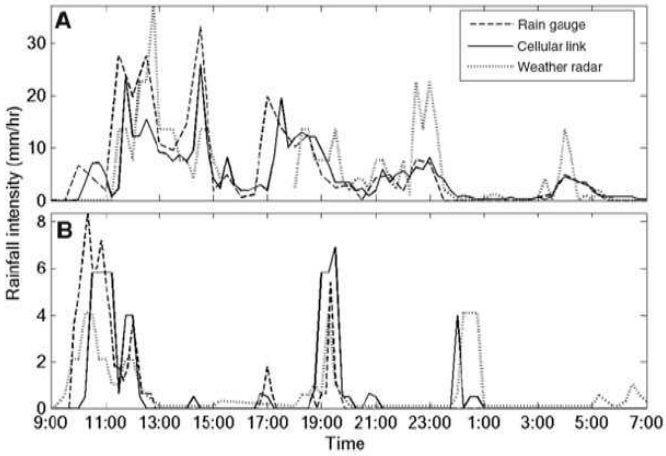

Figure 4.1: Rainfall intensity (mm/hr) measured by microwave links, rain gauges, and radar, in two places in Israel: (A) Tel-Aviv and (B) Haifa : source of figure *Messer et al.* 2006 [1].

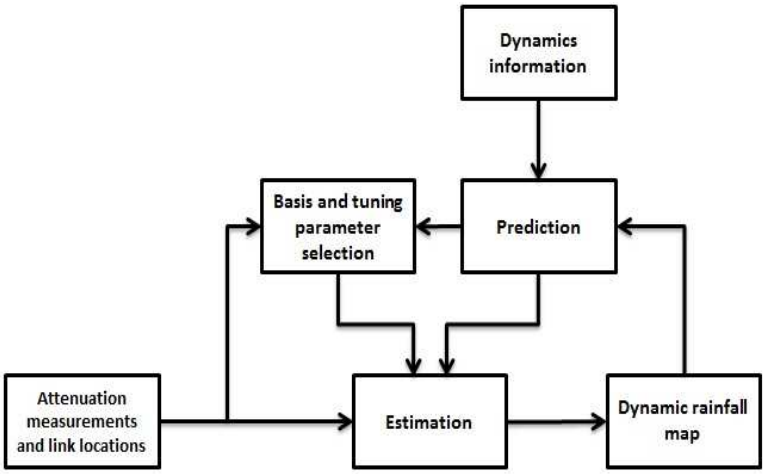

Figure 4.2: Proposed dynamic rainfall monitoring framework.

Recently, it has been observed that signal processing algorithms like a modified weighted least squares method can be implemented to spatially map the rainfall intensity on a regular grid, using microwave link attenuation measurements [12]. Also, a direct spatial reconstruction from non-linear measurements using a variable grid size is exhibited in [66]. The robustness of a practical application of "rainfall monitoring using microwave link attenuation" is illustrated in [67], where a country-wide (The Netherlands) rainfall mapping is shown to be possible using link attenuation measurements using a data set of 12 days (with a temporal resolution of 15 minutes). However, in order to achieve some desired spatial resolution of the rainfall field estimate (in terms of number of pixels), the number of microwave links, i.e., the number of attenuation measurements is always much smaller than the number of pixels in a given service area. In this case, to dynamically monitor the rainfall intensity, physical properties of rainfall like spatial sparsity and non-negativity can be exploited as extra information. In [68], a sparse reconstruction of the rainfall field from a limited number of non-linear measurements is presented. In [69], a sparsity- as well as a ridge-penalized, non-negativity constrained, ordinary least squares method is used to estimate the spatial rainfall map from linear path-averaged rainfall intensities, albeit for a single snapshot. Furthermore, incorporating the non-linearity of the measurements as well as a state-space model, a spatio-temporal rainfall monitoring method using an extended Kalman filter (EKF) is described in [13]. Recently, a linear Kalman filter is used for the reconstruction of rainfall maps inspired by object tracking algorithms [70]. However, none of the above dynamic rainfall monitoring methods exploits structural properties of the rainfall field like sparsity or non-negativity.

Commingling the concepts of the aforementioned literature, estimating a spatio-temporally evolving rainfall field can be viewed as a dynamic sparse field estimation problem, where the spatial sparsity of the rainfall field can be tailored by representing it as a sparse signal in a suitable "sparsifying" basis [37], [71]. Such a dynamic estimation of sparse signals, also known as sparsity-aware Kalman filtering, is a well-studied problem in the field of signal processing with quite a number of applications like target tracking, video coding etc. Next to the spatial sparsity also the temporal sparsity can be exploited in the state estimation [72]. Sparsity penalties lead to a faster convergence than a clairvoyant Kalman filter, as illustrated in [72]. Also, a non-negativity constrained sparsity-aware Kalman filter is applied to the target tracking problem in [73]. In [74], the "dynamic filtering" is implemented by introducing an iterative re-weighted ℓ_1 penalty. In that work, a Bayesian hierarchical model is used for the dynamically varying sparse coeffi-

cients of the signal. Also, in [75], the convergence of the aforementioned approach has been illustrated, formulating it as a basis pursuit denoising (BPDN) problem. Another notable approach of tracking a sparse signal in an underdetermined measurement scenario is viewing sparsity as a pseudo-measurement and implementing a parallel state and covariance update scheme for this extra measurement [76]. In the Bayesian paradigm, a sparsity-aware state estimation can be formulated as a constrained maximum a posteriori estimator (MAP) [77].

In this work, we assume that the spatial rainfall intensity can be represented as a sparse environmental signal. We assume two scenarios for the spatio-temporal evolution of the rainfall field. In the first case, we assume that the dynamics of the rainfall field are perfectly known. In this case, we use a linear but time-varying dynamical model for the space-time evolution of the rainfall event, which incorporates physical phenomena like advection, diffusion and convection [32], [78]. In the second case, we assume that the information regarding the dynamics are not perfectly known. In this case, we approximate the spatio-temporal evolution by a simple Gaussian random walk model.

We develop a complete structured framework to dynamically monitor the rainfall intensity exploiting the prior knowledge regarding the spatial sparsity, non-negativity and the dynamics of the rainfall field. The overall dynamic rainfall monitoring setup is pictorially represented in Figure 4.2. The proposed setup accepts attenuation measurements, in a given service area at any given snapshot from the operating links, whose geometry and operating frequencies are known. Accumulating these non-linear measurements, the spatial rainfall intensity in the given service area is computed in a centralized approach with a specified resolution. The developed dynamic rainfall monitoring algorithm has the following salient features:

- A non-linear, underdetermined, and time-varying measurement model is considered here. A dynamic linearization, followed by a state estimation is performed, where sparsity and non-negativity are exploited, in order to achieve a stable solution from the underdetermined measurement setup.

- The tuning parameter regulating the sparsity can be dynamically updated on every estimation step.

- The algorithm is generalized to dynamically select the representation basis that minimizes the mutual coherence between the basis matrix and the measurement matrix at a particular time instance, which represents the geometry of the available link measurements at that time instance.

4.2 Measurement model

The topology of the network of microwave links deployed by any telecommunication service provider in any service area is fixed. These links can be viewed as a fixed network of sensors to monitor rainfall since the received signal level (RSL) measurements related to these links depend on the rainfall. It should be noted that the signal attenuation on a microwave link is not only due to rainfall but also depends on other atmospheric effects like humidity, wet-antenna attenuation, and propagation loss. For simplicity, we assume that the attenuation caused by these other effects (except precipitation) can be pre-computed e.g., during "dry periods", and subtracted from the recorded RSL measurements. In this way, the effective measurements only include the rain-induced attenuation. The conventional empirical relationship between the rain-induced specific attenuation and the path-averaged rainfall rate is given by $y_{\mathrm{s}} = ar^b$, where y_{s} is the specific attenuation of the link (dB/km), and r is the path-averaged rainfall rate over the link (mm/hour) [79]. If L is the length (km) of the microwave link, then the total rain-induced attenuation over the link is $y = y_{\mathrm{s}}L = ar^bL$ dB. Parameters a and b are related to the drop size distribution (DSD) of the rain, the polarization and frequency of the transmitted electromagnetic wave, the length of the link, the ambient temperature, etc. It has been extensively studied and shown in several works that variations of the aforementioned environmental and non-environmental parameters affect the estimate of the path-averaged rainfall rate. A quantitative analysis of DSD related errors in estimating the path-averaged rainfall from direct rain-induced attenuation measurements is illustrated in [80], [81]. It can be observed that the attenuation for links operating in frequencies around 35 GHz can be treated as a linear measurement of the path-averaged rainfall rate [80]. A detailed analysis of the effects of the frequency, DSD, link length, and temporal sampling in estimating the path-averaged rainfall rate has been presented in [82], [83]. Also, in a wide coverage area the link (measurement) availability in different hours of the day may significantly vary. All of these aforementioned studies advocate a dynamic tuning of the a and b coefficients in order to better monitor the rainfall from link attenuation.

The non-linear attenuation measurements from the microwave links in any given service area for a fixed time can be used to estimate the spatial rainfall intensity over the same area. Let us consider a uniform discretization of the specified service area $\mathcal{A}$ (square) into N pixels where we would like to estimate the rainfall intensity. Here, we make the assumption that the rainfall intensity is constant within any pixel. This assumption is flexible as any resolution can be attained by tailoring

the areas of the square pixels. Let us assume that there are M links in the given service area. The length of the i-th link can be written as $L_i = \sum_{j=1}^{N} l_{ij}$, where l_{ij} is the length of the i-th link passing through the j-th pixel, where $i = 1, \ldots, M$. If the i-the link does not pass through the j-th pixel then $l_{ij} = 0$, otherwise it is computed by the link and the pixel coordinates. The total attenuation over a link can be modelled as the sum of the attenuations over the link-segments [12]. Using this, the attenuation over the i-th link at time t can be expressed as $y_{i,t} \approx \sum_{j=1}^{N} y_{ij,t}$, where $y_{ij,t}$ is the attenuation over the link-segment of length l_{ij}. Using the power-law relationship for the attenuations over the link-segments, the measurement model can be constructed in the following way,

$$y_{i,t} = a_{i,t} \sum_{j=1}^{N} u_{j,t}^{b_{i,t}} l_{ij} + e_{i,t}, \quad i = 1, \ldots, M, \tag{4.1}$$

where $y_{i,t}$ is the attenuation measurement of the i-th link, and $u_{j,t}$ is the intensity of the rainfall field in the j-th pixel at time t. The power-law coefficients of the i-th link at time t are given by $a_{i,t}$ and $b_{i,t}$. The measurement model in (4.1) is a generalized time-varying non-linear tomographic measurement model. In this work, we consider the fact that all the M links are operated in the same frequency and that the other environmental conditions (e.g., DSD, temperature) are fixed for all t. Based on these assumptions, the aforementioned measurement model can be simplified as

$$y_{i,t} = a \sum_{j=1}^{N} u_{j,t}^{b} l_{ij} + e_{i,t}, \quad i = 1, \ldots, M. \tag{4.2}$$

The measurement noise incurred at the i-th link measurement at time t is given by $e_{i,t}$. The measurements are corrupted by errors which are mainly due to quantization but also there are other sources of noise. A more detailed description of the statistical nature of the measurement noise can be found in [12]. For the sake of simplicity, let us assume that $e_{i,t}$ is zero-mean spatio-temporally white Gaussian noise with variance σ_e^2. Further, we assume that $e_{i,t}$ is uncorrelated with $u_{j,t}$.

Combining all the measurements from the M links at time t, we can construct the following non-linear measurement model at time t:

$$\mathbf{y}_t = \mathbf{\Phi}(\mathbf{u}_t) + \mathbf{e}_t, \tag{4.3}$$

where $\mathbf{y}_t \in \mathbb{R}^M$ stacks the measurements from the M links at time t, whereas $\mathbf{e}_t \in \mathbb{R}^M$ does the same for the noise. The vector $\mathbf{u}_t \in \mathbb{R}^N$ gathers the rainfall intensities for all of the N pixels at time t, i.e, it is the parameter to be estimated

dynamically. The non-linear mapping between the rainfall intensities and the attenuation measurements is given by $\mathbf{\Phi} : \mathbb{R}^N \rightarrow \mathbb{R}^M$ and it is assumed to be perfectly known. The elements of $\mathbf{u}_t$ are given by $[\mathbf{u}_t]_j = u_{j,t} = u_t(\mathbf{x}_j)$, where $u_t(\mathbf{x})$ represents the continious rainfall field at any arbitrary location $\mathbf{x} \in \mathbb{R}^2$ and $\mathbf{x}_j = [x_j, y_j]^T$ is the centroid of the j-th pixel of the service area. The measurement noise components associated with the M link measurements are characterized by $\mathbf{e}_t \sim \mathcal{N}(\mathbf{0}, \mathbf{R}_t)$, where $\mathbf{R}_t = \mathbf{R} = \sigma_e^2 \mathbf{I}_M$, where σ_e^2 is the measurement noise variance which is assumed to be known a priori.

4.3 Spatio-temporal variability of rainfall

4.3.1 Spatial variability of $\mathbf{u}_t$

At any snapshot t, the spatial rainfall intensity $u_t(\mathbf{x}_j)$, for $j = 1, \ldots, N$ can be viewed as a wide-sense stationary (WSS) random process. In spatial statistics, $u_t(\mathbf{x}_j)$ is WSS (or second-order stationary) if it satisfies $\mathbb{E}[u_t(\mathbf{x}_j)] = \mu_t$ (for all $j = 1, \ldots, N$ in the service area), and if the spatial covariance between any two points is dependent only on the distance between them (i.e., isotropic) [84]. The parameter μ_t is the mean/trend of the rainfall field. As mentioned in Section 2.2.1, a variogram model can be used to represent the spatial variations. Generally, several variogram models are used as it is computationally hard to calculate the spatial dependency for every lag distance h. Some statistical functions like a Gaussian, exponential or empirically fitted models like spherical functions are often used as variogram models [7]. From the analysis of [30], the spherical variogram model is seen to be an appropriate model to describe the spatial variability of rainfall. The mathematical expression of a spherical variogram ($2\gamma(h)$) or semivariogram ($\gamma(h)$) is given in (2.10).

The advantage of the spherical variogram model is that the parameters that charachterizes a spherical variogram, i.e., sill ($N_0 + S_0$), partial sill (S_0), nugget (N_0), and range(d) can be approximated in hourly scales for a specific day of the year [30]. Now, the spatial covariance function $C_v(h)$ can be defined as $C_v(h) = \mathbb{E}[(u_t(\mathbf{x}_i) - \mu_t)(u_t(\mathbf{x}_j) - \mu_t)]$. As mentioned in 2.2.1, using the second-order stationarity of the random process $u_t(\mathbf{x}_j)$, the semivariogram can be related to the spatial covariance function $C_v(h)$ by the relation $\gamma(h) = (N_0 + S_0) - C_v(h)$ [84]. Now, the elements of the spatial covariance matrix $\mathbf{\Sigma}_u$ can be computed as $[\mathbf{\Sigma}_u]_{ij} = C_v(\|\mathbf{x}_i - \mathbf{x}_j\|_2), \forall i, j \in \{1, \ldots, N\}$.

4.3.2 State model

The spatio-temporal evolution of rainfall is a complicated phenomenon involving many physical processes like diffusion, advection etc. In the following sections we present two approaches of modelling the dynamics of rainfall.

A Kernel-based state model

One standard approach of modelling the spatio-temporal evolution of any environmental field is based on the integro-difference equation (IDE) [7]. The aforementioned approach is similar to Section 3.3 . Following this approach, the dynamics of the rainfall field for any specific temporal sampling interval δ_t can be modelled as the following discrete time IDE

$$u_t(\mathbf{x}) = \int_{\mathcal{A}} g(\mathbf{x}, \mathbf{x}'; \boldsymbol{\theta}) u_{t-1}(\mathbf{x}') d\mathbf{x}' + q_t(\mathbf{x}). \tag{4.4}$$

Here, $g(\mathbf{x}, \mathbf{x}'; \boldsymbol{\theta})$ is the space-time interaction function parameterized by $\boldsymbol{\theta}$, which can be deterministic or random and dependent on the temporal sampling interval δ_t. The quantity $q_t(\mathbf{x})$ is the process noise which is generally modelled as independent in time but correlated over space.

The space-time interaction function $g(\cdot)$ can be modelled as a parameterized Gaussian dispersal kernel which captures the underlying physical processes behind the spatio-temporal evolution of rainfall, i.e., diffusion, advection and convection [32], [78]. In this case, the space-time interaction function is given as $g(\mathbf{x}, \mathbf{x}'; \mathbf{w}_t, \mathbf{D}, \alpha) = \alpha \exp[-(\mathbf{x} - \mathbf{x}' - \mathbf{w}_t)^T \mathbf{D}^{-1} (\mathbf{x} - \mathbf{x}' - \mathbf{w}_t)]$, i.e., a Gaussian kernel. The translation parameter of the kernel, i.e., $\mathbf{w}_t \in \mathbb{R}^2$ models the time-varying advective displacement, i.e., the spatial drift of the rain storm, and the dilation parameter of the kernel, i.e., $\mathbf{D} \in \mathbb{S}^2_{++}$, models the diffusion. Note that, $\mathbf{w}_t$ can also vary with space but we assume that it is averaged over the entire area and fixed. The diffusion coefficient $\mathbf{D}$ can be used to model isotropic as well as anisotropic diffusion. The amount and the directions of the spatial anisotropy can be introduced by $\mathbf{D}$. The parameter $\mathbf{D}$ can also vary with time but this is not considered here. The scalar scaling parameter $\alpha \in \mathbb{R}_{++}$ is used to control the stability (i.e., to avoid the explosive growth) of the dynamic process.

Here the entire service area is uniformly discritized into N pixels. We assume a state transition matrix $\mathbf{H}_t \in \mathbb{R}^{N \times N}$ whose elements are modelled by the aforementioned simple 2D Gaussian kernel. After proper vectorization of the field intensities

and state noise for N pixels we obtain

$$\mathbf{u}_t = \mathbf{H}_t \mathbf{u}_{t-1} + \mathbf{q}_t, \tag{4.5}$$

where the elements of the state transition matrix $\mathbf{H}_t$ are given by $[\mathbf{H}_t]_{ij} = \alpha \exp[-(\mathbf{x}_i - \mathbf{x}_j - \mathbf{w}_t)^T \mathbf{D}^{-1} (\mathbf{x}_i - \mathbf{x}_j - \mathbf{w}_t)]$, and $\mathbf{q}_t$ is the spatially colored yet temporally white Gaussian state noise vector. The quantity $\mathbf{w}_t$ is the advective displacement during the temporal sampling interval δ_t, which can be represented more precisely as $\mathbf{w}_t = \mathbf{v}_t \delta_t$, where $\mathbf{v}_t$ is the advection velocity. Note that the aforementioned model is non-stationary when the advection vector $\mathbf{w}_t$ changes with time, which happens in many real scenarios [32]. If there is no advection, i.e., $\mathbf{w}_t = \mathbf{0}$ and $\mathbf{D} = \mathbf{I}$, the model is stationary and isotropic. We assume that the dynamic model, i.e., the state transition matrix $\mathbf{H}_t$ is perfectly known through the parameters $\mathbf{w}_t$, $\mathbf{D}$, and α which are considered to be deterministic and known. Without loss of generality, we follow the assumptions of [32] and [33] that the distribution of $\mathbf{q}_t$ is given by $\mathbf{q}_t \sim \mathcal{N}(\mathbf{0}_N, \mathbf{Q}_t)$. But this assumption is not true in practical scenarios because the rainfall process cannot be negative. In the simulation section, after generating $\mathbf{u}_t$ using the sate model of (4.5), we set the negative elements of $\mathbf{u}_t$ to 0. This is a modelling approximation.

One notable advantage of the model in [32] is the linear relation of the rainfall intensities in one snapshot with the ones in the previous snapshot.

Gaussian random walk model

In the last section, we assume that the parameters of the state model are perfectly known. But in many practical scenarios for a large N, it can be computationally intractable to estimate the N^2 elements of the state transition matrix $\mathbf{H}_t$ using the available data. In this case, without any prior knowledge regarding the parameterization of $\mathbf{H}_t$, one way to approximate the dynamics is by assuming that the process follows a Gaussian random walk model [85]. In this case, we assume that $\mathbf{H}_t = \mathbf{H} = \mathbf{I}$ and the process model is given by

$$\mathbf{u}_t = \mathbf{u}_{t-1} + \mathbf{q}_t. \tag{4.6}$$

The benefit of a Gaussian random walk model is that it has very few model parameters rather than a parameterized process model as mentioned in the previous sub-section.

Note that the parameterized state model of (4.5) can be viewed as a random walk model by incorporating negligible diffusion, i.e., $\mathbf{D} = \epsilon \mathbf{I}$, where $\epsilon \ll 1$ and no advection, i.e., $\mathbf{w}_t = \mathbf{0}$. In this case, we have $\mathbf{H}_t \approx \mathbf{I}$ assuming $\alpha = 1$.

Structure of the state error covariance matrix

It is assumed that the state error, i.e., $\mathbf{q}_t$, is a spatially colored but temporally white Gaussian process. Assuming spatial isotropy and stationarity of the state error $\mathbf{q}_t$, the elements of the covariance matrix $\mathbf{Q}_t = \mathbf{Q}$ can be represented using the Matern covariance function as,

$$[\mathbf{Q}]_{ij} = \sigma_s^2 \frac{2^{1-p}}{\Gamma(p)} \left[\frac{\sqrt{2p}\|\mathbf{x}_i - \mathbf{x}_j\|_2}{\gamma} \right]^p K_p \left(\frac{\sqrt{2p}\|\mathbf{x}_i - \mathbf{x}_j\|_2}{\gamma} \right), \tag{4.7}$$

where $\Gamma(\cdot)$ is the Gamma function, $K_p(\cdot)$ is the modified Bessel function of the second kind, and γ is a positive shaping parameter [7]. With $p \to \infty$ and $p = 1/2$, (4.7) becomes the squared exponential and the exponential covariance functions, i.e., $[\mathbf{Q}]_{ij} = \sigma_s^2 \exp\left(-\frac{\|\mathbf{x}_i - \mathbf{x}_j\|_2^2}{2\gamma^2}\right)$, and $[\mathbf{Q}]_{ij} = \sigma_s^2 \exp\left(-\frac{\|\mathbf{x}_i - \mathbf{x}_j\|_2}{\gamma}\right)$, respectively.

4.4 Dynamic rainfall mapping

We dynamically estimate the rainfall intensities at the N pixels, i.e., $\mathbf{u}_t$ at $t = 1, \ldots, T$ snapshots from the attenuation measurements $\mathbf{y}_t$ at $t = 1, \ldots, T$. The measurement and state models can be represented in the following forms

$$\mathbf{y}_t = \mathbf{\Phi}(\mathbf{u}_t) + \mathbf{e}_t \tag{4.8}$$

$$\mathbf{u}_t = \mathbf{H}_t \mathbf{u}_{t-1} + \mathbf{q}_t. \tag{4.9}$$

A standard practice to estimate the rainfall intensity $\mathbf{u}_t$ at every time $t = 1, \ldots, T$ from the measurement and state equations of (4.8) and (4.9) is the non-linear semblance of the standard Kalman filter, i.e., the extended Kalman filter (EKF) [57]. Note that we have non-linearity only in the measurements.

As one of the criteria for the optimal behavior of the Kalman fiter, we assume that the measurement and the state noise statistics are completely known. The measurement and the state noises are characterized by $\mathbf{e}_t \sim \mathcal{N}(\mathbf{0}_M, \mathbf{R})$ and $\mathbf{q}_t \sim \mathcal{N}(\mathbf{0}_N, \mathbf{Q})$, respectively. The dimension of the measurement noise covariance matrix depends on the number of the available measurements at time t. As the state model is a linear function of $\mathbf{u}_t$, the standard Kalman fiter prediction steps are given by,

$$\hat{\mathbf{u}}_{t|t-1} = \mathbf{H}_t \hat{\mathbf{u}}_{t-1|t-1} \tag{4.10}$$

$$\mathbf{M}_{t|t-1} = \mathbf{H}_t \mathbf{M}_{t-1|t-1} \mathbf{H}_t^T + \mathbf{Q}, \tag{4.11}$$

where the prediction of $\mathbf{u}_t$ from the last $t-1$ observations is given by $\hat{\mathbf{u}}_{t|t-1}$ with the error covariance matrix $\mathbf{M}_{t|t-1} = \mathbb{E}[(\mathbf{u}_t - \hat{\mathbf{u}}_{t|t-1})(\mathbf{u}_t - \hat{\mathbf{u}}_{t|t-1})^T]$ [57]. The terms $\hat{\mathbf{u}}_{t-1|t-1}$ and $\mathbf{M}_{t-1|t-1}$ are calculated in the previous time step.

The prediction based on the state model is corrected by the measurements. But here we have a non-linear measurement model. To linearize that model, let us introduce the $M \times N$ Jacobian matrix computed at $\mathbf{u}_t = \hat{\mathbf{u}}_{t|t-1}$ as $\mathbf{J}_t = \left.\frac{\partial \mathbf{\Phi}}{\partial \mathbf{u}_t^T}\right|_{\mathbf{u}_t = \hat{\mathbf{u}}_{t|t-1}}$. The elements of the Jacobian matrix are given by $[\mathbf{J}_t]_{ij} = abl_{ij}[\hat{\mathbf{u}}_{t|t-1}]_j^{b-1}$, with $i = 1, \ldots, M$, and $j = 1, \ldots, N$. A first order Taylor series expansion of the non-linear measurement function around $\hat{\mathbf{u}}_{t|t-1}$ is then given as $\mathbf{\Phi}(\mathbf{u}_t) \approx \mathbf{\Phi}(\hat{\mathbf{u}}_{t|t-1}) + \mathbf{J}_t[\mathbf{u}_t - \hat{\mathbf{u}}_{t|t-1}]$. Substituting this in (4.8), we obtain the following linearized measurement equation:

$$\tilde{\mathbf{y}}_t = \mathbf{J}_t \mathbf{u}_t + \mathbf{e}_t, \tag{4.12}$$

where $\tilde{\mathbf{y}}_t = \mathbf{y}_t - \mathbf{\Phi}(\hat{\mathbf{u}}_{t|t-1}) + \mathbf{J}_t \hat{\mathbf{u}}_{t|t-1}$. Note that here we have less observations than unknowns, i.e., the number of links (M) is much smaller than the number of pixels (N), i.e., the dimension of $\mathbf{u}_t$. Hence, in the correction step, to utilize the measurements along with the state model, we need to solve the underdetermined system (4.12) in order to update $\hat{\mathbf{u}}_{t|t-1}$ leading to $\hat{\mathbf{u}}_{t|t}$. After the dynamic linearization, the state estimates can be obtained using a standard Kalman filter. In this case, both the expressions for the state estimate $\hat{\mathbf{u}}_{t|t}$ and its state error covariance $\mathbf{M}_{t|t}$ can be obtained in closed form [57].

4.4.1 Limitations of standard EKF

The estimation of $\mathbf{u}_t$ from only M measurements using an ordinary EKF has the following uncertainties.

- First of all, the quality of the estimate strongly depends on the degree of non-linearity and the accuracy of the linearization [57]. Also, for a highly underdetermined $(M \ll N)$ and unpredictable measurement matrix (many rows of $\mathbf{J}_t$ can be zero for any $\hat{\mathbf{u}}_{t|t-1}$) the solution can be highly inaccurate and dependent mainly on the predictions using the state model and the initialization.

- In the above case, if the available information regarding the dynamics are incomplete or imperfectly known then the prediction using the state model will be inaccurate. In this case, an ordinary EKF may produce unrealistic estimates in the presence of high measurement noise.

- Also, there is no guarantee that an ordinary EKF will always produce non-negative estimate of $\hat{\mathbf{u}}_{t|t}$. For instance, let us assume that an element of the predicted value, i.e., $[\hat{\mathbf{u}}_{t|t-1}]_j$ (predicted using (4.10)) is less than 0 at any t. In that case, if $l_{ij} \neq 0$ we may have an imaginary $[\mathbf{J}_t]_{ij} = abl_{ij}[\hat{\mathbf{u}}_{t|t-1}]_j^{b-1}$, if $b-1$ is a fractional quantity. As mentioned in [79], the standard values for b mainly lie in the interval of $0 < b < 2$.

In these circumstances, any further prior information about $\mathbf{u}_t$ (beyond the dynamics) is desirable to achieve a stable and more accurate solution.

4.4.2 Available prior knowledge regarding rainfall field

Prior information about $\mathbf{u}_t$ can be acquired from the physical properties of rainfall such as sparsity and non-negativity. In a given area, the rainfall intensity itself can be assumed to be a sparsely distributed environmental field over the entire service area [86], [68]. But sparsity can also be introduced by representing $\mathbf{u}_t$ in an orthonormal basis $\mathbf{\Psi}_t$, which can in principle be time-varying. When rainfall itself is sparse we simply have $\mathbf{\Psi}_t = \mathbf{I}$. Denoting $\mathbf{u}_t = \mathbf{\Psi}_t \mathbf{z}_t$, sparsity is measured by the number of non-zero entries in $\mathbf{z}_t$, i.e., $\|\mathbf{z}_t\|_0$.

As the rainfall intensity cannot be negative, another prior knowledge about $\mathbf{u}_t$ is the non-negativity of the rainfall field. For N pixels, this is represented as $\mathbf{u}_t \geq \mathbf{0}_N$.

Comment: Here we mention that the prior information regarding sparsity and non-negativity along with the measurements can be efficiently utilized to monitor the rainfall over multiple snapshots. For this we do not need any information regarding the dynamics. This can be implemented for both linear [69] as well as non-linear [68] measurement models. However, one limitation of this dynamics-agnostic method is that the rainfall events should occur in areas where microwave links are present for accurate estimation. Otherwise, the effect of the measurement noise can be dominant. In this case, we need other spatial/temporal information (e.g., covariance structure, dynamics) to interpolate the rainfall field over the entire service area.

In the next section, we illustrate iterative approaches to dynamically estimate the state of $\mathbf{u}_t$ for $t = 1, \ldots, T$, exploiting sparsity, non-negativity as well as dynamics.

4.4.3 Estimation of $\mathbf{u}_t$

A simple Kalman estimation step without the sparsity and the non-negativity constraint can be formulated as the following weighted least squares optimization problem [87]:

$$\hat{\mathbf{u}}_{t|t} = \arg\min_{\mathbf{u}_t} \|\hat{\mathbf{u}}_{t|t-1} - \mathbf{u}_t\|^2_{\mathbf{M}^{-1}_{t|t-1}} + \|\tilde{\mathbf{y}}_t - \mathbf{J}_t\mathbf{u}_t\|^2_{\mathbf{R}^{-1}}. \tag{4.13}$$

This estimation step is not aware of sparsity or non-negativity. The sparsity information can be incorporated in the optimization problem of (4.13), by adding an ℓ_1-penalty that enforces sparsity. Note that here we use the ℓ_1 norm as a convex relaxation of the non-convex ℓ_0 norm. Using the sparse representation of $\mathbf{u}_t$, i.e., $\mathbf{z}_t$, the optimization problem of (4.13) can be formulated as a sparsity and non-negativity constrained optimization problem. This can be given as,

$$\hat{\mathbf{z}}_t = \arg\min_{\mathbf{\Psi}_t\mathbf{z}_t \geq \mathbf{0}_N} \|\hat{\mathbf{u}}_{t|t-1} - \mathbf{\Psi}_t\mathbf{z}_t\|^2_{\mathbf{M}^{-1}_{t|t-1}} + \|\tilde{\mathbf{y}}_t - \mathbf{J}_t\mathbf{\Psi}_t\mathbf{z}_t\|^2_{\mathbf{R}^{-1}} + \lambda_t\|\mathbf{z}_t\|_1 \tag{4.14}$$

$$\hat{\mathbf{u}}_{t|t} = \mathbf{\Psi}_t\hat{\mathbf{z}}_t, \tag{4.15}$$

where λ_t is the tuning parameter that controls sparsity. The standard error covariance update of $\hat{\mathbf{u}}_{t|t}$ for the estimation step (4.13) is given by $\mathbf{M}_{t|t} = \mathbf{M}_{t|t-1} - \mathbf{M}_{t|t-1}\mathbf{J}_t^T(\mathbf{R}_t + \mathbf{J}_t\mathbf{M}_{t|t-1}\mathbf{J}_t^T)^{-1}\mathbf{J}_t\mathbf{M}_{t|t-1} = (\mathbf{M}^{-1}_{t|t-1} + \mathbf{J}_t^T\mathbf{R}_t^{-1}\mathbf{J}_t)^{-1}$ [57]. This expression of $\mathbf{M}_{t|t}$ can be used to update the covariance of the estimate of (4.14) but is an approximation as it is not aware of the sparsity and the non-negativity constraint. If we do not consider to propagate the second order statistics of the estimate, like in the traditional Kalman filter, the state noise minimization term in (4.14) can also be regularized by $\mathbf{Q}$ instead of $\mathbf{M}_{t|t-1}$. This can be viewed as a weighted least squares problem to estimate $\mathbf{u}_t$ using the measurement (4.12) and the state equation (4.9) constrained by sparsity and non-negativity. In this case, the simple iterative state estimates are given by,

$$\hat{\mathbf{u}}_{t|t-1} = \mathbf{H}_t\hat{\mathbf{u}}_{t-1|t-1}, \tag{4.16}$$

$$\hat{\mathbf{z}}_t = \arg\min_{\mathbf{\Psi}_t\mathbf{z}_t \geq \mathbf{0}_N} \|\hat{\mathbf{u}}_{t|t-1} - \mathbf{\Psi}_t\mathbf{z}_t\|^2_{\mathbf{Q}^{-1}} + \|\tilde{\mathbf{y}}_t - \mathbf{J}_t\mathbf{\Psi}_t\mathbf{z}_t\|^2_{\mathbf{R}^{-1}} + \lambda_t\|\mathbf{z}_t\|_1, \tag{4.17}$$

$$\hat{\mathbf{u}}_{t|t} = \mathbf{\Psi}_t\hat{\mathbf{z}}_t. \tag{4.18}$$

Note that this is a suboptimal approach to dynamically estimate the states $\mathbf{u}_t$ avoiding the computation of $\mathbf{M}_{t|t}$. As mentioned in [72], different penalties (like ℓ_2 or ℓ_1) can be applied to the state error minimization term in (4.17) depending on the nature of the sparse state ($\mathbf{u}_t$) and/or the state noise ($\mathbf{q}_t$).

4.4.4 Constrained MAP estimator for $\mathbf{u}_t$

Using the representation of $\mathbf{u}_t$ in the $\mathbf{\Psi}_t = \mathbf{\Psi}$ domain, the measurement and state equation of (4.12) and (4.9) can be written as,

$$\tilde{\mathbf{y}}_t = \mathbf{J}_t \mathbf{\Psi} \mathbf{z}_t + \mathbf{e}_t \tag{4.19}$$

$$\mathbf{z}_t = \tilde{\mathbf{H}}_t \mathbf{z}_{t-1} + \tilde{\mathbf{q}}_t, \tag{4.20}$$

where $\tilde{\mathbf{H}}_t = \mathbf{\Psi}^T \mathbf{H}_t \mathbf{\Psi}$, $\tilde{\mathbf{q}}_t = \mathbf{\Psi}^T \mathbf{q}_t$, and $\tilde{\mathbf{q}}_t \sim \mathcal{N}(\mathbf{0}, \mathbf{\Psi}^T \mathbf{Q} \mathbf{\Psi})$, where $\mathbf{q}_t \sim \mathcal{N}(\mathbf{0}, \mathbf{Q})$. From the above measurement and state equations, we can derive the conditional probability density functions $p(\tilde{\mathbf{y}}_t|\mathbf{z}_t) \sim \mathcal{N}(\mathbf{J}_t \mathbf{\Psi} \mathbf{z}_t, \mathbf{R})$ and $p(\mathbf{z}_t|\mathbf{z}_{t-1}) \sim \mathcal{N}(\tilde{\mathbf{H}}_t \mathbf{z}_{t-1}, \mathbf{\Psi}^T \mathbf{Q} \mathbf{\Psi})$. Using Bayes' rule, the posterior pdf $p(\mathbf{z}_t|\tilde{\mathbf{y}}_t)$ can be given as $p(\mathbf{z}_t|\tilde{\mathbf{y}}_t) \propto p(\tilde{\mathbf{y}}_t|\mathbf{z}_t) p(\mathbf{z}_t|\mathbf{z}_{t-1})$. So, a MAP estimator for $\mathbf{z}_t$ can be formulated as

$$\arg\max_{\mathbf{z}_t} \left[\ln p(\tilde{\mathbf{y}}_t|\mathbf{z}_t) + \ln p(\mathbf{z}_t|\mathbf{z}_{t-1})\right], \tag{4.21}$$

where $\mathbf{z}_{t-1}$ is computed from the previous time step. However, there is no guarantee that the estimator in (4.21) will produce a sparse estimate of $\mathbf{z}_t$. On the other hand, the representation of $\mathbf{u}_t$ in the $\mathbf{\Psi}$ domain is targeted to exploit sparsity. So, the estimator of (4.21) can be formulated as a constrained MAP estimator by adding the sparsity and non-negativity constraint in the optimization problem of (4.21). After substituting the pdfs, following the same approach as used in (4.14), the sparsity and non-negativity constrained MAP estimator can be given as

$$\hat{\mathbf{z}}_t = \arg\min_{\mathbf{\Psi}\mathbf{z}_t \geq \mathbf{0}_N} \|\mathbf{z}_t - \tilde{\mathbf{H}}_t \mathbf{z}_{t-1}\|^2_{(\mathbf{\Psi}^T \mathbf{Q} \mathbf{\Psi})^{-1}} + \|\tilde{\mathbf{y}}_t - \mathbf{J}_t \mathbf{\Psi} \mathbf{z}_t\|^2_{\mathbf{R}_t^{-1}} + \tilde{\lambda}_t \|\mathbf{z}_t\|_1, \tag{4.22}$$

where $\tilde{\lambda}_t$ controls the sparsity in the estimate $\hat{\mathbf{z}}_t$. From the solution of (4.22), the state estimate is given as $\hat{\mathbf{u}}_{t|t} = \mathbf{\Psi} \hat{\mathbf{z}}_t$. It is seen that resorting to a Bayesian paradigm, the developed constrained MAP estimator of (4.22) has a structure similar to the optimization problem of (4.17).

4.5 Selection of the representation basis

If the spatial rainfall distribution is physically sparse, then we simply solve the optimization problem of (4.17) for $\mathbf{\Psi}_t = \mathbf{I}$. But in the absence of physical sparsity, which is a more general case in many practical scenarios, we use a basis $\mathbf{\Psi}_t$. Revisiting the celebrated theory of compressive sampling, we know that some of the properties of both $\mathbf{\Psi}_t$ and $\mathbf{J}_t$, (or $\mathbf{\Theta}_t = \mathbf{J}_t \mathbf{\Psi}_t$) like mutual coherence, restricted

isometry property (RIP), etc. are important in the framework of sparse reconstruction [71]. Let us denote the quantity $\mu(\mathbf{\Theta}_t)$ as the mutual coherence of the matrix $\mathbf{\Theta}_t$, which is the maximum absolute inner product of different columns of $\mathbf{\Theta}_t$ [88]. Without the state error minimization term and the non-negativity constraint in (4.17), the problem is a simple basis-pursuit denoising (BPDN) problem. As derived in [89], if a suitable sparse representation of $\mathbf{z}_t$ is possible, which is given by $\|\mathbf{z}_t\|_0 < \frac{1}{2}(1 + \frac{1}{\mu(\mathbf{\Theta}_t)})$, then a "stable" solution with the standard BPDN algorithm can be obtained with a bound on the estimation error. Along the same lines, the cost function of (4.17) can be viewed as a BPDN problem by augmenting the measurement and the state noise minimization terms into a single least squares term [75]. In [75], the convergence guarantees of the aforementioned BPDN problem are also derived based on some assumptions on the dynamics and the measurement matrix (here $\mathbf{J}_t$).

In our application, the design of the measurement matrix $\mathbf{J}_t$, in every snapshot, is dictated by the link locations and the predicted state estimates ($\hat{\mathbf{u}}_{t|t-1}$). So, to maximally exploit the sparsity information of the rainfall field, we focus mainly on a suitable sparse representation of the state $\mathbf{u}_t$. Standard orthonormal bases such as a discrete cosine transform (DCT) basis $\mathbf{C}$ or wavelet basis $\mathbf{W}$ are quite popular in sparse signal representation for communications as well as image processing. Also, a Gaussian basis function can be used to sparsely represent environmental signals [22]. However, an orthonormal basis can also be constructed using the spatial covariance matrix of the rainfall field. An orthonormal basis can be constructed by the spatial covariance matrix $\mathbf{\Sigma}_u$ described in Section 4.3.1, by simply choosing $\mathbf{\Psi}_t = \mathbf{U}$, where $\mathbf{\Sigma}_u = \mathbf{U}\mathbf{\Lambda}\mathbf{U}^T$ is the eigenvalue decomposition of $\mathbf{\Sigma}_u$ with $\mathbf{U}^T\mathbf{U} = \mathbf{I}$ and $\mathbf{\Lambda}$ a diagonal matrix. In this case, $\mathbf{z}_t = \mathbf{U}^T\mathbf{u}_t$ is similar to applying a Karhunen-Loeve transform (KLT), which is also advocated as a sparse representation technique [37].

We choose a basis $\mathbf{\Psi}_t$, that has a minimum mutual coherence with the measurement matrix $\mathbf{J}_t$. Mutual coherence can be measured for the overall dictionary $\mathbf{\Theta}_t = \mathbf{J}_t\mathbf{\Psi}_t$. In this case, $\mu(\mathbf{\Theta}_t)$ can be quantified as the maximum magnitude off-diagonal element of $\mathbf{D}_t = \breve{\mathbf{\Theta}}_t^T\breve{\mathbf{\Theta}}_t$, where $\breve{\mathbf{\Theta}}_t$ is obtained by normalizing the columns of $\mathbf{\Theta}_t$. In this case, the mutual coherence can be defined as $\mu(\mathbf{J}_t\mathbf{\Psi}_t) = \mu(\mathbf{\Theta}_t) = \max_{l,k;\, l\neq k} |[\mathbf{D}_t]_{l,k}|$ [90]. So, given a set $\mathcal{U}$ of U sparsifying basis matrices, the minimal coherence basis matrix at time t can be selected by solving the following optimization problem,

$$\hat{\mathbf{\Psi}}_t = \arg\min_{\mathbf{\Psi}_t} \mu(\mathbf{J}_t\mathbf{\Psi}_t) \;\; \text{s.t.} \mathbf{\Psi}_t \in \mathcal{U}. \tag{4.23}$$

Note that to optimally select the basis we need to solve this optimization problem on every snapshot as the matrix $\mathbf{J}_t$ is recomputed at every time step t. In our simulations, we specifically use $\mathcal{U} = \{\mathbf{C}, \mathbf{U}\}$.

4.6 Selection of the tuning parameter

The sparsity regulating parameter λ_t in the optimization problem of (4.17), can be adapted dynamically. It can also be kept fixed for multiple snapshots for monitoring a short period of rainfall, within which the sparsity pattern can be assumed to be fixed. An upper bound on λ_t is given by $\lambda_t = \lambda_t^{\max}$, which gives the sparsest solution, i.e., $\hat{\mathbf{z}}_t = \mathbf{0}_N$ or $\hat{\mathbf{u}}_t = \mathbf{\Psi}_t \hat{\mathbf{z}}_t = \mathbf{0}_N$. Note that the cost function of (4.17) is non-differentiable but convex for $\lambda_t > 0$. So, following the methodologies of [73] and [91], we use a subdifferential based approach to compute $\lambda_t^{\max}$. The subgradient of the non-differentiable cost of (4.17) with respect to $\mathbf{z}_t$ can be written as,

$$\tilde{\nabla}_{\mathbf{z}_t} f(\mathbf{z}_t) = 2(-\mathbf{\Psi}_t^T \mathbf{Q}^{-1}(\mathbf{u}_{t|t-1} - \mathbf{\Psi}_t \mathbf{z}_t) - \mathbf{\Psi}_t^T \mathbf{J}_t^T \mathbf{R}^{-1}(\mathbf{y}_t - \mathbf{J}_t \mathbf{\Psi}_t \mathbf{z}_t)) + \lambda_t \tilde{\nabla}_{\mathbf{z}_t} \|\mathbf{z}_t\|_1, \tag{4.24}$$

where $\tilde{\nabla}_{\mathbf{z}_t}$ is the subgradient operator towards $\mathbf{z}_t$. Using the first order optimality condition we have,

$$[2(\mathbf{\Psi}_t^T \mathbf{Q}^{-1}(\hat{\mathbf{u}}_{t|t-1} - \mathbf{\Psi}_t \mathbf{z}_t) + \mathbf{\Psi}_t^T \mathbf{J}_t^T \mathbf{R}^{-1}(\mathbf{y}_t - \mathbf{J}_t \mathbf{\Psi}_t \mathbf{z}_t))]_j \in \begin{cases} \lambda_t & [\mathbf{z}_t]_j > 0, \\ -\lambda_t & [\mathbf{z}_t]_j < 0, \\ [-\lambda_t \ \lambda_t] & [\mathbf{z}_t]_j = 0, \end{cases}$$

where $j = 1, \ldots, N$. Now, let us consider the case $\mathbf{z}_t = \mathbf{0}$. Substituting this in the above equation the optimal value of $\lambda_t^{\max}$ can be selected as $\lambda_t^{\max} = \|2(\mathbf{\Psi}_t^T \mathbf{Q}^{-1} \hat{\mathbf{u}}_{t|t-1} + \mathbf{\Psi}_t^T \mathbf{J}_t^T \mathbf{R}^{-1} \mathbf{y}_t)\|_\infty$. In this way, a useful range for λ_t is given by $[0, \lambda_t^{\max})$.

Traditional approaches to select the tuning parameter for an ℓ_1-penalized regression problem are cross-validation and generalized cross-validation (GCV) [38]. Recent methods suggest information theoretic approaches like Mallow's Cp type criterion [92], Akaike information criterion (AIC) [93], Bayesian information criterion (BIC) [94] etc. to find an optimal λ_t. In all of these approaches, the optimal tuning parameter is selected that minimizes a cost function which depends upon the estimate of $\mathbf{u}_t$ using a set of $\{\lambda_t^k\}_{k=1}^K$, where the length of the search grid for λ_t is K. In this case, we need to solve the optimization problem of (4.17) K times in every iteration and select the optimal λ_t^k that minimizes any of these aforementioned model selection criteria. After that, (4.17) needs to be solved again with the

selected λ_t^k, in order to estimate $\mathbf{u}_t$. This seems to be computationally unrealistic for an online application of the dynamic rainfall monitoring over a large service area (large N). To circumvent this problem, the K optimization problems can be solved once and the selected λ_t can be used for multiple snapshots for a short term monitoring application.

It is clear that increasing the value of λ_t, i.e., the term $\|\mathbf{z}_t\|_1$ becomes smaller and vice versa. So, if an approximation of $\mathbf{z}_t$, i.e., $\mathbf{z}_t^{\text{approx}}$, is available, it can be related to the tuning parameter by $\lambda_t \propto 1/\|\mathbf{z}_t^{\text{approx}}\|_1$. Following this, a coarse but relatively fast approach to dynamically tune λ_t could be selecting a tuning parameter given by $\lambda_t = \nu(\|\mathbf{\Psi}_t^T \hat{\mathbf{u}}_{t|t-1}\|_1)^{-1}$, where $\hat{\mathbf{u}}_{t|t-1}$ can be regarded as an approximation of $\hat{\mathbf{u}}_{t|t}$ and $\nu > 0$ is a proportionality constant. In our simulations, we use $\nu = 1$.

For the sake of completeness, we summarize the steps of the two proposed dynamic rainfall monitoring algorithms. In algorithm 2, we follow the standard steps of dynamic state estimation, but we do not update the second order statistics of the estimate. In algorithm 3, we use the approximate approach, where we use the standard Kalman covariance update (unaware of sparsity and non-negativity).

The performance of both these algorithms strongly depends upon the initialization $\hat{\mathbf{u}}_{0|0}$. One should avoid initializations like an all zero vector or an $\hat{\mathbf{u}}_{0|0}$, that consists of negative elements. If we consider the initialization $\hat{\mathbf{u}}_{0|0} = \mathbf{0}_N$, it will produce $\mathbf{J}_t = \mathbf{0}_{M\times N}$, as $\hat{\mathbf{u}}_{1|0} = \mathbf{H}_t\hat{\mathbf{u}}_{0|0} = \mathbf{0}_N$. It is mentioned in [79], that the standard values for b mainly lie in the interval of $0 < b < 2$. It should also be noted that, for $b < 1$ (for frequencies in the range $1-3$ GHz, or frequencies above 40 GHz [79, Table II]) the Jacobian $[\mathbf{J}_t]_{ij} = abl_{ij}[\hat{\mathbf{u}}_{t|t-1}]_j^{b-1}$ is undefined if $[\hat{\mathbf{u}}_{t|t-1}]_j = 0$, if we have $l_{ij} \neq 0$. This problem can be circumvented by replacing the 0 rainfall scenario by a very small value (close to zero) like in the order of 10^{-4} mm denoting a no rainfall event, and the non-negativity constraint can be replaced by $\mathbf{u}_t \geq 10^{-4}\mathbf{1}_N$ in the optimization problems. However, in our simulations we use $b > 1$.

4.7 Simulation results

In this section, we present some simulation results to test the developed methodologies to dynamically monitor the rainfall in a given area. Here we perform numerical experiments for three scenarios.

In the first case, we assume that the dynamics/state model, i.e., $\mathbf{H}_t$ is perfectly known through the parameters α, $\mathbf{D}$, and $\mathbf{w}_t$.

Algorithm 2 : Dynamic rainfall monitoring (with no covariance update)

Initialize $t = 0$, $\hat{\mathbf{u}}_{0|0}$
for $t = 1, \ldots, T$
  given a, b, l_{ij}, $(i = 1, \ldots, M;\ j = 1, \ldots, N)$, $\mathbf{y}_t$, $\mathbf{R}_t$, $\mathbf{H}_t$, $\mathbf{Q}$
  Predict $\hat{\mathbf{u}}_{t|t-1} = \mathbf{H}_t \hat{\mathbf{u}}_{t-1|t-1}$.
  Compute $\mathbf{J}_t$, $\tilde{\mathbf{y}}_t$
  Select $\mathbf{\Psi}_t$ (using (4.23))
  Select $\lambda_t = (\|\mathbf{\Psi}_t^T \hat{\mathbf{u}}_{t|t-1}\|_1)^{-1}$
  Solve $\hat{\mathbf{z}}_t = \arg\min_{\mathbf{\Psi}_t \mathbf{z}_t \geq \mathbf{0}} [\|\hat{\mathbf{u}}_{t|t-1} - \mathbf{\Psi}_t \mathbf{z}_t\|^2_{\mathbf{Q}^{-1}} + \|\tilde{\mathbf{y}}_t - \mathbf{J}_t \mathbf{\Psi}_t \mathbf{z}_t\|^2_{\mathbf{R}_t^{-1}} + \lambda_t \|\mathbf{z}_t\|_1]$
  Compute $\hat{\mathbf{u}}_{t|t} = \mathbf{\Psi}_t \hat{\mathbf{z}}_t$
end for
end

In the second case, we consider that the dynamics are not perfectly known and we assume that the state model is a Gaussian random walk.

In the third case, we consider the scenario where we do not have any information regarding the state model/dynamics. The simulations for these three scenarios are presented below.

4.7.1 Ground truth with known dynamics

The ground truth is used from a practical rainfall event in an area of 25×25 square kilometers in Amsterdam, The Netherlands . We take one spatial map of 15 minutes gauge adjusted radar rainfall depth (mm) of the same area of the day June 11, 2011, which is shown as the first state, i.e, $\mathbf{u}_1$ in the Figure 4.3.

We assume that the state transition matrix, i.e., $\mathbf{H}_t$ and the process noise covariance matrix, i.e., $\mathbf{Q}_t = \mathbf{Q}$ is perfectly known in this case. The parameters of the state transition matrix $\mathbf{H}_t = \mathbf{H}$ are given as $\mathbf{w}_t = \mathbf{w} = [1, 0]^T$, $\alpha = 0.33$, and $\mathbf{D} = \mathbf{I}_2$ (isotropic diffusion) for all $t = 2, \ldots, T$ snapshots, where $T = 8$. We assume the temporal sampling interval, i.e., $\delta_t = 15$ minutes. The parameter $\mathbf{w}$ represents a constant advective displacement in 15 minutes. The covariance matrix of the state noise, i.e., $\mathbf{Q}$ is assumed to have an exponential structure given as $[\mathbf{Q}]_{ij} = \sigma_s^2 \exp\left(-\frac{\|\mathbf{x}_i - \mathbf{x}_j\|_2}{\gamma}\right)$, with $\sigma_s^2 = 10^{-3}$ and $\gamma = 3.33$. The state noise vector $\mathbf{q}_t$ at every snapshot is generated from the distribution $\mathbf{q}_t \sim \mathcal{N}(\mathbf{0}_N, \mathbf{Q})$.

Data courtesy: Royal Netherlands Meteorological Institute (KNMI), The Netherlands

Algorithm 3 : Dynamic rainfall monitoring (with standard Kalman covariance update)

Initialize $t = 0$, $\hat{\mathbf{u}}_{0|0}$, $\mathbf{M}_{0|0}$
for $t = 1, \ldots, T$
  given a, b, l_{ij}, $(i = 1, \ldots, M;\ j = 1, \ldots, N)$, $\mathbf{y}_t$, $\mathbf{R}_t$, $\mathbf{H}_t$, $\mathbf{Q}$
  Predict $\hat{\mathbf{u}}_{t|t-1} = \mathbf{H}_t \hat{\mathbf{u}}_{t-1|t-1}$, $\mathbf{M}_{t|t-1} = \mathbf{H}_t \mathbf{M}_{t-1|t-1} \mathbf{H}_t^T + \mathbf{Q}$
  Compute $\mathbf{J}_t$, $\tilde{\mathbf{y}}_t$
  Select $\mathbf{\Psi}_t$ (using (4.23))
  Select $\lambda_t = (\|\mathbf{\Psi}_t^T \hat{\mathbf{u}}_{t|t-1}\|_1)^{-1}$
  Solve $\hat{\mathbf{z}}_t = \arg\min_{\mathbf{\Psi}_t \mathbf{z}_t \geq \mathbf{0}} [\|\hat{\mathbf{u}}_{t|t-1} - \mathbf{\Psi}_t \mathbf{z}_t\|^2_{\mathbf{M}^{-1}_{t|t-1}} + \|\tilde{\mathbf{y}}_t - \mathbf{J}_t \mathbf{\Psi}_t \mathbf{z}_t\|^2_{\mathbf{R}_t^{-1}} + \lambda_t \|\mathbf{z}_t\|_1]$
  Compute $\hat{\mathbf{u}}_{t|t} = \mathbf{\Psi}_t \hat{\mathbf{z}}_t$
  Update $\mathbf{M}_{t|t} = (\mathbf{M}^{-1}_{t|t-1} + \mathbf{J}_t^T \mathbf{R}_t^{-1} \mathbf{J}_t)^{-1}$
end for
end

After generating the states of $\mathbf{u}_t$ using the state model of (4.5), we set the negative elements of $\mathbf{u}_t$ to 0. This is a modelling approximation adopted to avoid the generation of the negative rainfall values for very low rainfall intensities.

The total number of pixels is given as $N = 25 \times 25 = 625$, each of size 1 square km. Using this we generate the states $\mathbf{u}_2 \ldots \mathbf{u}_8$ using the state model mentioned in (4.5). Based on these parameters, the space-time evolution of rainfall over $t = 1, \ldots, 8$ snapshots (each of 15 minutes, i.e. in total 120 minutes) is shown in Figure 4.3. The unit of the rainfall field is millimeter (mm).

4.7.2 Ground truth with unknown dynamics

In this section, we consider 8 consecutive snapshots of 15 minutes radar rainfall depths of the same day and area as mentioned in the previous section. The 8 snapshots of the *true gauge adjusted radar rainfall depths* are shown in Figure 4.4. In this case, we have no information regarding the state model. We assume that the state model is a Gaussian random walk, i.e., $\mathbf{H}_t = \mathbf{I}$. The process noise covariance matrix $\mathbf{Q}$ is assumed to be the same as before.

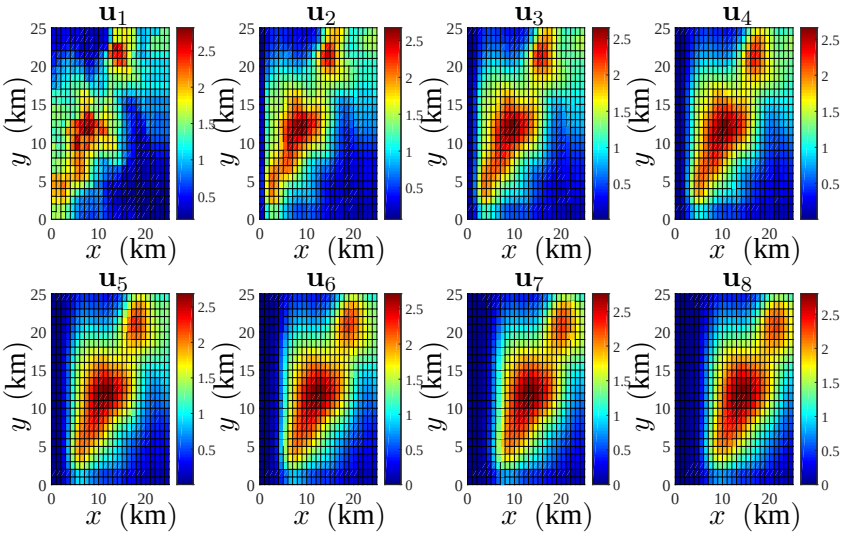

Figure 4.3: Spatio-temporal evolution of the rainfall (mm) (known dynamics);
The matrices $\mathbf{H}_t = \mathbf{H}$ for $t = 2, \ldots, 8$ are known and given in Section 4.7.1. The states are generated using the state model.

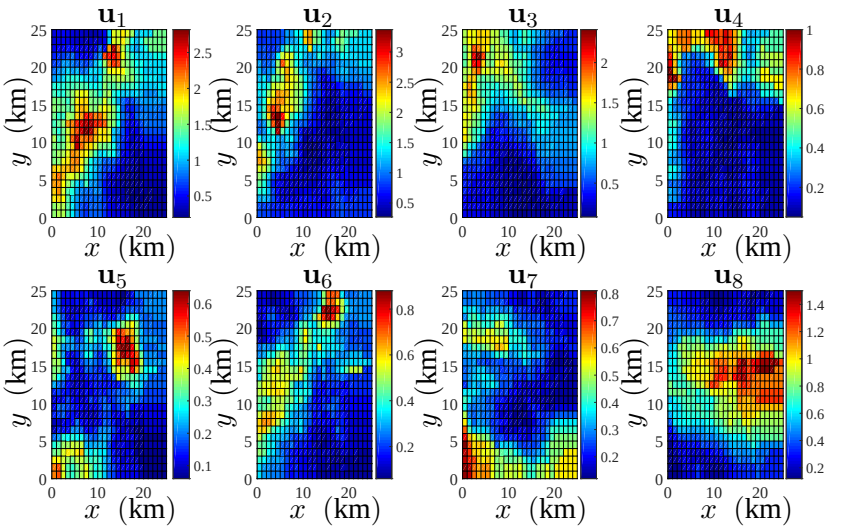

Figure 4.4: Spatio-temporal evolution of the rainfall (mm) (unknown dynamics). The states are generated using the ground truth.

4.7.3 Measurements

In this work, we simulate the measurements using the locations of the microwave links from a network of 151 microwave links. The total number of measurements for all $t = 1, \ldots, 8$ is $M = 151$. The locations of the microwave links in the service area along with the (1 square km) pixels, where we would like to estimate the rainfall intensities, are shown in Figure 4.5.

We would like to mention that most of the microwave links in the Netherlands (specially in the urban areas) are operated at 38 GHz. In that case, $b \approx 1$, i.e., the measurement model becomes linear. To check the estimation performance of the developed algorithms in a non-linear measurement framework, we intentionally choose $b \neq 1$. In this case, we assume that the rain temperature to be $20°$, which corresponds to [79, Table II]. We select the operating frequency to be 15 GHz, with $a = 3.28 \times 10^{-2}$ and $b = 1.173$. Using these, we simulate the measurements at 8 snapshots, i.e., $\{\mathbf{y}_t\}_{t=1}^{8}$, using the non-linear measurement model of (4.2), where $u_{j,t}$'s are the true values for $j = 1, \ldots, 625$, and $t = 1, \ldots 8$ as mentioned in the previous section. It is assumed that the M measurements are collected in every 15 minutes interval which are corrupted by additive white Gaussian noise characterized by $\mathbf{e}_t \sim \mathcal{N}(\mathbf{0}_M, \sigma_e^2 \mathbf{I}_M)$. Here we use $\sigma_{\mathrm{e}}^2 = 0.001$. The parameters L_i and l_{ij} are known from the geometry of the links as shown in Figure 4.5.

Here, we generate two different sets of measurements. The first set of measurements is for the 7 snapshots, i.e., $\{\mathbf{y}_t\}_{t=2}^{8}$. These measurements are computed using the ground truth where the dynamics, i.e., $\mathbf{H}_t = \mathbf{H}$ for $t = 2, \ldots, 8$ are perfectly known (Figure 4.3). The second set of measurements are computed using the exact radar rainfall maps (Figure 4.4) for 8 snapshots, i.e, $\{\mathbf{y}_t\}_{t=1}^{8}$ whose dynamics are unknown.

4.7.4 Dynamic rainfall monitoring

The noisy sets of measurements are used to estimate the rainfall depths at $N = 625$ pixels over $T = 8$ snapshots. In this section, we perform simulations for two different scenarios which are perfectly known dynamics and a Gaussian random walk dynamics.

Perfectly known dynamics

The measurements $\{\mathbf{y}_t\}_{t=2}^{8}$ are computed using the true values shown in Figure 4.3, i.e., $\{\mathbf{u}_t\}_{t=2}^{8}$. Here, we use $\sigma_e^2 = 10^{-3}$. These measurements are used to

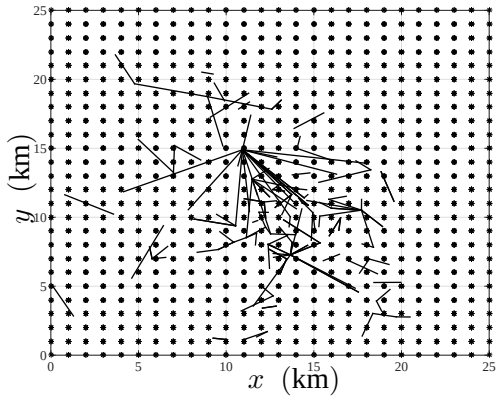

Figure 4.5: Locations of the M microwave links from where the measurements are collected (area: Amsterdam, The Netherlands).

estimate the states $\{\hat{\mathbf{u}}_t\}_{t=2}^{8}$. The parameters of the spherical variogram model are computed for the particular day of the year, i.e., June 11, 2011 [30], to compute $\mathbf{\Sigma}_u$. The sill (S_0) and the range (d) parameters are computed using (11) of [30], whose parameters are taken from of [30, Table 5]. The 15 minutes time interval is rescaled in hourly scales, i.e., 0.25 hrs. We assume that the nugget is $N_0 = 0$. The value of the range (d) is 17.4675 km and the sill (S_0) is $5.3328\ \mathrm{mm}^2$.

Based on the predictions and the available link locations, it is seen that the DCT matrix exhibits minimal coherence with $\mathbf{J}_t$, in every iteration. We initialize $\hat{\mathbf{u}}_{1|1} = \tilde{\mu}\mathbf{1}_N$, where $\tilde{\mu}$ is computed by empirically averaging the ground truth of the first state $\mathbf{u}_1$ over N pixels for both algorithms. In a real application, an appropriate initialization can be computed using the trend of the rainfall field, which is generally available from the climatological information of the area. For Algorithm 3, we initialize $\mathbf{M}_{1|1} = \mathbf{I}_N$. We use the software CVX [52] (parser CVX, solver SeDuMi [53]) to solve the convex optimization problems (i.e, (4.17) for Algorithm 2 and (4.14) for Algorithm 3).

In Figures 4.6 and 4.7, we show the reconstructed spatial rainfall map for the states $\hat{\mathbf{u}}_2$ and $\hat{\mathbf{u}}_8$, respectively using the Algorithm 2. The same estimates are shown in Figures 4.8 and 4.9, respectively using the Algorithm 3.

We plot the pixel-wise comparisons of the estimates with the true values for all the 7 snapshots, i.e., a total of $625 \times 7 = 4375$ pixels for the Algorithms 2 and 3 in Figure 4.10 and Figure 4.11, respectively. The dark black lines in the Figure 4.10 and Figure 4.11 represent the $y = x$ line. It is observed that Algorithm 3, i.e., using

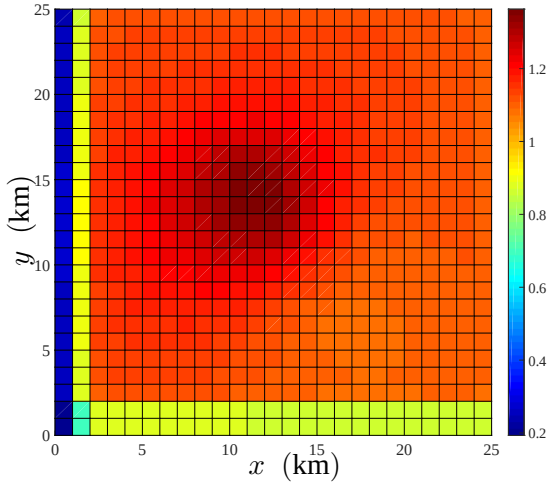

Figure 4.6: Estimate of the spatial rainfall (mm) map ($\hat{\mathbf{u}}_2$) with perfectly known dynamics (Figure 4.3); (Algorithm 2).

the standard Kalman covariance update exhibits better estimation performance than Algorithm 2, where the second order statistics are not updated.

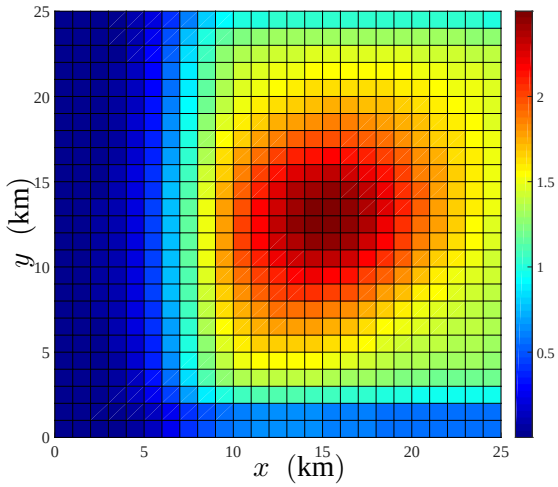

Figure 4.7: Estimate of the spatial rainfall (mm) map ($\hat{\mathbf{u}}_8$) with perfectly known dynamics (Figure 4.3); Algorithm 2.

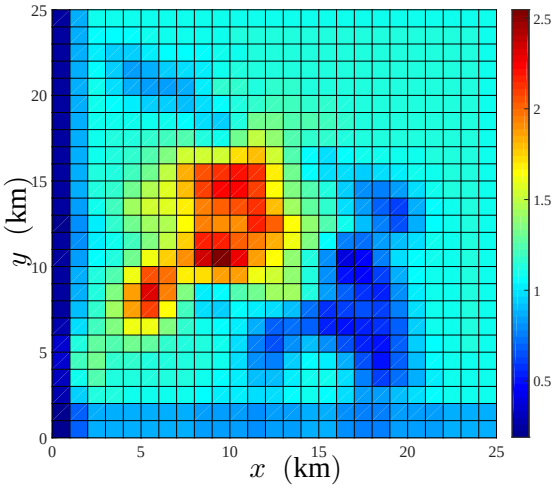

Figure 4.8: Estimate of the spatial rainfall (mm) map ($\hat{\mathbf{u}}_2$) with perfectly known dynamics (Figure 4.3); Algorithm 3.

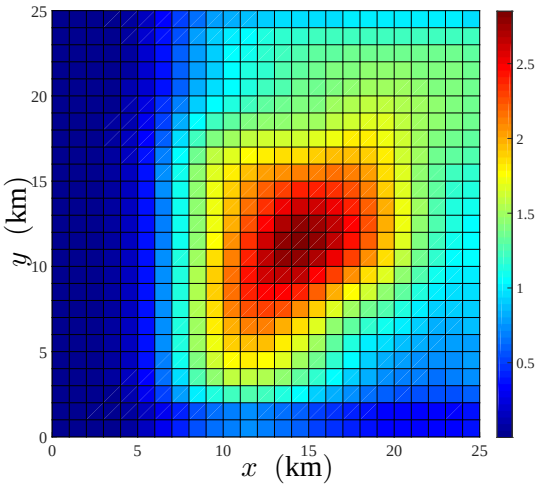

Figure 4.9: Estimate of the spatial rainfall (mm) map ($\hat{\mathbf{u}}_8$) with perfectly known dynamics (Figure 4.3); (Algorithm 3).

Gaussian random walk

In this section, the state model is considered to be a Gaussian random walk, i.e., $\mathbf{H}_t = \mathbf{I}$ for $t = 1, \ldots, 8$. The process noise statistics are considered to be same

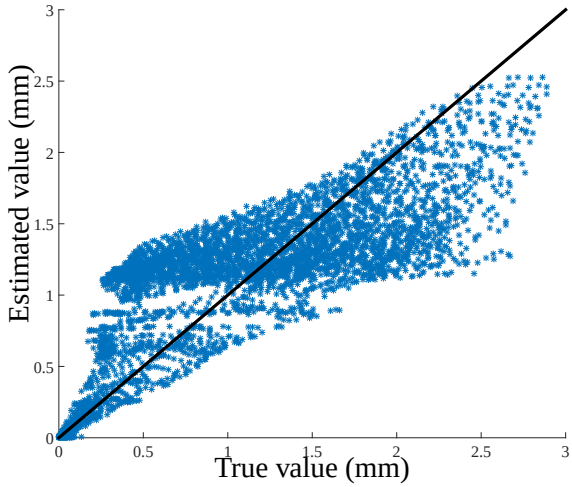

Figure 4.10: Pixel-wise comparison of the estimates [Algorithm 2 (known dynamics)].

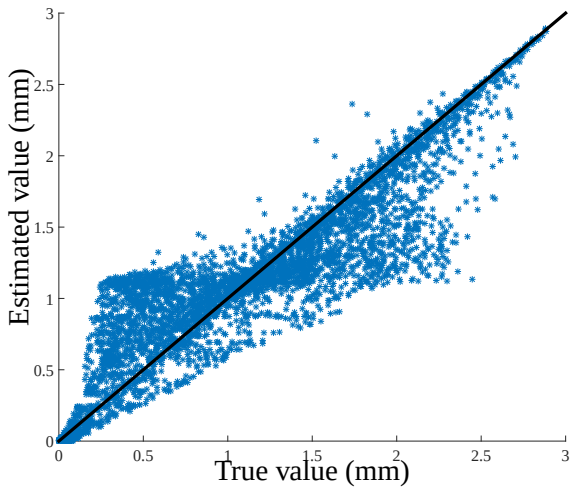

Figure 4.11: Pixel-wise comparison of the estimates [Algorithm 3 (known dynamics)].

as before. The measurements for 8 snapshots, i.e., $\{\mathbf{y}_t\}_{t=1}^{8}$ are generated using the *true radar rainfall depths* shown in Figure 4.4, using the meaurement model of (4.2) with the same a, b coefficients as the previous case. The measurements are

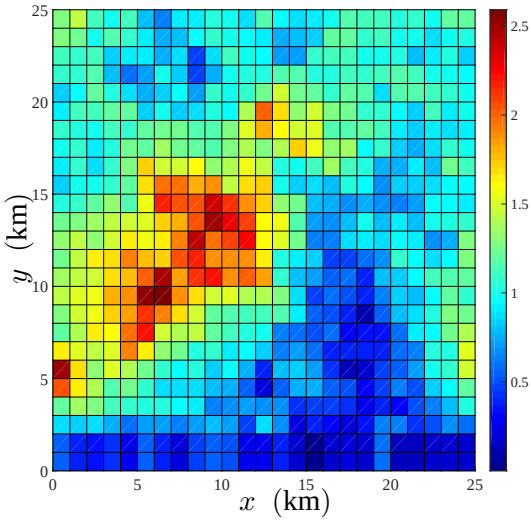

Figure 4.12: Estimate of the spatial rainfall (mm) map ($\hat{\mathbf{u}}_1$) with unknown dynamics (Figure 4.4).

different from the previous known dynamics case as the true values of $\{\mathbf{u}_t\}_{t=1}^{8}$, i.e, the true radar rainfall depths (as shown in Figure 4.4) are different. In this case, the measurement noise variance is reduced to $\sigma_e^2 = 10^{-5}$. Due to better estimation performance (as seen in the case of perfectly known dynamics), we select Algorithm 3 to estimate the states $\{\hat{\mathbf{u}}_t\}_{t=1}^{8}$ using the measurements generated by the true radar rainfall depths.

In this case, as the predictions using the sate model are not accurate in this case, we do not perform the tuning of λ_t based on the predictions. However, the tuning of λ_t, in this case can be performed using the standard methods mentioned in Section 4.6. In the current setup, to exploit the sparsity prior on every snapshot we fix $\lambda_t = \lambda = 2$ for the sake of simplicity. The initializations are given by $\hat{\mathbf{u}}_{0|0} = \tilde{\mu}\mathbf{1}_N$ and $\mathbf{M}_{0|0} = \mathbf{I}_N$.

In Figures 4.12 and 4.13, we show the estimated spatial rainfall maps of the states $\hat{\mathbf{u}}_1$ and $\hat{\mathbf{u}}_8$, respectively assuming that the state model is a Gaussian random walk. In Figure 4.14, we compare the estimation performance of the estimates of the 625 pixels over 8 snapshots, i.e., a total of $625 \times 8 = 5000$ pixels with the true gauge adjusted radar rainfall depths.

The following inferences can be drawn from the aforementioned simulation studies.

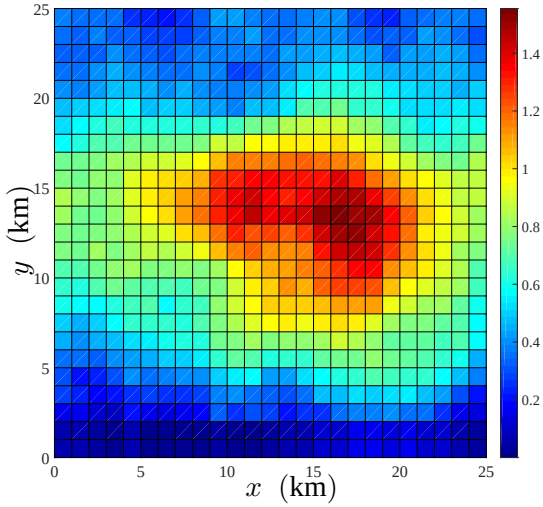

Figure 4.13: Estimate of the spatial rainfall (mm) map ($\hat{\mathbf{u}}_8$) with unknown dynamics (Figure 4.4).

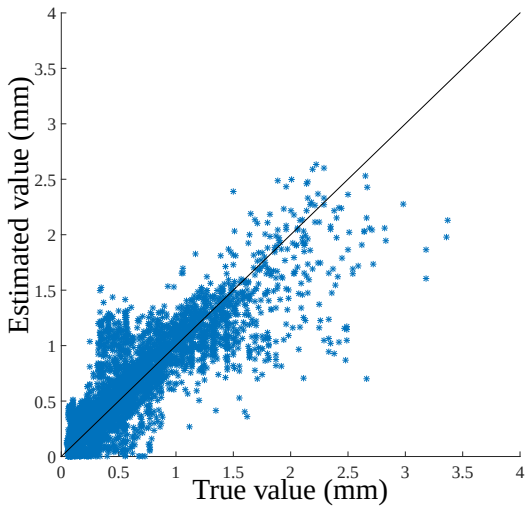

Figure 4.14: Pixel-wise comparison of the estimates [Algorithm 3, (Gaussian random walk)]; Performance comparison on real data.

- The estimation performances in the first two cases are highly dependent on the accuracy of the state model, availability of the measurements in any region, and the initialization of the algorithm. In Figure 4.9, the estimate of the state $\hat{\mathbf{u}}_8$ is much better than the same estimate in Figure 4.13, as the dynamics are perfectly known in the first case. Also, the estimation performance is improved with time as the state error is minimized with temporal iterations (Figure 4.9).

- As seen in Figure 4.5, there are many regions without any microwave links/ measurements but where a rainfall field is present. In these regions, the estimates are mainly dependent on the predictions. On the other hand, if there is no rainfall over any link, the rainfall can be overestimated or underestimated in those regions, due to the effects of the measurement noise. This effect severely impairs the estimation performance in the case when we do not have an accurate prediction (or no prediction).

- There is always a trade-off between the estimation performance and the "availability" of the measurements and/or the "accuracy" of the predictions.

- The reasons behind the scatter plots being not very symmetric are due to the biased estimates in the measurement-void regions and the rainfall-void links.

4.7.5 Performance metrics

To compare the estimation performances of the developed methods we use some performance metrics, which are described in the following part of this section. The performance of a rainfall monitoring method can be quantified by root mean square error (rmse in mm), the mean bias (mb in mm), and the correlation coefficient (ρ) [66]. We quantify the overall estimation performances of all the above scenarios for N pixels over T snapshots using the aforementioned metrics. If the true value and the estimate of the rainfall field at any t are given by $\mathbf{u}_t$ and $\hat{\mathbf{u}}_t$, respectively

then the performance metrics can be defined in the following ways

$$\text{rmse} = \sqrt{\frac{1}{NT}\sum_{t=1}^{T}\sum_{j=1}^{N}([\hat{\mathbf{u}}_t]_j - [\mathbf{u}_t]_j)^2}, \tag{4.25}$$

$$\text{mb} = \frac{1}{NT}\sum_{t=1}^{T}\sum_{j=1}^{N}([\hat{\mathbf{u}}_t]_j - [\mathbf{u}_t]_j), \tag{4.26}$$

$$\rho = \frac{\sum\limits_{t=1}^{T}\sum\limits_{j=1}^{N}([\hat{\mathbf{u}}_t]_j - \hat{\mu})([\mathbf{u}_t]_j - \mu)}{\sqrt{\sum\limits_{t=1}^{T}\sum\limits_{j=1}^{N}([\hat{\mathbf{u}}_t]_j - \hat{\mu})^2}\sqrt{\sum\limits_{t=1}^{T}\sum\limits_{j=1}^{N}([\mathbf{u}_t]_j - \mu)^2}}, \tag{4.27}$$

where $\hat{\mu} = \frac{1}{NT}\sum_{t=1}^{T}\sum_{j=1}^{N}[\hat{\mathbf{u}}_t]_j$ and $\mu = \frac{1}{NT}\sum_{t=1}^{T}\sum_{j=1}^{N}[\mathbf{u}_t]_j$ are the sample means of the estimated and the true values of rainfall for N pixels over T snapshots.

The performance metrics are computed for the estimates using Algorithm 3 for the scenarios of perfectly known dynamics and Gaussian random walk dynamics. For both of these scenarios, we also estimate the rainfall depths using a simple EKF without any sparsity and non-negativity constraint. To avoid the negative estimates produced by the EKF, we set the negative estimates to 0. While computing the performance metrics we fix the process and the measurement noise variances to $\sigma_s^2 = 10^{-4}$ and $\sigma_e^2 = 10^{-3}$, respectively in all the cases.

When the dynamics are perfectly known then the performance metrics are computed for the estimates of 625 pixels for 7 snapshots and averaged over 20 different measurement noise realizations. In Table 4.1, we present the performance metrics computed for Algorithm 3, and a simple EKF (with the thresholding) for the perfectly known dynamics case.

In Table 4.2, we present the aforementioned performance metrics computed for the estimates of 625 pixels for 8 snapshots using Algorithm 3 (with fixed $\lambda_t = \lambda = 2$) and an EKF (with the thresholding), where the state model is assumed to be a Gaussian random walk. Here, we also average the performance metrics for 20 different measurement noise realizations. In all of these realizations, the measurements are generated using the true radar rainfall depths as shown in Figure 4.4.

From the above results it can be seen that

- For a perfectly known state model extra information like sparsity and non-negativity does not play any significant role in terms of estimation accuracy.

Table 4.1: Performance comparison with EKF (with thresholding); Perfectly known dynamics ($\sigma_s^2 = 10^{-4},\ \sigma_e^2 = 10^{-3}$).

Performance metric	Algorithm 3	EKF (with thresholding)
rmse (mm)	0.3167	0.3178
mb (mm)	0.0014	0.0023
ρ	0.8973	0.8963

Table 4.2: Performance comparison with EKF (with thresholding); Dynamics is assumed to be a Gaussian random walk ($\sigma_s^2 = 10^{-4},\ \sigma_e^2 = 10^{-3}$).

Performance metric	Algorithm 3	EKF (with thresholding)
rmse (mm)	0.4719	0.6542
mb (mm)	0.2123	0.4334
ρ	0.5572	0.3034

This is clear from Table 1 where it is shown that the performance improvement over a simple EKF (with setting the negative estimates to 0) is negligible.

- When the information regarding the state model is unknown and approximated as a Gaussian random walk model then the performance of a simple EKF is very poor. In this case, the sparsity and non-negativity information along with the measurements improve the estimation performance (Table 2).

- The last mentioned observation is quite useful in practical cases, where the availability of an accurate state model is scarce.

The computation times for both Algorithm 2 and 3 including the basis selection part is less than a minute for $N = 625$ pixels using the aforementioned off-the-shelf solvers. The computation time is increased if N is higher than 625. Algorithm 2 is computationally simpler than Algorithm 3 because there is no covariance update state. But the price we pay is in terms of the estimation performance. However, the speed of the developed algorithms can be increased by using a projected subgradient method [95].

4.7.6 Spatial rainfall mapping (no dynamics)

In this case, we assume that we do not use any prior information regarding the dynamics. On every snapshot, we estimate $\hat{\mathbf{u}}_t$ using the measurements and exploiting the prior information regarding the sparsity and the non-negativity. In this case, for the sake of simplicity we assume that the measurement model is linear, i.e, the case when the links are operated around 38 GHz. Here we use $a, b = 1$.

The linear measurement model is given by $\mathbf{y}_t = \mathbf{\Phi}\mathbf{u}_t + \mathbf{e}_t$, where $y_{i,t} = \sum_{j=1}^{N} u_{j,t} l_{ij} + e_{i,t}$, where $i = 1, \ldots, M$. On every snapshot, we solve the sparsity-aware non-negativity constrained optimization problem given as

$$\hat{\mathbf{z}}_t = \underset{\mathbf{\Psi}\mathbf{z}_t \geq \mathbf{0}_N}{\arg\min} \|\mathbf{y}_t - \mathbf{\Phi}\mathbf{\Psi}\mathbf{z}_t\|^2_{\mathbf{R}^{-1}} + \lambda \|\mathbf{z}_t\|_1 \tag{4.28}$$

$$\hat{\mathbf{u}}_t = \mathbf{\Psi}\hat{\mathbf{z}}_t, \tag{4.29}$$

However, this can be easily extended to a non-linear measurement model by adopting an iterative linearization with respect to a suitable initial guess. Like in the previous case, here we also fix $\lambda = 2$ and the used basis is DCT matrix on every t. However, an upper bound on λ can be easily computed in this case by using the same methodology discussed in Section 4.6.

In Figures 4.15 and 4.16, we show the estimated states $\hat{\mathbf{u}}_1$ and $\hat{\mathbf{u}}_8$ by solving the optimization problem of equation (4.28). The measurement noise variance is set as $\sigma_e^2 = 10^{-5}$.

In Figure 4.17, we compare the estimation performance of the estimates of total $625 \times 8 = 5000$ pixels with the true gauge adjusted radar rainfall depths.

4.8 Conclusion

We have developed a generalized dynamic rainfall monitoring algorithm from limited non-linear attenuation measurements by utilizing the spatial sparsity and non-negativity of the rainfall field. We have formulated the dynamic rainfall monitoring algorithm as a constrained convex optimization problem. The performance of the developed algorithm is compared with the standard approaches like an EKF for the scenarios, where we have both perfect knowledge about the state model and an approximate state model. Numerical experiments show that the developed approach outperforms a simple EKF in scenarios, where the state model is not perfectly known. The proposed methodology can be equivalently implemented for dynamic field tracking in tomographic applications like MRI, microwave tomogra-

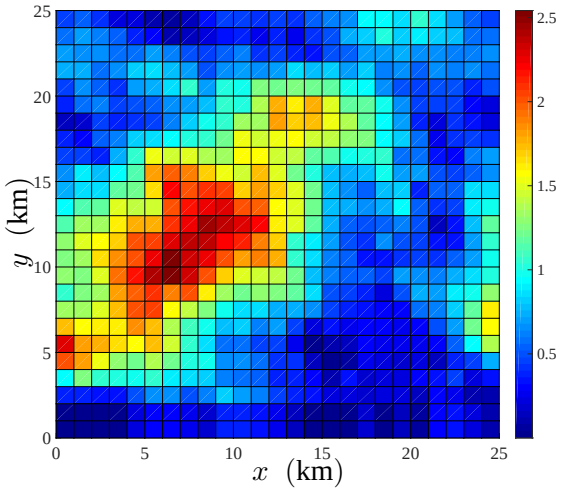

Figure 4.15: Estimate of the spatial rainfall (mm) map ($\hat{\mathbf{u}}_1$) with unknown dynamics (Figure 4.4) (exploiting only sparsity and non-negativity).

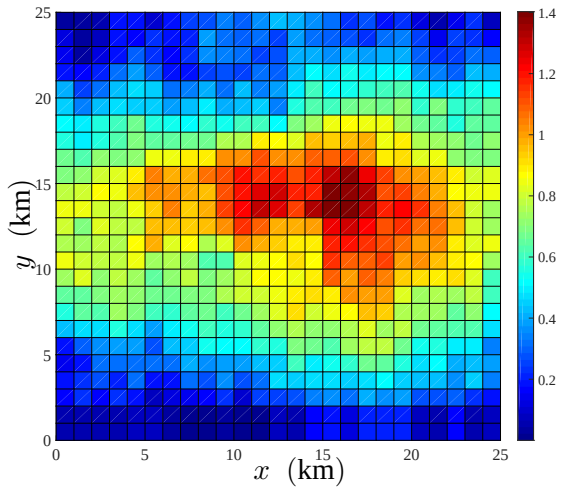

Figure 4.16: Estimate of the spatial rainfall (mm) map ($\hat{\mathbf{u}}_8$) with unknown dynamics (Figure 4.4) (exploiting only sparsity and non-negativity).

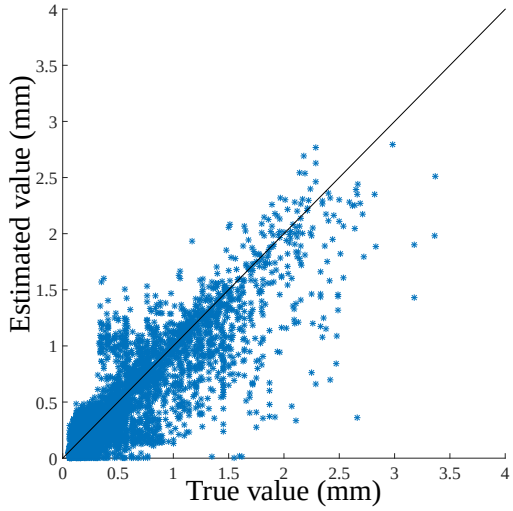

Figure 4.17: Pixel-wise comparison of the estimates (exploiting only sparsity and non-negativity (no dynamics, linear model, performance comparison on real data)).

phy etc., where we can assume to have path-integrated measurements corrupted by Gaussian noise.

However, tackling more complicated dynamics of the rain (possibly non-linear and highly time-varying), and non-Gaussian measurement noise could be possible future extensions of this work. In that case, both the state and the measurement models are non-linear. This triggers one to use an unscented Kalman filter (UKF), particle filtering based algorithms, or other heuristic approaches. Estimation of the underlying dynamics of rainfall from the available ground truth and using it for real time dynamic monitoring is also a part of the future research. A real time selection of the most informative attenuation measurements from the available links could be interesting in order to reduce the processing time and computational complexity.

Chapter 5

Spatio-Temporal Sensor Placement for Kriged Kalman Filter (KKF)

As mentioned in the earlier chapters, one of the most important applications of a homogeneous/heterogenous wireless sensor network (WSN) is to track the spatio-temporal evolution of an environmental field with a pre-prescribed accuracy. Different types of environmental, geophysical and biological processes exhibit complicated spatial as well as temporal variability. Spatial and temporal variability of a spatio-temporally stationary physical field can be modelled by its correlation over space and time [7]. If the field is non-stationary then a suitable dynamic model can be used to model the spatio-temporal evolution of the field [7]. If the field exhibits both a stationary and non-stationary behavior over space and time then the field can be dynamically monitored by the combination of kriging [7] and Kalman filtering, i.e, a kriged Kalman filter (KKF) [96] or space-time Kalman filter [19].

In this chapter, we propose a sensor placement method for spatio-temporal field estimation based on a kriged Kalman filter (KKF) using a network of static or mobile sensors. The developed framework dynamically designs the optimal constellation to place the sensors. We combine the estimation error (for the stationary as well as non-stationary component of the field) minimization problem with a sparsity-enforcing penalty to design the optimal sensor constellation in an eco-

This chapter is published as: V. Roy, A. Simonetto, and G. Leus, “Spatio-temporal field estimation using kriged Kalman filter (KKF) with sparsity-enforcing sensor placement”, *Sensors*, vol. 18, no. 6, pp. 1778, April, 2018.

nomic manner. The developed sensor placement method can be directly used for a general class of covariance matrices (ill-conditioned or well-conditioned) modelling the spatial variability of the stationary component of the field, which acts as a correlated observation noise, while estimating the non-stationary component of the field. Finally, a KKF estimator is used to estimate the field using the measurements from the selected sensing locations. Numerical results are provided to exhibit the feasibility of the proposed dynamic sensor placement followed by the KKF estimation method.

The outline of the chapter is as follows. The prior research works in this field along with the main contributions of this chapter is presented in 5.1. In Section 5.2, the measurement model and the main problem statement is presented. The statistical nature of the stationary and the non-stationary components of the field is presented in the Section 5.3. A simple KKF estimator is described in Section 5.4. In Section 5.5, the overall performance metric as a function of the sensor location selection vector is presented. The proposed sensor placement problem followed by a KKF estimator is presented in Section 5.6. The simulation results are shown in Section 5.7. The conclusion of the chapter along with the future research directions are presented in Section 5.8.

5.1 Prior art and contributions

The key idea behind the KKF is the liaison of kriging [7] and Kalman filtering. The unknown physical field is modelled as a combination of a non-stationary (capturing the dynamics) and a stationary (capturing the low magnitude spatial effects) stochastic component. Assuming that the dynamics of the non-stationary component and the second-order statistics of the stationary component (e.g., covariance structure) are perfectly known, KKF jointly estimates both of these field components using the spatial observations at every time instant. The KKF paradigm has been used for different applications like wireless communications (e.g., spectrum sensing [97] and path delay estimation [98]) and field estimation [19].

One of the important overheads of dynamic field estimation using a WSN is the lack of sufficient measurements at every time instant. This is related to the shortage of sensor life time, availability of bandwidth, and other resource-related economical constraints. In such scenarios, we need to efficiently place/move the available sensors into the most informative locations over space and time. Dynamic sensor scheduling is a well-cultivated topic in the fields of signal processing as well as control theory [99], [51], [100]. Prior knowledge regarding the corre-

lation of the field over space and time can be exploited in a multi-layer design of sensor networks [21]. Selecting the most informative sensing locations can be treated as a sensor selection problem, which can be formulated as a convex optimization problem [45]. This can be solved for linear [101] as well as non-linear measurement models [41]. Sparsity-promoting approaches for sensor placement are also exhibited in [51], [102], where the placement algorithm is formulated using the alternating direction method of multipliers (ADMM). In [103], a generalized sparsity-enforcing and performance-constrained sensor placement method is proposed, where the field can be either stationary or non-stationary. The aforementioned method can be implemented for a single snapshot or multiple snapshot ahead sensor placement and for a general class of spatio-temporal covariance matrices, which can either be ill-conditioned or well-conditioned. Seminal contributions on the convex formalism of sensor selection (like [45]) assume that the measurement noise components are spatio-temporally uncorrelated. However, this can be an unrealistic assumption in some practical scenarios [26]. But even in those scenarios, it has been shown that the sensor selection problem can be formulated as a convex optimization problem [100], [104].

In this work, we develop a unified framework of sensor placement followed by a KKF estimator to dynamically monitor a physical field that exhibits both stationarity and non-stationarity over space and time. In the first step, we select the most informative locations to deploy/move the sensors and in the second step we estimate the field by using the measurements from those selected locations. The key contributions can be summarized as follows,

- The performance metrics to estimate the stationary as well as the non-stationary components of the field are represented in closed form as an explicit function of the sensor location selection vector.

- The aforementioned analytical formalism tackles two important issues in the sensor placement step. First, the developed method takes care of the fact that the estimation of the non-stationary component of the field involves the stationary component of the field as a spatially correlated observation noise. Second, the proposed method is applicable for a general class of spatial covariance matrices of the stationary component of the field, even when they are ill-conditioned or close to singular [58].

- The proposed sensor placement problem is formulated in a way that minimizes a cost function that involves the sum of the mean square error (MSE)

of the stationary and the non-stationary component of the field as well as a spatial sparsity enforcing penalty. The overall optimization problem also satisfies a flexible resource constraint at every time instant.

One of the aspects that distinguishes the proposed sensor placement method from the prior works in sensor placement for environmental field estimation is the specific statistical nature of the unknown physical field, which yields an additive coupling of stationary and the non-stationary components. Secondly, we develop a unified framework for the efficient utilization of the spatio-temporal variability of the field in order to design an opportunistic sensor placement method using a convex approach. We develop a parsimonious sensor placement algorithm followed by a KKF estimator, which can be used to dynamically monitor a general class of environmental fields (based on the assumed process model and spatial statistics of the field components). However, the developed approach is similar to [103] in terms of the primary measurement model, which is considered to be underdetermined. We emphasize that the proposed technique is a model-based centralized sensor placement method, where we resort to the Bayesian estimation philosophy. We assume that the available prior statistical knowledge regarding the unknown physical field like spatial correlation information and dynamics are perfectly known a priori. It is also assumed that for the current centralized setup the communication range of the sensors are sufficient to communicate with the fusion center, which can be located inside/outside the given service area.

5.2 Measurement model and problem statement

5.2.1 Measurement model

Let us denote the spatially continuous field by $u_t(\mathbf{x})$, at any discrete time index t and location $\mathbf{x} \in \mathbb{R}^2$. We assume that the entire service area of interest is *uniformly discretized* over N pixels, where we would like to estimate the field intensities. The field intensities of the N pixels at time t are represented by $\mathbf{u}_t \in \mathbb{R}^N$. It is assumed that the field intensity is the same everywhere within a pixel, and it can be represented by $[\mathbf{u}_t]_j = u_t(\mathbf{x}_j)$, where $\mathbf{x}_j \in \mathbb{R}^2$ is the centroid of the j-th pixel, with $j = 1, \ldots, N$. We consider a linear underdetermined measurement model

$$\mathbf{y}_t = \mathbf{C}_t \mathbf{u}_t + \mathbf{e}_t \tag{5.1}$$

$$= \mathbf{C}_t(\mathbf{v}_t + \mathbf{s}_t) + \mathbf{e}_t, \tag{5.2}$$

where $\mathbf{v}_t \in \mathbb{R}^N$ is the non-stationary component of the field and $\mathbf{s}_t \in \mathbb{R}^N$ is a stationary component of the field capturing the non-dynamic spatial effects. It is assumed that $\mathbf{v}_t$ and $\mathbf{s}_t$ are mutually uncorrelated.

At any time t, the measurements are given by $\mathbf{y}_t \in \mathbb{R}^{M_t}$ collected from M_t ($M_t < N$) sensing locations (pixels) of the entire service area. The construction of the time-varying sensing or measurement matrix $\mathbf{C}_t \in \{0,1\}^{M_t \times N}$ is same as Chapter 3, i.e., $\mathbf{C}_t = \mathrm{diag}_X(\mathbf{w}_t)$, where $\mathbf{w}_t = [w_{t1}, \ldots, w_{tN}]^T \in \{0,1\}^N$ is the *sensor location selection vector* for time t, and $\mathrm{diag}_X(\mathbf{w}_t)$ removes the all zero rows from $\mathrm{diag}(\mathbf{w}_t)$. Similar to Chapter 3, we also have $[\mathbf{w}_t]_j = 1(0)$, when the j-the field location is selected (not selected) for sensor deployment at time t. Using these, we have

$$\mathbf{C}_t^T \mathbf{C}_t = \mathrm{diag}(\mathbf{w}_t); \qquad \mathbf{C}_t \mathbf{C}_t^T = \mathbf{I}_{M_t}. \tag{5.3}$$

Note that the type of measurement matrix used in this work is similar to an incidence matrix, which can be viewed as a flexible data collection method using heterogeneous sensing equipments. In practice, when different types of sensing modalities are used, we may not know the process by which any of the sensors gathers its measurement but only its recorded magnitude is important. Also, we rigorously exploit the property of the structure of $\mathbf{C}_t$ mentioned in (5.3), later in this chapter.

The error incurred by the measurement process is modelled through $\mathbf{e}_t$, which is uncorrelated with both $\mathbf{v}_t$ and $\mathbf{s}_t$, respectively. The spatio-temporally white measurement noise $\mathbf{e}_t$ is characterized by $\mathbf{e}_t \sim \mathcal{N}(\mathbf{0}_{M_t}, \sigma_e^2 \mathbf{I}_{M_t})$.

5.2.2 Main problem statement

The main problem is to design an optimal sensor placement pattern, i.e, to design $\mathbf{w}_t$, whose support gives the optimal locations to deploy the sensors. At any t, the design goal is to minimize the estimation error for both the stationary and the non-stationary components of the field as well as to enforce sparsity in $\mathbf{w}_t$, i.e, to reduce the number of required sensing locations. If the estimation error of the stationary and non-stationary components of the field can be represented by a single performance metric $g(\mathbf{w}_t)$, the sensor placement problem can be represented by

$$\underset{\mathbf{w}_t \in \{0,1\}^N}{\arg\min} \qquad g(\mathbf{w}_t) + \lambda_t \|\mathbf{w}_t\|_1 \tag{5.4a}$$

$$\text{s.t.} \qquad K_t^{\min} \leq \mathbf{1}^T \mathbf{w}_t \leq K_t^{\max}. \tag{5.4b}$$

At any t, $K_t^{\min}$ and $K_t^{\max}$ denote the lower bound on the number of available sensors, and a given budget on the maximum number of available sensors, respectively.

Sparsity is enforced through a sparsity-promoting penalty, i.e., an ℓ_1 norm of $\mathbf{w}_t$ in the second summand of the cost function (5.4a) with a time-varying regularization parameter $\lambda_t > 0$ controlling the sparsity of the elements of $\mathbf{w}_t$. A detailed description regarding the structure of the objective function and the importance of the constraints in the optimization problem (5.4) are discussed later in this chapter.

5.3 Modelling of the spatio-temporal variability

5.3.1 Spatial variability

The spatial effects of the field are modelled through a spatially colored yet temporally white discrete random process $\mathbf{s}_t \sim \mathcal{N}(\boldsymbol{\mu}_\mathrm{s}, \boldsymbol{\Sigma}_\mathrm{s})$, where $\boldsymbol{\mu}_\mathrm{s} \in \mathbb{R}^N$ is the mean and $\boldsymbol{\Sigma}_\mathrm{s} \in \mathbb{S}^N_{++}$ is the spatial covariance matrix of $\mathbf{s}_t$. We assume that the process $\mathbf{s}_t$ is spatially second-order stationary as well as isotropic, which means that

$$\boldsymbol{\mu}_\mathrm{s} = \mathbb{E}[\mathbf{s}_t] = \mu_\mathrm{s}\mathbf{1}_N, \tag{5.5}$$

$$[\boldsymbol{\Sigma}_\mathrm{s}]_{ij} = \mathbb{E}[(s_t(\mathbf{x}_i) - \mu_\mathrm{s})(s_t(\mathbf{x}_j) - \mu_\mathrm{s})] = f(\|\mathbf{x}_i - \mathbf{x}_j\|_2), \tag{5.6}$$

where $i, j = 1, \ldots, N$ [7]. Note that here we follow the same spatial discretization as mentioned in Section 5.2.1. There are several empirical as well as parametric model-based approaches to model the spatial covariance. In this work, we assume that the spatial covariance function is given by a simple squared exponential function:

$$f(\|\mathbf{x}_i - \mathbf{x}_j\|_2) = \sigma_\mathrm{s}^2 \exp(-\frac{\|\mathbf{x}_i - \mathbf{x}_j\|_2^2}{\theta^2}), \tag{5.7}$$

where $\theta > 0$ is the parameter controlling the strength of the spatial correlation. The covariance function mentioned in (5.7) is plotted in Fig. 5.1 for increasing values of the pairwise distance between the centroids of the pixels, i.e, $d_{ij} = \|\mathbf{x}_i - \mathbf{x}_j\|_2$ and the parameter θ. Note that the aforementioned covariance function belongs to the family of Matérn covariance functions [7], which are widely used to model the spatial variability of a field in geostatistics and environmental sciences.

Using the squared exponential covariance function, the elements of the $N \times N$ spatial covariance matrix ($\boldsymbol{\Sigma}_\mathrm{s}$) can be constructed by the relation (5.6). Let us consider a service area with $N = 36$ pixels. The centroids of these 36 pixels, which are also the candidate locations for sensor deployment are shown in Fig. 5.2. These centroids are indexed from the top left to the bottom right. The elements of $\boldsymbol{\Sigma}_\mathrm{s}$ are shown in Fig. 5.3. Note that based on the nature of the covariance function (5.7), the spatial covariance matrix $\boldsymbol{\Sigma}_\mathrm{s}$ is symmetric and based on the constellation

of the candidate sensing locations (Fig. 5.2), $\boldsymbol{\Sigma}_{\mathrm{s}}$ is also a block Toeplitz matrix. We assume that $\boldsymbol{\mu}_{\mathrm{s}}$ and $\boldsymbol{\Sigma}_{\mathrm{s}}$ are perfectly known a priori.

5.3.2 State model

The spatio-temporal evolution of the non-stationary component of the field, i.e., $\mathbf{v}_t$, can be modelled by the following state model

$$\mathbf{v}_t = \mathbf{H}_t \mathbf{v}_{t-1} + \mathbf{q}_t. \tag{5.8}$$

Here, the time-varying state transition/propagator matrix is given by $\mathbf{H}_t \in \mathbb{R}^{N \times N}$. The process noise vector $\mathbf{q}_t$ is assumed to be characterized by $\mathbf{q}_t \sim \mathcal{N}(\mathbf{0}, \mathbf{Q}_t)$. The elements of the state transition matrix $\mathbf{H}_t$ act as spatial redistribution weights for $\mathbf{v}_{t-1}$ for the temporal transition from $t-1$ to t [7]. Note that the spatial redistribution can be dependent on the temporal sampling interval. Similar to Chapters 3 and 4, we model the elements of $\mathbf{H}_t$ by using a parameterized Gaussian kernel function

$$[\mathbf{H}_t]_{ij} = \nu \exp[-(\mathbf{x}_i - \mathbf{x}_j - \mathbf{a}_t^{ij})^T [\mathbf{D}_t^{ij}]^{-1} (\mathbf{x}_i - \mathbf{x}_j - \mathbf{a}_t^{ij})], \tag{5.9}$$

where $i, j = 1, \ldots, N.$ and the spatio-temporally varying translation and dilation parameters are represented by $\mathbf{a}_t^{ij} \in \mathbb{R}^2$, and $\mathbf{D}_t^{ij} \in \mathbb{S}_{++}^2$, respectively. The scalar $\nu \in (0, 1)$ is a scaling parameter. In this work, we assume that the state transition matrix $\mathbf{H}_t$, whose elements are parameterized by $\{\mathbf{a}_t^{ij}\}$ and $\{\mathbf{D}_t^{ij}\}$ through the function (5.9) is perfectly known a priori.

5.4 Simple KKF estimator and estimation error covariance

Using the measurement and state models of (5.1) and (5.8), respectively, the state estimate $\hat{\mathbf{u}}_t$, for $t = 1, 2, \ldots,$ can be computed following the lines of a standard KKF [19], [97]. First, a simple Kalman filter is used to track the dynamic component $\mathbf{v}_t$, where the stationary component $\mathbf{s}_t$ is interpreted as a noise term. In this case, the measurement model is given by

$$\breve{\mathbf{y}}_t = \mathbf{C}_t \mathbf{v}_t + \breve{\mathbf{e}}_t, \tag{5.10}$$

where $\breve{\mathbf{y}}_t = \mathbf{y}_t - \mathbf{C}_t \boldsymbol{\mu}_{\mathrm{s}}$, $\breve{\mathbf{e}}_t = \mathbf{C}_t \breve{\mathbf{s}}_t + \mathbf{e}_t$, and $\breve{\mathbf{s}}_t = \mathbf{s}_t - \boldsymbol{\mu}_{\mathrm{s}}$. Furthermore, $\breve{\mathbf{s}}_t \sim \mathcal{N}(\mathbf{0}_N, \boldsymbol{\Sigma}_{\mathrm{s}})$, and $\breve{\mathbf{e}}_t \sim \mathcal{N}(\mathbf{0}_{M_t}, \breve{\mathbf{R}}_t)$, with $\breve{\mathbf{R}}_t = \mathbf{C}_t \boldsymbol{\Sigma}_{\mathrm{s}} \mathbf{C}_t^T + \sigma_e^2 \mathbf{I}_{M_t}$. It can be easily shown that $\mathbf{v}_t$ and $\breve{\mathbf{e}}_t$ are mutually uncorrelated as it is already assumed in Section

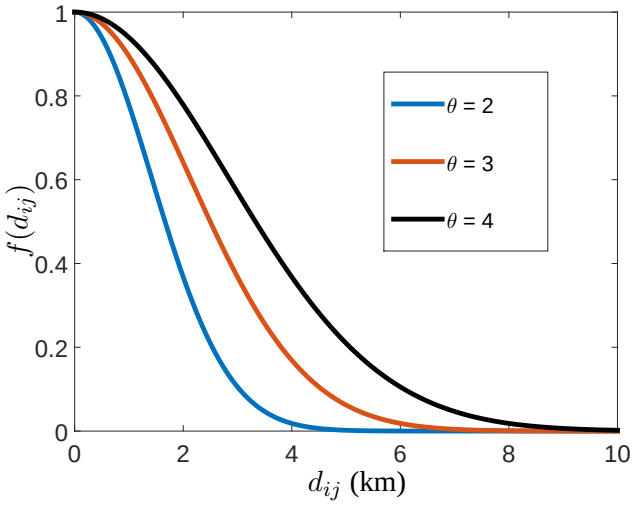

Figure 5.1: Squared exponential covariance function for different values of θ (variance $\sigma_{\mathrm{s}}^2 = 1$).

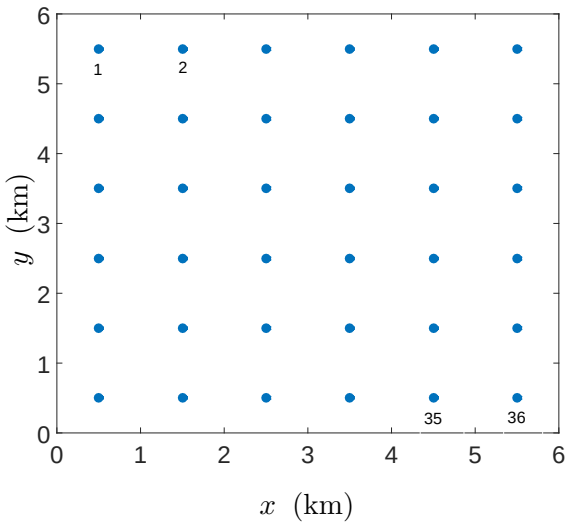

Figure 5.2: Service area with $N = 36$ candidate sensing locations.

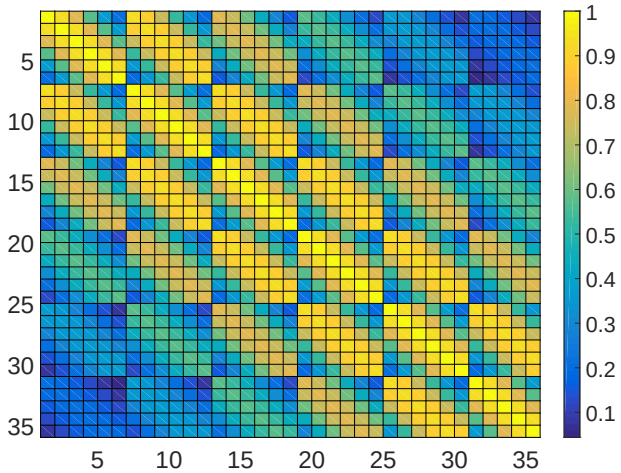

Figure 5.3: Spatial covariance matrix.

5.2.1 that $\mathbf{v}_t$ is mutually uncorrelated with $\mathbf{s}_t$ and $\mathbf{e}_t$, respectively. Now, using the state model of (5.8) and the measurement model of (5.10), the non-stationary component $\mathbf{v}_t$ can be estimated following the lines of a simple Kalman filter [57]. In this case, the recursive state estimate at time t is given by

$$\hat{\mathbf{v}}_t = \mathbf{H}_t\hat{\mathbf{v}}_{t-1} + \mathbf{G}_t(\breve{\mathbf{y}}_t - \mathbf{C}_t\mathbf{H}_t\hat{\mathbf{v}}_{t-1}), \tag{5.11}$$

where the Kalman gain $\mathbf{G}_t$ can be expressed as

$$\begin{aligned}\mathbf{G}_t = [\mathbf{H}_t\mathbf{M}_{\mathbf{v}_{t-1}}\mathbf{H}_t^T + \mathbf{Q}_t]\mathbf{C}_t^T \times \\ [\breve{\mathbf{R}}_t + \mathbf{C}_t(\mathbf{H}_t\mathbf{M}_{\mathbf{v}_{t-1}}\mathbf{H}_t^T + \mathbf{Q}_t)\mathbf{C}_t^T]^{-1}.\end{aligned} \tag{5.12}$$

The MSE matrix of the estimate $\hat{\mathbf{v}}_t$ at time t is given by $\mathbb{E}[(\mathbf{v}_t - \hat{\mathbf{v}}_t)(\mathbf{v}_t - \hat{\mathbf{v}}_t)^T] = \mathbf{M}_{\mathbf{v}_t}$, which is related to the MSE matrix of the estimate at time $t-1$, i.e., $\mathbf{M}_{\mathbf{v}_{t-1}}$, by the recursive relation [57]

$$\mathbf{M}_{\mathbf{v}_t} = [(\mathbf{H}_t\mathbf{M}_{\mathbf{v}_{t-1}}\mathbf{H}_t^T + \mathbf{Q}_t)^{-1} + \mathbf{C}_t^T\breve{\mathbf{R}}_t^{-1}\mathbf{C}_t]^{-1}. \tag{5.13}$$

In the next stage, the estimate of $\hat{\mathbf{v}}_t$ in (5.11) is used to compute the stationary component $\mathbf{s}_t$ using kriging, i.e, a simple linear minimum mean square error (LMMSE) estimator [57]. The linear model is given by $\mathbf{y}_t - \mathbf{C}_t\hat{\mathbf{v}}_t = \mathbf{C}_t\mathbf{s}_t + \mathbf{e}_t$ and the related estimator has the form

$$\hat{\mathbf{s}}_t = \boldsymbol{\mu}_\mathrm{s} + \boldsymbol{\Sigma}_\mathrm{s}\mathbf{C}_t^T(\mathbf{C}_t\boldsymbol{\Sigma}_\mathrm{s}\mathbf{C}_t^T + \sigma_e^2\mathbf{I}_M)^{-1}(\mathbf{y}_t - \mathbf{C}_t\hat{\mathbf{v}}_t - \mathbf{C}_t\boldsymbol{\mu}_\mathrm{s}), \tag{5.14}$$

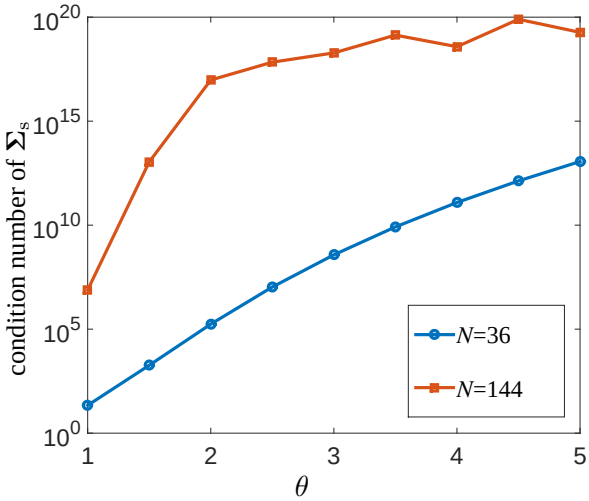

Figure 5.4: Plot of the condition number of $\mathbf{\Sigma}_{\mathrm{s}}$ vs. θ with different number of candidate sensing locations (N).

where we use the prior information $\mathbf{s}_t \sim \mathcal{N}(\boldsymbol{\mu}_s, \mathbf{\Sigma}_s)$. The MSE matrix [57] of the estimate $\hat{\mathbf{s}}_t$, i.e, $\mathbf{M}_{\mathbf{s}_t}$ is given by

$$\mathbf{M}_{\mathbf{s}_t} = [\mathbf{\Sigma}_{\mathrm{s}}^{-1} + \sigma_e^{-2}\mathbf{C}_t^T\mathbf{C}_t]^{-1}. \tag{5.15}$$

Finally, the overall field estimate at time t is given by $\hat{\mathbf{u}}_t = \hat{\mathbf{v}}_t + \hat{\mathbf{s}}_t$.

5.5 Performance metrics as a function of $\mathbf{w}_t$

In this section, we express the MSE matrices, i.e., $\mathbf{M}_{\mathbf{v}_t}$ and $\mathbf{M}_{\mathbf{s}_t}$ as functions of $\mathbf{w}_t$. First of all, we mention some facts regarding the structure of the error covariance matrices presented in the expressions (5.13) and (5.15).

It should be noted that the measurement noise in (5.10) is correlated over space through the off-diagonal elements of $\breve{\mathbf{R}}_t$. Due to this fact, sensor selection approaches using the standard convex framework like [45], [41], and [103], i.e., designing a $\mathbf{w}_t$ by directly optimizing the expression (5.13) is difficult due to the presence of the off-diagonal elements of $\breve{\mathbf{R}}_t$. It should also be noted that the expression of $\breve{\mathbf{R}}_t$ is a function of the measurement matrix $\mathbf{C}_t$ and thus the selection vector $\mathbf{w}_t$. However, we do not encounter this issue in the performance metric to estimate the stationary component $\mathbf{s}_t$, i.e, (5.15), as the measurement noise $\mathbf{e}_t$ is assumed to be spatially uncorrelated in this case.

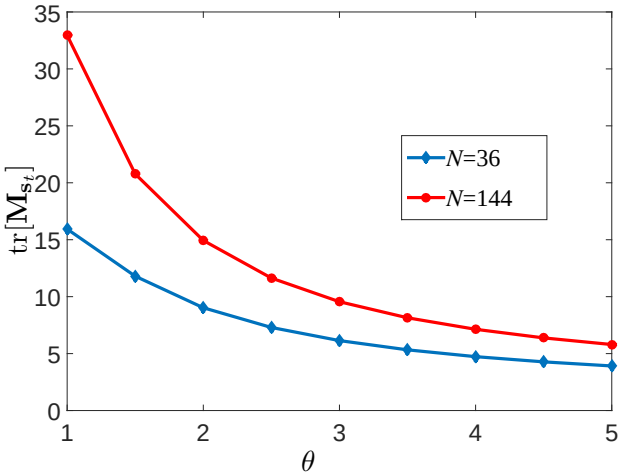

Figure 5.5: MSE of the estimate of $\mathbf{s}_t$ vs. θ for different numbers of candidate sensing locations (N); $M_t = N$; $\sigma_{\mathrm{e}}^2 = 1$; The spatial resolution is increased by representing one pixel of Fig. 5.2 by 4 pixels.

In the expression of $\mathbf{M}_{\mathbf{s}_t}$, i.e., (5.15), we assume that $\mathbf{\Sigma}_{\mathrm{s}}$ is well-conditioned, i.e., accurately invertible. But this may not be the case in some scenarios. The condition number of $\mathbf{\Sigma}_{\mathrm{s}}$ strongly depends on the correlation of the field, spatial sampling distance, grid size etc. [58]. The variation of the condition number of $\mathbf{\Sigma}_{\mathrm{s}}$ with different values of θ for both $N = 36$ and $N = 144$ is plotted in Fig. 5.4. It is seen that for a higher resolution or a strong spatial correlation, the spatial covariance matrix becomes increasingly ill-conditioned and thus close to singular. In such circumstances, we cannot compute the estimation error covariance matrix $\mathbf{M}_{\mathbf{s}_t}$ using the expression (5.15). In that case, $\mathbf{M}_{\mathbf{s}_t}$ can be computed using the alternate expression of (5.15) given by

$$\begin{aligned}\mathbf{M}_{\mathbf{s}_t} &= [\mathbf{\Sigma}_{\mathrm{s}}^{-1} + \sigma_e^{-2}\mathbf{C}_t^T\mathbf{C}_t]^{-1} \\ &= \mathbf{\Sigma}_{\mathrm{s}} - \mathbf{\Sigma}_{\mathrm{s}}\mathbf{C}_t^T(\mathbf{C}_t\mathbf{\Sigma}_{\mathrm{s}}\mathbf{C}_t^T + \sigma_e^2\mathbf{I}_{M_t})^{-1}\mathbf{C}_t\mathbf{\Sigma}_{\mathrm{s}},\end{aligned} \tag{5.16}$$

which is obtained using the matrix inversion lemma (MIL). It should be noted that the alternative expression of the MSE can be used to compute the MSE (without inverting $\mathbf{\Sigma}_{\mathrm{s}}$), but it is difficult to express it as an explicit function of $\mathbf{w}_t$.

In Fig. 5.5, we plot $\mathrm{tr}[\mathbf{M}_{\mathbf{s}_t}]$ for the best case, i.e., the MSE with all the pixel centroids equipped with sensors ($\mathbf{w}_t = \mathbf{1}_N$ or $\mathbf{C}_t = \mathbf{I}_N$) for different values of θ, and for two different spatial resolutions ($N = 36$ and $N = 144$) of the same

6×6 square km service area. It is seen that $\mathrm{tr}[\mathbf{M}_{\mathbf{s}_t}]$ decreases as the strength of the correlation is increased by increasing θ.

To circumvent the effect of ill-conditioning as well as to handle the correlated measurement noise in the expression of $\mathbf{M}_{\mathbf{v}_t}$, we propose the following approach. We start by introducing the substitution

$$\mathbf{\Sigma}_{\mathrm{sr}} = \mathbf{\Sigma}_{\mathrm{s}} + \alpha \mathbf{I}, \tag{5.17}$$

where $\mathbf{\Sigma}_{\mathrm{sr}}$ is a well-conditioned matrix and $\alpha \in \mathbb{R}$. Substituting $\mathbf{\Sigma}_{\mathrm{s}} = \mathbf{\Sigma}_{\mathrm{sr}} - \alpha \mathbf{I}$, we can represent the measurement error covariance matrix of (5.10) as, $\breve{\mathbf{R}}_t = \mathbf{C}_t \mathbf{\Sigma}_{\mathrm{sr}} \mathbf{C}_t^T + \zeta \mathbf{I}_{M_t}$, where $\zeta = \sigma_e^2 - \alpha$ and where we used $\mathbf{C}_t \mathbf{C}_t^T = \mathbf{I}_{M_t}$. Substituting $\breve{\mathbf{R}}_t = \mathbf{C}_t \mathbf{\Sigma}_{\mathrm{sr}} \mathbf{C}_t^T + \zeta \mathbf{I}_{M_t}$ in (5.13), the MSE matrix for the estimate of the non-stationary component is given by

$$\begin{aligned} \mathbf{M}_{\mathbf{v}_t} = [(\mathbf{H}_t \mathbf{M}_{\mathbf{v}_{t-1}} \mathbf{H}_t^T + \mathbf{Q}_t)^{-1} + \\ \mathbf{C}_t^T (\mathbf{C}_t \mathbf{\Sigma}_{\mathrm{sr}} \mathbf{C}_t^T + \zeta \mathbf{I}_{M_t})^{-1} \mathbf{C}_t]^{-1}. \end{aligned} \tag{5.18}$$

Using the MIL, we have the following matrix identity

$$\begin{aligned} (\mathbf{\Sigma}_{\mathrm{sr}}^{-1} + \mathbf{C}_t^T (\zeta \mathbf{I}_{M_t})^{-1} \mathbf{C}_t)^{-1} = \mathbf{\Sigma}_{\mathrm{sr}} \\ - \mathbf{\Sigma}_{\mathrm{sr}} \mathbf{C}_t^T (\mathbf{C}_t \mathbf{\Sigma}_{\mathrm{sr}} \mathbf{C}_t^T + \zeta \mathbf{I}_{M_t})^{-1} \mathbf{C}_t \mathbf{\Sigma}_{\mathrm{sr}}, \end{aligned} \tag{5.19}$$

from which we can derive

$$\begin{aligned} \mathbf{C}_t^T (\mathbf{C}_t \mathbf{\Sigma}_{\mathrm{sr}} \mathbf{C}_t^T + \zeta \mathbf{I}_{M_t})^{-1} \mathbf{C}_t = \mathbf{\Sigma}_{\mathrm{sr}}^{-1} \\ - \mathbf{\Sigma}_{\mathrm{sr}}^{-1} (\mathbf{\Sigma}_{\mathrm{sr}}^{-1} + \zeta^{-1} \mathrm{diag}(\mathbf{w}_t))^{-1} \mathbf{\Sigma}_{\mathrm{sr}}^{-1}, \end{aligned} \tag{5.20}$$

where we used $\mathbf{C}_t^T \mathbf{C}_t = \mathrm{diag}(\mathbf{w}_t)$. Substituting (5.20) in (5.18) we obtain the following expression for $\mathbf{M}_{\mathbf{v}_t}$:

$$\begin{aligned} \mathbf{M}_{\mathbf{v}_t} = [(\mathbf{H}_t \mathbf{M}_{\mathbf{v}_{t-1}} \mathbf{H}_t^T + \mathbf{Q}_t)^{-1} + \mathbf{\Sigma}_{\mathrm{sr}}^{-1} \\ - \mathbf{\Sigma}_{\mathrm{sr}}^{-1} (\mathbf{\Sigma}_{\mathrm{sr}}^{-1} + \zeta^{-1} \mathrm{diag}(\mathbf{w}_t))^{-1} \mathbf{\Sigma}_{\mathrm{sr}}^{-1}]^{-1}. \end{aligned} \tag{5.21}$$

Next, substituting $\mathbf{\Sigma}_{\mathrm{s}} = \mathbf{\Sigma}_{\mathrm{sr}} - \alpha \mathbf{I}$ in the inverse of the right most term of (5.16) and using $\mathbf{C}_t \mathbf{C}_t^T = \mathbf{I}_{M_t}$, we obtain

$$\mathbf{M}_{\mathbf{s}_t} = \mathbf{\Sigma}_{\mathrm{s}} - \mathbf{\Sigma}_{\mathrm{s}} \mathbf{C}_t^T (\mathbf{C}_t \mathbf{\Sigma}_{\mathrm{sr}} \mathbf{C}_t^T + \zeta \mathbf{I}_{M_t})^{-1} \mathbf{C}_t \mathbf{\Sigma}_{\mathrm{s}}. \tag{5.22}$$

Substituting the identity (5.20) into (5.22), we obtain the following expression of $\mathbf{M}_{\mathbf{s}_t}$:

$$\begin{aligned} \mathbf{M}_{\mathbf{s}_t} = \mathbf{\Sigma}_{\mathrm{s}} - \mathbf{\Sigma}_{\mathrm{s}} \mathbf{\Sigma}_{\mathrm{sr}}^{-1} \mathbf{\Sigma}_{\mathrm{s}} \\ + \mathbf{\Sigma}_{\mathrm{s}} \mathbf{\Sigma}_{\mathrm{sr}}^{-1} (\mathbf{\Sigma}_{\mathrm{sr}}^{-1} + \zeta^{-1} \mathrm{diag}(\mathbf{w}_t))^{-1} \mathbf{\Sigma}_{\mathrm{sr}}^{-1} \mathbf{\Sigma}_{\mathrm{s}}. \end{aligned} \tag{5.23}$$

Note that, the expression of (5.23) avoids the inversion of an ill-conditioned $\mathbf{\Sigma}_{\mathrm{s}}$. Here, we only need to invert the well-conditioned $\mathbf{\Sigma}_{\mathrm{sr}}$.

In this work, we consider the overall MSE as a performance metric for sensor placement, i.e, $g(\mathbf{w}_t)$ as mentioned in (5.4a). This is given by

$$\begin{aligned} g(\mathbf{w}_t) &= \mathrm{tr}(\mathbf{M}_{\mathbf{v}_t}) + \mathrm{tr}(\mathbf{M}_{\mathbf{s}_t}) \\ &= \mathrm{tr}[\mathbf{X} - \mathbf{F}[\mathbf{F} + \zeta^{-1}\mathrm{diag}(\mathbf{w}_t)]^{-1}\mathbf{F}]^{-1} + \mathrm{tr}[\mathbf{Y}] \\ &+ \mathrm{tr}[\mathbf{Z}^T[\mathbf{F} + \zeta^{-1}\mathrm{diag}(\mathbf{w}_t)]^{-1}\mathbf{Z}], \end{aligned} \tag{5.24}$$

where $\mathbf{X} = (\mathbf{H}_t\mathbf{M}_{\mathbf{v}_{t-1}}\mathbf{H}_t^T + \mathbf{Q}_t)^{-1} + \mathbf{\Sigma}_{\mathrm{sr}}^{-1}$, $\mathbf{F} = \mathbf{\Sigma}_{\mathrm{sr}}^{-1}$, $\mathbf{Y} = \mathbf{\Sigma}_{\mathrm{s}} - \mathbf{\Sigma}_{\mathrm{s}}\mathbf{\Sigma}_{\mathrm{sr}}^{-1}\mathbf{\Sigma}_{\mathrm{s}}$, and $\mathbf{Z} = \mathbf{\Sigma}_{\mathrm{sr}}^{-1}\mathbf{\Sigma}_{\mathrm{s}}$. Note that the matrices $\mathbf{X}$, $\mathbf{F}$, $\mathbf{Y}$, and $\mathbf{Z}$ are all independent of $\mathbf{w}_t$. To model $\mathbf{\Sigma}_{\mathrm{sr}}$ and $\mathbf{F}+\zeta^{-1}\mathrm{diag}(\mathbf{w}_t)$ as positive definite matrices we need $0 < \alpha < \sigma_e^2$.

The performance metric derived in (5.24) incorporates the MSE matrices of the estimates of the non-stationary ($\mathbf{v}_t$) as well as the stationary ($\mathbf{s}_t$) component of the field, as explicit functions of the sensor location selection vector $\mathbf{w}_t$. Note that a formulation similar to (5.23), for the computation of the MSE matrix as a function of $\mathbf{w}_t$ is proposed in [103], where the field is considered to be either purely stationary or non-stationary.

5.6 KKF with Sensor Placement

In this section, we relax and reformulate the proposed sensor placement problem (5.4) as a semidefinite programming (SDP) problem. Then we present the overall KKF estimator followed by the sensor placement to dynamically monitor the field using only the measurements from the selected sensing locations.

5.6.1 Sensor placement problem as an SDP

Solving for the best subset of sensing locations is a combinatorially complex problem. However, it can be relaxed to a convex problem [45], [101], [41]. As discussed in Section 5.2.1, the sensor location selection vector $\mathbf{w}_t \in \{0,1\}^N$ acts as a weighting vector for all the N candidate pixels. Following the main optimization problem, i.e., (5.4), a sparsity-enforcing, low estimation error, and resource-constrained design of $\mathbf{w}_t$ can be obtained by solving

$$\underset{\mathbf{w}_t \in [0,1]^N}{\arg\min} \quad g(\mathbf{w}_t) + \lambda_t \|\mathbf{w}_t\|_1 \tag{5.25a}$$

$$\text{s.t.} \quad K_t^{\min} \leq \mathbf{1}^T\mathbf{w}_t \leq K_t^{\max}, \tag{5.25b}$$

where the expression of $g(\mathbf{w}_t)$ is given by (5.24). Here, we have relaxed the non-convex Boolean constraint $\mathbf{w}_t \in \{0,1\}^N$ of (5.4) to a convex box constraint $\mathbf{w}_t \in [0,1]^N$. The resource constraint of (5.25b) is affine and thus convex. Some comments regarding the formulation of the proposed sensor placement problem of (5.25) are presented next.

- First of all, let us consider the non-convex version of the optimization problem of (5.25) with $\lambda_t = 0$. This is given as

$$\underset{\mathbf{w}_t \in \{0,1\}^N}{\arg\min} \quad g(\mathbf{w}_t) \tag{5.26a}$$

$$\text{s.t.} \quad K_t^{\min} \leq \mathbf{1}^T \mathbf{w}_t \leq K_t^{\max}. \tag{5.26b}$$

  In this case, the MSE cost will be minimum, i.e, the best estimation performance is achieved, when we select the maximum number of available candidate locations or in other words, when $\mathbf{1}^T \mathbf{w}_t = K_t^{\max}$. Then, there is no way to reduce the number of selected locations below $K_t^{\max}$ and the constraint $\mathbf{1}^T \mathbf{w}_t \geq K_t^{\min}$ becomes redundant. In the aforementioned case, it is difficult to reduce the number of selected sensing locations below $K_t^{\max}$.

- Notice that, dropping the resource constraint (5.25b) and increasing λ_t will reduce the number of selected sensing locations. But, there is no explicit relation between λ_t and $\mathbf{1}^T \mathbf{w}_t$, i.e., it is difficult to directly control the resource allocation (i.e., $K_t^{\max}$) through λ_t.

- We mention that the proposed formulation of (5.25) is not a direct MSE minimization problem but it attains a specific MSE along with enforcing sparsity in spatial sensor location selection through the second summand of (5.25a). The sparsity enforcement is lower bounded by the minimum number of sensing locations to be selected at any t, i.e., $K_t^{\min}$. It should be noted that for an arbitrary selection of λ_t, the minimum number of selected sensing locations will always be $K_t^{\min}$.

- Lastly, it should be noted that a sparsity-enforcing design of $\mathbf{w}_t$ can be achieved by retaining only the second summand of the objective function of (5.25a) and using a separate performance constraint given as $g(\mathbf{w}_t) \leq \gamma_{t,\mathrm{MSE}}$ [103], [41]. The desired performance threshold $\gamma_{t,\mathrm{MSE}}$ can be time-varying or independent of t based on the application. But in many practical scenarios, it could be difficult to set the performance threshold $\gamma_{t,\mathrm{MSE}}$ a priori for every t.

Based on the aforementioned arguments, we advocate the proposed design approach (5.25) that lowers the MSE along with enforcing sparsity in sensor placement satisfying a flexible resource allocation constraint.

After solving (5.25), we obtain $\hat{\mathbf{w}}_t \in [0,1]^N$ which can be converted to a Boolean selection vector $\mathbf{w}_t \in \{0,1\}^N$. This can be performed by either deterministic or stochastic rounding procedures as discussed below.

- The simplest approach could be to set the non-zero entries of $\hat{\mathbf{w}}_t$ to 1. However, there can be a huge difference between the magnitudes of any two non-zero elements in $\hat{\mathbf{w}}_t$. Considering the fact that the indices of the high magnitude (close to 1) elements of $\hat{\mathbf{w}}_t$ signify a more informative sensing location, $\hat{\mathbf{w}}_t$ can be sorted in ascending order of magnitude [45] and a selection threshold (γ) can be selected based on the magnitudes of the elements of the sorted $\hat{\mathbf{w}}_t$. The entries of the Boolean selection vector can be computed as $[\mathbf{w}_t]_j = 1$ if $[\hat{\mathbf{w}}_t]_j \geq \gamma$ else $[\mathbf{w}_t]_j = 0$, for $j = 1, \ldots, N$.

- Another approach could be a stochastic approach, where every entry of $\hat{\mathbf{w}}_t$ is assumed to be the probability that this sensing location is selected at time t. Based on this, multiple random realizations of $\mathbf{w}_t \in \{0,1\}^N$ are generated, where the probability that $[\mathbf{w}_t]_j = 1$ is given by $[\hat{\mathbf{w}}_t]_j$, for $j = 1, \ldots, N$. Then the realization that satisfies the constraints and minimizes the estimation error, i.e., $g(\mathbf{w}_t)$ is selected [41].

Let us now transform the optimization problem of (5.25) into an SDP. From the expression of (5.24), it is clear that minimizing $g(\mathbf{w}_t)$ w.r.t. $\mathbf{w}_t$ is equivalent to minimizing the expression $\mathrm{tr}[\mathbf{X} - \mathbf{F}[\mathbf{F} + \zeta^{-1}\mathrm{diag}(\mathbf{w}_t)]^{-1}\mathbf{F}]^{-1} + \mathrm{tr}[\mathbf{Z}^T[\mathbf{F} + \zeta^{-1}\mathrm{diag}(\mathbf{w}_t)]^{-1}\mathbf{Z}]$ as the matrix $\mathrm{tr}[\mathbf{Y}]$ is independent of $\mathbf{w}_t$. In the first step, we represent the optimization problem of (5.25) in an epigraph form [46, p. 134], [45, Eq. (25)-(26)] which is given by

$$\underset{\mathbf{w}_t \in [0,1]^N, \mathbf{V} \in \mathbb{S}^N, \mathbf{B} \in \mathbb{S}^N}{\arg\min} \quad \mathrm{tr}[\mathbf{V}] + \mathrm{tr}[\mathbf{B}] + \lambda_t \|\mathbf{w}_t\|_1 \tag{5.27a}$$

$$\text{s.t.} \quad \mathbf{V} \succeq [\mathbf{X} - \mathbf{F}[\mathbf{F} + \zeta^{-1}\mathrm{diag}(\mathbf{w}_t)]^{-1}\mathbf{F}]^{-1}, \tag{5.27b}$$

$$\mathbf{B} \succeq \mathbf{Z}^T[\mathbf{F} + \zeta^{-1}\mathrm{diag}(\mathbf{w}_t)]^{-1}\mathbf{Z}, \tag{5.27c}$$

$$K_t^{\min} \leq \mathbf{1}^T\mathbf{w}_t \leq K_t^{\max}, \tag{5.27d}$$

where we introduce the auxiliary variables $\mathbf{V} \in \mathbb{S}^N$ and $\mathbf{B} \in \mathbb{S}^N$. We notice that the epigraph form (5.27) is well-posed since by choosing $0 < \alpha < \sigma_e^2$ in (5.17) the matrix $[\mathbf{F} + \zeta^{-1}\mathrm{diag}(\mathbf{w}_t)]$ is always positive definite and symmetric. In

addition, also the matrix $[\mathbf{X} - \mathbf{F}[\mathbf{F} + \zeta^{-1}\mathrm{diag}(\mathbf{w}_t)]^{-1}\mathbf{F}]$ is also positive definite by construction as derived in (5.18)-(5.21).

The epigraph form (5.27) is not a strictly convex program, in the sense that there are multiple $\mathbf{V}$ and $\mathbf{B}$ matrices that achieve the minimal cost value. This is due to the inequality constraints of (5.27b) and (5.27c). At optimality, the eigenvalues of $\mathbf{V}$ and $\mathbf{B}$ must be equivalent to their lower bounds in (5.27b) and (5.27c). Hence, an optimizer of the problem is $\mathbf{V} = [\mathbf{X} - \mathbf{F}[\mathbf{F} + \zeta^{-1}\mathrm{diag}(\mathbf{w}_t)]^{-1}\mathbf{F}]^{-1}$ and $\mathbf{B} = \mathbf{Z}^T[\mathbf{F} + \zeta^{-1}\mathrm{diag}(\mathbf{w}_t)]^{-1}\mathbf{Z}$.

We proceed by simplifying the constraint (5.27b). Let us introduce another auxiliary variable $\mathbf{A} \in \mathbb{S}^N$ and substitute (5.27b) with two constraints

$$\mathbf{V} \succeq [\mathbf{X} - \mathbf{A}]^{-1}, \tag{5.28}$$

$$\mathbf{A} \succeq \mathbf{F}[\mathbf{F} + \zeta^{-1}\mathrm{diag}(\mathbf{w}_t)]^{-1}\mathbf{F}. \tag{5.29}$$

With this in place, the optimization problem (5.27) can be formulated as

$$\underset{\mathbf{w}_t \in [0,1]^N, \mathbf{V}, \mathbf{A}, \mathbf{B} \in \mathbb{S}^N}{\arg\min} \quad \mathrm{tr}[\mathbf{V}] + \mathrm{tr}[\mathbf{B}] + \lambda_t \|\mathbf{w}_t\|_1 \tag{5.30a}$$

$$\text{s.t.} \quad \mathbf{V} \succeq [\mathbf{X} - \mathbf{A}]^{-1}, \tag{5.30b}$$

$$\mathbf{A} \succeq \mathbf{F}[\mathbf{F} + \zeta^{-1}\mathrm{diag}(\mathbf{w}_t)]^{-1}\mathbf{F}, \tag{5.30c}$$

$$\mathbf{B} \succeq \mathbf{Z}^T[\mathbf{F} + \zeta^{-1}\mathrm{diag}(\mathbf{w}_t)]^{-1}\mathbf{Z}, \tag{5.30d}$$

$$K_t^{\min} \leq \mathbf{1}^T\mathbf{w}_t \leq K_t^{\max}, \tag{5.30e}$$

It can be claimed that the optimization problem (5.30) is equivalent to (5.27) given that it yields a decision variable $\mathbf{w}_t$ with the same optimal cost of (5.27). To prove this, let us choose an arbitrary $\mathbf{w}_t$ say $\bar{\mathbf{w}}$. For a fixed yet arbitrary $\bar{\mathbf{w}}$ verifying (5.30e), the optimization problem (5.30) minimizes both $\mathbf{V}$ and $\mathbf{B}$. This means that due to (5.30b) it minimizes also $\mathbf{A}$: in fact, as $\mathbf{V} \succeq [\mathbf{X} - \mathbf{A}]^{-1}$ the lower bound for $\mathbf{V}$ is minimal if the positive definite matrix $[\mathbf{X} - \mathbf{A}]$ is maximal, that is $\mathbf{A}$ is minimal. Therefore, $\mathbf{A}$ must attain its lower bound. As mentioned earlier, there are multiple optimizers, yet one is $\mathbf{A} = \mathbf{F}[\mathbf{F} + \zeta^{-1}\mathrm{diag}(\mathbf{w}_t)]^{-1}\mathbf{F}$. In addition, $\mathbf{V} = [\mathbf{X} - \mathbf{A}]^{-1} = [\mathbf{X} - \mathbf{F}[\mathbf{F} + \zeta^{-1}\mathrm{diag}(\bar{\mathbf{w}})]^{-1}\mathbf{F}]^{-1}$ at optimality, as well. The same reasoning holds also for $\mathbf{B}$, which at optimality is $\mathbf{B} = \mathbf{Z}^T[\mathbf{F} + \zeta^{-1}\mathrm{diag}(\bar{\mathbf{w}})]^{-1}\mathbf{Z}$. Since this reasoning is valid for any feasible $\bar{\mathbf{w}}$, it is also valid for an optimal one and therefore the equivalence claim follows. It should be noted that a similar argument was also presented in [104], where only the issue of correlated measurement noise is considered.

Using the Schur complement lemma the constraints (5.30b) and (5.30c) can be equivalently represented by the linear matrix inequalities (LMI) :

$$\begin{bmatrix} \mathbf{X}-\mathbf{A} & \mathbf{I} \\ \mathbf{I} & \mathbf{V} \end{bmatrix} \succeq \mathbf{0} \tag{5.31a}$$

$$\begin{bmatrix} \mathbf{A} & \mathbf{F} \\ \mathbf{F} & \mathbf{F}+\zeta^{-1}\mathrm{diag}(\mathbf{w}_t) \end{bmatrix} \succeq \mathbf{0} \tag{5.31b}$$

The constraint (5.30c) can be equivalently represented by an LMI using the Schur complement [46]. In other words, using the fact that $[\mathbf{F}+\zeta^{-1}\mathrm{diag}(\mathbf{w}_t)] \succ \mathbf{0}$, we obtain

$$\begin{bmatrix} \mathbf{B} & \mathbf{Z}^T \\ \mathbf{Z} & \mathbf{F}+\zeta^{-1}\mathrm{diag}(\mathbf{w}_t) \end{bmatrix} \succeq \mathbf{0}. \tag{5.32}$$

Finally, an SDP representation of the overall optimization problem of (5.27) can be expressed as

$$\underset{\mathbf{w}_t\in[0,1]^N,\mathbf{A},\mathbf{B},\mathbf{V}\in\mathbb{S}^N}{\arg\min} \quad \mathrm{tr}[\mathbf{V}]+\mathrm{tr}[\mathbf{B}]+\lambda_t\|\mathbf{w}_t\|_1, \tag{5.33a}$$

$$\text{s.t.} \quad \text{LMIs in (5.31a), (5.31b), (5.32)} \tag{5.33b}$$

$$K_t^{\min} \leq \mathbf{1}^T\mathbf{w}_t \leq K_t^{\max} \tag{5.33c}$$

The solution of the aforementioned SDP is a selection vector $\hat{\mathbf{w}}_t \in [0,1]^N$.

5.6.2 Spatial sensor placement for stationary field estimation

Let us consider the effect of the stationary component of the field $\mathbf{s}_t$ for any t. In this case, we consider that $\mathbf{v}_t = \mathbf{0}$. In this case, the measurement model of (5.1) is given by $\mathbf{y}_t = \mathbf{C}_t\mathbf{s}_t + \mathbf{e}_t$. Exploiting the prior information regarding $\mathbf{s}_t$, i.e., $\mathbf{s}_t \sim \mathcal{N}(\boldsymbol{\mu}_\mathrm{s}, \boldsymbol{\Sigma}_\mathrm{s})$ an LMMSE estimator of $\mathbf{s}_t$ can be presented by $\hat{\mathbf{s}}_t = \boldsymbol{\mu}_\mathrm{s}+\boldsymbol{\Sigma}_\mathrm{s}\mathbf{C}_t^T(\mathbf{C}_t\boldsymbol{\Sigma}_s\mathbf{C}_t^T+\sigma_e^2\mathbf{I}_{M_t})^{-1}(\mathbf{y}_t-\mathbf{C}_t\boldsymbol{\mu}_\mathrm{s})$. The performance of the aforementioned estimator is given by the MSE matrix $\mathbf{M}_{\mathbf{s}_t} = [\boldsymbol{\Sigma}_\mathrm{s}^{-1}+\sigma_e^{-2}\mathbf{C}_t^T\mathbf{C}_t]^{-1} = \boldsymbol{\Sigma}_\mathrm{s} - \boldsymbol{\Sigma}_\mathrm{s}\mathbf{C}_t^T(\mathbf{C}_t\boldsymbol{\Sigma}_\mathrm{s}\mathbf{C}_t^T+\sigma_e^2\mathbf{I}_{M_t})^{-1}\mathbf{C}_t\boldsymbol{\Sigma}_\mathrm{s}$. Considering the fact that $\boldsymbol{\Sigma}_\mathrm{s}$ can be ill-conditioned, following the formulation of (5.23), the expression of $\mathbf{M}_{\mathbf{s}_t}$ can be expressed as a function of $\mathbf{w}_t$ as

$$\mathbf{M}_{\mathbf{s}_t} = \mathbf{Y}+\mathbf{Z}^T[\mathbf{F}+\zeta^{-1}\mathrm{diag}(\mathbf{w}_t)]^{-1}\mathbf{Z}, \tag{5.34}$$

where $\mathbf{Y} = \boldsymbol{\Sigma}_\mathrm{s}-\boldsymbol{\Sigma}_\mathrm{s}\boldsymbol{\Sigma}_\mathrm{sr}^{-1}\boldsymbol{\Sigma}_\mathrm{s}$, $\mathbf{Z} = \boldsymbol{\Sigma}_\mathrm{sr}^{-1}\boldsymbol{\Sigma}_\mathrm{s}$, and $\mathbf{F} = \boldsymbol{\Sigma}_\mathrm{sr}^{-1}$. Note that the matrices $\mathbf{F}$, $\mathbf{Y}$, and $\mathbf{Z}$ are all independent of $\mathbf{w}_t$. Considering $g(\mathbf{w}_t) = \mathrm{tr}[\mathbf{M}_{\mathbf{s}_t}]$ and following

the same SDP formulation of Section 5.6.1, the proposed sensor placement problem of (5.4) can be represented as

$$\underset{\mathbf{w}_t \in [0,1]^N, \mathbf{B} \in \mathbb{S}^N}{\arg\min} \quad \mathrm{tr}[\mathbf{B}] + \lambda_t \|\mathbf{w}_t\|_1, \tag{5.35a}$$

$$\text{s.t.} \quad \begin{bmatrix} \mathbf{B} & \mathbf{Z}^T \\ \mathbf{Z} & \mathbf{F} + \zeta^{-1}\mathrm{diag}(\mathbf{w}_t) \end{bmatrix} \succeq \mathbf{0}, \tag{5.35b}$$

$$K_t^{\min} \leq \mathbf{1}^T \mathbf{w}_t \leq K_t^{\max}. \tag{5.35c}$$

The optimization problem of (5.35) gives the spatial sensor placement pattern for any snapshot t, when the field is stationary over space. However, if the field is also temporally stationary then the sensor placement problem of (5.35) can be extended to blocks of multiple snapshots. In this case, the performance metric can be computed using the same approach as [103]. In the simulation section, we show the effects of spatial correlation on sensor placement.

5.6.3 Sparsity-enhancing iterative design

In order to eschew the effect of the magnitude dependencies of the elements of $\hat{\mathbf{w}}_t$, we individually weigh each element of $\mathbf{w}_t$. In this case, we consider a vector form for the regularization parameter : $\boldsymbol{\lambda}_t \in \mathbb{R}^N$. The weight associated to the each element of $\mathbf{w}_t$ is the corresponding element of $\boldsymbol{\lambda}_t \in \mathbb{R}^N$. We iteratively refine the weighting vector $\boldsymbol{\lambda}_t$ in the ℓ_1 minimization term of the problem (5.33) [56]. Using this approach, higher weights are applied on the smaller elements of $\mathbf{w}_t$ to push them towards 0 and the magnitudes of the larger elements are maintained by applying a smaller weight. In this way, a sparser solution can be obtained compared to the standard sparsity-promoting method. The iterative algorithm can be summarized as

- **Initialize** $i = 0$, weight vector $\boldsymbol{\lambda}_t^0 = \mathbf{1}_N$, ϵ, and maximum number of iterations I.

- **for** $i = 0, \ldots, I$

$$\hat{\mathbf{w}}_t^i = \underset{\mathbf{w}_t \in [0,1]^N, \mathbf{A}, \mathbf{B}, \mathbf{V} \in \mathbb{S}^N}{\arg\min} \quad \mathrm{tr}[\mathbf{V}] + \mathrm{tr}[\mathbf{B}] + (\boldsymbol{\lambda}_t^i)^T \mathbf{w}_t, \tag{5.36a}$$

$$\text{s.t.} \quad \text{LMIs in (5.31a), (5.31b), (5.32)} \tag{5.36b}$$

$$K_t^{\min} \leq \mathbf{1}^T \mathbf{w}_t \leq K_t^{\max} \tag{5.36c}$$

- $[\boldsymbol{\lambda}_t^{i+1}]_j = \frac{1}{\epsilon+[\hat{\mathbf{w}}_t^i]_j}$, for every $j = 1, \ldots, N$
- **end**;
- **set** $\hat{\mathbf{w}}_t = \hat{\mathbf{w}}_t^I$.

After solving the above algorithm, we still obtain $\hat{\mathbf{w}}_t \in [0,1]^N$. We convert this to a Boolean selection vector $\mathbf{w}_t \in \{0,1\}^N$ using a deterministic/stochastic rounding method as mentioned in Section 5.6.1.

5.6.4 KKF algorithm with sensor placement

The informative M_t locations to deploy/move the sensors at any t is denoted by $\mathrm{supp}(\hat{\mathbf{w}}_t)$, where $\mathbf{1}^T\hat{\mathbf{w}}_t = M_t$. The noisy measurements collected from the aforementioned M_t locations are stored in $\mathbf{y}_t$. The sensing matrix $\mathbf{C}_t$ is constructed by removing the all-zero rows of $\mathrm{diag}(\hat{\mathbf{w}}_t)$ at every t. This measurement matrix is used for the estimation of the non-stationary and the stationary components by (5.11) and (5.14), respectively. Then the overall field estimate at time t is computed by $\hat{\mathbf{u}}_t = \hat{\mathbf{v}}_t + \hat{\mathbf{s}}_t$. Note that the estimation steps, i.e, (5.11) and (5.14) do not require the computation of the inverse of $\boldsymbol{\Sigma}_{\mathrm{s}}$. The error covariance of the non-stationary component can be updated by (5.13), which also does not require the inverse of $\boldsymbol{\Sigma}_{\mathrm{s}}$. At every t, the overall estimation performance can be computed by the expression of (5.24). The best case performance, i.e, the performance with all the locations selected can also be computed by the expression of (5.24) by using $\mathbf{w}_t = \mathbf{1}_N$.

In many practical environmental fields (such as rainfall), the field is generally non-negative. To achieve a non-negative estimate at every t, the estimates of the stationary and non-stationary components can be projected onto the non-negative orthant, i.e., the negative values are set to zero. This is obtained by adopting

$$\hat{\mathbf{u}}_t = [\hat{\mathbf{v}}_t + \hat{\mathbf{s}}_t]_+. \tag{5.37}$$

However, in this case, the performance metrics $\mathrm{tr}[\mathbf{M}_{\mathbf{v}_t}]$ and $\mathrm{tr}[\mathbf{M}_{\mathbf{s}_t}]$ are only the approximations.

5.7 Simulation results

In this section, we perform some numerical experiments to exhibit the practicality of the developed sparsity-enforcing sensor placement followed by the KKF estimation method. We select a service area of 6×6 square km with 1 square km spatial

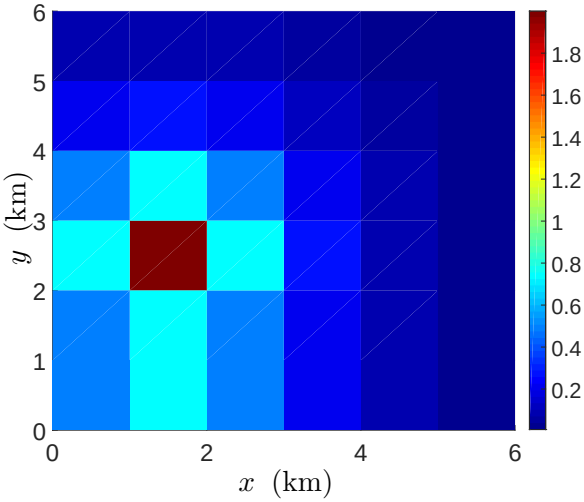

Figure 5.6: Field distribution at $t = 0$ with a single source: $K = 1$, $\boldsymbol{\rho}_1 = [1.5, 1.5]^T$, $s_1 = 2$, $d_1 = 1$.

resolution as illustrated in Fig. 5.2. The spatial distribution of the non-stationary component at time $t = 0$, i.e, $\mathbf{v}_0$, is generated by the following exponential source-field model

$$[\mathbf{v}_0]_j = \sum_{k=1}^{K} s_k \exp(-d_k \|\mathbf{x}_j - \boldsymbol{\rho}_k\|_2), \quad j = 1, \ldots, N, \tag{5.38}$$

where K is the number of field-generating points/sources. The parameters $\boldsymbol{\rho}_k$, s_k, and d_k are the location, amplitude, and the spatial decaying factor of the k-th source at time $t = 0$. Based on this function, we generate the non-stationary component of the field at time $t = 0$, i.e., $\mathbf{v}_0 \in \mathbb{R}^N$ using the parameters $K = 1$, $\boldsymbol{\rho}_1 = [1.5, 1.5]^T$, $s_1 = 2$, and $d_1 = 1$. The spatial distribution of $\mathbf{v}_0$ in the specified service area is shown in Fig. 5.6.

The state model of the non-stationary component $\mathbf{v}_t$ is modelled by (5.8). The state transition matrix is modelled by the Gaussian kernel function given by (5.9). For the sake of simplicity, we consider a spatially invariant translation parameter and spatio-temporally invariant dilation parameters given as $\mathbf{a}_t^{ij} = \mathbf{a}_t$ and $\mathbf{D}_t^{ij} = \mathbf{D}$, respectively, for $i, j = 1, \ldots, N$. The elements of the state transition matrix are given by

$$[\mathbf{H}_t]_{ij} = \nu \exp[-(\mathbf{x}_i - \mathbf{x}_j - \mathbf{a}_t)^T \mathbf{D}^{-1} (\mathbf{x}_i - \mathbf{x}_j - \mathbf{a}_t)]. \tag{5.39}$$

The spatio-temporal evolution of the true value of the field, i.e., $\mathbf{u}_t = \mathbf{v}_t + \mathbf{s}_t$ is generated in the following two ways.

In the **first** case, we consider a pure advective process, i.e., we select a very low dilation parameter given by $\mathbf{D} = 10^{-4}\mathbf{I}_2$ for all $t = 1, \ldots, 8$ and $\nu = 0.8$. It is assumed that the temporal resolution is 1 minute. The translation vectors, i.e., $\mathbf{a}_t$, are assumed to be changing every t as $[1,1]^T$, $[-1,-1]^T$, $[1,1]^T$, $[0,0]^T$, $[1,1]^T$, $[-1,-1]^T$, $[0,1]^T$, and $[-1,-1]^T$. It is assumed that at $t = 0$, $\mathbf{v}_t$ is generated by the source as shown in Fig. 5.6. The different states of $\mathbf{v}_t$ for $t = 1, \ldots, 8$ are generated by the state model of (5.8). The spatially colored yet temporally uncorrelated process noise is characterized by $\mathbf{q}_t \sim \mathcal{N}(\mathbf{0}_N, \mathbf{Q})$, where $[\mathbf{Q}]_{ij} = 10^{-4}\exp(-\|\mathbf{x}_i - \mathbf{x}_j\|_2)$. The stationary component $\mathbf{s}_t$ is modelled by $\mathbf{s}_t \sim \mathcal{N}(\mathbf{1}_N, \mathbf{\Sigma}_\mathrm{s})$. The parameters of the squared exponential covariance function of (5.7) are given by $\sigma_s^2 = 0.001$ and $\theta = 1$. Note that increasing the value of θ, the field becomes spatially more correlated and the condition number of $\mathbf{\Sigma}_\mathrm{s}$ increases. However, as mentioned earlier, our proposed formulation, i.e., both the selection and the estimation, does not involve the inversion of $\mathbf{\Sigma}_\mathrm{s}$. A highly spatially correlated $\mathbf{s}_t$ is considered in the next case. For the first case, the true field $\mathbf{u}_t = \mathbf{v}_t + \mathbf{s}_t$ for $t = 1, \ldots, 8$ can be simulated as shown in Fig. 5.7.

In the **second** case, we consider $\mathbf{D} = \mathbf{I}_2$ for all $t = 1, \ldots, 8$ and the translation parameters are fixed as $\mathbf{a}_t = [0.4, 0.4]^T$ for $t = 1, \ldots, 4$, and no translation for the last 4 snapshots, i.e., $\mathbf{a}_t = [0,0]^T$ for $t = 5, \ldots, 8$. The state of $\mathbf{v}_t$ at $t = 0$ is the same as before. The scaling parameter is given by $\nu = 0.35$. The process noise $\mathbf{q}_t$ is the same as before. In this case, we assume that the stationary component $\mathbf{s}_t$ is spatially more correlated than the last case. The parameters of the covariance function (5.7) are taken as $\sigma_\mathrm{s}^2 = 0.01$ and $\theta = 4$, which generates an ill-conditioned $\mathbf{\Sigma}_\mathrm{s}$ (Fig. 5.4). Using these, the true field, i.e., $\mathbf{u}_t = \mathbf{v}_t + \mathbf{s}_t$ for $t = 1, \ldots, 8$ is shown in Fig. 5.8.

5.7.1 Sensor placement followed by field estimation using KKF

We select the optimal sensing locations and use them to estimate the field for $t = 1, \ldots, 8$ snapshots for the two different scenarios of the spatio-temporal evolution of the field, as mentioned in the previous section. We use the same service area shown in Fig. 5.2, where the centroids of the $N = 36$ pixels are the candidate sensing locations. We assume that the measurement noise variance is given by $\sigma_e^2 = 0.001$. We solve the optimization problem of (5.36) with the parameters $I = 2$ and $\epsilon = 10^{-6}$. The weighting vectors are initialized as $\boldsymbol{\lambda}_0 = \mathbf{1}_N$. The

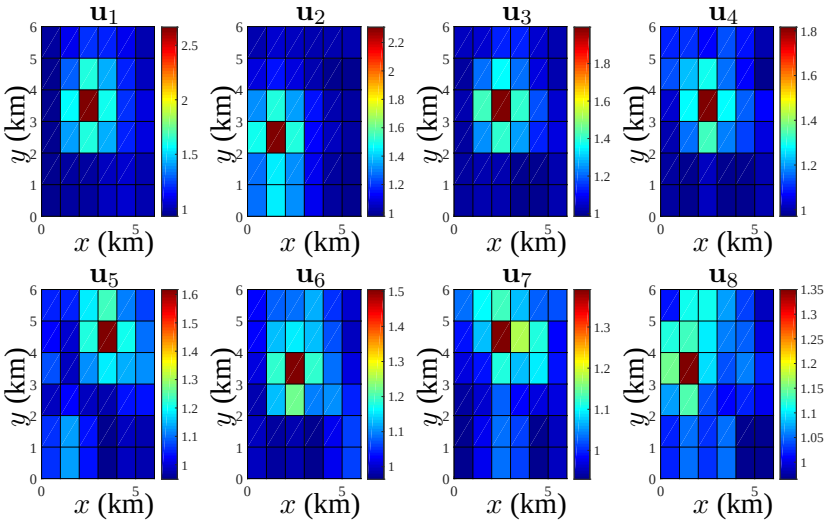

Figure 5.7: Spatio-temporal evolution of $\mathbf{u}_t$ in a 6×6 square km area; Spatial resolution: 1×1 square km; Time varying $\mathbf{H}_t$ for $t = 1, \ldots, 8$; strength of spatial correlation: $\theta = 1$.

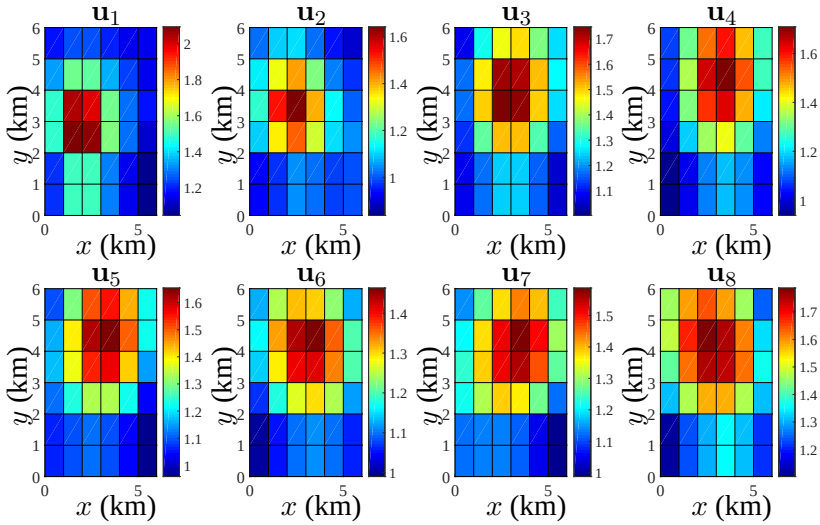

Figure 5.8: Spatio-temporal evolution of $\mathbf{u}_t$ in a 6×6 square km area; Spatial resolution: 1×1 square km; Time varying $\mathbf{H}_t$ for $t = 1, \ldots, 8$; strength of spatial correlation: $\theta = 4$.

resource constraints are given as $K_t^{\max} = 30$ and $K_t^{\min} = 25$ for all t. To extract the Boolean solution $\mathbf{w}_t \in \{0,1\}^N$ from $\hat{\mathbf{w}}_t \in [0,1]^N$, we adopt the randomized rounding method. We use the software CVX [105] (parser CVX, solver SeDuMi [53]) to solve the SDP problem (5.36). Following the above simulation setup, the selected sensing locations for the first and the second scenario are shown in Fig. 5.9 and Fig. 5.10, respectively for the 8 snapshots. The indices of the pixel midpoints (vertical axis) are the same as in Fig. 5.2. The main observations from the selected locations are listed below.

- First of all, it is clearly seen that the selected sensing locations depend on the dynamics. Note that, Fig. 5.9 gives the optimal placement pattern, when $\mathbf{H}_t$ is changing every t (different $\mathbf{a}_t$ on every t). Fig. 5.10 shows the optimal sensing locations when we have the same $\mathbf{H}_t$ for $t = 1, ..., 4$ ($\mathbf{a}_t = [0.4, 0.4]^T$) and another $\mathbf{H}_t$ for $t = 5, ..., 8$ ($\mathbf{a}_t = [0, 0]^T$).

- When $\mathbf{H}_t$ is changing every t, i.e., the spatio-temporal evolution of the field is guided by the time-varying spatial translation parameter $\mathbf{a}_t$ (Fig. 5.2), the optimal selection pattern also depends upon this translation (Fig. 5.9).

- In the second scenario, we have assumed a very low and fixed translation, i.e, $\mathbf{a}_t = [0.4, 0.4]^T$ for the first 4 snapshots and $\mathbf{a}_t = [0, 0]^T$, i.e, no translation, for the last 4 snapshots (Fig. 5.8). It is seen that almost the same set of sensors are selected in the last 4 snapshots of Fig. 5.10. In general, when $\mathbf{H}_t$ is not changing with time, the estimation error of the non-stationary component reaches a steady state after a number of snapshots and the same set of sensors are selected every t.

The overall estimation performance using the measurements from the selected locations of Fig. 5.9 and Fig. 5.10 is shown in Fig. 5.11 and Fig. 5.12, respectively. In these figures, we exhibit the pixel-wise comparison of the estimates for $T = 8$ snapshots, i.e, the estimation performance of $36 \times 8 = 288$ pixels. We initialize the KKF iterations with $\hat{\mathbf{v}}_t = \mathbf{1}_N$ and $\mathbf{M}_{\mathbf{v}_t} = 0.001\mathbf{I}_N$ at $t = 0$.

5.7.2 Performance analysis

We compare the estimation performance of the developed sensor placement method by comparing the performance metric, i.e, $g(\hat{\mathbf{w}}_t) = \mathrm{tr}[\mathbf{M}_{\mathbf{s}_t}] + \mathrm{tr}[\mathbf{M}_{\mathbf{v}_t}]$ with a random sensor placement (with the same M_t, i.e., $\|\hat{\mathbf{w}}_t\|_0 = M_t$ as for the developed method) and with the best case performance (i.e., $M_t = N$ or $\mathbf{w}_t = \mathbf{1}_N$). For

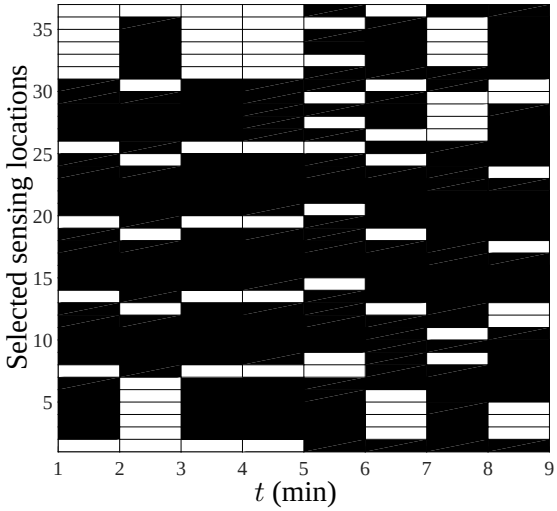

Figure 5.9: Selected sensing locations to estimate the field with the first scenario of the true value.

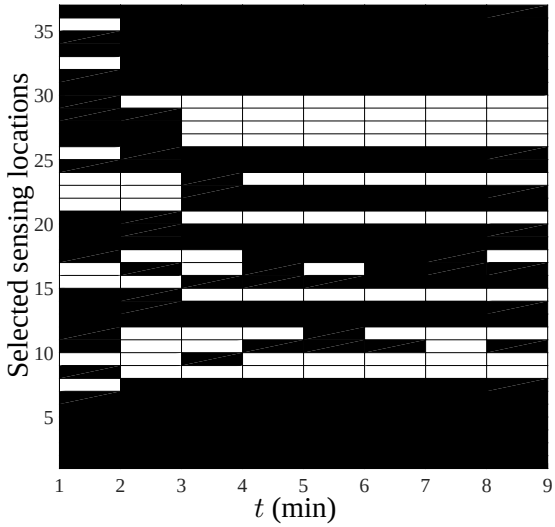

Figure 5.10: Selected sensing locations to estimate the field with the second scenario of the true value.

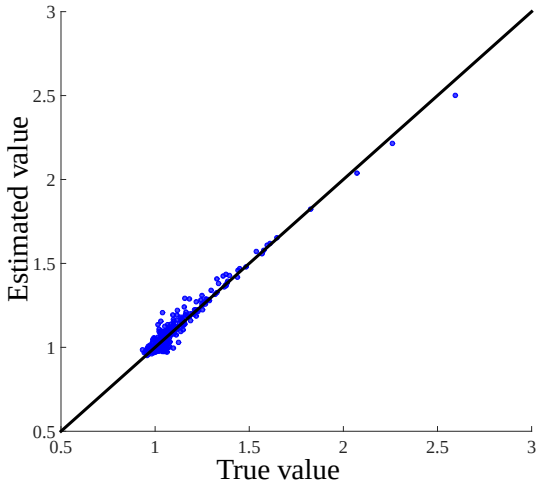

Figure 5.11: Comparison of the KKF estimate with the true value (Fig. 5.7) with the measurements from the selected locations shown in Fig. 5.9.

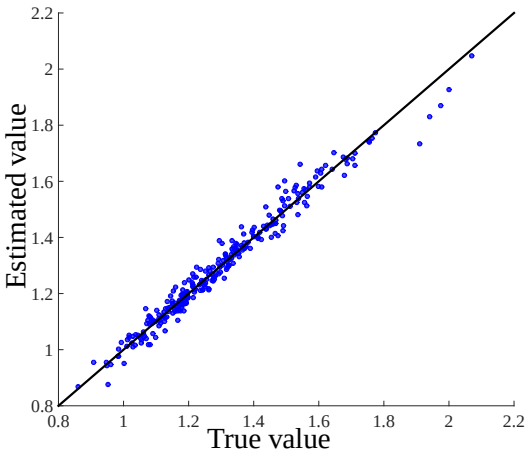

Figure 5.12: Comparison of the KKF estimate with the true value (Fig. 5.8) with the measurements from the selected locations shown in Fig. 5.10.

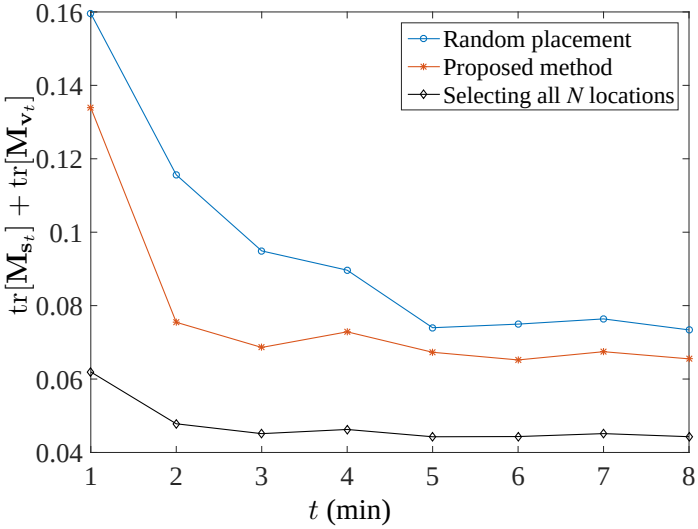

Figure 5.13: Comparison of the performance metric for the random placement, proposed method, and the best case.

the random placement, we generate 100 different realizations of $\mathbf{w}_t \in \{0,1\}^N$ at every t with the same M_t as for the proposed method. Then $g(\mathbf{w}_t)$ is computed for every $\mathbf{w}_t$ and their average is considered. Similarly, we compute the best case performance, i.e, $g(\mathbf{1}_N)$ for every t and in this case $\mathbf{M}_{\mathbf{v}_t}$ is updated with $\mathbf{w}_t = \mathbf{1}_N$. We use the same set of parameters as mentioned in the first case of Section 5.7.1. Only the resource allocation constraint is simplified as $\mathbf{1}^T\mathbf{w}_t = 15$, i.e, we fix that only 15 sensing locations will be selected every t. The performance comparison is shown in Fig. 5.13. It is seen that the proposed approach slightly outperforms the random placement. However, the random placement of sensors does not optimize any performance criterion.

5.7.3 Spatial sensor placement for stationary field estimation

In this section, we show the effects of different spatial correlation patterns on sensor placement assuming the field is purely stationary. We solve the optimization problem of (5.35), for two different spatial covariance matrices ($\mathbf{\Sigma}_\mathrm{s}$). In the first case, we consider that $\mathbf{\Sigma}_\mathrm{s}$ is generated by the squared exponential function (5.7) with $\theta = 2$ and $\sigma_\mathrm{s}^2 = 0.01$ (Fig. 5.14). In the second case, we consider a randomly generated $\mathbf{\Sigma}_\mathrm{s}$ (Fig. 5.15). The resource allocation constraint is the same as before,

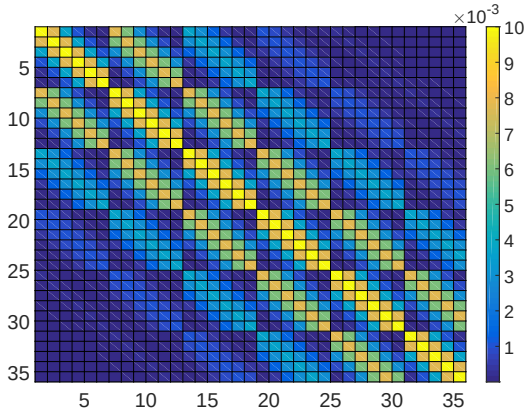

Figure 5.14: Spatial covariance matrix generated by the squared exponential function ($\sigma_{\mathrm{s}}^2 = 0.01, \theta = 2$)

i.e, $K_t^{\min} = 25$, and $K_t^{\max} = 30$. We solve the optimization problem of (5.35), with the iterative approach of (5.36) with the same parameters as mentioned in the previous section. The selected locations (marked by black squares where the blue dots are the candidate locations as shown in Fig 5.2) to deploy sensors are shown in Fig. 5.16 and Fig. 5.17 for the spatial covariance matrices shown in Fig. 5.14 and Fig. 5.15, respectively.

First of all, it is observed that the spatial distribution of the optimal sensing locations depends upon the correlation pattern of the field. It is seen that when $\mathbf{\Sigma}_{\mathrm{s}}$ is generated by a squared exponential covariance (stationary) function then the optimal sensor placement pattern is more or less symmetrically and uniformly distributed over the entire service area. But for a random spatial covariance matrix the optimal sensing locations do not follow any specific pattern.

5.8 Conclusion and Future work

In this chapter, we have developed a sparsity-enforcing sensor placement followed by a field estimation technique using a KKF. The proposed methodology selects the most informative sensing locations over space and time in a specified service area of interest. Along with minimizing the estimation error, the developed method also economizes the sensor placement (in terms of resources) at every temporal interval. The salient features of the proposed method include handling a general class of spatial covariance matrices and tackling correlated measurement noise. Numerical

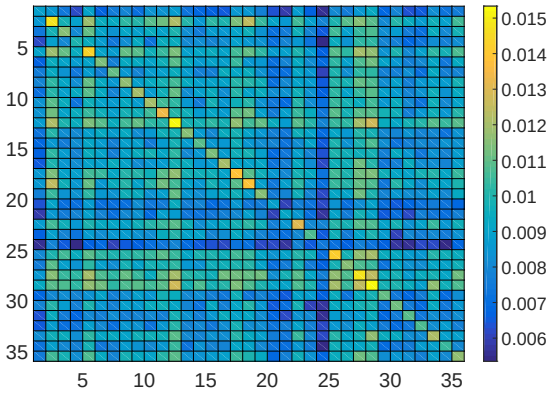

Figure 5.15: Randomly generated spatial covariance matrix

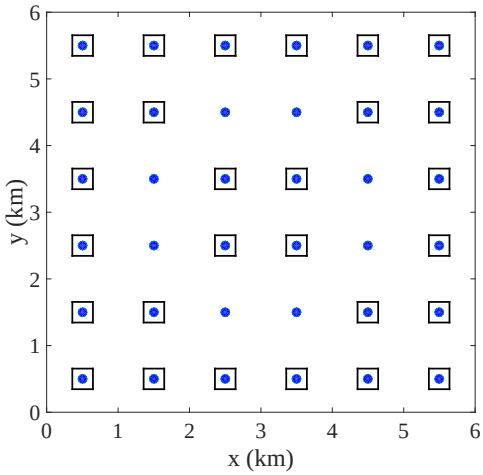

Figure 5.16: Sensor placement pattern for the $\mathbf{\Sigma}_s$ as shown in Fig. 5.14.

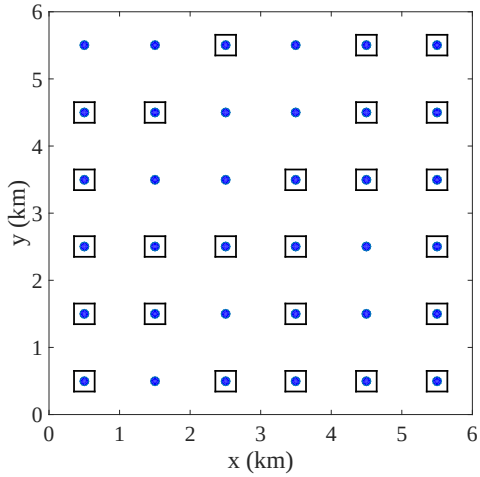

Figure 5.17: Sensor placement pattern for the $\mathbf{\Sigma}_{\mathrm{s}}$ as shown in Fig. 5.15.

analysis shows the feasibility of the method. The effects of the dynamics and spatial correlation of the field in spatio-temporal sensor placement are discussed with numerical experiments.

In this chapter, we have considered the fact that the prior knowledge regarding the spatial variability and the dynamics are perfectly known a priori. In that case, the performance of a clairvoyant Kalman setup with Gaussian measurement and process noise is optimal. But in many practical scenarios, the aforementioned spatio-temporal prior information may not be accurate and we require more information regarding the unknown field in the estimation step. Future research is envisioned to incorporate the effects of model imperfections in the developed method. Another future research area could be using distributed algorithms to apply the developed method for large scale sensor network applications. It will also be interesting to tailor the recent progress in time-varying optimization [106] to solve the SDPs in a tracking fashion, rather than at optimality at each sampling time.

Chapter 6

Dynamic Model Estimation Followed by Field Estimation

The spatio-temporal evolution of an environmental field can be estimated by the predictions of a state model followed by the corrections by the available measurements. It is already seen in Chapter 4, that the sensitivity of the estimation performance strongly depends upon the accuracy of the available state model. Standard state estimation methods (such as a Kalman filter) can produce inaccurate estimates, if the state model is incomplete or inaccurate. However, there are also other factors like the number of available measurements, magnitude of the measurement noise etc. which can create a major impact on the estimation performance. It should be noted that in the previous chapters it is assumed that the state model is perfectly known in most of the cases.

In this chapter, we assume that the state model is unknown and present some methods to estimate the state model. We describe two approaches to estimate the state model. In the first case, it is assumed that the true value/ground truth of the environmental field is completely known. In the second case, it is assumed that the ground truth of the field is unknown but some prior information regarding the state model is available. Simulations are presented for both synthetic data and real data (gauge adjusted radar rainfall data) scenarios.

The outline of the chapter is as follows. A brief survey of similar research works along with the main topics of this chapter is presented in Section 6.1. In Section 6.2, the measurement model and the main problem statement are illustrated. The estimation of the state model incorporating the knowledge regarding the true

value of the field is described in Section 6.3. In the next section, Section 6.4 it is assumed that the true value of the field is not available but some prior information regarding the state model is available. Both Sections 6.3 and 6.4 are accompanied by simulation results. The chapter is concluded in Section 6.5.

6.1 Prior art and contributions

The estimation of the state model of a dynamic process is similar to a system identification problem [36]. In case of environmental field estimation there are several non-Bayesian and Bayesian methods to estimate or approximate the model parameters [7]. Spatio-temporal variability of an environmental field can be modelled by a time-varying covariance function which can be approximated by a Gaussian smoothing kernel [33]. The approach of using a kernel representation to model the spatio-temporal evolution of an environmental process can also be applied to non-Gaussian fields [35]. In [32], a parametric Gaussian dispersal kernel is used for short-term prediction of the rainfall field. The parameters of this kernel can be estimated using a Bayesian or non-Bayesian method [7], [32].

In this chapter, we describe two methods to estimate the underlying dynamics of an environmental field. In the first case, we estimate the dynamics incorporating the fact that the true field intensities are known. In the next case, it is assumed that the true field estimates are unknown but we consider that we have some prior information regarding the dynamics.

The main contributions of the chapter are listed below.

- A generalized dynamic model estimation problem is formulated as an underdetermined system of linear equations. The aforementioned system is solved as a sparsity-cognizant linear regression problem. It is considered that the parameters related to the state transition matrix can be represented as a sparse vector using an orthonormal sparsifying basis.

- Simulations are carried out using both synthetic and real data. The environmental field is estimated using a Kalman filter, where the estimated state model is used for prediction. The estimation performance is compared with the true value of the field.

6.2 Measurement model and problem statement

We consider a spatially continuous yet temporally discrete environmental field represented by $u_t(\mathbf{x})$, where $\mathbf{x} \in \mathbb{R}^2$ is the location and t is the time index similar to Chapter 4. We assume that the entire service area of interest is uniformly discretized into N square pixels and the field within any pixel is constant everywhere. The overall field in the service area at any t is characterized by an N-dimensional unknown parameter vector $\mathbf{u}_t \in \mathbb{R}^N$. Following the same notations of Chapter 4, the elements of $\mathbf{u}_t$ are given by $[\mathbf{u}_t]_j = u_{j,t} = u_t(\mathbf{x}_j)$, where $\mathbf{x}_j = [x_j, y_j]^T$ is the centroid of the j-th pixel of the service area, where $j = 1, \ldots, N$. The discretized service area along with the pixel centroids are shown in Fig. 6.1. Note that, we follow a row-wise vectorization of the field magnitudes of the N pixels in the field vector $\mathbf{u}_t$.

6.2.1 Measurement model

We consider a linear underdetermined measurement model

$$\mathbf{y}_t = \mathbf{\Phi}_t \mathbf{u}_t + \mathbf{e}_t, \qquad t = 1, \ldots, T, \tag{6.1}$$

where the vector $\mathbf{y}_t \in \mathbb{R}^{M_t}$ collects the M_t spatial measurements at time t. It should be noted that, the elements of the generalized measurement matrix $\mathbf{\Phi}_t \in \mathbb{R}^{M_t \times N}$, ($M_t < N$) of (6.1) can be designed based on the sensing modality. The observations at time t are corrupted by noise incurred by the measurement process or due to the imperfections in the measuring equipment. At any t, due to the uncertainty regarding the knowledge of this measurement noise, we model it as a Gaussian random process characterized by $\mathbf{e}_t \sim \mathcal{N}(\mathbf{0}_{M_t}, \mathbf{R}_t)$, where $\mathbf{R}_t$ is an accurately invertible noise covariance matrix. It is also assumed that $\mathbf{e}_t$ is uncorrelated with $\mathbf{u}_t$.

6.2.2 State model

The dynamics of the environmental field can be represented by the linear state model

$$\mathbf{u}_t = \mathbf{H}_t \mathbf{u}_{t-1} + \mathbf{q}_t, \qquad t = 1, \ldots, T, \tag{6.2}$$

where $\mathbf{H}_t \in \mathbb{R}^{N \times N}$ is the state transition matrix or the propagator matrix that models the spatio-temporal evolution of the field from the $(t-1)$-th snapshot to the t-th snapshot. The vector $\mathbf{q}_t \in \mathbb{R}^N$ models the spatially colored yet temporally white

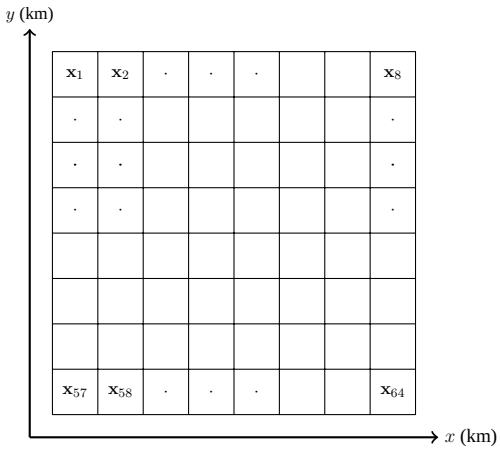

Figure 6.1: Discretized service area with $N = 64$ pixels.

process noise characterized by $\mathbf{q}_t \sim \mathcal{N}(\mathbf{0}, \mathbf{Q})$, which is assumed to be uncorrelated with $\mathbf{u}_t$ as well as $\mathbf{e}_t$.

6.2.3 Problem statement

It is assumed that the elements of the state transition matrix $\mathbf{H}_t$ are unknown. The estimation of the elements of the state transition matrices $\mathbf{H}_t$ for $t = 1, \ldots, T$ snapshots can be viewed as a linear system identification problem [36]. We estimate $\mathbf{H}_t$ for the following two scenarios.

- In the first case, it is assumed that the set of model inputs, i.e., the true field values $\{\mathbf{u}_t\}_{t=1}^T$, first and second order statistics of the measurement and process noise, i.e., $\{\mathbf{q}_t, \mathbf{e}_t\}_{t=1}^T$, the outputs, i.e., the measurements $\{\mathbf{y}_t\}_{t=1}^T$, and the measurement matrices $\{\mathbf{\Phi}_t\}_{t=1}^T$ are all known. The overall model can be compactly represented as in Fig. 6.2. For this scenario, the only unknown is $\{\mathbf{H}_t\}_{t=1}^T$.

- In the next case, we assume that the model inputs $\{\mathbf{u}_t\}_{t=1}^T$ are unknown. But we assume that the first and second order statistics of the measurement noise $\{\mathbf{e}_t\}_{t=1}^T$ are known. We also assume some prior information regarding the structure of the state transition matrix $\mathbf{H}_t$. This approach is similar to the "gray box modelling" in system identification problems [36].

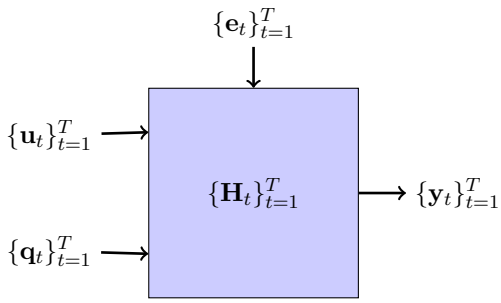

Figure 6.2: Overall system model with inputs and outputs.

6.3 Estimation of $\mathbf{H}_t$ using the known true value

In the first case, it is assumed that the true field values $\{\mathbf{u}_t\}_{t=0}^T$ are known. The state transition matrices, i.e., $\{\mathbf{H}_t\}_{t=1}^T$ are unknown. One simplification of the system model $\mathbf{u}_t = \mathbf{H}_t\mathbf{u}_{t-1} + \mathbf{q}_t$ could be a time invariant state transition matrix, i.e, $\mathbf{H}_t = \mathbf{H}$ for $t = 1, \ldots, T$. Based on this assumption, a linear model can be constructed, which can be used to estimate the elements of $\mathbf{H}$. This is given as

$$\tilde{\mathbf{u}} = \mathbf{X}\mathrm{vec}(\mathbf{H}) + \tilde{\mathbf{q}}, \tag{6.3}$$

where $\tilde{\mathbf{u}} = [\mathbf{u}_1^T, \ldots, \mathbf{u}_T^T]^T \in \mathbb{R}^{NT}$, $\tilde{\mathbf{q}} = [\mathbf{q}_1^T, \ldots, \mathbf{q}_T^T]^T \in \mathbb{R}^{NT}$, and the overall measurement matrix is given by

$$\mathbf{X} = \begin{bmatrix} \mathbf{u}_0^T \otimes \mathbf{I}_N \\ \mathbf{u}_1^T \otimes \mathbf{I}_N \\ \vdots \\ \mathbf{u}_{T-1}^T \otimes \mathbf{I}_N \end{bmatrix}, \tag{6.4}$$

where the dimension of $\mathbf{X}$ is given by $NT \times N^2$. When we have sufficient snapshots, i.e., $NT \geq N^2$, and $\mathbf{X}$ is well-conditioned, a simple least squares estimate $\mathbf{X}^\dagger\tilde{\mathbf{u}}$ can give us the maximum likelihood solution in case of Gaussian process noise.

In many practical environmental monitoring scenarios however we have $NT \ll N^2$, which makes (6.3) an underdetermined noisy system of linear equations, which has an infinite number of solutions for the elements of $\mathbf{H}$. So, a suitable regularization is required in order to achieve a stable solution for the underdetermined system. Here, we use a regularization exploiting the sparsity of the elements of $\mathbf{H}$ when represented in a sparsifying basis.

Let us consider the unknown as $\mathrm{vec}(\mathbf{H}) = \mathbf{h} \in \mathbb{R}^{N^2}$. Let us also consider a sparse representation of $\mathbf{h}$ as $\mathbf{z}$, where $\mathbf{z} = \mathbf{\Psi}^{-1}\mathbf{h}$. Here, $\mathbf{\Psi}$ is an orthonormal dictionary (such as a DCT basis as mentioned in Chapter 4). Exploiting the fact that $\mathbf{\Psi}^{-1}\mathbf{h}$ has a sparse representation a sparsity regularized least squares solution for the elements of $\mathbf{H}$ can be obtained as

$$\hat{\mathbf{h}} = \arg\min_{\mathbf{h}} \|\tilde{\mathbf{u}} - \mathbf{X}\mathbf{h}\|_2^2 + \lambda\|\mathbf{\Psi}^{-1}\mathbf{h}\|_1, \tag{6.5}$$

where λ is a tuning parameter. After solving the optimization problem (6.5) the time-invariant state transition matrix is given by $\hat{\mathbf{H}} = \mathrm{vec}^{-1}(\hat{\mathbf{h}})$, where the $\mathrm{vec}^{-1}()$ operator reshapes the $N^2 \times 1$ vector $\hat{\mathbf{h}}$ to an $N \times N$ matrix $\hat{\mathbf{H}}$.

6.3.1 Simulation results

We perform some numerical experiments with synthetic data for the first scenario of the problem statement mentioned in Section 6.2.3. It is assumed that the number of pixels are $N = 36$ and the number of snapshots of interest are $T = 8$. The set of true values which is $\mathbf{u}_0$ and $\{\mathbf{u}_t\}_{t=1}^{T=8}$ are shown in Fig. 6.3 and Fig. 6.4, respectively. The true values are simulated using the similar method mentioned in Section 5.7 of Chapter 5. In this case, the state transition matrix is kept fixed for all the snapshots.

In order to estimate the elements of $\mathbf{H}_t = \mathbf{H}$, first we construct the matrix $\mathbf{X}$ from 6.4 using the knowledge of the true field values. The optimization problem (6.5) is solved and the estimates of the elements of $\mathbf{H}$, i.e., $\hat{\mathbf{h}}$ are estimated. Here, we consider $\mathbf{\Psi}$ to be a DCT matrix and for the sparse representation and we take $\lambda = 2$. The software CVX [52] (parser CVX, solver SeDuMi [53]) is used to solve the convex optimization problem (6.5).

The $M_t = M$ measurements in every snapshot are computed using (6.1), where the $M \times N$ measurement matrix $\mathbf{\Phi}_t = \mathbf{\Phi}$ is randomly generated. The structure of $\mathbf{\Phi}$ is the same as mentioned in Section 5.2, i.e, it is constructed by randomly selecting M rows of the identity matrix $\mathbf{I}_N$. The number of measurements are $M = 33$. The measurement noise is characterized as $\mathbf{e}_t \sim \mathcal{N}(\mathbf{0}_M, 10^{-4}\mathbf{I}_M)$. Finally, a simple Kalman filter is used to estimate the states $\{\hat{\mathbf{u}}_t\}_{t=1}^{8}$. The pixel-wise comparison of the estimates and the true value is presented in Fig. 6.5.

6.4 Estimation of $\mathbf{H}_t$ using prior information

The problem formulation mentioned in Section 6.3 has the following bottlenecks.

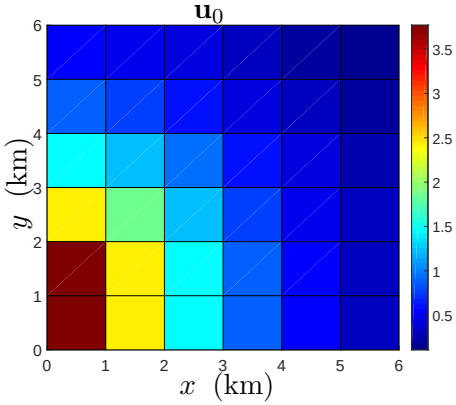

Figure 6.3: Field distribution at $t = 0$.

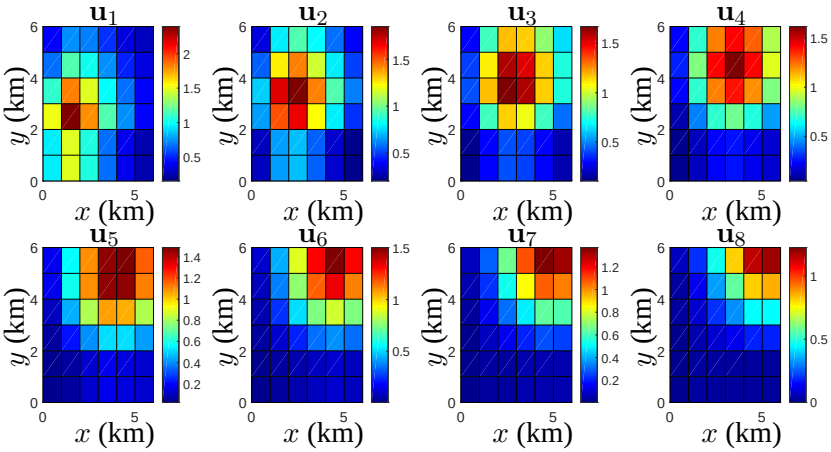

Figure 6.4: Spatio-temporal evolution of $\mathbf{u}_t$ in a 6×6 square km area; Spatial resolution: 1×1 square km.

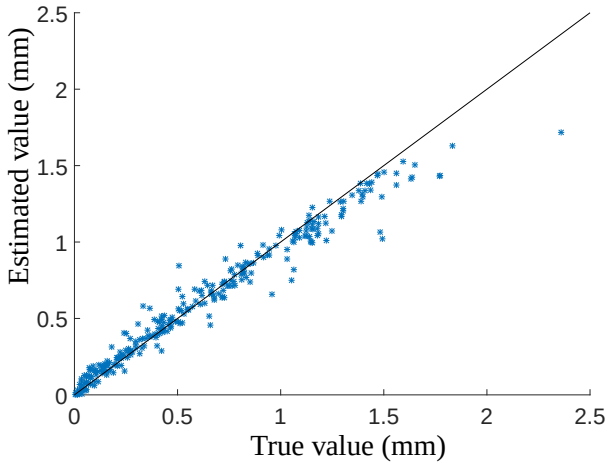

Figure 6.5: Estimation comparsion for $N = 36$ pixels for $T = 8$ snapshots.

- It is assumed that the true values, i.e., $\{\mathbf{u}_t\}_{t=1}^{T}$ are all known. But in many practical scenarios the true field values are difficult to obtain.
- For a high resolution field estimate, the number of pixels, i.e., N (Fig. 6.1) can be quite high and in that case, the dimension of the unknown $\mathbf{h}$ is extremely high (N^2). In this case, the system of linear equations (6.3) will become highly underdetermined.
- For a practical environmental field monitoring application, the assumption that the state transition matrix is time-invariant ($\mathbf{H}_t = \mathbf{H}$) may not be realistic.

In this section, we propose a method, where we assume some structure in $\mathbf{H}_t$ and estimate the elements of $\mathbf{H}_t$ on every t. The estimated $\mathbf{H}_t$s are then again used to estimate the states using a simple Kalman filter.

6.4.1 Modelling assumption of $\mathbf{H}_t$

Modelling the state model using some prior information regarding the structure of the state transition matrix is similar to the gray box modelling in system identification [36]. Prior information regarding $\mathbf{H}_t$ could be the rank of $\mathbf{H}_t$ or some specific structure of $\mathbf{H}_t$ like Toeplitz or Hankel [107].

One well-known approach to model the state transition matrix, specifically for environmental fields, is to discretize an integro-difference equation (IDE) based

dynamic model [7]. In this way, a kernel models the spatio-temporal evolution of the field. The kernel parameters can be obtained using a non-Bayesian or Bayesian framework. As mentioned in Chapter 4, a Gaussian dispersal kernel can for instance be used to model the dynamics of the rainfall field. It should be noted that to incorporate complex phenomena like anisotropic diffusion and advection [32] the state transition matrix should be assymetric, i.e., $[\mathbf{H}_t]_{ij} \neq [\mathbf{H}_t]_{ji}$. The structure of a Gaussian dispersal kernel is given as

$$[\mathbf{H}_t]_{ij} = \nu_t \exp[-(\mathbf{x}_i - \mathbf{x}_j - \mathbf{a}_t)^T \mathbf{D}_t^{-1} (\mathbf{x}_i - \mathbf{x}_j - \mathbf{a}_t)], \tag{6.6}$$

where the translation parameter $\mathbf{a}_t \in \mathbb{R}^2$ and the dilation parameter $\mathbf{D}_t \in \mathbb{S}^2_{++}$ can be used to model the advection and the diffusion of the field, respectively. The scalar $\nu_t \in (0, 1]$ is used as a scaling parameter to avoid the explosive growth of the field [35], [32]. Note that the parameters $\mathbf{a}_t$ and $\mathbf{D}_t$ can vary spatially (for every element of $\mathbf{H}_t$), as well as temporally. For spatially varying $\mathbf{a}_t$ and $\mathbf{D}_t$ over N pixels, at any t, the total number of parameters that characterizes $\mathbf{H}_t$ is given by $6N^2 + 1$, as the total number of elements in $\mathbf{a}_t$ and $\mathbf{D}_t$ are 6 and one scalar ν_t. One simple abstraction of (6.6) could be $\mathbf{D}_t = \mathbf{I}_2$ (for all t and the elements of $\mathbf{H}_t$) and $\mathbf{a}_t = \mathbf{0}_2$. This can model the dynamics with less parameters but it is symmetric in nature and may not capture all the space-time effects [32]. In order to introduce asymmetry, in the state transition matrix we propose a decomposition of the state transition matrix as a multiplication of a symmetric matrix and a diagonal matrix. This is given as

$$\mathbf{H}_t = \mathbf{B}\mathrm{diag}(\mathbf{h}_t), \tag{6.7}$$

where $\mathbf{h}_t \in \mathbb{R}^N$ models an asymmetric $\mathbf{H}_t$. The motivation behind the aforementioned decomposition is to model an asymmetric and time-varying $\mathbf{H}_t$ whose parameters (i.e., $\mathbf{h}_t$ in this case, assuming $\mathbf{B}$ is fixed on every t) can be estimated by solving a linear inverse problem on every t (discussed in the following sub-section). Also, the structure of $\mathbf{B}$ is chosen in such a way that it incorporates an isotropic diffusion. We compute the elements of the symmetric matrix $\mathbf{B}$ by a Gaussian kernel, i.e., (6.6), with $\mathbf{a}_t = \mathbf{0}$ and $\mathbf{D}_t = \mathbf{I}_2$ given by

$$[\mathbf{B}]_{ij} = \nu \exp[-\|\mathbf{x}_i - \mathbf{x}_j\|_2^2]. \tag{6.8}$$

Note that $\mathbf{B}$ can be used as a valid state-transition matrix but being symmetric it has some drawbacks as mentioned in [32]. The next step is to estimate $\mathbf{h}_t$ for every t.

6.4.2 Estimation of $\mathbf{H}_t$

Let us assume that an estimate of $\hat{\mathbf{u}}_{t-1}$ is available at t. Then the measurement equation (6.1) can be written as

$$\begin{aligned}\mathbf{y}_t &= \mathbf{\Phi}_t(\mathbf{H}_t\hat{\mathbf{u}}_{t-1} + \mathbf{q}_t) + \mathbf{e}_t \\ &= \mathbf{\Phi}_t\mathbf{B}\mathrm{diag}(\mathbf{h}_t)\hat{\mathbf{u}}_{t-1} + \breve{\mathbf{e}}_t \\ &= \mathbf{\Phi}_t\mathbf{B}\mathrm{diag}(\hat{\mathbf{u}}_{t-1})\mathbf{h}_t + \breve{\mathbf{e}}_t \\ &= \mathbf{A}_t\mathbf{h}_t + \breve{\mathbf{e}}_t, \end{aligned} \tag{6.9}$$

where the measurement noise vector $\breve{\mathbf{e}}_t$ in the modified measurement equation (6.9) is characterized as $\breve{\mathbf{e}}_t = \mathbf{\Phi}_t\mathbf{q}_t + \mathbf{e}_t$ with $\breve{\mathbf{e}}_t \sim \mathcal{N}(\mathbf{0}, \breve{\mathbf{R}}_t)$, where $\breve{\mathbf{R}}_t = \mathbf{\Phi}_t\mathbf{Q}_t\mathbf{\Phi}_t^T + \mathbf{R}_t$. Note that at any time t the matrix $\mathbf{A}_t = \mathbf{\Phi}_t\mathbf{B}\mathrm{diag}(\hat{\mathbf{u}}_{t-1}) \in \mathbb{R}^{M_t \times N}$ is perfectly known. It should also be noted that the dimension of the system in (6.9), i.e., $M_t \times N$ is much less underdetermined than (6.3), i.e., $M_t \times N^2$. In order to achieve a stable solution of the underdetermined system of linear equations (6.9) for $\mathbf{h}_t$, we impose some regularizations on $\mathbf{h}_t$. They are as follows.

1. The first constraint is a non-negativity constraint on $\mathbf{h}_t$, i.e., $\mathbf{h}_t \geq 0$. The motivation behind using this constraint is to model the elements of $\mathbf{H}_t = \mathbf{B}\mathrm{diag}(\mathbf{h}_t)$ as non-negative, which is one of the properties of $\mathbf{H}_t$ using a Gaussian kernel based modelling.

2. We use a regularization on the elements of $\mathbf{h}_t$ assuming that $\mathbf{h}_t$ can be sparsely represented using an orthonormal basis $\mathbf{\Psi}$. We exploit the fact that the transformed vector $\mathbf{\Psi}^{-1}\mathbf{h}_t$ has a sparse representation.

To utlize this sparse representation, we use an ℓ_1 regularization on $\mathbf{\Psi}^{-1}\mathbf{h}_t$, while solving the underdetermined system (6.9). We estimate $\mathbf{h}_t$ on every t using the following ℓ_1 regularized non-negativity constrained weighted least squares (WLS) problem:

$$\hat{\mathbf{h}}_t = \underset{\mathbf{h}_t \geq \mathbf{0}_N}{\arg\min} \|\mathbf{y}_t - \mathbf{A}_t\mathbf{h}_t\|^2_{\breve{\mathbf{R}}_t^{-1}} + \gamma\|\mathbf{\Psi}^{-1}\mathbf{h}_t\|_1, \tag{6.10}$$

$$\hat{\mathbf{H}}_t = \mathbf{B}\mathrm{diag}(\hat{\mathbf{h}}_t). \tag{6.11}$$

Here, γ is a tuning parameter for the sparsity promoting regularization in (6.10). After the estimation of $\mathbf{h}_t$, the state transition matrix can be estimated using the relation of (6.7). To achieve asymptotic / bounded input bounded output (BIBO)

stability, we ensure that the maximum eigen value of $\hat{\mathbf{H}}_t$, i.e., $\lambda_{\max}[\hat{\mathbf{H}}_t]$ must be less than 1. This can be achieved by selecting a proper scaling factor $\nu \in (0, 1]$. In this case, first it is checked that if $\lambda_{\max}[\hat{\mathbf{H}}_t]$ is already less than 1. If that is the case, then we simply choose $\nu = 1$. Otherwise, we manually select a $\nu \in (0, 1)$ in order to avoid the explosive growth of the system.

Algorithm 4 Dynamics estimation followed by rainfall monitoring

Initialize $t = 0$, $\hat{\mathbf{u}}_{0|0} = \mathbf{u}_0$, $\mathbf{M}_{0|0}$
for $t = 1, \ldots, T$
  given $\mathbf{\Phi}_t = \mathbf{\Phi}$, $\mathbf{\Psi}$, $\mathbf{y}_t$, $\sigma_e^2 \mathbf{I}_{M_t}$, $\mathbf{Q}_t = \mathbf{Q}$, γ, ν.
Dynamics estimation:
$\hat{\mathbf{z}}_t = \arg\min_{\mathbf{h}_t \geq \mathbf{0}_N} [\|\mathbf{y}_t - \mathbf{A}_t \mathbf{h}_t\|^2_{\breve{\mathbf{R}}_t^{-1}} + \gamma \|\mathbf{\Psi}^{-1} \mathbf{h}_t\|_1]$,
$\hat{\mathbf{H}}_t = \mathbf{B}\mathrm{diag}(\mathbf{h}_t)$.
Select ν; $\hat{\mathbf{H}}_t = \nu \hat{\mathbf{H}}_t$.
  Predict:
$\hat{\mathbf{u}}_{t|t-1} = \hat{\mathbf{H}}_t \hat{\mathbf{u}}_{t-1|t-1}, \quad \mathbf{M}_{t|t-1} = \hat{\mathbf{H}}_t \mathbf{M}_{t-1|t-1} \hat{\mathbf{H}}_t^T + \mathbf{Q}$
  Correct:
$\mathbf{G}_t = \mathbf{M}_{t|t-1} \mathbf{\Phi}^T (\mathbf{\Phi} \mathbf{M}_{t|t-1} \mathbf{\Phi}^T + \mathbf{R}_t)^{-1}, \quad \hat{\mathbf{u}}_t = [\hat{\mathbf{u}}_{t|t-1} + \mathbf{G}_t (\mathbf{y}_t - \mathbf{\Phi} \hat{\mathbf{u}}_{t|t-1})]_+$
  Covariance update:
$\mathbf{M}_{t|t} = (\mathbf{I}_N - \mathbf{G}_t \mathbf{\Phi}) \mathbf{M}_{t|t-1} = (\mathbf{M}_{t|t-1}^{-1} + \mathbf{\Phi}^T \mathbf{R}_t^{-1} \mathbf{\Phi})^{-1}$
end for
end

6.4.3 Dynamics estimation followed by state estimation

In this section, we describe the overall algorithm for the dynamics estimation technique proposed in the previous section followed by field estimation. We use a simple Kalman filter to estimate the states of $\mathbf{u}_t$. In many practical scenarios, the environmental field to be monitored (such as rainfall, concentration of pollutants, humidity) is non-negative. To incorporate this fact, at any t, we set any negative elements of the estimate $\hat{\mathbf{u}}_t$ to 0. We denote the estimate of $\mathbf{u}_t$ at t, using the measurements up to time $t - 1$ and t as $\hat{\mathbf{u}}_{t|t-1}$ and $\hat{\mathbf{u}}_{t|t}$, respectively. The estimation error covariances of the estimates $\hat{\mathbf{u}}_{t|t-1}$ and $\hat{\mathbf{u}}_{t|t}$ are denoted by $\mathbf{M}_{t|t-1}$ and $\mathbf{M}_{t|t}$, respectively. The overall algorithm is presented as Algorithm 4. Here, we comment that the covariance update of the Kalman filter is approximate, as we set the negative elements of the estimate $\hat{\mathbf{u}}_t$ to 0.

6.4.4 Simulation results

In this section, we present some simulation results to exhibit the feasibilty of the proposed algorithm.

Ground truth

The ground truth or the true value of the rainfall intensities is given by 15 minutes guage adjusted radar rainfall depths. We show a total of 9 snapshots of rainfall maps over an area of approximately 625 square kilometer. The spatial resolution is 1×1 square kilometer. The gauge adjusted radar rainfall depths of 9 snapshots at 625 pixels are shown in Figs. 6.6 and 6.7, respectively (data courtesy : KNMI).

Measurements

We estimate the states $T = 8$ snapshots of 15 minute rainfall intensities using the measurements of 151 microwave links in an area of 25×25 square km. The locations of the links and the $N = 625$ pixels are shown in Fig. 6.8 (data courtesy: KNMI). It is assumed that the links are all operated at 35 Ghz and the temperature is 20° C. Based on this, we take the power law coefficients as $a = 0.235$ and $b = 1.009 \approx 1$(see Table II of [79]). The measurements at $T = 8$ snapshots are computed using the measurement model of (6.1), where the measurement matrix is computed as $[\mathbf{\Phi}]_{ij} = al_{ij}$, and the length of the link segments are computed using the location of the links and the pixels as shown in Fig. 6.8. The measurement noise variance is assumed to be $\sigma_e^2 = 10^{-4}$.

Results

Using the above measurement setup, we estimate the states of $\mathbf{u}_t$ for $t = 1, \ldots, 8$ using Algorithm 4. As mentioned earlier, we initialize the algorithm with $\hat{\mathbf{u}}_{0|0} = \zeta \mathbf{1}_N$, where $\zeta = \frac{1}{N}\sum_{k=1}^{N}[\mathbf{u}_0]_k$, i.e, the sample mean of the true value at $t = 0$. We assume that the process noise has the same structure as mentioned in Section 4.7.1. The motivation behind assuming a process noise having a covariance matrix computed using an exponential function is to introduce a smooth temporal transition. The error covariance matrix is initialized as $\mathbf{M}_{0|0} = 0.001\mathbf{I}_N$. The regularization parameter is fixed as $\gamma = 2$.

The estimated rainfall maps for all the 8 snapshots, i.e, $\hat{\mathbf{u}}_t$ for $t = 1, \ldots, 8$ are shown in Fig. 6.9. The pixel-wise comparison of the estimates for $T = 8$ snapshots for $N = 625$ pixels is also shown in Fig. 6.10.

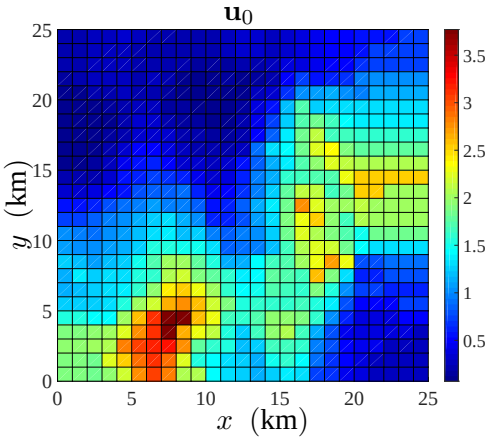

Figure 6.6: Initial state $\mathbf{u}_0$ at $t = 0$, which is used to initialize Algorithm 4, i.e., $\hat{\mathbf{u}}_{0|0} = \mathbf{u}_0$.

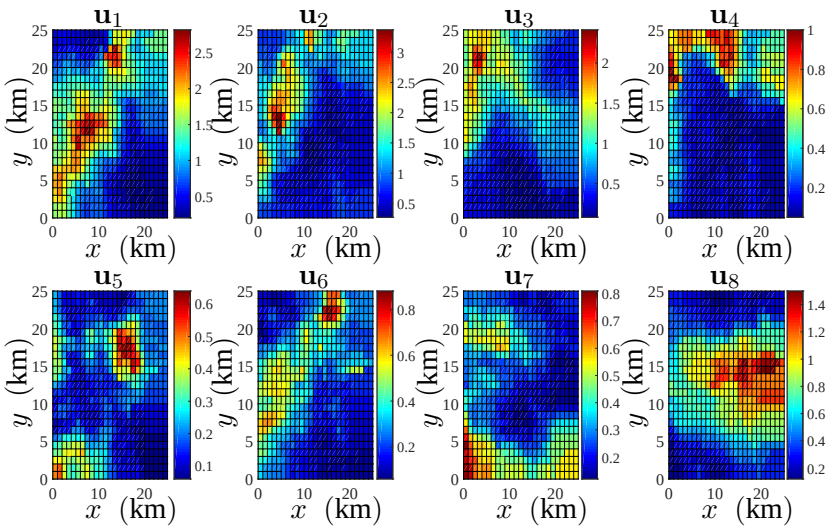

Figure 6.7: True spatio-temporal evolution of the rainfall field (mm).

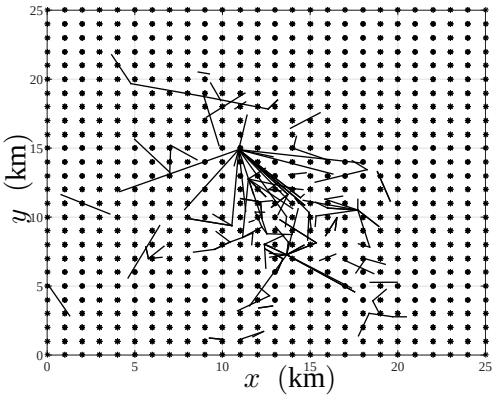

Figure 6.8: Locations of the M microwave links from where the measurements are collected.

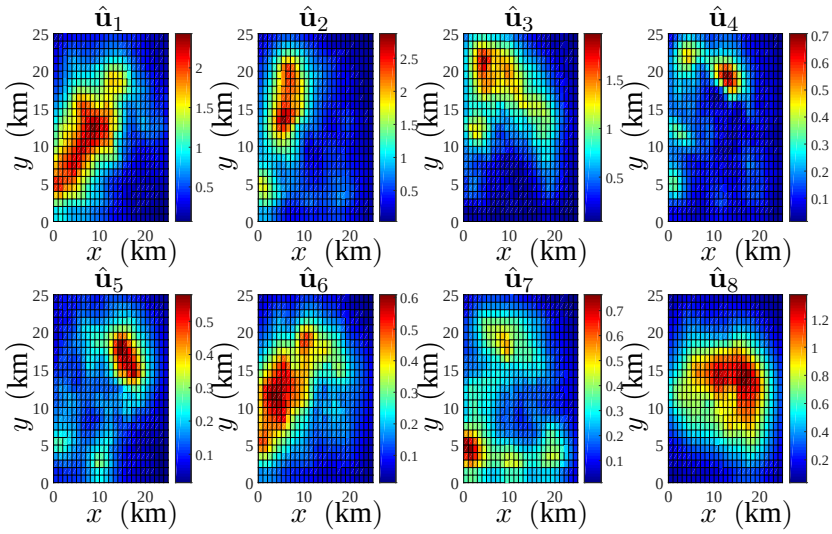

Figure 6.9: Estimated spatio-temporal evolution of the rainfall field (mm).

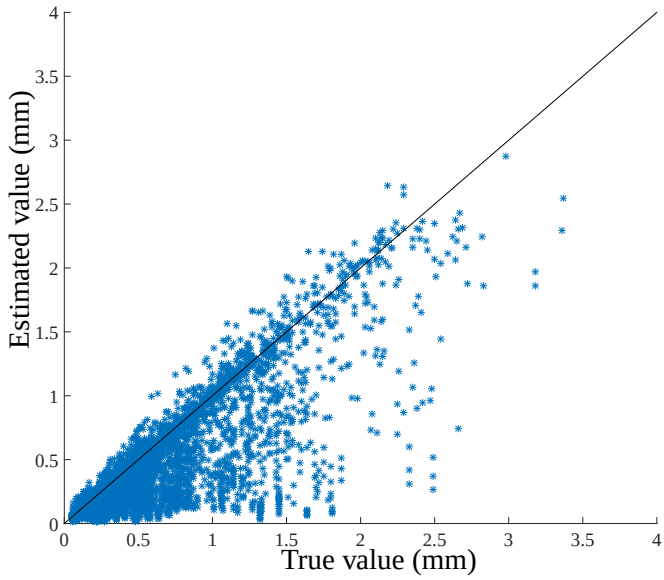

Figure 6.10: Estimation comparsion for $N = 625$ pixels for $T = 8$ snapshots.

6.5 Conclusion

We have presented two different methods to estimate the spatio-temporal evolution of an environmental field. In the first method, it is assumed that the true values of the field over different snapshots are known. In the second method, the true field values are assumed to be unknown. In this case, some prior information regarding the structure of the state transition matrix (inspired by physics) is exploited. Finally, a simple Kalman filter is used to estimate the field over every snapshot using the estimated state model along with the measurements. The performance of both the methods are analysed by comparing the estimates with the true values. Simulation results show that dynamics of a physical field can be estimated from the measurements with some prior information regarding the nature of the spatio-temporal evolution. However, a more accurate knowledge regarding the field propagation over space and/or time will improve the estimation performance.

Chapter 7

Conclusion and Future Research Directions

In this chapter we conclude the thesis. We also mention related contributions and future research directions.

7.1 Conclusions

In this thesis, we have developed a spatio-temporal environment monitoring framework that encompasses sensor management as well as dynamic monitoring of the environmental field. We have presented several methods to efficiently utlize the prior information regarding the physical properties of the environmental field both for the deployment of sensors as well as for monitoring the field.

We have discussed the representations of the linear/non-linear measurement models for dynamic environment monitoring. The different statistical modelling approaches of the physical properties of the environmental fields (such as correlation over space and time, dynamics of the field etc.) are also discussed. We have also presented a generalized environmental field estimation framework that incorporates sparse-sensing, dynamic field reconstruction exploiting prior information, and estimation of the physical properties of the field (if unknown/inaccurate).

We have developed a unified framework for spatio-temporal sensor management, when the environmental field is spatio-temporally stationary as well as non-stationary. A generalized expression for the performance metric (for stationary as well as non-stationary fields) is derived, which can efficiently utilize the prior infor-

mation regarding the environmental field (such as a highly correlated field) in order to deploy the sensors over space and time. It is seen that less sensing locations are selected if the spatio-temporal correlation is strong. From a dynamic sensor placement perspective, the sensor deployment strongly depends upon the nature of the evolution of the field.

We have presented a practical example of environmental field estimation, i.e., dynamic rainfall monitoring using the attenuation measurements of commercial microwave links. We have described how the physical information regarding the rainfall field (such as spatial sparsity and non-negativity) can be exploited in dynamic rainfall monitoring using a traditional Kalman setup. We have also presented cases, where the rainfall dynamics are inaccurately known or unknown. We have exhibited the performance improvement of a sparsity-aware method over a simple extended Kalman filter (EKF).

We have extended the spatio-temporal sensor management method for a more general class of environmental fields, leading to a combination of stationary and non-stationary components. We have described the spatio-temporal sensor management for a kriged Kalman filter (KKF) estimator. We used the selected sensing locations for the estimation of the field using KKF. The combined effect of spatial phenomena as well as field dynamics on the sensor placement are presented.

We have also presented some methods to estimate the state model responsible for the evolution of an environmental field. We have described how the state model, i.e., the elements of the state transition matrix can be estimated exploiting prior information regarding the nature of the evolution of the field. It is also seen that using a partial prior information regarding the dynamics of the field, the state model can be estimated without the knowledge of the true field intensities.

7.2 Future research directions

In this thesis, we have presented signal processing methods for opportunistic sensor placement as well as dynamic monitoring of the spatio-temporal evolution of an environment field. Some future research directions are presented below.

1. First of all, we have mainly focused on model-driven methods that enforce sparsity in deploying sensors over space/time achieving some desired accuracy. An extension of the proposed method to a fully data-driven approach could be a future direction.

2. It is observed that, MSE-optimal sensor deployment can be designed to be

resource-efficient availing the prior physical information of spatio-temporal correlation and dynamics. But as described in Chapter 4, environmental fields exhibit sparsity (either naturally or using a representation basis). It could be interesting to develop an optimal measurement matrix, which is jointly MSE-optimal and guarantees the criteria for a stable solution [89] in a sparse reconstruction framework.

3. In the dynamic rainfall monitoring scenario (Chapter 4), it is considered that the state model is linear. Furthermore, we only consider spatial sparsity. Assuming a non-linear dynamic model and exploiting temporal sparsity could be possible future extensions of this work. With both nonlinear state and measurement models, studying the performance of an unscented Kalman filter (UKF), particle filtering based algorithms, or other heuristic approaches could be possible future research directions.

4. A direct application of the proposed sensor management method could be the real-time selection of the most informative attenuation measurements, i.e., the links (in order to reduce the processing load and computational complexity).

5. Extensions of the proposed sparsity-leveraging sensor placement, field estimation and dynamics estimation techniques for highly correlated non-Gaussian measurements open different modelling challenges.

Bibliography

[1] H. Messer, A. Zinevich, and P. Alpert, "Environmental monitoring by wireless communication networks," *Science*, vol. 312, no. 5774, pp. 713–713, 2006.

[2] I. F. Akyildiz, W. Su, Y. Sankarasubramaniam, and E. Cayirci, "Wireless sensor networks: a survey," *Computer networks*, vol. 38, no. 4, pp. 393–422, March 2002.

[3] C. Y. Chong and S. P. Kumar, "Sensor networks: evolution, opportunities, and challenges," *Proceedings of the IEEE*, vol. 91, no. 8, pp. 1247–1256, August 2003.

[4] J. K. Hart and K. Martinez, "Environmental sensor networks: A revolution in the earth system science?" *Earth-Science Reviews*, vol. 78, no. 3, pp. 177–191, October 2006.

[5] O. Sendik and H. Messer, "A new approach to precipitation monitoring: A critical survey of existing technologies and challenges," *IEEE Signal Processing Magazine*, vol. 32, no. 3, pp. 110–122, 2015.

[6] "Sensing Heterogeneous Information Network Environment (SHINE)," http://shine.tudelft.nl/home/, 2012.

[7] N. Cressie and K. Wikle, *Statistics for spatio-temporal data*. John Wiley & Sons, 2011.

[8] G. Barrenetxea, F. Ingelrest, Y. M. Lu, and M. Vetterli, "Assessing the challenges of environmental signal processing through the sensorscope project,"

in *IEEE International Conference on Acoustics, Speech and Signal Processing (ICASSP)*, Las Vegas, March 2008, pp. 5149–5152.

[9] F. Ingelrest, G. Barrenetxea, G. Schaefer, M. Vetterli, O. Couach, and M. Parlange, "Sensorscope: Application-specific sensor network for environmental monitoring," *ACM Trans. Sen. Netw.*, vol. 6, no. 2, pp. 17:1–17:32, Mar. 2010. [Online]. Available: http://doi.acm.org/10.1145/1689239.1689247

[10] M. Martinez-Camara, I. Dokmanić, J. Ranieri, R. Scheibler, M. Vetterli, and A. Stohl, "The fukushima inverse problem," in *IEEE International Conference on Acoustics, Speech and Signal Processing (ICASSP)*. Vancouver, Canada: IEEE, May 2013, pp. 4330–4334.

[11] M. Martinez-Camara, M. Vetterli, and A. Stohl, "Outlier removal for improved source estimation in atmospheric inverse problems," in *IEEE International Conference on Acoustics, Speech and Signal Processing (ICASSP)*. Florence, Italy: IEEE, May 2014, pp. 6820–6824.

[12] O. Goldshtein, H. Messer, and A. Zinevich, "Rain rate estimation using measurements from commercial telecommunications links," *IEEE Transactions on Signal Processing*, vol. 57, no. 4, pp. 1616–1625, April 2009.

[13] A. Zinevich, H. Messer, and P. Alpert, "Frontal rainfall observation by a commercial microwave communication network," *Journal of Applied Meteorology and Climatology*, vol. 48, no. 7, pp. 1317–1334, 2009.

[14] A. Nehorai, B. Porat, and E. Paldi, "Detection and localization of vapor-emitting sources," *IEEE Transactions on Signal Processing*, vol. 43, no. 1, pp. 243–253, January 1995.

[15] J. Murray-Bruce and P. L. Dragotti, "Estimating localized sources of diffusion fields using spatiotemporal sensor measurements," *IEEE Transactions on Signal Processing*, vol. 63, no. 12, pp. 3018–3031, June 2015.

[16] T. Tchrakian and S. Zhuk, "A fast distributed data-assimilation algorithm for divergence-free advection," *arXiv preprint arXiv:1707.07316*, 2017.

[17] R. Marchant and F. Ramos, "Bayesian optimisation for intelligent environmental monitoring," in *International Conference on Intelligent Robots and Systems*. Vilamoura, Portugal: IEEE, October 2012, pp. 2242–2249.

[18] N. Cressie, “The origins of kriging,” *Mathematical geology*, vol. 22, no. 3, pp. 239–252, 1990.

[19] C. K. Wikle and N. Cressie, “A dimension-reduced approach to space-time Kalman filtering,” *Biometrika*, vol. 86, no. 4, pp. 815–829, 1999.

[20] K. V. Sahu, S. K.and Mardia, “A bayesian kriged Kalman model for short-term forecasting of air pollution levels,” *Journal of the Royal Statistical Society: Series C (Applied Statistics)*, vol. 54, no. 1, pp. 223–244, 2005.

[21] I. F. Akyildiz, M. C. Vuran, and O. B. Akan, “On exploiting spatial and temporal correlation in wireless sensor networks,” in *Proceedings of WiOpt*, vol. 4, Cambridge, UK, March 2004, pp. 71–80.

[22] S. Yan, C. Wu, W. Dai, M. Ghanem, and Y. Guo, “Environmental monitoring via compressive sensing,” in *Proceedings of the Sixth International Workshop on Knowledge Discovery from Sensor Data*. ACM, 2012, pp. 61–68.

[23] E. Candes and M. Wakin, “An introduction to compressive sampling,” *Signal Processing Magazine, IEEE*, vol. 25, no. 2, pp. 21–30, 2008.

[24] T. van Waterschoot and G. Leus, “Static field estimation using a wireless sensor network based on the finite element method,” in *Proc. Int. Workshop Comput. Adv. Multi-Sensor Adaptive Process. (CAMSAP ’11)*, San Juan, PR, USA, Dec. 2011, pp. 369–372.

[25] V. Roy, S. Gishkori, and G. Leus, “Dynamic rainfall monitoring using microwave links,” *EURASIP Journal on Advances in Signal Processing*, vol. 2016, no. 1, pp. 1–17, December 2016.

[26] A. Jindal and K. Psounis, “Modeling spatially correlated data in sensor networks,” *ACM Transactions on Sensor Networks (TOSN)*, vol. 2, no. 4, pp. 466–499, November 2006.

[27] N. Cressie and H. Huang, “Classes of nonseparable, spatio-temporal stationary covariance functions,” *Journal of the American Statistical Association*, vol. 94, no. 448, pp. 1330–1339, December 1999.

[28] N. Cressie, *Statistics for spatial data*. John Wiley & Sons, 2015.

[29] ——, "Spatial prediction and ordinary kriging," *Mathematical geology*, vol. 20, no. 4, pp. 405–421, 1988.

[30] C. Van de Beek, H. Leijnse, P. Torfs, and R. Uijlenhoet, "Seasonal semi-variance of dutch rainfall at hourly to daily scales," *Advances in Water Resources*, vol. 45, pp. 76–85, September 2012.

[31] P. Goovaerts, "Geostatistical approaches for incorporating elevation into the spatial interpolation of rainfall," *Journal of hydrology*, vol. 228, no. 1, pp. 113–129, February 2000.

[32] F. Sigrist, H. R. Künsch, and W. A. Stahel, "A dynamic nonstationary spatio-temporal model for short term prediction of precipitation," *The Annals of Applied Statistics*, vol. 6, no. 4, pp. 1452–1477, December 2012.

[33] P. E. Brown, G. O. Roberts, K. F. Kåresen, and S. Tonellato, "Blur-generated non-separable space–time models," *Journal of the Royal Statistical Society: Series B (Statistical Methodology)*, vol. 62, no. 4, pp. 847–860, 2000.

[34] M. Kot, M. A. Lewis, and P. van den Driessche, "Dispersal data and the spread of invading organisms," *Ecology*, vol. 77, no. 7, pp. 2027–2042, 1996.

[35] C. K. Wikle, "A kernel-based spectral model for non-gaussian spatio-temporal processes," *Statistical Modelling*, vol. 2, no. 4, pp. 299–314, 2002.

[36] L. Ljung, *Systems identification theory for the user*. Prentice-Hall PTR, Upper saddle river, NJ, 1999.

[37] R. Rubinstein, A. M. Bruckstein, and M. Elad, "Dictionaries for sparse representation modeling," *Proceedings of the IEEE*, vol. 98, no. 6, pp. 1045–1057, 2010.

[38] R. Tibshirani, "Regression shrinkage and selection via the lasso," *Journal of the Royal Statistical Society. Series B (Methodological)*, pp. 267–288, 1996.

[39] L. M. Berliner, "Hierarchical bayesian time series models," in *Maximum entropy and Bayesian methods*. Springer, 1996, pp. 15–22.

[40] S. Liu, A. Vempaty, M. Fardad, E. Masazade, and P. Varshney, "Energy-aware sensor selection in field reconstruction," *IEEE Signal Processing Letters*, vol. 21, no. 12, pp. 1476–1480, December 2014.

[41] S. Chepuri and G. Leus, "Sparsity-promoting sensor selection for non-linear measurement models," *IEEE Transactions on Signal Processing*, vol. 63, no. 3, pp. 684–698, Feb 2015.

[42] E. Masazade, M. Fardad, and P. K. Varshney, "Sparsity-promoting extended Kalman filtering for target tracking in wireless sensor networks," *IEEE Signal Processing Letters*, vol. 19, no. 12, pp. 845–848, 2012.

[43] S. Liu, E. Masazade, M. Fardad, and P. K. Varshney, "Sparsity-aware field estimation via ordinary kriging," in *IEEE International Conference on Acoustics, Speech and Signal Processing (ICASSP)*. IEEE, 2014, pp. 3948–3952.

[44] V. Roy and G. Leus, "Correlation-aware sparsity-enforcing sensor placement for spatio-temporal field estimation," in *Proc. IEEE International Conference on Acoustics, Speech and Signal Processing (ICASSP)*, Brisbane, Australia, April 2015, pp. 340–343.

[45] S. Joshi and S. Boyd, "Sensor selection via convex optimization," *IEEE Transactions on Signal Processing*, vol. 57, no. 2, pp. 451–462, February 2009.

[46] S. Boyd and S. Vandenberghe, *Convex optimization*. Cambridge university press, 2009.

[47] H. Jamali-Rad, A. Simonetto, and G. Leus, "Sparsity-aware sensor selection: centralized and distributed algorithms," *IEEE Signal Processing Letters*, vol. 21, no. 2, pp. 217–220, 2014.

[48] A. Krause, A. Singh, and C. Guestrin, "Near-optimal sensor placements in Gaussian processes: theory, efficient algorithms and empirical studies," *The Journal of Machine Learning Research*, vol. 9, pp. 235–284, 2008.

[49] E. Feron and C. Olivier, "Targets, sensors and infinite-horizon tracking optimality," in *Proceedings of the 29th IEEE Conference on Decision and Control*. IEEE, 1990, pp. 2291–2292.

[50] W. Zhang, M. P. Vitus, J. Hu, A. Abate, and C. J. Tomlin, "On the optimal solutions of the infinite-horizon linear sensor scheduling problem," in *Proceedings of the 49th IEEE Conference on Decision and Control*. IEEE, 2010, pp. 396–401.

[51] S. Liu, M. Fardad, P. K. Varshney, and E. Masazade, "Optimal periodic sensor scheduling in networks of dynamical systems," *IEEE Transactions on Signal Processing*, vol. 62, no. 12, pp. 3055–3068, 2014.

[52] C. Research Inc., "CVX: Matlab Software for Disciplined Convex Programming, version 2.0," http://cvxr.com/cvx, Aug. 2012.

[53] J. F. Sturm, "Using sedumi 1.02, a matlab toolbox for optimization over symmetric cones," *Optimization methods and software*, vol. 11, no. 1-4, pp. 625–653, 1999.

[54] J. Ranieri, A. Chebira, and M. Vetterli, "Near-optimal sensor placement for linear inverse problems," *IEEE Transactions on Signal Processing*, vol. 62, no. 5, pp. 1135–1146, March 2014.

[55] I. Rodriguez-Iturbe, M. Marani, P. D'Odorico, and A. Rinaldo, "On space-time scaling of cumulated rainfall fields," *Water resources research*, vol. 34, no. 12, pp. 3461–3469, December 1998.

[56] E. Candes, M. Wakin, and S. Boyd, "Enhancing sparsity by reweighted ℓ_1 minimization," *Journal of Fourier analysis and applications*, vol. 14, no. 5-6, pp. 877–905, 2008.

[57] S. M. Kay, *Fundamentals of statistical signal processing: estimation theory*. PTR Prentice-Hall, Englewood Cliffs, NJ, 1993.

[58] R. Ababou, A. C. Bagtzoglou, and E. F. Wood, "On the condition number of covariance matrices in kriging, estimation, and simulation of random fields," *Mathematical Geology*, vol. 26, no. 1, pp. 99–133, 1994.

[59] S. P. Chepuri and G. Leus, "Sparsity-promoting adaptive sensor selection for non-linear filtering," in *International Conference on Acoustics, Speech and Signal Processing (ICASSP)*. IEEE, 2014, pp. 5080–5084.

[60] L. Vandenberghe and S. Boyd, "Semidefinite programming," *SIAM review*, vol. 38, no. 1, pp. 49–95, 1996.

[61] A. Nedić and A. Ozdaglar, "Subgradient methods for saddle-point problems," *Journal of optimization theory and applications*, vol. 142, no. 1, pp. 205–228, 2009.

[62] K. B. Petersen and M. S. Pedersen, "The matrix cookbook," *Technical University of Denmark*, vol. 7, p. 15, 2008.

[63] H. Messer, A. Zinevich, and P. Alpert, "Environmental sensor networks using existing wireless communication systems for rainfall and wind velocity measurements," *IEEE Instrumentation & Measurement Magazine*, vol. 15, no. 2, pp. 32–38, 2012.

[64] D. Giuli, A. Toccafondi, G. B. Gentili, and A. Freni, "Tomographic reconstruction of rainfall fields through microwave attenuation measurements," *Journal of Applied Meteorology*, vol. 30, no. 9, pp. 1323–1340, 1991.

[65] D. Giuli, L. Facheris, and S. Tanelli, "Microwave tomographic inversion technique based on stochastic approach for rainfall fields monitoring," *IEEE Transactions on Geoscience and Remote Sensing*, vol. 37, no. 5, pp. 2536–2555, 1999.

[66] A. Zinevich, P. Alpert, and H. Messer, "Estimation of rainfall fields using commercial microwave communication networks of variable density," *Advances in water resources*, vol. 31, no. 11, pp. 1470–1480, April 2008.

[67] A. Overeem, H. Leijnse, and R. Uijlenhoet, "Country-wide rainfall maps from cellular communication networks," *Proceedings of the National Academy of Sciences*, vol. 110, no. 8, pp. 2741–2745, 2013.

[68] Y. Liberman and H. Messer, "Accurate reconstruction of rain field maps from commercial microwave networks using sparse field modeling," in *IEEE International Conference on Acoustics, Speech and Signal Processing (ICASSP)*, Florence, Italy, May 2014, pp. 6786–6789.

[69] V. Roy, S. Gishkori, and G. Leus, "Spatial rainfall mapping from Path-Averaged rainfall measurements exploiting sparsity," in *GlobalSIP 2014: Information Processing for Big Data*, Atlanta, USA, Dec. 2014.

[70] Y. Liberman, "Object tracking extensions for accurate recovery of rainfall maps using microwave sensor network," in *Proceedings of the 22nd European Signal Processing Conference (EUSIPCO)*. IEEE, 2014, pp. 1322–1326.

[71] E. J. Candès and M. B. Wakin, "An introduction to compressive sampling," *IEEE Signal Processing Magazine*, vol. 25, no. 2, pp. 21–30, 2008.

[72] A. Charles, M. S. Asif, J. Romberg, and C. Rozell, "Sparsity penalties in dynamical system estimation," in *45th Annual Conference on Information Sciences and Systems (CISS), 2011*. IEEE, 2011, pp. 1–6.

[73] S. Farahmand, G. B. Giannakis, G. Leus, and Z. Tian, "Tracking target signal strengths on a grid using sparsity," *EURASIP Journal on Advances in Signal Processing*, vol. 2014, no. 1, pp. 1–17, 2014.

[74] A. S. Charles and C. J. Rozell, "Re-weighted l_1 dynamic filtering for time-varying sparse signal estimation," *arXiv preprint arXiv:1208.0325*, 2012.

[75] ——, "Convergence of basis pursuit de-noising with dynamic filtering," in *GlobalSIP 2014: Information Processing for Big Data*, Atlanta, USA, Dec. 2014.

[76] A. Carmi, P. Gurfil, and D. Kanevsky, "Methods for sparse signal recovery using Kalman filtering with embedded pseudo-measurement norms and quasi-norms," *IEEE Transactions on Signal Processing*, vol. 58, no. 4, pp. 2405–2409, 2010.

[77] W. Dai, D. Sejdinovic, and O. Milenkovic, "Gaussian dynamic compressive sensing," in *International Conference on Sampling Theory and Application(SampTA)*, 2011.

[78] K. Xu, C. K. Wikle, and N. I. Fox, "A kernel-based spatio-temporal dynamical model for nowcasting weather radar reflectivities," *Journal of the American Statistical Association*, vol. 100, no. 472, pp. 1133–1144, 2005.

[79] R. Olsen, D. Rogers, and D. B. Hodge, "The ar^b relation in the calculation of rain attenuation," *IEEE Transactions on Antennas and Propagation*, vol. 26, no. 2, pp. 318–329, Mar 1978.

[80] D. Atlas and C. Ulbrich, "Path-and area-integrated rainfall measurement by microwave attenuation in the 1-3 cm band," *Journal of Applied Meteorology*, vol. 16, no. 12, pp. 1322–1331, 1977.

[81] A. Jameson, "A comparison of microwave techniques for measuring rainfall," *Journal of Applied Meteorology*, vol. 30, no. 1, pp. 32–54, 1991.

[82] H. Leijnse, R. Uijlenhoet, and J. Stricker, "Microwave link rainfall estimation: Effects of link length and frequency, temporal sampling, power reso-

lution, and wet antenna attenuation," *Advances in Water Resources*, vol. 31, no. 11, pp. 1481–1493, 2008.

[83] A. Berne and R. Uijlenhoet, "Path-averaged rainfall estimation using microwave links: Uncertainty due to spatial rainfall variability," *Geophysical research letters*, vol. 34, no. 7, 2007.

[84] N. Cressie, *Statistics for Spatial Data: Wiley Series in Probability and Statistics*. Wiley-Interscience New York, 1993.

[85] J. Stroud, P. Muller, and B. Sansó, "Dynamic models for spatiotemporal data," *Journal of the Royal Statistical Society. Series B, Statistical Methodology*, pp. 673–689, 2001.

[86] E. Morin, D. C. Goodrich, A. Maddox, Robert, X. Gao, H. V. Gupta, and S. Sorooshian, "Spatial patterns in thunderstorm rainfall events and their coupling with watershed hydrological response," *Advances in Water Resources*, vol. 29, no. 6, pp. 843–860, 2006.

[87] M. Tanaka and T. Katayama, "Robust fixed-lag smoother for linear systems including outliers in the system and observation noises," *International journal of systems science*, vol. 19, no. 11, pp. 2243–2259, 1988.

[88] D. L. Donoho and X. Huo, "Uncertainty principles and ideal atomic decomposition," *IEEE Transactions on Information Theory*, vol. 47, no. 7, pp. 2845–2862, November 2001.

[89] D. L. Donoho, M. Elad, and V. N. Temlyakov, "Stable recovery of sparse overcomplete representations in the presence of noise," *IEEE Transactions on Information Theory*, vol. 52, no. 1, pp. 6–18, December 2005.

[90] M. Elad, "Optimized projections for compressed sensing," *IEEE Transactions on Signal Processing*, vol. 55, no. 12, pp. 5695–5702, November 2007.

[91] S. J. Kim, K. Koh, M. Lustig, S. Boyd, and D. Gorinevsky, "An interior-point method for large-scale l 1-regularized least squares," *IEEE Journal of Selected Topics in Signal Processing*, vol. 1, no. 4, pp. 606–617, December 2007.

[92] C. Mallows, "Some comments on cp," *Technometrics*, vol. 42, no. 1, pp. 87–94, 2000.

[93] H. Akaike, *Information theory and an extension of the maximum likelihood principle*. Springer, 1998.

[94] G. Schwarz, "Estimating the dimension of a model," *The annals of statistics*, vol. 6, no. 2, pp. 461–464, 1978.

[95] D. P. Bertsekas and J. N. Tsitsiklis, *Parallel and distributed computation: numerical methods*. Prentice hall Englewood Cliffs, NJ, 1989, vol. 23.

[96] K. V. Mardia, C. Goodall, E. J. Redfern, and F. J. Alonso, "The kriged Kalman filter," *Test*, vol. 7, no. 2, pp. 217–282, 1998.

[97] S. J. Kim, E. D. Anese, and G. B. Giannakis, "Cooperative spectrum sensing for cognitive radios using kriged Kalman filtering," *IEEE Journal of Selected Topics in Signal Processing*, vol. 5, no. 1, pp. 24–36, February 2011.

[98] K. Rajawat, E. Dall'Anese, and G. Giannakis, "Dynamic network delay cartography," *IEEE Transactions on Information Theory*, vol. 60, no. 5, pp. 2910–2920, May 2014.

[99] M. Patan, *Optimal sensor networks scheduling in identification of distributed parameter systems*. Springer Science & Business Media, 2012, vol. 425.

[100] Y. Mo, R. Ambrosino, and B. Sinopoli, "Sensor selection strategies for state estimation in energy constrained wireless sensor networks," *Automatica*, vol. 47, no. 7, pp. 1330–1338, July 2011.

[101] H. Jamali-Rad, A. Simonetto, X. Ma, and G. Leus, "Distributed sparsity-aware sensor selection," *IEEE Transactions on Signal Processing*, vol. 63, no. 22, pp. 5951–5964, November 2015.

[102] S. Liu, N. Cao, and P. K. Varshney, "Sensor placement for field estimation via poisson disk sampling," in *IEEE Global Conference on Signal and Information Processing (GlobalSIP)*. Washington, DC, USA: IEEE, December 2016, pp. 520–524.

[103] V. Roy, A. Simonetto, and G. Leus, "Spatio-temporal sensor management for environmental field estimation," *Signal Processing*, vol. 128, pp. 369–381, November 2016.

[104] S. Liu, S. P. C. Chepuri, M. Fardad, E. Maşazade, G. Leus, and P. K. Varshney, "Sensor selection for estimation with correlated measurement noise,"

IEEE Transactions on Signal Processing, vol. 64, no. 13, pp. 3509–3522, April 2016.

[105] M. Grant, S. Boyd, and Y. Ye, "CVX: Matlab software for disciplined convex programming," 2008.

[106] A. Simonetto and E. Dall'Anese, "Prediction-correction algorithms for time-varying constrained optimization," *IEEE Transactions on Signal Processing*, vol. 65, no. 2, pp. 5481–5494, October 2017.

[107] M. J. D. Zachariah, M. Sundin and S. Chatterjee, "Alternating least-squares for low-rank matrix reconstruction," *IEEE Signal Processing Letters*, vol. 19, no. 4, pp. 231–234, February 2012.

Samenvatting

Als we onze steeds veranderende omgeving beter kunnen observeren en voorspellen, dan leidt dit tot een veiligere and gezondere samenleving. Sensornetwerken spelen hierbij een belangrijke rol. De twee fundamentele aspecten van zulke sensornetwerken zijn de nauwkeurigheid en energiezuinigheid. Daarom zoeken we naar manieren om de kosten van sensornetwerken te verlagen (het aantal sensoren, hun energieverbruik, het onderhoud) zonder nefaste impact op de prestatie van het sensornetwerk. Dit kan bijvoorbeeld door de fysische eigenschappen van de omgeving uit te buiten via stochastische omgevingsmodellen. In deze thesis stellen we signaalverwerkingstechnieken, voor die gebruik maken van zulke stochastische omgevingsmodellen om het aantal sensoren in een sensornetwerk te verlagen zonder een al te grote impact op de kwaliteit van de resultaten. We richten ons hierbij op een klasse van omgevingsmodellen die voldoet aan typische fysische eigenschappen (zoals diffusie en advectie) verantwoordelijk voor de spatiotemporele evolutie van het omgevingsveld.

We ontwikkelen eerst een wiskundig model dat de sensorobservaties verbindt met de intensiteit van het omgevingsveld. Op basis van dit model stellen we daarna een uitgebreid omgevingsobservatiesysteem inclusief sensormanagement voor, voor het vergaren van de metingen, en het schatten van de spatiotemporele evolutie van de veldintensiteit.

De ontwikkelde sensormanagement techniek kan zowel gebruikt worden voor stationaire als niet-stationaire omgevingsvelden. Deze techniek is gebaseerd op het oplossen van een optimalisatieprobleem en geeft aan hoeveel sensoren er nodig zijn en waar/wanneer die moeten geactiveerd worden om een bepaalde prestatie te behalen in de zin van gemiddelde kwadratische fout. Dus het belangrijkste doel van deze sparse-sensing techniek is om zo min mogelijk sensoren te activeren zonder

een al te groot prestatieverlies. Verschillende methodes om het hierboven vermelde optimalisatieprobleem op te lossen worden voorgesteld, zowel voor offline als online toepassingen.

We presenteren verder een praktische toepassing, namelijk een regenradar gebaseerd op de verzwakking van microgolfverbindingen. We beschrijven verschillende manieren waarop de fysische eigenschappen van regenval in het wiskundig model kunnen worden opgenomen. We vergelijken daarna de prestatie van ons systeem met klassieke methodes, zoals het *extended* Kalman filter.

We breiden ons systeem ook uit naar een bredere klasse van omgevingsvelden waarbij we zowel stationaire als niet-stationaire componenten van het veld in rekening kunnen brengen. Hiervoor ontwikkelen we een sensormanagement systeem (plaatsing van sensoren in ruimte en tijd) en veldschattingsalgoritme op basis van het zogenaamde *kriged* Kalman filter.

We behandelen ook het scenario waarbij de fysische voorkennis van het omgevingsveld ontbreekt of onnauwkeurig is. In dat geval moeten de onderliggende dynamische karakteristieken van het veld worden geschat. Hierbij kan worden verondersteld dat het echte omgevingsveld gekend is of niet.

Propositions

1. Cognizance of the statistical nature of the spatio-temporal variability of the environmental field is instrumental for future smart weather monitoring systems.

2. It is often better to have accurate a-priori knowledge about the environment than additional measurements in an environmental sensor network.

3. More correlation over space and time of an environmental field allows for less measurements for the same estimation performance. So, a highly correlated environmental field is a good platform for the implementation of "sparse sensing".

4. Rainfall monitoring using cellular networks can be engineered as robust as the state-of-the-art monitoring systems (such as gauge-adjusted radar) by exploiting spatial and/or temporal properties of rainfall.

5. To solve an underdetermined tracking scenario, a suboptimal Kalman filter leads to a viable solution.

6. Philosophically, compressive sampling (CS) can be viewed as a subset of Bayesian learning.

7. Cost and feasibility of a practical implementation are as important as the scientific novelty for the acceptance of an application-specific signal processing paper.

8. For an ideal society, "politics" and "religion" should be strongly uncorrelated.

9. The climate of The Netherlands is one of the motivating factors behind the sportive nature of Dutch people.

10. A cat is a better pet than a dog for a PhD student.
11. "*The only thing I know, is that I know nothing*"- Socrates

Acknowledgments

Life is full of surprises. I perfectly understood this after I left my country, when I was 24 years old and came to a country of friendly and sportive people, overwhelming wind, picturesque landscapes, beautiful tall women, cheese, and “bitterballen”. I can proudly say, I love Netherlands!

First of all, I would like to thank my supervisor, Prof. Geert Leus, for all his teaching and guidance throughout my PhD. In every step of my PhD research, he was the best teacher of my life. He is a person with remarkable intelligence, deep knowledge, always full of energy and a wonderful sense of humor. We really enjoyed traveling together in conferences in Saint Martin, Dutch Antilles and in Atlanta, USA. Also, in a tough time of my personal life (during my PhD) he was the greatest support. Finally, I also thank him to translate my thesis summary in Dutch. I really feel honored to pursue my PhD work under his supervision.

I would like to thank Prof. Alexander Yarovoy for being my co-promoter. His all time inspirations and positive comments made my life easier during my PhD. I would like to thank Prof. Alle-Jan van der Veen. Every technical discussion with him and his comments on my presentations were extremely important for the next step of my research. Also, I thank him for his endless effort to maintain the integrity of the CAS group. I also thank Prof. M.C. Veraar, TU Delft for the interesting discussions regarding stochastic PDEs. I thank Prof. Herman Russchenberg for all the nice discussions we had during SHINE project meetings or meetings at TU Delft. I thank Prof. R. Uijlenhoet, Dr. Aart Overeem and Dr. Hidde Leijnse from KNMI and Wageningen University. I thank my project leader Dr. Birna van Riemsdijk and all other SHINE project members. I thank Dr. H. Nikookar for his guidance, when I was an Erasmus student.

I sincerely thank the committee members for their comments which helped me

to improve my thesis.

I thank all of my colleagues at the 17th floor of the TU Delft EWI building with whom I had my memorable five years of PhD life. My special thanks to my first office-mate Dony, who was always very helpful in the first days of my PhD life. I thank Shahzad for all his help in my starting days. It was also a great pleasure to work with him. The most of the time of my PhD days, I spent with Maria, Seyran and Andrea as they were my longest office-mates. I do not have enough words to thank Maria for all her empathy, love and support. Lots of thanks to Seyran for all her help and support. It was a great pleasure to see her daughter Dariya growing up in front of our eyes. Finally, my sincere thanks to Andrea, the mathematician, who always had some solution to all the problems. He helped not only me but many people in the 17th floor to make their all non-convex problems to a simple convex one! I thank Elvin both as a friend and also as a course-mate. We really had fun time, when we attended the convex optimization course together. Last year of my PhD, I had two amazing colleagues, Tarik and Farnaz. Special thanks to Tarik for your help in the last days of my PhD. Finally, I thank Minaksie for always being with me since last six years and always taking care of me even when I left Delft.

I also had amazing friends in Delft outside my work. I thank Merima for all her love and support. Specially, thanks for all the sandwiches for dinner, when me and Tarik were working late in the evening. I thank Hanaa and Rohit for all their love and kindness. Special thanks to Hanaa for surprising me every time by cooking some delicious dishes, whenever I visited her house. I thank Qurrah and Waqas for always supporting me. Also, special thanks to Waqas, who was my first office-mate at TU Delft in my Erasmus days and now he is my colleague.

In my current workplace, i.e., NXP Semiconductors, High Tech Campus, Eindhoven, I first thank my manager Nur, who was always supportive with my PhD. I also thank my project leader Alessio. I thank all of my present colleagues in the Algorithms and Software Innovation section. I specially thank Arie, Feike, Francesco, Hong, Massimo, Jeroen, Marco, Ozgun, Harish, Liang, Baris, Marinas and Giorgio.

Life beyond work in Eindhoven is exciting! I thank all of my friends in Eindhoven, who are a part of my everyday life in Eindhoven. First, I thank Anna and Arjan for all your company, help, friendship and support. I thank Rowan for always being my friend since the first time we met. I thank Cherrysa for always being with me as a sweet sister. I must say my life outside work in Eindhoven would never be so much exciting without Rowan and Cherry. I thank Mariette (my landlady) for all her love and care. I also thank Niek, Farid, Chantal, Anna (Italy), Iris, Mathias,

Elkan, Evi, Franka, Yvonne, Stijn, Dillon, Fred and Jos (the principal!).

Finally, one important person in my life is Ladli, my pet dog since I was 23. I always wish her to stay happy and healthy for the rest of her life. I believe that she is in good hands!

Curriculum Vitae

Venkat Roy was born in 19th December, 1985 in Pondicherry, India. He received the Bachelor of Technology (B.Tech.) degree in electronics and communication engineering, in 2008 from the West Bengal University of Technology (WBUT), West Bengal, India. In 2010, he received the Master of Technology (M.Tech.) degree in Radio Physics and Electronics from the University of Calcutta, India. He was an Erasmus Mundus "Mobility for Life" scholar (funded by European Commission) for one year (2011) at the Delft University of Technology, Delft, The Netherlands. In this period, he received the best student paper award at the 18th IEEE Symposium on Communications and Vehicular Technology in Benelux, Ghent, Belgium. In 2012, he joined the circuits and systems (CAS) group at the Faculty of Electrical Engineering, Mathematics and Computer Science (EEMCS) of the Delft University of Technology in pursuance of the Ph.D. degree. During his Ph.D., he had actively collaborated with the Royal Netherlands Meteorological Institute (KNMI). His research interests include statistical signal processing, compressed sensing, signal processing for environment monitoring and radar signal processing.

Publications

Journals

- V. Roy, A. Simonetto, and G. Leus, “Spatio-temporal field estimation using kriged Kalman filter (KKF) with sparsity-enforcing sensor placement”, *Sensors*, vol. 18, no. 6, pp. 1778, April, 2018.

- V. Roy, A. Simonetto, and G. Leus, “Spatio-temporal sensor management for environmental field estimation”, *Elsevier Signal Processing*, vol. 128, pp. 369-381, November 2016.

- V. Roy, S. Gishkori, and G. Leus, “Dynamic rainfall monitoring using microwave links,” *EURASIP Journal on Advances in Signal Processing*, vol. 2016, no. 1, pp. 1-17, December 2016.

Conferences

- V. Roy and G. Leus, “Correlation-aware sparsity-enforcing sensor placement for spatio-temporal field estimation”, in *Proc. IEEE International Conference on Acoustics, Speech and Signal Processing (ICASSP)*, Brisbane, Australia, April 2015, pp. 340-343.

- V. Roy, S. Gishkori, and G. Leus, “Spatial rainfall mapping from path- averaged rainfall measurements exploiting sparsity”, in *Proc. IEEE Global Conference on Signal and Information Processing (GlobalSIP)*, Atlanta, USA, December 2014, pp. 321-325.

- V. Roy, S. P. Chepuri, and G. Leus, “Sparsity-enforcing sensor selection for DOA estimation”, in *Proc. IEEE Computational Advances in Multi-Sensor Adaptive Processing (CAMSAP)*, Saint Martin, December 2013, pp. 340-343.

Glossary

Notations

x	Scalar x.
$\mathbf{x}$	Vector $\mathbf{x}$.
$\hat{\mathbf{x}}$	Estimate of vector $\mathbf{x}$.
$\mathbf{x}^T$	Transpose of vector $\mathbf{x}$.
$[\mathbf{x}]_i$	i-th entry of the vector $\mathbf{x}$.
$\mathbf{X}$	Matrix $\mathbf{X}$.
$\mathbf{X}^{-1}$	Inverse of matrix $\mathbf{X}$.
$[\mathbf{X}]_{i,j}$	(i,j)-th element of the matrix $\mathbf{X}$.
$\mathrm{vec}(\mathbf{X})$	Column-wise vectorization of the elements of matrix $\mathbf{X}$.
$\mathbf{I}_N$	Identity matrix of size $N \times N$.
$\mathbf{1}_{M\times N}$	$M \times N$ matrix with all components one.
$\mathbf{0}_{M\times N}$	$M \times N$ matrix with all components zero.
$\otimes$	Kronecker product.
$\mathrm{diag}(\mathbf{x})$	Diagonal matrix with the elements of $\mathbf{x}$ on the main diagonal.
$\mathrm{diag}(\mathbf{X})$	Vector with the elements of the main diagonal of $\mathbf{X}$.

$\mathrm{diag}_X(\mathbf{x})$ Diagonal matrix with the elements of $\mathbf{x}$ on the main diagonal without any all-zero rows.

$\mathrm{blkdiag}(\cdot)$ Block diagonal matrix with the matrix blocks in its argument on the main diagonal.

$||\mathbf{x}||_p$ ℓ_p-norm of $\mathbf{x}$, i.e., $(\sum_{i=0}^{N-1} |[\mathbf{x}]_i|^p)^{1/p}$.

$\mathrm{tr}(\mathbf{X})$ Trace of matrix $\mathbf{X}$, i.e, sum of its diagonal elements.

$\mathbb{E}[x]$ Statistical expectation of x.

$(x)_+$ $(x)_+ = x$ iff $x > 0$ otherwise $(x)_+ = 0$.

$\mathbb{R}$ Set of real numbers.

$\mathbb{R}_+$ Set of non-negative real numbers.

$\mathbb{R}^N$ Set of N-length vectors with real elements.

$\mathbb{R}^{M\times N}$ Set of matrices of size $M \times N$ with real elements.

$\mathbb{S}^N$ Set of symmetric matrices of size $N \times N$.

$\mathbb{S}^N_+$ Set of symmetric positive semidefinite matrices of size $N \times N$.

$\mathbb{S}^N_{++}$ Set of symmetric positive definite matrices of size $N \times N$.

Abbreviations

ADC	analog-to-digital converter
BHM	Bayesian hierarchical modelling
BIBO	bounded input bounded output
CRB	Cramér-Rao bound
CS	compressive sensing
DCT	discrete cosine transform
DOA	direction of arrival
EKF	extended Kalman filter

EHM	empirical hierarchical modelling
IDE	integro-difference equation
KLT	Karhunen-Loeve transform
LMMSE	linear minimum mean square error
MCMC	Markov chain Monte Carlo
MIL	matrix inversion lemma
MSE	mean square error
PDE	partial differential equation
PDF	probability density function
POI	point of interest
SNR	signal to noise ratio
SPDE	stochastic partial differential equation
UKF	unscented Kalman filter
WLS	weighted least square
WSN	wireless sensor network